Theoretical studies for revealing the co-evolution of galaxies and supermassive black holes

銀河と超大質量ブラックホールの共進化についての理論的研究

Hikari SHIRAKATA 白方 光
Department of Cosmosciences, Graduate School of Science,
Hokkaido University

March 2019

Abstract

To reveal the co-evolution between galaxies and supermassive black holes (SMBHs), I have updated a semi-analytic model of galaxy formation, *"New Numerical Galaxy Catalogue"* (ν^2 GC). I can employ large volume N-body merger trees. Because of the broad dynamic range from an SMBH to its host galaxy, the co-evolution scenario is unclear even after 30 years from the discovery of its possibility. The important things to understand the co-evolution are: (1) to create theoretical models which can explain the observational properties of galaxies and SMBHs, (2) to carefully analyse whether the model is unique, i.e. whether the other models cannot produce the same results. I present three new findings in this thesis. First, I show the effect of the seed black hole (BH) mass on the $M_{\rm BH}$ – $M_{\rm bulge}$ relation. I compare the model results, in which I employ three different types of the seed mass distribution, with the observational data. I find that to explain the relation, the seed BH mass should be dominated by $10^3 M_\odot$, not direct collapse BHs with $10^5 M_\odot$. Also, I find that to get more stringent constraints on the seed BH mass distribution, observations of less massive galaxies at low redshift is more powerful than those of massive galaxies at high redshift because the difference resulting from the seed BH mass becomes difficult to detect. Second, I discuss the growth timescale of SMBHs, considering the effect of the angular momentum loss timescale in the circumnuclear disc and/or accretion disc, which has been neglected in other semi-analytic models. I find that the number density of AGNs at $z < 1.5$ and at hard X-ray luminosity $< 10^{44}$ erg/s is underestimated compared with recent observational estimates when I assume the exponentially decreasing accretion rate and the accretion timescale which is proportional to the dynamical time of the host halo or the bulge, as is often assumed in SA models. This problem can be achieved when I assume the angular momentum loss timescale, which is a function of the SMBH mass and the accreted gas mass. Such models predict a longer accretion timescale for less luminous AGNs at $z < 1.0$ than luminous QSOs whose accretion timescale would be 10^{7-8} yr. With this newly introduced accretion timescale, our model can explain the observed luminosity functions of AGNs at $z < 6.0$. Finally, I show the theoretical prediction of the Eddington ratio distribution functions at $0 < z < 8$. The distribution is qualitatively consistent with observational estimates at low redshift. I find that the growth rate of BHs at higher redshift exceeds the Eddington limit more easily because the typical gas fraction of the host galaxies is higher at higher redshift. Moreover, I also find that the super-Eddington growth is more common for less massive SMBHs, supporting an idea that SMBHs have grown via super-Eddington accretion. These results indicate the "slowing-down" of cosmic growth of SMBHs. I also show the effect of the sample selection on the shape of the Eddington ratio distribution functions and find that shallower observations miss AGNs with both a smaller and higher Eddington ratio. From these three results, I conclude that less massive SMBHs (naively, less luminous AGNs) in the local Universe play a role for revealing the co-evolution, although recent observations have focused on (mid-) luminous AGNs at higher redshift.

Table 1: List of abbreviations used in this thesis.

AD	accretion disc
ADAF	advection dominated accretion flow
AGB	asymptotic giant branch
AGN	active galactic nucleus
ALMA	Arecibo large millimeter/submillimeter array
BH	black hole
BHL	Bondi-Hoyle-Littleton
BLR	broad line region
CMB	cosmic microwave background
CND	circumnuclear disc
DI	disc instability
DM	dark matter
DOG	dust obscured galaxy
ERDF	Eddington ratio distribution function
FWHM	full width half maximum
GMC	giant molecular cloud
HSC	hyper sprime-cam
HSC-SSP	hyper sprime-cam subaru strategic project
HyLIRG	hyper-luminous infrared galaxy
IR	infrared
ISM	initial mass function
KS relation	Kennicutt-Schmidt relation
LF	luminosity function
MCMC	Markov Chain Monte Carlo
MF	mass function
NFW	Navarro-Frenk-White
NLR	narrow line region
QSO	quasi-stellar object
quasar	quasi-stelar radio source
RIAF	radiative inefficient advection flow
SA model	semi-analytic model of galaxy formation
(s)SFR	(specific) star formation rate
SMBH	supermassive black hole
SNe	supernovae
ULIRG	ultra-luminous infrared galaxy
UV	ultraviolet

Table 2: Definitions of parameters and variables which appears in this thesis. They have broadly been used in previous studies.

Ω_0	matter fraction
Ω_b	baryon fraction
λ_0	Λ fraction
σ_8	present root-mean-square matter fluctuation averaged over a sphere of radius $8h^{-1}$ Mpc
n_s	scalar spectral index
H_0	current Hubble constant
h	current hubble parameter
z	redshift
c	speed of light
m_p	proton mass
μ	mean molecular weight
G	gravitational constant
$k_{\rm B}$	Boltzman constant
σ_T	cross section of Tompson scattering
α	locked-up mass fraction
p	chemical yield
$M_\odot$	solar mass
$Z_\odot$	solar metallicity
η	radiation efficiency of AGNs
$r_{\rm Sch}$	Schwarzschild radius
$\dot{m}$	accretion rate normalised by the Eddington rate
$\lambda_{\rm Edd}$	bolometric luminosity of AGNs normalised by the Eddington luminosity

Table 3: List of variables and adjustable parameters which are originally used in this thesis.

Notation	Definition	First appearance
$\langle f_b \rangle$	averaged mass fraction of baryon to the matter fraction ($\Omega_{\rm b}/\Omega_0$)	2.2
$f_b(M_h, z)$	mass fraction as a function of the halo mass and redshift	
M_h	hotst halo mass	
$M_c(z)$	characteristic mass as a function of redshift, under which the halo is sensitive to the photoionisation heating	
$\rho_{\rm NFW}(r)$	dark matter halo density profile assuming NFW profile	
r_s	scale radius of DM haloes	
$\rho_{\rm hot}(r)$	hot gas halo density profile assuming the isothermal profile	
r_c	scale radius of hot gas haloes	
$r_{\rm cool}(t)$	cooling radius	
$t_{\rm cool}$	cooling time	
c_r	concentration parameter of dark matter haloes	
n_e	electron number density	
$T_{\rm Vir}$	Virial temperature	
$\Lambda(T_{\rm vir}, Z_{\rm hot})$	cooling function as a function of the Virial temperature and hot gas metallicity	
$V_{\rm circ}$	circular velocity of DM haloes	
$r_{\rm acc}$	accretion radius	
$r_{\rm ff}$	free fall radius	
$t_{\rm ff}$	free fall time	
Ψ	star formation rate	2.3
$M_{\rm cold}$	cold gas mass of a galaxy	
$\tau_{\rm star}$	star formation timescale	
$\tau_{\rm d}$	dynamical timescale of a galactic disc	
$\epsilon_{\rm star}$	adjustable parameter determining star formation efficiency	
$V_{\rm star}$	adjustable parameter of the critical disc velocity for star formation	
$\alpha_{\rm star}$	adjustable parameter for star formation	
$\tau_{\rm reheat}$	reheating timescale	
$\beta(V_d)$	mass loading factor	
$V_{\rm d}$	disc velocity	
$V_{\rm hot}$	adjustable parameter of the critical disc velocity for mass loading factor	
$\alpha_{\rm hot}$	adjustable parameter for the mass-loading factor	
$M_{\rm reheat}$	reheated mass by SNe	
$\alpha_{\rm return}$	returned gas fraction from the reservoir	
$M_{\rm ej}$	returned gas mass from the reservoir before the halo mass doubles	
$M_{\rm star}$	stellar mass	
$M_{\rm BH}$	BH mass	
$Z_{\rm cold}$	cold gas metallicity	
$Z_{\rm hot}$	hot gas metallicity	

continued on the next page

continued from the previous page

$\tau_{\rm mrg}$	merger timescale of galaxies	2.4
$\tau_{\rm fric}$	dynamical friction timescale	
$f_{\rm mrg}$	adjustable parameter of the ratio between merger and dynamical friction timescales	
ϵ	orbital circularity	
$R_{\rm circ,s}$	radius of the circular orbit of satellite haloes	
M_s	satellite halo mass	
C	fitting parameter for the dynamical friction timescale	
$k_{\rm MH}$	merger rate by random collisions per 1 Gyr	
$R_{\rm vir}$	virial radius of the host halo	
$r_{\rm gal}$	galaxy radius	
$\sigma_{\rm gal}$	1D velocity dispersion of a galaxy	
$\sigma_{\rm halo}$	1D velocity dispersion of a halo	
$M_i (i = 0, 1, 2)$	baryon mass (cold gas + stars + a BH) 0: merger remnant 1: primary 2: secondary	
$\Delta M_{\rm 1ds}$	migrated stellar mass from primary's disc	
μ	baryon mass ratio of merging galaxy pair	
$f_*(\mu)$	destroyed fraction of the disc	
$M_{\rm 1ds}$	disc stellar mass of the primary galaxy	
$M_{\rm 1dg}$	disc gas mass of the primary galaxy	
$f_{\rm 1d}$	disc fraction of the primary galaxy	
$f_{\rm 1g}$	gas fraction of the primary's disc	
b	peri-galacticon distance before coalescence	
θ	inclination of the orbit of the secondary relative to the primary's disc	
$R_{\rm gas}$	radius in which the disc gas migrates to the bulge	
$r_{\rm ds}$	disc scale radius	
$f_{\rm major}$	baryon mass ratio of merging pair above which primary's disc is completely destroyed	
$\Delta M_{\rm star,burst}$	stellar mass formed in a starburst	
$M^0_{\rm cold}$	cold gas mass in the bulge immediately after a merger	
$V_{\rm max}$	maximum rotation velocity which reflects the gravitational potential	
$V_{\rm max,NFW}$	maximum rotation velocity of DM haloes with the NFW profile	
$V_{\rm max,bulge}$	maximum rotation velocity of the bulge	
$M_{\rm disc}$	disc mass (cold gas + stars)	
$M_{\rm bulge}$	bulge mass (cold gas + stars)	
$\epsilon_{\rm DI,crit}$	adjustable parameter of stable disc threshold	
$\langle \lambda_{\rm H} \rangle$	mean value of the dimensionless spin parameter	
$R_{\rm init}$	initial radius of the hot gas halo	
$\sigma_{\rm 1D}$	1-dimensional velocity dispersion of the bulge	
$r_{\rm b}$	bulge size	
$\Delta M_{\rm ds,DI}$	stellar mass which migrates from disc to bulge by disc instabilities	

continued on the next page

continued from the previous page

$\Delta M_{\rm dg,DI}$	gas mass which migrates from disc to bulge by disc instabilities	
$f_{\rm bar}$	migrated disc fraction by disc instabilities	
$\lambda_{\rm H}$	dimensionless spin parameter	2.5
$R_{\rm d}$	effective radius of a cold gas disc	
$R_{\rm d,new}$	new effective radius after mergers or disc instabilities	
$M_{\rm 0d}$	disc mass of a galaxy after a merger	
E_i	total energy of each galaxy 0: merger remnant 1: primary 2: secondary	
M_b	mass of bulge stars	
M_d	mass of disc stars	
$M_{\rm cold}$	mass of cold gas	
V_b	velocity dispersion of bulges	
$M_{\rm DM,1}$	DM mass which affects the bulge potential	
$M_{\rm h0}$	adjustable parameter of typical halo mass above which the DM affects the bulge potential	
$\alpha_{\rm h}$	adjustable parameter for the DM effects on the bulge potential	
$E_{\rm 0,b}$	bulge total energy of the merger remnant	
$E_{\rm 0,d}$	disc total energy of the merger remnant	
$f_{\rm diss}$	fraction of dissipated energy from the merging system	
$E_{\rm orb}$	orbital energy	
$\kappa_{\rm diss}$	adjustable parameter for the dissipated energy	
$f_{\rm gas}$	gas fraction of the merging system (primary + secondary)	
$M_{\rm seed}$	seed black hole mass	
$\Delta M_{\rm acc}$	accreted gas mass per a starburst	
$\dot{M}_{\rm BH}$	mass accretion rate onto a black hole	
$t_{\rm acc}$	accretion timescale of a black hole	
$t_{\rm start}$	starting time of the gas accretion	
$\dot{m}_{\rm crit}$	accretion rate normarised by the Eddington limit at which the accretion is the Eddington limit	
$L_{\rm bol}$	bolometric luminosity of an AGN	
$M_{\rm UV}$	absolute UV (1450 Å) magnitude (AB)	
$M_{\rm B}$	absolute B-band magnitude (AB)	
$L_{\rm UV}$	UV (1450 Å) luminosity	
L_X	X-ray (2-10 keV) luminosity	
$t_{\rm dyn}$	dynamical time of the halo	
$\alpha_{\rm cool}$	adjustable parameter for the AGN feedback	
$\epsilon_{\rm SMBH}$	adjustable parameter for the AGN feedback	
$\tau_{\rm dust}$	dust optical depth	2.7
r_d	effective radius of the disc	
τ_0	adjustable parameter for the scaling of the optical depth	
B/T	bulge to total ratio	
$f_{obs,UV}$	observable fraction of AGNs in UV-band	
$A(z)$	scaling of the observable fraction	

continued on the next page

continued from the previous page

$\beta(z)$	slope of the luminosity for determining the observable fraction	
$A_i(i=0,1)$	adjustable parameters for $A(z)$	
$\beta_i(i=0,1)$	adjustable parameters for $\beta(z)$	
r	Pearson's r	2.8
$M_{\rm HI}$	HI gas mass	
$f_{\rm gas,test}$	gas fraction of a galaxy which depends on the disc mass	
M_K	absolute K-band magnitute (AB)	
$M_{\rm FUV}$	absolute GALEX FUV band magnitude (AB)	
M_*	stellar mass of a galaxy	
$z_{\rm form}$	redshift at which galaxies newly form	3.3
$\langle M_{\rm BH}\rangle_3$	the average black hole mass when $M_{\rm seed}=10^3M_\odot$	3.4
$\langle M_{\rm BH}\rangle_5$	the average black hole mass when $M_{\rm seed}=10^5M_\odot$	
$t_{\rm dyn,bulge}$	dynamical time of the bulge	4.2
$\alpha_{\rm bulge}$	adjustable parameter of accretion timescale	
$t_{\rm loss}$	timescale for angular momentum loss in CND and accretion tdisc	
$t_{\rm loss,0}$	adjustable parameter of $t_{\rm loss}$	
$\gamma_{\rm BH}$	adjustable parameter of $t_{\rm loss}$	
$\gamma_{\rm gas}$	adjustable parameter of $t_{\rm loss}$	
$\lvert v_{\rm r}\rvert$	radial velocity of the accreted gas	
$\hat{r}$	distance from the black hole normalised by the Schwaltzshild radius	
α	viscous parameter	
$r_{\rm sg}$	radius of the self gravitating accretion disc	
f	non-dimensional variable for viscous timescale	
$t_{\rm vis}$	viscous timescale	
$\dot{M}_{\rm peak}$	peak accretion rate	4.3
$\dot{m}_{\rm knee}$	the accretion rate normalised by the Eddington accretion rate at which the slope of the Eddington ratio distribution function becomes -1	5.2
$t_{\rm age}$	age of the Universe	
i	apparent i-band magnitude (AB)	
g	apparent g-band magnitude (AB)	

Contents

Chapter 1

Introduction

Galaxies are one of the main components of the Universe. Understanding galaxy formation and evolution is thus one of the main goals of astrophysics. It is well-known that almost all galaxies have a supermassive black hole (SMBH) at their centre and the mass of SMBHs correlates with properties of their host galaxies, such as the mass and velocity dispersion of the bulges (e.g. Magorrian et al. 1998; Ferrarese & Merritt 2000; Häring & Rix 2004; McConnell & Ma 2013). SMBHs and their host galaxies would thus have co-evolved with each other; their growth mechanisms would have been involved (see, however, Jahnke & Macciò 2011). The growth of the SMBHs is considered to relates to that of especially bulges and galactic bars (e.g. Mihos & Hernquist 1994; Wada & Habe 1995) rather than the growth of whole galaxies. The growth of the SMBHs is mainly the gas accretion, which causes active galactic nuclei (AGNs). AGN radiation, jets, and outflow inject the energy and/or angular momentum to the surrounding gas, which would cause the increase/decrease of the star formation rate (SFR) of their host galaxies (e.g. Wagner et al. 2016; for a review). This "co-evolution" is a standing question in astrophysics and has been investigated for more than three decades theoretically and observationally. Such work has focussed on the mechanism of black hole (BH) feeding and the energetic feedback resulting from the BH growth in the context of galaxy formation. In this chapter, I briefly review the structure formation in the Universe, galaxy formation, and evolution of SMBHs and AGNs. After that, I focus on the progress of the studies about the co-evolution.

1.1 Structure Formation

The Universe consists of baryon, dark matter (DM), and "dark energy", which is the unknown energy components accelerating the expansion of the Universe. The density parameters of each component are obtained by observing the cosmic microwave background (CMB) radiation by artificial satellites, COBE (Smoot et al. 1992), the *Wilkinson* Microwave Anisotropy Probe (WMAP) (Bennett et al. 2003; 2013), and *Planck* (Planck Collaboration et al. 2014). The latest estimated value of the density parameters, which is defined as the energy density fraction of each component normalised by the critical density, $3H^2c^2/8\pi G$ (H, G, and c are the hubble and gravitational constants and speed of light, respectively), are ~ 4.8 % for baryon, ~ 25.6 % for DM, and ~ 69.6 % for the dark energy (Planck Collaboration et al. 2014). (Planck Collaboration et al. 2014) show that their estimates of the cosmological parameters support

the cosmological model with Λ and cold dark matter (i.e. ΛCDM model), where Λ is the cosmological constant in the Einstein equation.

The small density perturbation in the early epoch grows by the gravity of the DM, resulting in the formation of DM haloes. Small scale structures can grow after the decoupling between photons and the DM, i.e. after the DM becomes non-relativistic. The word "cold DM" has been used in contradiction to the "hot DM", whose difference is the time when the DM decouples from photons; "cold" DM decouples earlier, and its velocity becomes smaller. Therefore, in the ΛCDM Universe, small structures can form earlier and grow to the larger structure by mergers of DM haloes, which is consistent with observational suggestions about the correlation function of galaxies (e.g. Hamilton et al. 1991).

The baryon couples with the DM in the early epoch of the structure formation. In this epoch, baryon exists as 'hot' gas, whose temperature is about the Virial temperature. Although DM halo cannot gravitationally collapse after reaching the Virial equilibrium (i.e. a gravitationally bounded system is supported by its velocity dispersion and the total energy of the system is conserved), the baryon can collapse further by the Compton cooling and radiative cooling. The cooling and heating processes of baryon are important for the galaxy formation and thus, has been investigated theoretically (e.g. Sutherland & Dopita 1993).

1.2 Galaxy Formation

1.2.1 Formation and properties of galactic discs

Since the collapsed DM haloes are not the perfect sphere, the tidal torque plays an important role in the growth of angular momentum in haloes (e.g. Efstathiou & Jones 1979). The gas inside the DM haloes contracts due to the cooling and flow inwards conserving its specific angular momentum. Such gas prefers the state with the lowest energy level, and thus the gas forms a gaseous disc with the aligned angular momentum vectors for all mass elements. Considering the angular momentum conservation and the Navarro-Frenk-White (NFW) density profile (Navarro et al. 1997) for the DM halo, the disc has an exponential surface density profile.

Galactic discs show a more complicated structure than the simply exponential discs. The characteristic features are spiral arms and bars induced by density perturbations, which are determined by the circular frequency and the real angular frequency of the gas. For spiral arms (see Lin & Shu 1964; 1966), the gas in the disk generally have different angular speeds from that of the spiral structure. The gas, therefore, moves in and out of the spiral pattern, meaning that spiral patterns are composed of different material at a different time. The material is compressed when it is swept by a spiral density wave, and then the gas (if cold) can form stars at the density maxima. The spiral arms, therefore, generally have a large SFR.

If the kinetic energy of the rotation term is sufficiently larger than that of the random motion (i.e. 2 times larger; see Mo et al. 2010), then the perturbation results in the bar-mode instability. The stellar bar and gaseous bar have different rotational velocity and the stellar bar trails behind the gas bar with a few-degree offset. The gas, thus, can lose its angular momentum and flow inward (e.g. Hopkins et al. 2009a) resulting in the growth of the central SMBH (see, however, Sec. 1.3). With the bending mode instability, which is caused by the perturbation in a vertical direction to the disc plane, the bar structure appears like peanuts shape, called "pseudo-bulge". It is observationally supported that the pseudo-bulges are bars

(e.g. Kuijken & Merrifield 1995; Bureau & Freeman 1999; Kormendy & Barentine 2010)

1.2.2 Spheroid formation

Another important component of a galaxy is the spheroid, i.e. bulge, which has spherical and featureless shape with old (red) stellar components. The galaxies whose mass is dominated by the bulge component are called as elliptical galaxies. Such elliptical galaxies are considered to form mainly by mergers of two or more galaxies (Toomre 1977). The gravitational potential of the merging galaxies rapidly changes. Then, the total energy of each star should change with time. This process is called as violent relaxation, which is essential for forming elliptical galaxies by mergers of galaxies. The timescale for the violent relaxation is the same order as the free-fall timescale (Lynden-Bell 1967). In addition to this effect, if some phase mixing processes are valid, the energy distribution of stars becomes broader and the time derivative of the probability of finding a star in the phase-space volume becomes constant with time (the main mixing process is phase mixing). Mergers of galaxies induce a starburst and gas inflow to the central region if the galaxies have the plentiful gas due to the compression of the gas, tidal perturbations, and change of the gravitational potential. Galaxy mergers are considered the crucial process not only for the bulge growth but also the SMBH growth.

Mergers of galaxies occur via dynamical friction (Chandrasekhar 1943). A satellite galaxy, which resides in one of the merging DM haloes (not the largest one), falls to the bottom of the gravitational potential of the new host halo. During this travel, the satellite galaxy interacts with field particles and lose its energy and momentum. In this sense, the satellite galaxy receives a kind of resistance and slows down, which is called as dynamical friction. The timescale for the galaxy mergers via dynamical friction is estimated in (e.g. Binney & Tremaine 1987). The mergers via dynamical friction result in the mergers of a central galaxy and satellite galaxies. The mergers of satellite galaxies are also possible, whose merging probability is determined from the number of satellite galaxies in a halo and gravitational potential (Makino & Hut 1997). Such mergers are called random collisions.

1.2.3 Star formation and feedbacks

In galactic discs and bulges, the gas can cool and concentrate resulting in the star formation activity. Observationally, there is a well-known correlation between the surface density of the cold gas, $\Sigma_{\rm gas}$, and the SFR density (e.g. Schmidt 1959; Kennicutt 1998). The SFR density of local galaxies is proportional to $\Sigma_{\rm gas}^{1.4}$, which is called the Kennicutt-Schmidt (KS) relation. The KS relation can be applied for various types of galaxies from purely disc galaxies with a mild star formation to starburst galaxies. However, more recent work (e.g. Bigiel et al. 2008) has found that the molecular hydrogen surface density, Σ_{H_2} is the better tracer of the SFR than $\Sigma_{\rm gas}$. Also, the KS relation would differ in galactic structures (e.g. galactic bars, spiral arms, bulges) and would differ in normal and bursty star formation (e.g. Roychowdhury et al. 2015).

Stars form in a part of the giant molecular clouds (GMCs), whose mass is $\sim 10^{5-6} M_\odot$ and molecular hydrogen number density is extremely high compared with that of the field gas, namely $\sim 100 - 500 {\rm cm}^{-3}$. GMCs are formed via thermal instability of the gas and some perturbations induced by, e.g. gravitational instabilities, turbulence, spiral arms, and galaxy mergers. GMCs produce stars which have a mass distribution. Although the distribution

should differ in each GMC, we employ the averaged mass distribution in a galaxy as "Initial Mass Function" (IMF), which is the number density distribution of stars at a fixed mass. To model the star formation in simulations and semi-analytic models of galaxy formation (hereafter SA models), We usually use the *universal* IMF. A few observations support the universality with several local galaxies (e.g. Elmegreen 2006) only for the massive end of the IMF. The popular IMFs are presented in, e.g. Salpeter (1955),Kroupa (2002), and Chabrier (2003), suggesting the power law shape IMF with negative powers of stellar masses. However, especially for starburst galaxies, IMF is not necessarily the same as global IMFs since starburst galaxies contain a large amount of more concentrated clouds, potentially forming more massive stars.

Star formation makes galaxies more chemically enriched. Stars with mass $< 8M_{\odot}$ end up as white dwarfs after their asymptotic giant branch (AGB) phase. In the AGB phase, the H and He shells outside the carbon core cools, and the resulting temperature gradient causes the convection and mass loss from the AGB stars. Then, AGB stars supply carbon and α elements to the surrounding interstellar medium (ISM). Massive stars with mass $> 8M_{\odot}$ largely contribute to the metal enrichment of the ISM by stellar winds and the final explosion as core-collapse supernovae (SNe). They produce mainly carbon, and α elements although the production of heavy elements such as Ne, Mg, and Fe is small. Core-collapse occurs when the shock is created in the inner Fe shell with the photodisintegration of Fe to He nuclei. These He nuclei may become seeds of r-process elements. [1] The leading producer of Fe is the Type Ia SN, which is a white dwarf with the mass accretion from its companion star. The production mass of Fe is $5-10$ times larger than a core-collapse SN. Observationally, the relation of abundance ratios between [α/Fe] and [Fe/H] of the ISM is important for understanding the star formation history. The abundance ratio of [Fe/H] is the indicator of the time elapsed from the onset of the star formation, and the [α/Fe] is the metalllicity indicator. Core-collapse SNe occur after $\sim 10^7$ yr and Type Ia SNe after $\sim 10^8$ yr from the onset of the star formation. Since the core-collapse SNe do not produce much iron, the [α/Fe] is nearly constant with [Fe/H]. After 10^8 yr, the [α/Fe] decreases due to the Type Ia SNe.

SNe are also important as regulating sources of star formation activity itself, which output mass-loaded kinetic energy with typically $\sim 10^{51}$ erg per each event. [2] The wind velocity of SNe can reach at $\sqrt{2.5}$ times the adiabatic sound speed of the gas (Efstathiou 2000), i.e. supersonic flow. The fate of the outflowing gas is, therefore, determined by the outflowing gas temperature and gravitational potential of the host halo. If the outflow velocity exceeds the escape velocity of the halo, the gas leaves from the halo. On the other hand, the gas falls back if its velocity is less than the escape velocity. The fall-back gas produces a hot corona in the halo if the cooling is ineffective. For less massive haloes, whose circular velocity corresponds to $\sim$ 100km/s (Dekel & Silk 1986), the gas removal by SNe is effective. Statistical studies of galaxy formation support this suggestion. Benson et al. (2003) show that luminosity functions (LFs) of galaxies cannot be reproduced with the converted LFs from halo mass functions (MFs) with a constant mass-luminosity ratio (see also Fig. 1.1). The LFs overproduce the number density of faint and bright galaxies, meaning that the SFR should be lower for such galaxies. For faint ones, the important effect is SNe effects described above, since their halo circular velocity corresponds to $\sim$ 100km/s.

[1] Recently, the r-process elements are mainly supplied by neutron star mergers (Freiburghaus et al. 1999).

[2] Stellar winds can also output the mass-loaded kinetic energy at the same order as SNe, although they contributes as the mass sources due to the 100 times smaller terminal velocity.

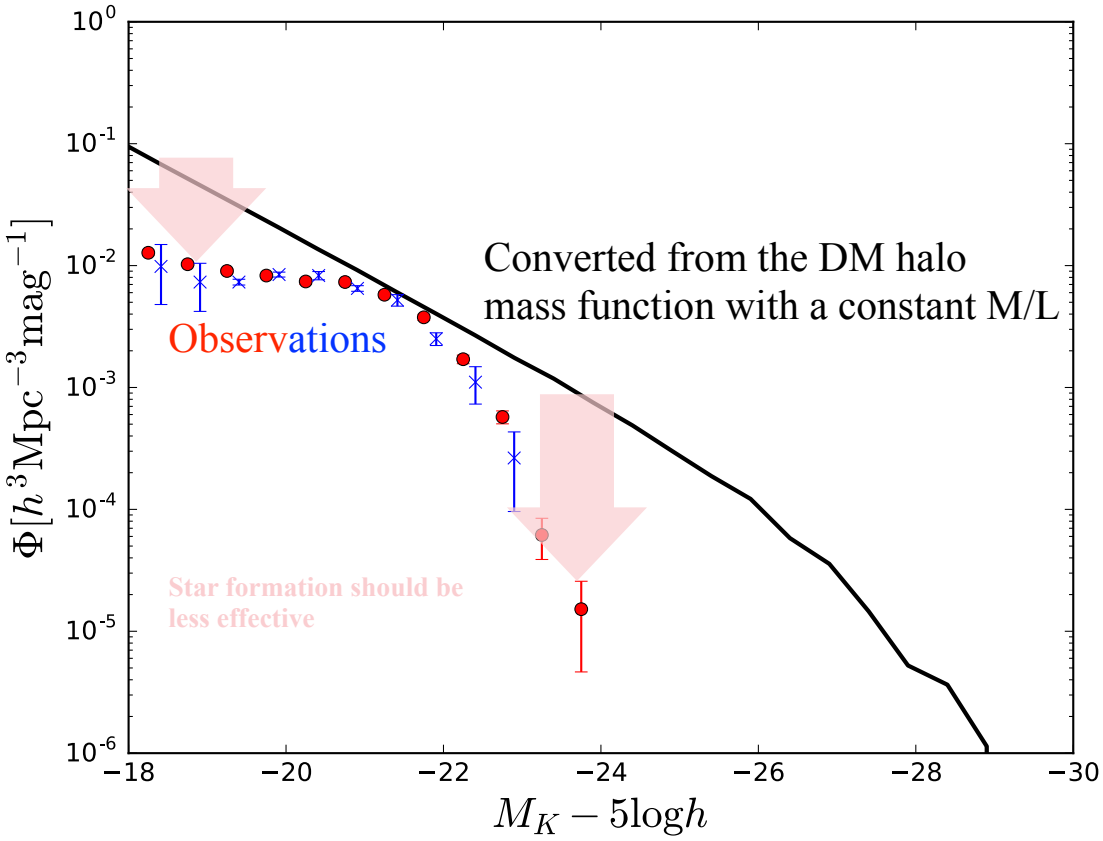

Figure 1.1: K-band LFs of galaxies at $z \sim 0$. Blue crosses and red circles are observational results obtained by Devereux et al. (2009) and Driver et al. (2012), respectively. Black solid line is LFs obtained by using simulated halo MF at $z \sim 0$ (Ishiyama et al. 2015) with a constant mass-luminosity ratio (ML).

We would need other mechanisms that regulate star formation activity in massive and bright galaxies, as Benson et al. (2003) suggested. Observations of galaxy clusters (e.g. Cowie & Binney 1977; Fabian & Nulsen 1977) show that the age of the clusters is about one-order longer than the cooling time of the system, estimated with from their X-ray emission. Thus, the inflow of the cold gas should exist, although the inflow is not observed. To solve this "cooling flow problem", mechanisms that quench the gas cooling in a long (at least a few Gyr) are required. SNe and stellar winds cannot regulate star formation in massive galaxies because of the deep gravitational potential. Instead, "radio mode" AGN feedback has been considered as a candidate. X-ray maps of galaxy clusters show interactions between radio lobes and their intracluster gas (e.g. McNamara et al. 2000; Fabian et al. 2003). Also, Burns et al. (1981) find that massive clusters have massive and active radio galaxy at the centre. These will indirectly support the importance of the "radio mode" AGN feedback. Croton et al. (2006) and Bower et al. (2006), using SA models show that observed LFs of galaxies are well reproduced with the phenomenological models of "radio mode" AGN feedback, although the modellings are not well constrained.

1.3 Supermassive Black Hole Growth

The existence of SMBHs is suggested from observations of, e.g. the velocity dispersion profile of M87 (van der Marel 1994) and NGC4342 (van den Bosch et al. 1998). The AGN engine has been considered to be an SMBH originally suggested by Salpeter (1964) and Lynden-Bell (1969). AGNs are powerful energetic sources, which should have a compact radiative region. Here, I describe the basic properties of SMBHs and surrounding structures. I define the Eddington luminosity, $L_{\rm Edd}$, and Eddington mass accretion rate, $\dot{M}_{\rm Edd}$, as

$$L_{\rm Edd} = \frac{4\pi G m_p c M_{\rm BH}}{\sigma_T}, \tag{1.1}$$

$$\dot{M}_{\rm Edd} = L_{\rm Edd}/c^2, \tag{1.2}$$

where $M_{\rm BH}$ is the SMBH mass, σ_T, G, m_p, c, are the cross section of Tompson scattering, gravitational constant, proton mass, and speed of light, respectively. The gravitational force balances radiative pressure on the accreted gas in a spherical accretion and illumination case, when the accretion rate, $\dot{M}_{\rm BH}$, is $\sim 10\dot{M}_{\rm Edd}$.

1.3.1 Structure surrounding active SMBHs

Fig. 1.2 shows a schematic view of the structure surrounding active SMBHs. The central engine of an AGN is the gravitational potential of an SMBH. A part of the energy which is possessed in the accreted gas onto an SMBH is converted to the radiation, outflow energy, and kinetic jet energy.

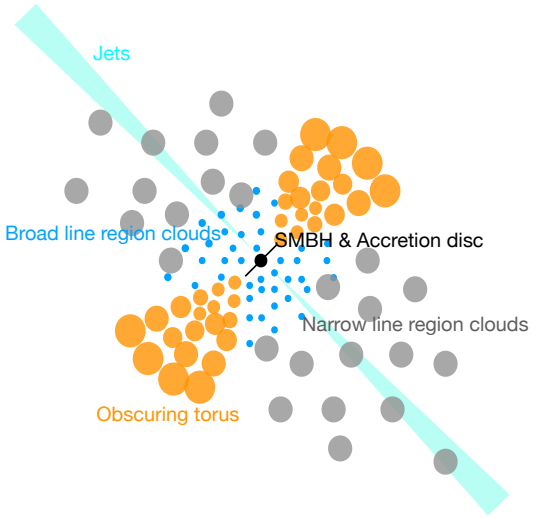

Figure 1.2: Schematic view of the structure surrounding an active SMBH.

Accretion discs

The energy of the accreted gas is converted to the radiation in the accretion disc surrounding the SMBH. Due to the viscosity by the turbulence and/or magnetic field, the angular momentum of the gas is transferred from inside to the outside of the accretion disc. The accretion

disc radiates energy with the spectra which can be described as the sum of the black-body radiations with different effective temperatures because of the temperature gradient in the disc.

Theoretically, there are some physical solutions for the accretion disc, which depends on, e.g. the Eddington ratio and SMBH mass. The first one is usually called as "standard accretion disc" (Shakura & Sunyaev 1973), in which the energy of the gas is efficiently converted to the radiation (radiation efficiency, η, is ~ 0.1; e.g. Sołtan 1982; Fabian & Iwasawa 1999; Shankar et al. 2004) with α viscosity; the efficiency of the angular momentum loss is proportional to the gas pressure. Because of the radiation, the accretion disc cools well and the scale hight becomes small. This model could explain observed properties of optical selected QSOs, the most luminous class of AGNs. The AGN bolometric luminosity is proportional to the accretion rate, $\dot{M}$.

The second one is the "Radiative Inefficient Advection Flow" (RIAF), which is the one of the Advection Dominated Accreting Flow (ADAF). When the gas surface density, Σ, of the accretion disc is low and the disc is optically thin, the radiative cooling rate (i.e. energy loss per unit time by the radiative cooling) becomes smaller with proportion to Σ^2. Then the gravitational energy of the gas is stored in the accretion disc itself and the temperature increases. The inflowing gas to the accretion disc has the lower entropy than that in the accretion disc. The inflowing gas gain entropy by viscous heat dissipation. Since kinetic viscosity becomes higher with higher temperature, the gas can efficiently lose their angular momentum and get accreted onto the central BH. In the model, the bolometric luminosity decreases with decreasing $\dot{M}$ more rapidly than the standard disc, namely $\propto \dot{M}^2$ (Mahadevan 1997). Since $\dot{M} \propto \Sigma$ in the advection-dominated regime, the RIAF is a solution for AGNs with low accretion rate.

Next, we consider the high Σ accretion disc. The disc cannot be in the thermal equilibrium at all when we assume an optically thin disc since the viscous heating rate is independent of Σ, while the radiative cooling rate increases with $\propto \Sigma^2$. The acceptable solution for the high accretion rate, namely $\dot{M} > \dot{M}_{\rm Edd}$ is "optically thick" ADAF. When the accretion disc is optically thick, the interaction between materials and photons frequently occurs, causing the delay of the liberation of radiation energy from the accretion disc. The radiation energy advects inward faster than the liberation and gets accreted onto SMBHs. Therefore, the radiative cooling rate is, reduced and the flow becomes advection-dominated. This accretion disc is called as "slim disc", whose bolometric luminosity is saturated to several $\times L_{\rm Edd}$. It means that even $\dot{M}$ exceeds the Eddington limit, luminosity is almost constant. Therefore, the super-Eddington accretion is allowed in case of the slim disc.

There will be the high-temperature ($\sim 10^9$ K) corona surrounding the accretion disc, which contains high-energy electrons although the origin of the corona has been unclear. The hot corona emits X-ray by the inverse-Compton process induced by the UV and optical photons coming from the accretion disc. The low energy (soft) band of X-ray is susceptible to the Compton scattering when the hydrogen column density $\gtrsim 10^{22}{\rm cm}^{-2}$. Since the effect becomes weaker in high energy (hard) band, the hardness ratio of the X-ray spectrum changes with the column density and thus, we can estimate the column density surrounding the AGNs. When the column density exceeds 10^{24}cm, the optical depth of the Compton scattering becomes a unity, and the absorption of X-ray photons is not negligible. Such AGNs are called "Compton thick AGNs". The Compton thick AGNs are only ~ 20 % of the X-ray selected AGNs, at maximum (e.g. Ueda et al. 2014).

The spectral energy distribution changes with accretion disc models. The standard accretion disc, which is valid for roughly $0.03 \lesssim (\dot{M}/\dot{M}_{\rm Edd}) \lesssim 20.0$, has optical-UV spectra with a multi-color spectrum, which can be approximated by a broken power-law form ($L_\nu \propto \nu^\alpha$) with $\alpha = -0.44$ in 1 νm $< \lambda <$ 1300 Å and $\alpha = -1.76$ in 1200-500 Å (e.g. Telfer et al. 2002; Vanden Berk et al. 2001). The X-ray spectrum with a power law index, $\alpha_{\rm OX}$ (Zamorani et al. 1981), depends on the optical luminosity since the origin of the X-ray photon is the UV-optical photon produced in the accretion disc. For example, Vignali et al. (2003) describe

$$\alpha_{\rm OX} = -0.11 \log L_\nu(2500\mathring{A}) + 1.85. \tag{1.3}$$

Using this relation, we can estimate the bolometric correction, f_b, which is defined as the conversion factor from the bolometric luminosity, $L_{\rm bol}$, to the luminosity in a given band, b, as $f_b \equiv L_{\rm bol}/L_b$. The resulting bolometric correction depends only on the bolometric luminosity itself (e.g. Marconi et al. 2004; Hopkins et al. 2007). On the other hand, for the RIAF and slim disc, their spectrum must change since the radiative cooling is inefficient and other processes (e.g. inverse Compton scattering) are important for producing high-energy photons. Cao (2009) present the difference of the bolometric correction between the standard and RIAF-like discs. The bolometric correction, therefore, should depend not only on the bolometric luminosity but also on the Eddington ratio, which is also suggested by the observational study (Lusso et al. 2012). Because of the difficulties for describing the bolometric correction applicable for whole AGN population, the bolometric correction for the standard discs has been employed for all AGNs.

A part of AGNs has broad lines such as $Ly\alpha$, $MgII$, CIV, and $H\beta$. Such lines are emitted from gas clouds, whose temperature is $\sim 10^4$ K, moving towards or against the observer. The full width half maximum (FWHM) of the lines can reach at $\sim 10^4$ km/s at maximum. Some broad lines are made use of the SMBH mass estimates as follows. Considering that the region in which the broad lines are emitted (broad line region; BLR) is in the virial equilibrium, the mass inside the BLR is estimated by the line width. Because of the Doppler shift of the wavelength, the mass of SMBHs at different redshift is estimated with a different line. It is noteworthy that the mass estimates by this way will not be accurate in the case with a strong outflow, since the BLR should not be in virial equilibrium.

There are AGNs without broad lines. Their emission lines are narrow, whose FWMH is typically less than 900 km/s. The emission comes from a larger scale than BLR. The region (narrow line region; NLR) corresponds to the maximum region in which the emission from the host galaxies dominates the nuclear emission. Since the NLR is outer than the dust sublimation radius, the emission is affected by the dust attenuation. The FWHM of the NLR is correlated with the host bulge luminosity (e.g. Whittle 1992). This suggests that the NLR is virialised reflecting the stellar potential of the host bulge, not the central SMBH.

Jets and outflow

Some AGNs have jets and outflows, which can be affected by the gas properties of their host galaxies. Radio-loud AGNs, defined by the ratio between optical and radio flaxes, sometimes have jets. Such kind of jets has been found usually with radio lobes in massive local elliptical galaxies (e.g. Bridle et al. 1994). The radio emission will be produced by the Synchrotron emission, and jets will also be created by the magnetic field. The magnetic field would be induced by hot plasma and/or the electron and positron pair. It means that the effect of

the magnetic field becomes important for the accretion disc with a high temperature. Also, the jets tend to be produced only in the "low/hard" state, in which the X-ray flux increases towards the high energy (Fender et al. 2004). Such condition occurs only for AGNs with low Eddington ratio ($\lambda_{\rm Edd} \lesssim 0.02$). Outflows, on the other hand, will be supported by thermal or radiation pressure, which can be observed as absorption lines in the gas far from the AGN.

Obscuring torus

Outside of the accretion disc, there is an "obscuring torus". Seyfert 1 galaxies are defined as Seyfert galaxies with broad emission lines in their spectra. Seyfert 2 galaxies, on the other hand, do not have such broad components and X-ray and UV continua although some of them show the broad polarised lines (e.g. Antonucci & Miller 1985). The difference between Seyfert 1,2, and the polarised lines can be explained considering a dense torus which is opaque to the broad line emissions and continuum photons. The "unified model" of AGNs is based on this torus assumption (Osterbrock 1978; Urry & Padovani 1995). The model suggests that the difference of the observed AGN properties comes only from the difference of the observed angle.

Considering the gas and dust with a smooth toroidal distribution, the gas temperature should be $> 10^5$ K, which is so high that the dust grains will be destroyed. In this picture, we assume the ratio between scale hight and radius of the torus $\sim c_s/v_{\rm obs}$, where c_s and $v_{\rm obs}$ are the sound speed and the rotational speed, respectively. There are some solutions to overcome this problem. One is the "clumpy torus" model (e.g. Krolik & Begelman 1988), in which the gas is highly clumpy and distributes as a torus. However, unless the collision of clouds is elastic, clumps distributes in the equatorial plane if the collision rate is large. Even when the collision rate is small, the resulting torus should be transient, which cannot explain the large fraction of AGNs whose luminosity is affected by the obscuration.

The intermediate structure between the accretion disc and their host galaxy such as the obscuring torus is also required from the "angular momentum problem". Even when the major merger of galaxies which will be one of the triggering mechanisms of AGNs (see Sec, 1.3.2), the gas can not lose sufficient angular momentum for getting accreted onto the central SMBH (e.g. Hopkins et al. 2009a). To reach the SMBH, the gas should lose > 99.9 % of the angular momentum from the initial value. The inflowing gas from the host galaxy, thus, forms a "reservoir" in which gas can lose their angular momentum. In this sense, I sometimes call the intermediate structure as the "circumnuclear disc" (CND). CNDs are not necessarily geometrically thick to the z-direction. The mechanisms for the angular momentum loss is unclear. Thompson et al. (2005) suggest the disc with a starburst. In the CNDs, the gas can lose their angular momentum via global torques (e.g. bars, and spirals) considering Toomre's local stability criterion (Toomre 1964). The CND structure is supported by the radiation pressure of stars formed in the CND. Kawakatu & Wada (2008), on the other hand, propose the turbulent pressure supported disc induced by SNe. The gas loses the angular momentum via the turbulence. The SFR in the CND becomes high, the scale height of the CND becomes high. In this case, the CND will have the same effect as the obscuring torus. The difference of the obscuring torus with a smoothed density distribution and the CND is the existence of the star formation, e.g., external turbulent sources.

The intermediate structure has been observed with Arecibo Large Millimeter/submillimeter Array (ALMA) in Chile. Izumi et al. (2016) find dense molecular gas in the central region of

the galaxies, which is sufficiently dense for producing stars. Also, Diamond-Stanic & Rieke (2012) shows the tighter correlation between the accretion rate onto SMBHs and the SFR inner 1 kpc region than the SFR outer 1 kpc. These studies imply the importance of the star formation in the central region of galaxies.

1.3.2 Gas fueling from host galaxies

SMBHs accrete the gas from their host galaxies. Their growth will have an impact on the evolution of host galaxies (Sec. 1.2.3). However, the growth of SMBHs and their connection to their host galaxies have been under discussions for over four decades. As the mechanisms for fueling of the central BHs, major mergers (merging mass ratio of galaxies $> 0.3 - 0.4$) are the first candidates. Negroponte & White (1983), Barnes & Hernquist (1991), and Mihos & Hernquist (1994), for example, show that major mergers, which are considered to play a role of the bulge formation, drive gas towards the centre of galaxies and nuclear starbursts and gas accretion onto SMBHs can occur. Ultraluminous infrared galaxies (ULIRGs), which have a high SFR ($> 100 M_{\odot}$/yr) and their UV emission is attenuated by the surrounding dust components, are always associated with merging systems Sanders & Mirabel (1996). Also, the fraction of hosting an AGN in ULIRGs is higher than that in normal galaxies (e.g. Hopkins et al. 2006; Donley et al. 2010), which will support merger-driven gas fueling of SMBHs. SA models in early days followed these points and create models of the gas fueling to SMBHs by major mergers (e.g. Kauffmann & Haehnelt 2000; Enoki et al. 2003). Even with the simple modellings, the SA models can explain observed QSO LFs in optical bands at $z \lesssim 2$. Also, Enoki et al. (2014) find their model qualitatively explains the evolution of the number density of QSOs. One of the critical problems of this major merger-driven AGN scenario is that the model underestimates the number density of less luminous AGNs than QSOs with the bolometric luminosity less than $\sim 5 \times 10^{45}$ erg/s. Such less luminous AGNs are difficult to be classified as AGNs in optical bands because UV and optical light from the nuclear is blended by those from their host galaxies. Therefore, this problem was discovered with the progress of the X-ray observations.

To solve this problem of the underproduction of less luminous AGNs, some SA models introduce other fueling mechanisms. If the axisymmetric perturbations are induced by minor mergers or interaction to other galaxies which closely pass near the SMBH host galaxy, galactic bars form and the gas can lose their angular momentum due to the gravitational torque Then the gas can reach to the central region of the galaxies. Minor mergers and interaction of galaxies can induce the perturbation, by which the galaxy mildly change their morphology, i.e. a part of the galactic disc survive, on the contrary to the case of major mergers. Croton et al. (2006) and Lagos et al. (2009), for example, employ major + minor mergers modelling for fueling to SMBHs, although the contribution of minor mergers is not investigated. The conclusion of Menci et al. (2014); Gatti et al. (2016) is that interactions of galaxies play a crucial role in the SMBH growth. In their model, the accreted gas mass is smaller than the case of mergers, reflecting the larger separation of galaxies. Therefore, the interaction produces less luminous AGNs. The host halo mass of interaction driven AGNs is similar to that of the merger-driven AGNs, since the occurrence rate of the interaction becomes higher in haloes which have a large number of the satellite galaxies.

Another perturbation inducer is disc instabilities. In this case, SMBHs do not necessarily have the companions. Disc instabilities are, thus, a possible candidate of AGNs especially in

isolated galaxies. The classical, but easy criterion to introduce is derived in Efstathiou et al. (1982). Considering the balance between gravitation of their DM halo and self-gravity of the disc, if the disc becomes gravitationally unstable, the disc forms bars, Since the growing timescale of the bar is unclear and since the time resolution of the SA models is always rough ($\sim$ dynamical time of the halo), the morphological change is considered to complete instantaneously and a starburst occur. The modelling of disc instabilities in SA models are, however, too simple because the criteria of Efstathiou et al. (1982) should be employed limited case but SA models employ this criterion for all types of galaxies; The Efstathiou et al. (1982) criterion can be used for *cold and pure* disc galaxies, i.e. velocity dispersion of the disc is negligibly small and infinitesimally thin without bulge component. The effect of velocity dispersion of the disc and bulges is to stabilise the disc component. Therefore, SA models would overestimate the occurrence of disc instabilities. Also, some SA models assume that the galactic disc is destroyed like major merger case although a part of the galactic disc can survive. Using these too-simplified assumptions, some previous studies conclude that disc instabilities are main triggering mechanisms of the gas accretion onto SMBHs (e.g. Hirschmann et al. 2012).

As a heating source of massive galaxies, Bower et al. (2006) and Croton et al. (2006) introduce the "hot mode" or "radio mode" accretion of SMBHs. This model is naively that the hot gas in the gas halo directly gets accreted onto SMBHs and a part of its energy heat the host halo, resulting in quenching gas cooling. Bower et al. (2006), Croton et al. (2006), and other previous studies showing the importance of the radio mode do not show the mechanisms of the direct hot gas accretion in details. Therefore, the contribution of the radio mode accretion to the cosmic SMBH growth should be doubtful. AGNs with radio jets in local galaxies always have a small $< 10^{-2}$ Eddington ratio, i.e. the RIAF-like accretion disc. Hydrodynamic simulations, therefore, sometimes define AGNs that would contribute to the radio mode AGN feedback by their Eddington ratio (e.g. Sijacki et al. 2007; Okamoto et al. 2008a) Such simulations succeed from quenching the star formation activity, although the duration of the quenching could be shorter than the required one. Observationally, the importance of the AGN feedback is also under the extensive discussions (Sec. 1.3.3).

1.3.3 Observational progress

AGNs were originally found as quasi-stellar radio sources (quasars). As the name describes, these are radio-loud AGNs in local Universe. AGNs without strong radio emissions are seemed to be point sources and called Quasi-Stellar Objects (QSOs). QSOs are the brightest class of AGNs, by definition, $M_B < -21.5 + 5 \log h_0$, where h_0 is the current Hubble parameter. The second brightest class is Seyfert galaxies, whose luminosity is lower than QSOs. Although QSOs and Seyfert galaxies have different properties, e.g. line width compared to the continuum emission, the origin and basic properties are considered to be the same. Those can be classified as type-1 and -2 by observing direction (Sec. 1.3.1) in optical bands. As for X-ray, QSOs and Seyfert galaxies are classified as obscured and unobscured AGNs. The classification is slightly different from that in optical bands; some type-1 AGNs are classified as obscured AGNs and vice verse. The "obscured fraction" becomes higher at less luminous AGNs (e.g. Ueda et al. 2014), suggesting that the difference of the opening angle, i.e. the structure of obscuring torus. When we go down to $L_{\rm bol} \sim 10^{42}$ erg/s, obscured fraction decreases (e.g. Burlon et al. 2011), supporting that the torus clouds are generated by the accretion disc

driven outflow (Shlosman 2006; Elitzur & Ho 2009). Also, the obscured fraction also changes by the Eddington ratio (Lusso et al. 2012; Ricci et al. 2017b).

The important and notable properties of AGNs is their evolution of the number density. Observations show that the number density of optically luminous AGNs peaks at higher redshift than less luminous AGNs (e.g. Croom et al. 2009; Ikeda et al. 2011). This trend is also found from X-ray observations (e.g. Ueda et al. 2003; Hasinger et al. 2005). We sometimes call this trend as "anti-hierarchical" trend or "down-sizing" trend of AGNs. Considering a constant Eddington ratio, this trend means that heavier SMBHs form earlier. The origin of this trend is one of the hot topics in the context of co-evolution of galaxies and SMBHs.

Since the AGN luminosity is the convolution of the BH mass and the Eddington ratio, Not only the AGN luminosity but also these two properties play an important role in unveiling the SMBH growth. In the local Universe, the "quiescent" BH mass is estimated by using stellar kinematics (e.g. Richstone et al. 1990; Kormendy et al. 1996a;b), and gas kinematics (e.g. Sarzi et al. 2001; Ho et al. 2002; Davis et al. 2013; Onishi et al. 2017). The "active" BH mass is estimated by using the water maser (e.g. Kuo et al. 2011), and reverberation mapping (e.g. Peterson 1993). Especially, reverberation mapping is traditionally and usually used. I can estimate the gravitational potential by the time delay of the emission line variation and the Doppler velocity field. We can then obtain the SMBH mass by using the Virial theorem. Since the estimation of the BH mass by the reverberation mapping requires long and regular observing time and can be accepted to the local AGNs, we usually use the phenomenological way based on the reverberation mapping achievements for estimating the BH mass. Assuming that the BLR is virialised, the line width reflects the velocity dispersion, ΔV, in the virialised region. Then, the BH mass can be estimated by (Peterson & Wandel 1999):

$$M_{\rm BH} = f\frac{\Delta V^2 R}{G},$$

where R and f are the line emitted region size and the virial factor, that reflects the inclination to the accretion disc, respectively. The virial factor, f, has large uncertainty and is assumed as a free parameter. Recent observations, however, increase the AGNs with reverberation mapping SMBH mass (e.g. Bentz et al. 2009) and statistically find the relation between BLR size and f (e.g. Liu et al. 2017). I have to note that, in the first place, if the central region is not virialised, e.g. having the outflow, this method cannot be used although observations may not care about the effect of unvirialized motion sufficiently. Recently, SMBHs at $z > 6$ have been found and their SMBH masses are estimated with this method. However, since they also have the outflow (e.g. Cicone et al. 2015), the error of the SMBH mass is unclear (M. Vestergaard, in private communication).

With these SMBH mass estimates, I can derive BH MF and Eddington ratio distribution. For local galaxies, the BH MF including both quiescent and active galaxies can be estimated, simply by converting from the bulge MF assuming the local relationship between SMBH mass and bulge mass (e.g. Shankar et al. 2004). The active BH MF and the Eddington ratio distribution has been investigated from $z \sim 0$ to ~ 4 with large uncertainties (e.g. Schulze & Wisotzki 2010; Nobuta et al. 2012; Kelly & Shen 2013). Such observations reveal that the AGNs at higher redshift grow with the higher Eddington ratio. The details will appear in Sec. 5.1.

As for the triggering mechanisms of AGNs, recent observations suggest the importance of other mechanisms besides mergers of galaxies. By analysing the image obtained with the

Hubble Space Telescope (HST), Floyd et al. (2004), for example, shows that only a small fraction of the local AGNs shows evidence of the galaxy mergers. The contribution of mergers depends on the AGN luminosity and it increases from 3% to $\sim$ 100 % with the bolometric luminosity from 10^{42} to 10^{46} erg/s at $0 < z < 3$ (Treister et al. 2012). Also, the contribution would become higher for AGNs detected in infrared bands, not optical bands (e.g. Urrutia et al. 2008). In summary, triggering mechanisms of the AGN activity would be more important for less luminous, optically selected AGNs, although optically selected AGN phase might occur after dust obscured phases induced by mergers (e.g. Hopkins et al. 2005). Although the results should depend on the observational depth (i.e. how faint galaxies I can detect), detailed understandings about the triggering mechanisms of AGNs have been required.

Recent observations also have progress about the redshift. There are $>$ 100 of QSOs at $z > 6$ (e.g. Fan et al. 2003; Willott et al. 2010a; Matsuoka et al. 2017) and a few QSOs even at $z > 7$ (Mortlock et al. 2011; Bañados et al. 2018), whose SMBH masses are estimated as $> 10^8 M_\odot$, although the mass estimates may include a large uncertainty. Such population brings some new questions for the co-evolution between galaxies and SMBHs. First, when and how does the "seed" BH form? Assuming the Eddington-limited accretion, the seed BH should be placed at $z > 10$ with $10^3 M_\odot$ and at $z \sim 8$ with $10^5 M_\odot$. As the formation processes of the seed BHs, there are mainly two different processes (see Sec. 3.1), which is important for understanding the "origin" of the co-evolution and the environment of the birthplace of BHs. The other question brought from the high redshift QSOs is also related to the origin of the co-evolution. Izumi et al. (2018) show the relationship between the dynamical mass of the host galaxies and SMBH mass for $z \sim 6$ QSOs. They have a flatter relationship than the local one; galaxies with the smaller dynamical mass host the more massive SMBHs. On the other hand, less luminous AGNs at $z \sim 6$ follow the local relationship, suggesting that SMBH growth in early Universe cannot be explained in the same manner as that in the more recent Universe. Although the sample size is small and the statistics are not sufficient, these findings fascinates theoretical studies to investigate the origin of the co-evolution.

Also, the connection between the AGN and star formation activities has been investigated. Since SMBHs grow by the gas accretion and galaxies grow by the star formation, the relation between the accretion rate (or AGN luminosity) and SFR shows the connection of the time evolution of the co-evolution in a single epoch. Rosario et al. (2012) find that AGN X-ray luminosity and SFR have a positive correlation for local and luminous AGNs, although they have almost no correlation for less luminous AGNs at higher ($z > 0.8$) redshift. Rosario et al. (2012) conclude that less luminous AGNs at lower redshift should be triggered by secular processes without mergers and the importance of major mergers as the AGN triggering become important at higher redshift. However, the relation changes with the estimation of the AGN luminosity and SFR. When the instantaneous AGN luminosity and SFR are employed, they have a positive correlation (Hickox et al. 2014). Also, even when the SFR estimated in the host galaxy does not correlate with the AGN luminosity, SFR in the central region sometimes correlates (e.g. Diamond-Stanic & Rieke 2012).

Some AGNs cannot be observed in optical bands. These AGNs are buried in the surrounding dust and their radiation is mainly observed in the infrared bands. They are called as ULIRGs, "Hyper-Luminous Infrared galaxies (HyLIRGs)", and "Dust Obscured Galaxies (DOGs)", a large fraction of which hosts AGNs. ULIRGs (Sanders & Mirabel 1996) and HyLIRGs (Eisenhardt et al. 2012) are defined by their infrared luminosity. DOGs, on the other hand, are selected by their colour (Dey et al. 2008) and they are a subclass of ULIRGs

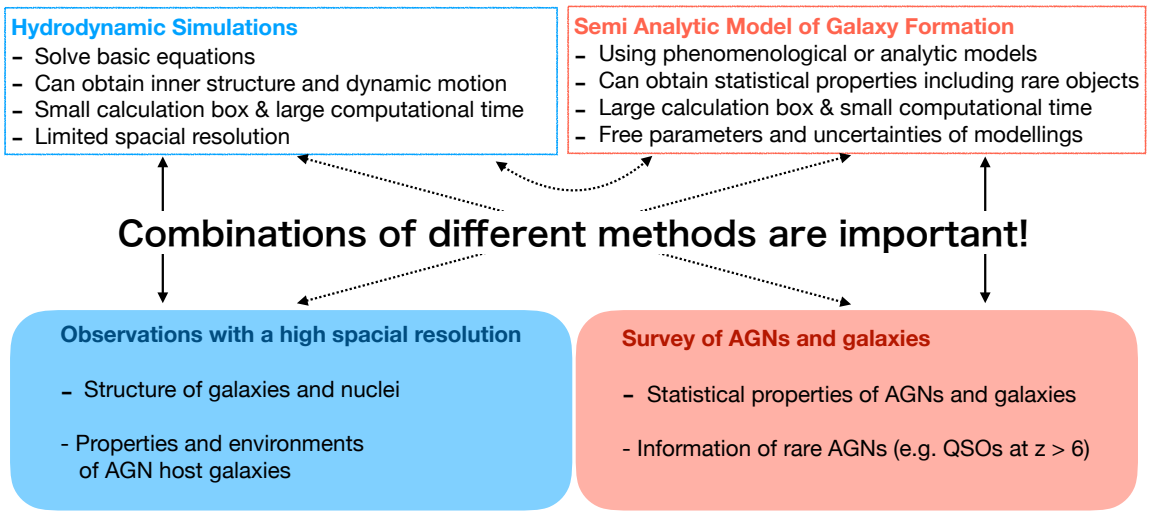

Figure 1.3: The relation of observations and different theoretical methods.

(Melbourne et al. 2012). Their SFR is higher than the main sequence galaxies (i.e. starburst-like SF) and the bolometric luminosity of AGNs can reach the QSO level (Toba et al. 2015). Some theoretical studies (e.g. Hopkins et al. 2005) suggest that ULIRGs occur before QSO phase; the gas and dust surrounding the SMBH is blown away due to the AGN outflow and the nuclear can be observed in optical bands. Although the ULIRG phase is important for revealing the elusive growth of SMBHs, the dust distribution is unclear, which is important for discussing the effect of the AGN feedback. Some observations suggest that the dust is not in AGN host galaxies but the nuclear region (Assef et al. 2015).

ALMA enable us to reveal the central structure surrounding the SMBHs. Izumi et al. (2016), for example, observe the HCN (1-0) line of 10 Seyfert galaxies and estimate the dense molecular gas mass in the CND. Such kind of observations will be useful for making constraints on the CND structure and dynamics.

These observational findings stated here to enable us to investigate co-evolution of galaxies and SMBHs in more details. To do so, the comparison between observational data and theoretical models is important. There are mainly two theoretical approaches for investigating the co-evolution. One is the hydrodynamic simulations (cosmological and non-cosmological), which is powerful to understand the inner structure of galaxies and obtain the position of galaxies. The results can be compared with observations especially with high spatial resolutions. The other is the SA models, which is powerful to obtain statistical properties of galaxies and AGNs. Since these two approaches are complementary, the combination of these two are also important (Fig. 1.3).

1.4 Reviews of other semi analytic models of galaxy formation

SA models are powerful tools for making theoretical predictions that can be directly compared with statistical data obtained by observations. The evolution of baryonic components such as gas haloes, galaxies, and SMBHs is followed by phenomenological modellings to diminish

the computational cost and to enlarge the sample size. SA models, thus, are an excellent approach for statistical studies of galaxies and SMBHs and particularly useful for theoretical studies of rare objects such as AGNs. Here I give the brief review of the history of SA models.

The origin of semi-analytical approach appears in White & Rees (1978) which estimate the halo mass distribution using the density perturbation theory. Solving hierarchical growth of DM haloes, dissipation of the gas, and gas cooling, they show that luminosity density of the Universe and size of galaxy can be explained. In their model, mass of "observable" galaxies are estimated with a constant mass-to-light ratio.

White & Frenk (1991); Lacey & Silk (1991) added the more detailed treatment of star formation in galactic discs, super novae feedback, chemical enrichment and luminosity evolution of stellar population in the context of the structure formation model with CDM. Their model can broadly explain galaxy luminosity functions in the B-band. The difference of these models are the trigger of the star formation. White & Frenk (1991) consider the energy balance between dissipation by gas cooling and heating by SNe. The SFR is self-regulated by this energy balance. Lacey & Silk (1991), on the other hand, consider that the star formation occurs by tidal interactions of galaxies in a group. Then, the star formation starts at the collapse time of the group and the star formation timescale is proportional to the collision timescale of group galaxies.

The effect of galaxy mergers on the galactic age distribution is investigated in Lacey & Cole (1993). They find that to explain observed age distribution of galaxy, Ω_0 should be large (> 0.5). The first SA models, which solve galaxy formation and evolution with evolutionary history of DM haloes including gas cooling, star formation, galaxy mergers, and chemical enrichment, are Kauffmann et al. (1993) and Cole et al. (1994). In these papers, galaxy mergers are treated as the trigger of the formation of elliptical galaxies, not the triggers of star formations. Before Kauffmann et al. (1993) and Cole et al. (1994), the main interests in studies with SA models are the structure formation; to investigating the cosmological model by comparing properties of galaxies. From Kauffmann et al. (1993) and Cole et al. (1994), the interests start to move from such structure formation to the galaxy formation and evolution itself. The SA models reproduce, e.g. galaxy luminosity functions, colours, and Tully-Fisher relation.

Primarily, SA models are developed mainly in two groups; Durham in UK (e.g. Cole et al. 1994; Heyl et al. 1995; Baugh et al. 1996a;b) and Munich in Germany (e.g. Kauffmann et al. 1993; 1994; Kauffmann 1996; Mo et al. 1998). The other groups appeared (e.g. Wu et al. 1998; Somerville & Primack 1999; Menci et al. 2002; Nagashima et al. 2005) thanks to the statistical data, which were newly obtained by observations. These studies explained, for example, the evolution of the Hubble sequence (Baugh et al. 1996b), galaxy clustering (Kauffmann et al. 1999; Benson et al. 2000), and Lyman α absorption (Kauffmann 1996; Kobayashi et al. 2007a). The remaining problems in the models are the size evolution of elliptical galaxies, feedback effect on the star formation (Benson et al. 2003), dust attenuation, and growth of SMBHs. Such modellings which had not been introduced could be taken into account after 2000 since observational data with small errors became available in that time. Cole et al. (2000), whose model framework has been used in other SA models, enable to compare their results with observations in detail, including dust attenuation, size estimation of not only discs but also bulges. The model of Cole et al. (2000) has been developed as `GALFORM` and has used for many studies with updates.

Also, halo merger trees based on cosmological N-body simulation became available. It was

achieved by Roukema et al. (1997) while the most famous work is Kauffmann et al. (1999). After that, merger trees obtained from N-body simulations and the Press-Schecter formalism have been used. The Press-Schecter formalism is still useful since the spacial resolution is infinity, i.e. we can follow the DM halo formation and growth with smaller DM halo mass than N-body simulations. To investigate the spacial distributions of galaxies or galaxy mergers in detail, DM halo merger trees obtained with N-body simulations are preferable.

For star formation quenching, i.e. "negative" feedback, Benson et al. (2003) compare observed LFs of galaxies, results of their SA model, and LFs obtained from DM halo MFs assuming a constant mass-to-light ratio. They demonstrate that feedback by SNe is affected to the evolution of less massive galaxies because of their shallow gravitational potential. They also show that to explain the star formation quenching in massive galaxies, SNe cannot play a role and other mechanisms such as AGN feedback are required.

In the early days of SMBH and AGN studies with SA models, the SMBH growth is assumed to be triggered by major mergers of galaxies (e.g. Kauffmann & Haehnelt 2000; Enoki et al. 2003). Such SA models can explain QSO LFs in optical bands at $z < 2$. Other SA models introduce other triggering mechanisms of AGN activities such as minor mergers (e.g. Croton et al. 2006; Lagos et al. 2009), disc instabilities (e.g. Lagos et al. 2008; Fanidakis et al. 2011; Hirschmann et al. 2012), "hot-mode" accretion (e.g. Croton et al. 2006; Bower et al. 2006) and galaxy interactions (e.g. Menci et al. 2014). Such triggering mechanisms are required to explain LFs less luminous AGNs such as Seyfert galaxies (Hirschmann et al. 2012). The SMBH growth studies focus on the effect of AGN feedback (Croton et al. 2006; Bower et al. 2006), BH spins (e.g. Lagos et al. 2009; Fanidakis et al. 2011; Griffin, Lacey, Gonzalez-Perez, del P. Lagos, Baugh & Fanidakis Griffin et al.), the seed BH mass (e.g. Volonteri & Natarajan 2009; Shirakata et al. 2015), and AGN clustering (e.g. Fanidakis et al. 2013; Oogi et al. 2015; Oogi et al. 2016). The detection probability of gravitational waves by BH-BH coalescence is also investigated by Enoki et al. (2004).

Recent SA models also focus on the detailed galaxy evolution, such as the chemical enrichment (De Lucia et al. 2017), IMF shape (Baugh et al. 2005; Fontanot et al. 2017), and star formation mechanisms (Lagos et al. 2011; Makiya et al. 2014). Although cosmological simulations enlarge their calculation box size and become to be used for statistical studies of galaxies, the feature of studies with SA models is that they can test a large number of different models for a physical phenomenon. On the other hand, a disadvantage of SA models is that the models are possible to be too simplified. Recently, properties of galaxies obtained with SA models have been compared to that obtained with cosmological simulations with the same DM halo merger trees (e.g. Monaco et al. 2014; Guo et al. 2016; Mitchell et al. 2018; Wang et al. 2018). Such studies are helpful for develop both SA models and cosmological simulations.

1.5 Aim of this Thesis

The final goal of my studies is to understand the co-evolution between galaxies and SMBHs. As shown in Sec. 1.3.3, observations have brought fruitful information of AGNs and their host galaxies. To interpret the data and to understand the co-evolution, theoretical studies are important. Therefore, I have updated an SA model to reveal the history of the co-evolution and to interpret "statistical" data of AGNs and their host galaxies obtained by observations.

The critical problem for updating SA models in terms of the SMBH growth is that there are many uncertainties of modellings and the model contains a large number of free parameters. To achieve this problem, it is important to test different models for a single phenomenon and separate the effects of the model. In this thesis, I concentrate on the two different phenomena related to the SMBH growth and show the results of three different studies. In Chapter 3, I show the effect of the seed BH mass on the $M_{\rm BH}$ – $M_{\rm bulge}$ relation (Shirakata et al. 2016). Next, I show the importance of the accretion timescale for cosmic growth of SMBHs and AGNs in Sec. 4 (Shirakata et al. 2019) and theoretical predictions of the Eddington ratio distribution functions at $0 < z < 8$ in Sec. 5 (Shirakata *et al. in prep.*).

Chapter 2

Method

I present the modellings of the semi-analytic model of galaxy formation, "*New Numerical Galaxy Catalogue*" (ν^2GC ; Makiya et al. 2016; hereafter M16). This model originates from Nagashima & Yoshii (2004) and Nagashima et al. (2005) (νGC model). Both νGC and $\nu^2 GC$ models have been used for a variety of astrophysical studies including gravitational waves, Lyα emitters, star formation, and AGN clustering (Enoki et al. 2003; Enoki & Nagashima 2007; Kobayashi et al. 2007b; Makiya et al. 2014; Oogi et al. 2016; 2017). The SMBH growth and AGN properties in M16 are based on Enoki et al. (2003), Enoki et al. (2014). I have updated the original version of ν^2GC for investigating the cosmic growth of SMBHs with that of galaxies in more detail (Shirakata et al. 2016; 2019). In this chapter, I explain (1) the cosmological parameters and N-body simulations which I have employed as initial conditions (Sec. 2.1), (2) structure formation (Sec. 2.2), (3) star formation (Sec. 2.3), (4) growth of the bulges (Sec. 2.4), (5) velocity and size of galaxies (Sec. 2.5), (6) growth of SMBHs (Sec. 2.6), and (7) methods for obtaining the "observable" properties of galaxies (Sec. 2.7). I show the schematics of the model calculation in Fig. 2.1. This calculation is repeated in several (~ 50) time steps, from $z \sim 20$ to ~ 0. Finally, we show the results of MCMC fitting and properties of galaxies in Sec. 2.8.

2.1 Cosmological Parameters and N-body Simulations

I use merging histories of DM haloes from large cosmological N-body simulations (Ishiyama et al. 2015) [1], which have higher mass resolution and larger volume compared with previous simulations (e.g. 4 times better mass resolution compared with Millennium simulations, Springel et al. 2005). Table 2.1 summarises basic properties of the simulations. Simulations with the higher mass resolution and larger volume are favorable. However, I have to find the trade-off between the mass resolution and volume considering the available computational resources. In terms of the SMBH and AGN studies, the computational volume is more important than the mass resolution since AGNs are rare, namely, one AGN will be found in 100 galaxies.

Throughout this thesis, I assume a ΛCDM Universe with the following parameters: $\Omega_0 = 0.31$, $\lambda_0 = 0.69$, $\Omega_{\rm b} = 0.048$, $\sigma_8 = 0.83$, $n_{\rm s} = 0.96$, and a Hubble constant of $H_0 =$

[1] Cosmological simulation data are available from the following link: http://hpc.imit.chiba-u.jp/~ishiymtm/db.html

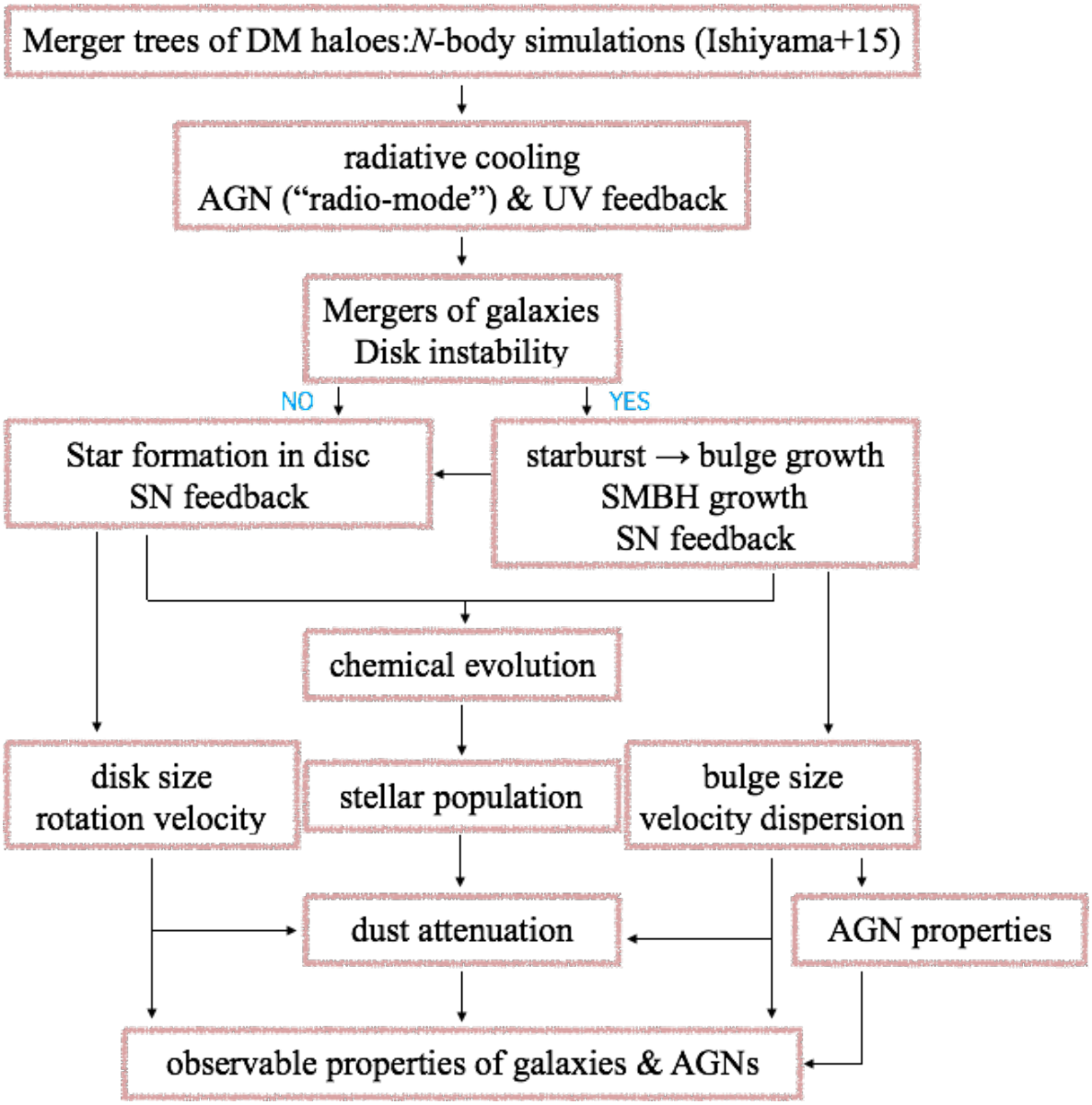

Figure 2.1: Schematics of the model showing the determination of observable properties of galaxies and AGNs.

Name	N	L [h^{-1} Mpc]	m [$h^{-1}M_\odot$]	$M_{\rm min}$ [$h^{-1}M_\odot$]	$M_{\rm max}$ [$h^{-1}M_\odot$]
ν^2GC -L	8192^3	1120.0	2.20×10^8	8.79×10^9	4.11×10^{15}
ν^2GC -M	4096^3	560.0	2.20×10^8	8.79×10^9	2.67×10^{15}
ν^2GC -S	2048^3	280.0	2.20×10^8	8.79×10^9	1.56×10^{15}
ν^2GC -SS	512^3	70.0	2.20×10^8	8.79×10^9	6.58×10^{14}
ν^2GC -H2	2048^3	70.0	3.44×10^6	1.37×10^8	4.00×10^{14}

Table 2.1: Properties of the ν^2GC simulations. N is the number of simulated particles, L is the comoving box size, m is the individual mass of a dark matter particle, $M_{\rm min}$ is the mass of the smallest haloes ($= 40 \times m$) which corresponds to the mass resolution, and $M_{\rm max}$ is the mass of the largest halo in each simulation.

100 h km s^{-1} Mpc^{-1}, where $h = 0.68$ (Planck Collaboration et al. 2014; 2016).

2.2 Galaxy Formation

The mass fraction of the baryonic matter in a DM halo has been calculated with the following procedures, identical to that of M16. Before reionisation of the Universe, the mass fraction is given as $\langle f_b \rangle \equiv \Omega_{\rm b}/\Omega_0$. The mass fraction, however, deviates from $\langle f_b \rangle$ after cosmic reionisation because of the photoionisation heating due to the UV radiation from galaxies and quasars. Small haloes with shallow gravitational potential wells cannot hold the gas heated by photoionisation. We treat this effect following Okamoto et al. (2008b) who performed high-resolution cosmological hydrodynamical simulations with a time-dependent UV background radiation field. They proposed the fitting formulae of the mass fraction of the baryonic matter as a function of the halo mass, M_h, and redshift, z, which was originally proposed by Gnedin (2000):

$$f_{\rm b}(M_h, z) = \langle f_{\rm b} \rangle \times \left\{ 1 + (2^{\alpha_{\rm UV}/3} - 1) \left[\frac{M_h}{M_c(z)} \right]^{-\alpha_{\rm UV}} \right\}^{-3/\alpha_{\rm UV}}, \tag{2.1}$$

where $\alpha_{\rm UV} = 2$ controls the rate of decrease of $f_{\rm b}$ in low mass haloes. The characteristic mass as a function of z, $M_c(z)$, is described by using the fitting formula to the simulation results of Okamoto et al. (2008b):

$$M_c(z) = 6.5 \times 10^9 \exp(-0.604z) \exp[-(z/8.37)^{17.6}] h^{-1} M_\odot. \tag{2.2}$$

We assume reionization occurs at $z = 9.0$. See Sec. 2.3 of M16 for a more in-depth description.

All baryonic matter in a halo is diffuse hot gas soon after halo formation. To calculate the cold gas mass, We firstly calculate cooling radius, $r_{\rm cool}(t)$. We assume the NFW density profile (Navarro et al. 1997) for DM haloes and the isothermal density profile with a finite core radius, r_c, for hot gas haloes;

$$\rho_{\rm NFW}(r) = \frac{\rho_{\rm DM,0}}{(r/r_{\rm s})(1 + r/r_{\rm s})^2}, \tag{2.3}$$

$$\rho_{\rm hot}(r) = \frac{\rho_{\rm hot,0}}{1 + (r/r_{\rm c})^2}, \tag{2.4}$$

where $r_{\rm s}$ is the scale radius of the DM halo, which is described by using the concentration parameter, c_r, and virial radius, $R_{\rm vir}$, as $R_{\rm vir}/r_s \equiv c_r$. We assume $r_{\rm c} = 0.22\, r_{\rm s}$ (Makino et al. 1998), and use an analytical formulation of c_r, as a function of redshift, obtained by fitting to the results of cosmological N-body simulations (Prada et al. 2012). After the collapse of a DM halo, the hot gas gradually cools via radiative cooling. Considering that the hot gas halo is initially virialised, the cooling time at a radius is defined as

$$t_{\rm cool}(r) = \frac{3}{2}\frac{\rho_{\rm hot}(r)}{\mu m_{\rm p}}\frac{k_{\rm B}T_{\rm vir}}{n_{\rm e}^2(r)\Lambda(T_{\rm vir}, Z_{\rm hot})}, \tag{2.5}$$

where $\mu, m_{\rm p}, k_{\rm B}$, and $n_{\rm e}$ are the mean molecular weight, proton mass, Boltzmann constant, and electron number density, respectively. We employ a cooling function, Λ, provided by Sutherland & Dopita (1993), which is a function of hot gas metallicity, $Z_{\rm hot}$, and virial temperature, $T_{\rm vir}$. Virial temperature is calculated from the circular velocity of the host DM halo, $V_{\rm circ}$, as

$$T_{\rm vir} = \frac{1}{2}\frac{\mu m_{\rm p}}{k_{\rm B}}V_{\rm circ}^2. \tag{2.6}$$

The cooling radius, $r_{\rm cool}(t)$, is defined as the radius at which $t_{\rm cool}$ (Eq. 2.5) is equal to the time elapsed since the halo formation epoch. We can calculate the mass which cools in a given time step from Eqs. 2.4 and 2.5.

I evaluate the accretion radius, $r_{\rm acc}(t)$, in which gas can cool and be accreted onto the central galaxy. I set $r_{\rm acc}$ as $MIN\{r_{\rm cool}, r_{\rm ff}(t_{\rm ff} = t_{\rm cool}), R_{\rm vir}\}$, similar to Lacey et al. (2016). Free-fall time, $t_{\rm ff}$, and free-fall radius, $r_{\rm ff}$, have the following relationship:

$$t_{\rm ff}(r_{\rm ff}) = \frac{\pi}{2}\sqrt{\frac{r_{\rm ff}^3}{2GM(r < r_{\rm ff})}}, \tag{2.7}$$

where G is the gravitational constant and $M(r < r_{\rm ff})$ is obtained by the volume integration of Eq. 2.3 from $r = 0$ to $r = r_{\rm ff}$.

I note that we assume the existence of a "cooling hole" in the same way as M16. Since we assume that the radial profile of the remaining hot gas is unchanged until the DM halo mass doubles, there is no hot gas at $r < r_{\rm cool}$ once the gas cools and is accreted onto the central galaxy. This treatment of the hot gas haloes and their cooling are standard for SA models. However, the "cooling hole" is unphysical since the outer hot gas should cool and concentrate on the centre of the halo. To treat the time evolution of the density distribution of the halo, we must solve energy equations and obtain temperature, density, and cooling/heating rate at each radius and find the new thermally or ionisation equilibrium state reflecting the cooling condition. Since SA models do not solve the hydrodynamic equations, such detailed treatment is almost impossible and requires other free parameters. The evolution of the hot haloes should be the evolution averaged in several times the dynamical time of the haloes ($> 10^8$ yr). For the same reason, it is difficult to employ the local cooling rates, which depends on the temperature, number density of the hydrogen, and metallicity at each radius.

2.3 Star Formation in Galaxies

The model includes star formation in cold gas discs and bulges, and reheating of the gas by SNe. The implementation is similar to that of M16.

When the diffuse hot gas cools, it forms a cold gas disc and triggers star formation. The SFR, Ψ, is given by $\Psi = M_{\rm cold}/\tau_{\rm star}$, where $M_{\rm cold}$ is the cold gas mass in a disc and $\tau_{\rm star}$ is the star formation timescale. We assume that $\tau_{\rm star}$ can be described with the dynamical timescale of the disc, $\tau_{\rm d} = r_{\rm d}/V_{\rm d}$ (where $r_{\rm d}$ and $V_{\rm d}$ are the half-mass radius and the circular velocity of the disc, respectively), as

$$\tau_{\rm star} = \epsilon_{\rm star}^{-1}\tau_{\rm d}\left[1+\left(\frac{V_{\rm d}}{V_{\rm star}}\right)^{\alpha_{\rm star}}\right], \tag{2.8}$$

where $\epsilon_{\rm star}, V_{\rm star}$, and $\alpha_{\rm star}$ are free parameters, whose values are $0.46, 197$ km/s, and -2.14, respectively. This determination of the star formation timescale is the same as previous SA models (e.g. Cole et al. 2000). The cold gas is reheated by SNe explosions at a rate of $M_{\rm cold}/\tau_{\rm reheat}$. The timescale for the reheating is given as follows:

$$\tau_{\rm reheat} = \frac{\tau_{\rm star}}{\beta(V_{\rm d})}, \tag{2.9}$$

and

$$\beta(V_{\rm d}) = \left(\frac{V_{\rm d}}{V_{\rm hot}}\right)^{-\alpha_{\rm hot}}. \tag{2.10}$$

Equations 2.8 to 2.10 reflect the depth of the gravitational potential of the galactic disc itself. Small V_d means the shallow gravitational potential, in which the gas can easily escape from the galaxy and stars cannot form rapidly. We also calculate the chemical enrichment associated with the star formation and SNe explosions following Maeder (1992). We assume instantaneous recycling for SNe II and neglect any effects by SNe Ia.

The gas reheated by SNe would not be available for gas cooling immediately. In the model, the gas cannot cool immediately and is stored in a reservoir due to the reheating and ejection by SNe. [2] A fraction of this gas might return to the hot gas halo and cool with a timescale. Lacey et al. (2016) assume the returned gas mass as $\alpha_{\rm return}\ M_{\rm reheat}$ where $\alpha_{\rm return}$ is a free parameter. We, however, simply assume that $\alpha_{\rm return} = 0$ and that all of the reheated gas falls back to the halo as hot gas when the halo mass doubles without escaping from the halo. If I set $\alpha_{\rm return} = 1.0$, the cosmic star formation density at $z < 1.0$ becomes only ~ 1.3 times larger.

We obtain the time evolution of the masses of stars, hot gas, BHs, cold gas, and metals in cold and hot gas for a given SFR, $\Psi(t)$, as follows:

$$\dot{M}_{\rm star} = \alpha\Psi(t), \tag{2.11}$$
$$\dot{M}_{\rm BH} = f_{\rm BH}\Psi(t), \tag{2.12}$$
$$\dot{M}_{\rm reheat} = \beta\Psi(t), \tag{2.13}$$
$$\dot{M}_{\rm cold} = -(\alpha+\beta+f_{\rm BH})\Psi(t), \tag{2.14}$$
$$\dot{(M_{\rm cold}Z_{\rm cold})} = [p-(\alpha+\beta+f_{\rm BH})Z_{\rm cold}]\Psi(t), \tag{2.15}$$
$$\dot{(M_{\rm reheat}Z_{\rm hot})} = \beta Z_{\rm cold}\Psi(t), \tag{2.16}$$

[2] In this thesis, I do not severely differentiate the ejected and reheated gas by SNe since SNe should have the marginal effects.

where $M_{\rm star}, M_{\rm BH}$, and $M_{\rm reheat}$ are the masses of stars, central BHs, and reheated gas mass by SNe in a galaxy, respectively, and $f_{\rm BH}$ is a free parameter tuned to match observational estimates of the relation between masses of bulges and SMBHs at $z \sim 0$. The metallicities of the cold and hot gas are denoted by $Z_{\rm cold}$ and $Z_{\rm hot}$, respectively. The value of the locked-up mass fraction, α, and chemical yield, p, depend on the initial mass function (IMF). We adopt the Chabrier IMF (Chabrier 2003) with which the corresponding values are $(\alpha, p) = (0.52, 1.68 Z_\odot)$. In the model, We assume $Z_\odot = 0.019$. From Eq. 2.11 to 2.16, We analytically derive increments/decrements of the mass and metallicity of each component during a time step (see Eq.15 - 19 of M16).

2.4 Bulge Growth

In this section, I describe how I treat the growth of bulges (spheroid). I assume that the bulge within a galaxy grows via starbursts and the migration of disc stars, both of which are triggered by mergers of galaxies and disc instabilities. The model for these processes is based on Shirakata et al. (2016) and Shirakata et al. (2019). The central SMBHs also grow with their host bulges, whose growth is explained in Sec. 2.6.

2.4.1 Galaxy mergers

When DM haloes merge with each other, the newly formed halo should contain several galaxies which are classified as satellite galaxies and a single central galaxy. [3] All members of this galaxy group would eventually merge under the gravitational attraction of the resultant halo. Mergers of galaxies occur via dynamical friction (central-satellite merger) and random collision (satellite-satellite merger). These types of mergers induce bulge formation and growth within a galaxy.

For the dynamical friction, we set the merger timescale, $\tau_{\rm mrg}$, as $\tau_{\rm mrg} = f_{\rm mrg}\, \tau_{\rm fric}$, where $f_{\rm mrg}$ is an adjustable parameter (in this thesis, $f_{\rm mrg} = 0.81$) and $\tau_{\rm fric}$ is the timescale of dynamical friction. We adopt the fitting function of $\tau_{\rm fric}$Jiang et al. (2008; 2010) which is obtained from N-body simulations:

$$\tau_{\rm fric} = \frac{f(\epsilon)}{2C} \frac{V_{\rm circ} R_{\rm circ}^2}{G M_s \ln(1 + M_h/M_s)}, \tag{2.17}$$

where $C = 0.43$ is a constant fitting parameter, $V_{\rm circ}$ is the circular velocity of the common halo, $R_{\rm circ,s}$ is the radius of the circular orbit of a satellite halo. We assume $R_{\rm circ,s}$ is the virial radius of the host halo, for simplicity. The parameter, M_s, is the total mass of the satellite halo. The dependence on the orbital circularity, ϵ, is described by $f(\epsilon) = 0.90\epsilon^{0.47} + 0.60$. M16 set the orbital circularity as 0.5 for determining $\tau_{\rm fric}$, which is the average value obtained from Wetzel (2011). In this thesis, I consider the halo mass dependence on the circularity obtained from the same previous work (Wetzel 2011). Although we can get the timescale

[3] In principle, the central galaxy is the central galaxy of the most massive progenitor halo since it resides at the gravitational potential well. In this case, the central galaxy is not necessarily the "most massive galaxy" in the halo, because of the feedback (SNe and AGNs) effects. In the case with galaxy merger between the central galaxy and a more massive satellite galaxy, I replace the central galaxy to the more massive satellite, and recalculate the velocity and size of the central galaxy.

from N-body simulations of ν^2GC , The treatments of dynamical friction timescale are used in order to diminish computational time.

For random collision, we follow the results of Makino & Hut (1997), in which they find the merger rate, $k_{\rm MH}$ from an N-body simulation;

$$k_{\rm MH} = \frac{N}{500}\left(\frac{1\ {\rm Mpc}}{R_{\rm vir}}\right)^3 \left(\frac{r_{\rm gal}}{0.1\ {\rm Mpc}}\right)^2 \left(\frac{\sigma_{\rm gal}}{100\ {\rm km\ s^{-1}}}\right)^4 \left(\frac{300\ {\rm km\ s^{-1}}}{\sigma_{\rm halo}}\right)^3 {\rm Gyr}^{-1}, \quad (2.18)$$

where $N, r_{\rm gal}, \sigma_{\rm gal}$, and $\sigma_{\rm halo}$ are the number of satellite galaxies, galaxy radius, 1D velocity dispersions of galaxy and parent halo, respectively. We assume that M_1 scales with $\sim r_{\rm gal}$ and the virial relation, namely, $M_1 \simeq r_{\rm gal}\sigma^2_{\rm gal}/G$. We choose two galaxy pair randomly, which collide in a time step, Δt using Eq. 2.18.

I newly introduce the model of the merger-driven bulge growth proposed by Hopkins et al. (2009a) based on hydrodynamic simulations, similar to other SA model (Somerville et al. 2015). When galaxies merge, stars and gas lose their angular momentum through bar instabilities induced by the merger.

I define a primary galaxy as the galaxy with a larger baryon mass, M_1 (cold gas + stars + a central BH), between the merging pair, and secondary galaxy as the one with smaller baryon mass, M_2. I assume that the secondary is absorbed in the bulge of the primary. The bulge also obtains the cold gas and stars from the primary's disc. The migrated stellar mass, $\Delta M_{\rm 1ds}$, is determined as $MIN(f_* M_2, M_{\rm 1ds})$, where $f_* = G(\mu) = 2\mu\ /\ (1+\mu)$ is the mass fraction of the disc that is destroyed as a function of $\mu = M_2/M_1$ (Hopkins et al. 2009a). This results in the bulge of the primary gaining the stellar mass of $M_2 + \Delta M_{\rm 1ds} \lesssim 2M_2$ per a merger.

The gas mass which migrates in from the primary's disc is assumed to depend on the disc fraction of the primary, $f_{\rm 1d} = (M_{\rm 1ds} + M_{\rm 1dg})/M_1$ ($M_{\rm 1dg}$ is the cold gas mass in a primary's disc before the merger), the gas mass fraction in the primary's disc, $f_{\rm 1g}$, and a pair of orbital parameters, b and θ. The parameter, b, is the peri-galacticon distance before coalescence and θ is the inclination of the orbit of the secondary relative to the primary's disc. Assuming the disc has an exponential surface density profile, I obtain the radius in which the gas migrates to the bulge, $R_{\rm gas}$, following the Eq. 7 of Hopkins et al. (2009a):

$$\frac{R_{\rm gas}}{r_{\rm ds}} = (1 - f_{\rm 1g}) f_{\rm 1d} F(\theta, b) G(\mu), \quad (2.19)$$

where $r_{\rm ds}$ is the scale radius of the disc and $F(\theta, b)$ is a function of b and θ. [4] Since we cannot obtain b and θ from merger trees of the DM haloes, I employ the average value of $F(\theta, b)$ suggested by Hopkins et al. (2009a), $\langle F(\theta, b)\rangle = 1.2$. The mass of the cold gas inside $R_{\rm gas}$, $\Delta M_{\rm 1dg}(< R_{\rm gas})$, migrates to the bulge and is exhausted by a starburst. The mass is described as follows:

$$\Delta M_{\rm 1dg} = M_{\rm 1dg} \times \left\{1 - \left(1 + \frac{R_{\rm gas}}{r_{\rm ds}}\right)\exp(-R_{\rm gas}/r_{\rm ds})\right\}. \quad (2.20)$$

As seen in Eq. 2.19, $R_{\rm gas}$ is larger for smaller $f_{\rm 1g}$ because gas can lose its angular momentum by the torques induced by stars (Hopkins et al. 2009a).

As shown in Eqs. 2.19 and 2.20, $\Delta M_{\rm 1dg}$ is smaller than $M_{\rm 1dg}$ even when $\mu = 1$ (i.e., an equal-mass merger). In this case, pure bulge galaxies cannot be formed. I thus assume that

[4] I assume that gas and stars in the disc have the same scale radius (see, however, Mitchell et al. 2018).

the disc of the primary galaxy is completely destroyed when $\mu > f_{\rm major}$, where $f_{\rm major}$ is a free parameter ($f_{\rm major} = 0.89$). I then set $\Delta M_{\rm 1ds} = M_{\rm 1ds}$ and $\Delta M_{\rm 1dg} = M_{\rm 1dg}$.

The cold gas in the bulge is consumed by a starburst even when only a minor merger occurs. The time evolution of the mass of stars, gas, metals (hot and cold phases), and BHs are calculated by Eqs. 2.11, 2.12, 2.13, 2.14, 2.15, and 2.16 with $\tau_{\rm star} \to 0$. The mass of newly formed stars by a starburst, $\Delta M_{\rm star,burst}$ is described as:

$$\Delta M_{\rm star,burst} = \frac{\alpha}{\alpha + \beta + f_{\rm BH}} M^0_{\rm cold}, \tag{2.21}$$

where $M^0_{\rm cold}$ is the cold gas mass in the bulge immediately after a merger, α is the locked-up mass fraction, $f_{\rm BH}$ is the fraction of the gas which gets accreted onto the SMBH, and β is defined in Eq 2.10 in Sec. 2.3. Most of the cold gas in the bulge is turned into stars by the starburst and the remaining small fraction of the gas is accreted onto the central BH as described in Sec. 2.6.

2.4.2 Disc instability

I also introduce bulge growths via disc instabilities. When a galactic disc becomes gravitationally unstable, a small fraction, $f_{\rm bar}$, of the galactic disc is assumed to migrate to the bulge. Following Efstathiou et al. (1982), a galactic disc becomes unstable when

$$\frac{V_{\rm max}}{(GM_{\rm disc}/r_{\rm ds})^{1/2}} < \epsilon_{\rm DI,crit}, \tag{2.22}$$

where $V_{\rm max}$ is the maximum rotation velocity. The scale length, $r_{\rm ds}$, is estimated as $r_{\rm ds} = (1/\sqrt{2})\langle\lambda_{\rm H}\rangle R_{\rm init}$, where $R_{\rm init}$ is the initial radius of the hot gas sphere and $\langle\lambda_{\rm H}\rangle$ is the mean value of the dimensionless spin parameter. I employ $\langle\lambda_{\rm H}\rangle = 0.042$ (Bett et al. 2007), for simplicity, because the time evolution of the spin parameter is unclear. Note that to calculate the statistical properties of galaxies, such as the size distribution of the discs at $z \sim 0$, we take the distribution of the spin parameter into account (Sec. 2.5). I note that some other SA models (e.g. Cole et al. 2000; Lacey et al. 2016) and our previous model (Shirakata et al. 2016) use the circular velocity and the half-mass radius of the disc instead of $V_{\rm max}$ and $r_{\rm ds}$. The circular velocity would change by the effect of SNe. I thus use $V_{\rm max}$ following original prescription by Efstathiou et al. (1982). If I assume an exponential disc, the effective radius is only ~ 1.67 times larger than the scale length.

Here, the unstable condition in Eq. 2.22 is for the perturbation, whose wavelength corresponds to the scale length of the disc itself. This type of instabilities are called as "global disc instabilities" since the perturbation affects the properties of hole discs. Originally, unstable condition is obtained from the dispersion relation (i.e. solving hydrodynamic equations with a small perturbation). The dispersion relation is, however, difficult to obtain because the galactic disc has complicated structure and dynamical motion. By simple assumptions about the disc circular frequency and density distribution, we can find that the unstable condition of discs is described by the kinetic energy for the rotation and random motion. Eq. 2.22 is also described these two energy terms. $V_{\rm max}$ describes the gravitational potential of the host halo, which relates to the random motion. The denominator describes the rotation energy of the disc.

Galactic discs are more stable when bulges are present. I consider this effect by calculating $V_{\rm max}$ as follows:

$$V_{\rm max} = \sqrt{V_{\rm max,NFW}^2 + V_{\rm max,bulge}^2}, \tag{2.23}$$

$$V_{\rm max,NFW} \sim 0.465 \sqrt{\frac{c_r}{\ln(1+c_r) - c_r/(1+c_r)}} V_{\rm circ}, \tag{2.24}$$

$$V_{\rm max,bulge} = \begin{cases} \sigma_{\rm 1D} & (r_{\rm ds} \lesssim r_{\rm b}) \\ \sqrt{\frac{M_{\rm bulge} G}{r_{\rm ds}}} & (r_{\rm ds} > r_{\rm b}), \end{cases} \tag{2.25}$$

where $\sigma_{\rm 1D}$ and $r_{\rm b}$ are the 1D velocity dispersion and the size of the bulge, respectively. We assume that a bulge has the isothermal density profile (see Sec. 2.4).

The critical value for disc stabilities, $\epsilon_{\rm DI,crit}$ (Eq. 2.22), depends on the gas fraction and density profile of a galactic disc (e.g. Efstathiou et al. 1982; Christodoulou et al. 1995). If the velocity dispersion of galactic discs is neglected, the value of $\epsilon_{\rm DI,crit}$ is ~ 1.1 for the exponential stellar disc (Efstathiou et al. 1982) and ~ 0.9 for the gaseous disc (Christodoulou et al. 1995). We, however, treat $\epsilon_{\rm DI,crit}$ as an adjustable parameter, whose value should be ≤ 1.1 since the disc actually has the velocity dispersion and becomes more stable. I set $\epsilon_{\rm DI,crit} = 0.75$ to explain the observed cosmic SFR density.

When a galactic disc becomes gravitationally unstable, a fraction of the cold gas and stars in the disc is added to the bulge component. The migrated stellar mass from the disc to bulge, $\Delta M_{\rm ds,DI}$, is determined as:

$$\Delta M_{\rm ds,DI} = f_{\rm bar} M_{\rm ds}, \tag{2.26}$$

where $f_{\rm bar}$ is a free parameter and $M_{\rm ds}$ is the stellar mass of the disc. The gas mass which migrates in from the disc, $\Delta M_{\rm dg,DI}$, is determined as:

$$\Delta M_{\rm dg,DI} = M_{\rm 1dg} \times \left\{ 1 - \left(1 + \frac{R_{\rm gas}}{r_{\rm ds}} \right) \exp(-R_{\rm gas}/r_{\rm ds}) \right\}, \tag{2.27}$$

$$\frac{R_{\rm gas}}{r_{\rm ds}} = (1 - f_{\rm 1g}) f_{\rm 1d} f_{\rm bar}, \tag{2.28}$$

$$\tag{2.29}$$

where $M_{\rm dg}$ is the gas mass of the disc. Eqs. 2.27, and 2.28 are analogous to our galaxy merger case with $G(\mu) = f_{\rm bar}$ and $F(\theta, b) = 1.0$. The value of the free parameter, $f_{\rm bar}$, is set to 0.63. Some SA models assume that the unstable galactic disc is completely destroyed and the galaxy possess only the bulge component, consuming the cold gas by a starburst. This treatment contradicts with local barred galaxies, which are considered to form via disc instabilities since the barred galaxies also lie on the main sequence of the star formation (e.g. Abdurro'uf & Akiyama 2017). However, such kind of "violent" bulge growth without galaxy mergers might be necessary to form SMBHs with $\sim 10^9 M_\odot$ at $z > 6$ (see Sec. 3.4).

The spheroids formed through this process might be so-called 'pseudo-bulges', although I do not differentiate between bulges formed by these instabilities and those formed by mergers. Starbursts triggered by these instabilities are also treated in the same way as those by mergers.

2.5 Size of Galaxies

Here I describe how to estimate galaxy size, the circular velocity of galactic discs, and the velocity dispersion of bulges.

2.5.1 Disc size and circular velocity

We assume that DM and hot gas haloes have the same specific angular momentum and that the angular momentum is conserved during the formation of a cold gas disc. We adopt the log-normal distribution for the dimensionless spin parameter, $\lambda_{\rm H} \equiv L\,|E|^{1/2}\,/GM^{5/2}$, where L, E, and M are the angular momentum, binding energy, and DM halo mass, respectively. The mean value of $\lambda_{\rm H}$ is 0.042 and the logarithmic variance is 0.26, which are obtained from N-body simulations of Bett et al. (2007).

The effective radius of a cold gas disc, $R_{\rm d}$, is given by the following relation:

$$R_{\rm d} = (1.68/\sqrt{2})\lambda_{\rm H} R_{\rm init}, \tag{2.30}$$

where the initial radius of the hot gas sphere, $R_{\rm init}$, is set to the accretion radius, $r_{\rm acc}$, introduced in Sec. 2.2. Disc rotation velocity, $V_{\rm d}$, is given as the circular velocity of its host halo. In the model, $R_{\rm init}$ and $V_{\rm d}$ are renewed when the disc mass increases from the previous time step and when the new $R_{\rm init}$ is larger than the previous time step.

I note that $R_{\rm d}$ becomes smaller than that at the previous time step when a merger of galaxies or disc instability occurs, by which the disc mass of the primary galaxy decreases. I then consider the conservation of the angular momentum and set the new effective radius, $R_{\rm d,new}$, as $R_{\rm d,new} = (M_{\rm 0d}/M_{\rm 1d}) \times R_{\rm d}$, where $M_{\rm 0d}$ and $M_{\rm 1d}$ are the disc mass (stellar + cold gas) of the primary galaxy after and before the merger or disc instability, respectively.

2.5.2 Bulge size and velocity dispersion

I describe how to estimate bulge size and velocity dispersion when a merger of galaxies or a disc instability occurs. There have been several previous studies (e.g. Hopkins et al. 2009b; Covington et al. 2011; Shankar et al. 2013) which investigate how to calculate the size and velocity dispersion of the bulge from the Virial theorem and energy conservation. They, however, only study the major merger case. Applying their result to galaxies experiencing minor mergers or a disc instability, by which a galactic disc is not completely destroyed, is not straightforward. In this thesis, I apply the similar formula (with some updates, described below) to M16 [5] to obtain size and velocity dispersion of bulges formed not only by major mergers but also by minor mergers and disc instability.

I first consider merging galaxies. The total energy of each galaxy which contributes to the bulge formation is given by the Virial theorem:

$$E_i = -\frac{1}{2}[(M_{{\rm b},i} + M_{{\rm BH},i})V_{{\rm b},i}^2 + (M_{d,i} + M_{{\rm cold},i})V_{{\rm d},i}^2], \tag{2.31}$$

where $M_{\rm b}, M_{\rm d}$, and $M_{\rm cold}$ are the masses of the bulge stars, disc stars, and cold gas, respectively, and $V_{\rm b}$ and $V_{\rm d}$ denote the velocity dispersion of the bulge and the rotation velocity

[5] M16 assume that only major mergers are induced starbursts in bulges and a galactic disc is completely destroyed by a major merger while it does not change by a minor merger.

of the disc, respectively. The subscripts, $i = \{0, 1, 2\}$, indicate the merger remnant, the primary progenitor, and the secondary progenitor, respectively.

I consider the effect of the gravitational potential of the DM halo which hosts the primary galaxy on the bulge dynamics. The method is similar but slightly different from Lacey et al. (2016). Assuming that a fraction of the DM halo mass, $M_{\rm DM,1}$, affects the bulge dynamics, I simply replace $M_{\rm b,1}$ to $M_{\rm b,1} + M_{\rm DM,1}$ in Eq. 2.31. The mass, $M_{\rm DM,1}$ is given by:

$$M_{\rm DM,1} = \frac{\Omega_0}{\Omega_{\rm b}} \left(\frac{M_{\rm h}}{M_{\rm h0}} \right)^{\alpha_{\rm h}}, \tag{2.32}$$

where $M_{\rm h0}$ and $\alpha_{\rm h}$ are free parameters and the values are determined to reproduce the observed relation between the bulge size and K-band magnitude of galaxies at $z \sim 0$. In this thesis, the values of $M_{\rm h0}$ and $\alpha_{\rm h}$ are $10^{14} M_\odot$ and 1.82, respectively. Since we do not utilize sub-halo merger trees, I ignore the effect of the DM potential for the secondary galaxies. However, the sub-halo would have only a small impact due to the shallow potential. As described in Sec. 2.4.1, a fraction of the disc mass in the primary galaxy, $\Delta M_{\rm 1ds} + \Delta M_{\rm 1dg}$, migrates to the bulge. The remaining energy in the disc, $E_{\rm 0,d}$, is then:

$$E_{\rm 0,d} = -\frac{1}{2} \{ M_{\rm d,1} + M_{\rm cold,1} - (\Delta M_{\rm 1ds} + \Delta M_{\rm 1dg}) \} V_{\rm d,1}^2. \tag{2.33}$$

The total energy of the bulge of the merger remnant, $E_{\rm 0,b}$, can be described as follows:

$$E_{\rm 0,b} = E_0 - E_{\rm 0,d}. \tag{2.34}$$

Considering the energy dissipation, we obtain the energy conservation relation as follows:

$$f_{\rm diss}(E_1 + E_2 + E_{\rm orb}) = E_{\rm 0,b}, \tag{2.35}$$

where $f_{\rm diss}$ is the fraction of energy dissipated from the merging system. By following M16, $f_{\rm diss}$ is described as:

$$f_{\rm diss} = 1 + \kappa_{\rm diss} f_{\rm gas}, \tag{2.36}$$

where

$$f_{\rm gas} = \frac{\Delta M_{\rm 1g} + M_{\rm 2g}}{M_1 + M_2}. \tag{2.37}$$

The orbital energy, $E_{\rm orb}$, is given as follows:

$$E_{\rm orb} = -\frac{E_1 E_2}{(M_2/(M_1 + M_{\rm DM,1}))E_1 + ((M_1 + M_{\rm DM,1})/M_2)E_2}, \tag{2.38}$$

where M_1 and M_2 are the total mass of each galaxy (cold gas + stars + a BH).

I calculate the velocity dispersion and the size of a bulge, $r_{\rm b}$, as

$$V_{\rm b,0}^2 = -\frac{2E_{\rm 0,b}}{M_{\rm tot,0}}, \tag{2.39}$$

$$r_{\rm b,0} = \frac{G M_{\rm tot,0}}{2V_{\rm b,0}^2}, \tag{2.40}$$

where $M_{\rm tot,0}$ is the total mass of the merger remnant (including $M_{\rm DM,1}$). To obtain the 1D velocity dispersions, $\sigma_{\rm 1D}$, we assume the bulge structure can be described by an isothermal sphere. The 1D velocity dispersion is simply given by $\sigma_{\rm 1D} = V_{\rm b,0} / \sqrt{3}$.

For the disc instability, I employ the same formulae as those for the merger of galaxies while subscripts, $i = \{1, 2\}$, indicate the bulge and disc, respectively and the orbital energy, $E_{\rm orb}$, is set to be 0.

2.5.3 Dynamical response caused by SNe feedback

We consider the change of the size and velocity caused by SN feedback. The SN feedback continuously expels gas from a galaxy. As a result, the gravitational potential well becomes shallower and the gravitationally bound system expands and its rotation speed slows down (Yoshii & Arimoto 1987). We refer to this effect as *dynamical response*, which is taken into account the same way as M16. This affects the size of galactic discs and bulges, the rotation velocity of galactic discs and their host haloes, and the velocity dispersion of galactic bulges. See Sec. 2.8 of M16 for farther details.

2.6 SMBH Growth and AGN Properties

2.6.1 BH seeding

We place a seed BH, immediately after a galaxy forms. The seed mass, $M_{\rm seed}$ is investigated in Sec. 3.3. The mass of the host halo, in which a seed BH is placed, depends on the redshift and the mass resolution of N-body simulations. The minimum halo mass in which gas cools and possibly forms a galaxy is determined by the mass resolution and the strength of the UV background (see Sec. 2.2). I show the redshift evolution of this minimum halo mass in Fig. 2.2. The effect of the UV background are important when using N-body simulations with higher mass resolution, meaning that UV background plays a role in smaller galaxies. Since observable AGNs, which are the main target of our studies, do not reside in such smaller galaxies, I do not show the details about this effect. I have confirmed that the mass resolution of N-body simulations does not change our final results and conclusions.

2.6.2 Mass accretion onto SMBHs

When a starburst is triggered by a galaxy merger or disc instability (Sec. 2.4), a small fraction of the gas is supplied to the central SMBH. The accreted gas mass per a starburst, $\Delta M_{\rm acc}$, is given by:

$$\Delta M_{\rm acc} = f_{\rm BH} \Delta M_{\rm star,burst}. \tag{2.41}$$

We calculate the time evolution of the mass accretion rate, $\dot{M}_{\rm BH}$, from $\Delta M_{\rm acc}$ and the accretion timescale, $t_{\rm acc}$, as

$$\dot{M}_{\rm BH} = \frac{\Delta M_{\rm acc}}{t_{\rm acc}} \exp\left(\frac{t - t_{\rm start}}{t_{\rm acc}}\right), \tag{2.42}$$

where $t_{\rm start}$ is the starting time of the accretion, which is the same as that of the starburst. The prescription for $t_{\rm acc}$ is one of the main topic of this thesis and will be described in Sec. 4.2 in detail. The starting time of the starburst, $t_{\rm start}$, is assigned randomly within the time step. Shirakata et al. (2015) suggests that $t_{\rm start}$ must be delayed from the starting time of the starburst so that the dust extinction of a galaxy becomes negligible for AGNs. In this thesis, I do not include this delay to show clearly the effect of varying the modelling of the accretion timescale.

I note that Eqs. 2.41 and 2.42 are valid for SMBH growth via both galaxy mergers and disc instabilities. Practically, the value of $f_{\rm BH}$ is not necessarily the same for both galaxy mergers and disc instabilities. There are, however, almost no suggestions about the difference of the

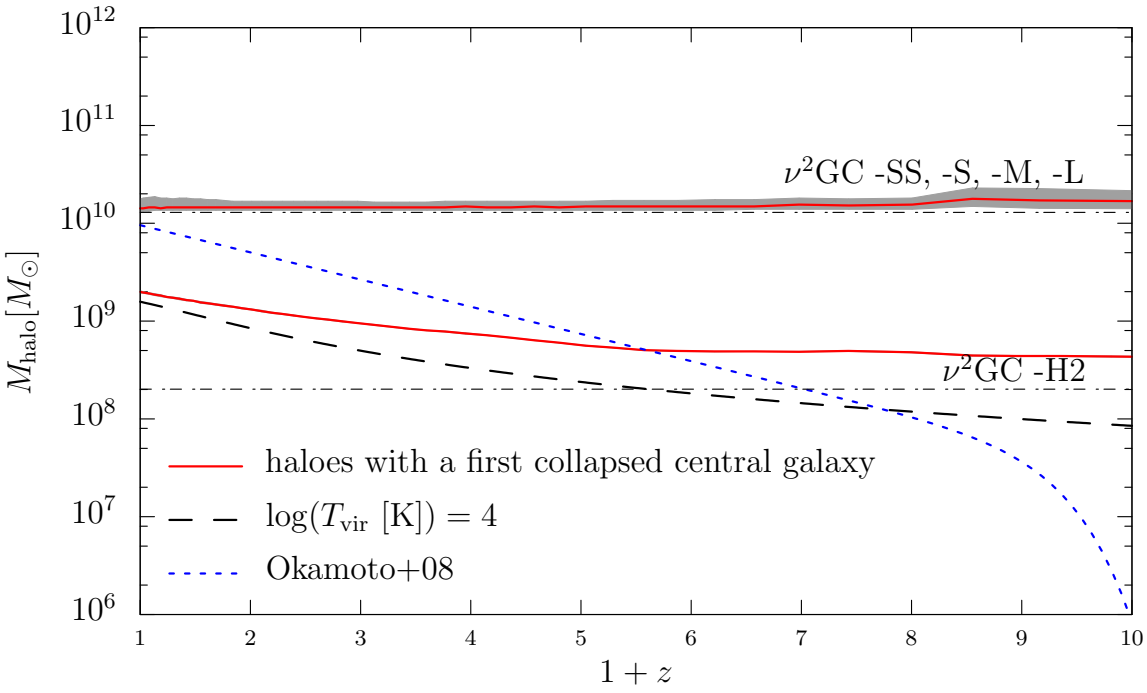

Figure 2.2: Redshift evolution of the mass of haloes which contain newly formed central galaxies with different N-body simulations. Red solid line shows the median mass of such haloes and shaded region indicates 75 percentile. Blue dotted line depicts the characteristic halo mass, $M_c(z)$, below which a halo cannot cool because of the photoionisation (Okamoto et al. 2008b). Black dashed line depicts the halo mass that corresponds to $T_{\rm Vir} = 10^4$ [K]. The mass resolutions of ν^2GC simulations are shown by black dot-dashed lines.

fraction of the cold gas mass which gets accreted onto an SMBH with different triggering mechanisms. We, thus, employ the common $f_{\rm BH}$, for diminishing the degree of freedom.

SMBHs also increase their mass via SMBH-SMBH coalescence following mergers of galaxies. As in M16, we simply assume that SMBHs merge instantaneously after the merger of their host galaxies.

2.6.3 AGN luminosity

I calculate the AGN bolometric luminosity, $L_{\rm bol}$, from the accretion rate (Eq. 2.42). Hereafter I define the bolometric luminosity normalised by the Eddington luminosity ($L_{\rm Edd}$) as $\lambda_{\rm Edd} \equiv L_{\rm bol}/L_{\rm Edd}$ and the accretion rate normalised by Eddington rate ($\dot{M}_{\rm Edd} = L_{\rm Edd}/c^2$) as $\dot{m}$. I employ the following relation between $\lambda_{\rm Edd}$ and $\dot{m}$ (based on Kawaguchi 2003):

$$\lambda_{\rm Edd} = \left[\frac{1}{1+3.5\{1+\tanh(\log(\dot{m}/\dot{m}_{\rm crit}))\}} + \frac{\dot{m}_{\rm crit}}{\dot{m}}\right]^{-1}, \tag{2.43}$$

where $\dot{m}_{\rm crit}$ is an adjustable parameter, whose value should be $2.5 \lesssim \dot{m}_{\rm crit} \lesssim 16.0$. I set $\dot{m}_{\rm crit} = 10.0$ and in this case, $\lambda_{\rm Edd}$ has similar dependence on $\dot{m}$ to that obtained by Watarai et al. (2000) and Mineshige et al. (2000).

Although the gas accretion rate (Eq. 2.42) decreases monotonically with time, $L_{\rm bol}$ does not necessarily decrease with time due to the difference of the change rate between $\lambda_{\rm Edd}$ and $L_{\rm Edd}$. When the following condition is satisfied, $L_{\rm bol}(t)$ becomes larger than $L_{\rm bol}(t_{\rm start})$:

$$\frac{\lambda_{\rm Edd}(t)}{\lambda_{\rm Edd}(t_{\rm start})} > \frac{L_{\rm Edd}(t_{\rm start})}{L_{\rm Edd}(t)}. \tag{2.44}$$

A part of AGNs with $\lambda_{\rm Edd} > 1.0$ satisfies this condition. I show the evolution of two SMBHs with $M_{\rm BH} = 10^6 M_\odot$ in Fig. 2.3. I assume $t_{\rm acc} = 10^7$ yr and $\Delta M_{\rm acc} = 10^6$ and $10^7 M_\odot$ (top and bottom panels, respectively).

In order to obtain AGN luminosity in the optical or X-ray range, we employ the bolometric correction estimated by Marconi et al. (2004):

$$\log[L/L_{\rm Y}] = a + b\mathcal{L} + c\mathcal{L}^2 + d\mathcal{L}^3, \tag{2.45}$$

where $\mathcal{L} = (\log L - 12)$, L is the intrinsic bolometric luminosity in units of $L_\odot$ ($= 3.826 \times 10^{33}$ erg/s), and $L_{\rm Y}$ is the luminosity in hard X-ray (2-10 keV), L_X, or B-band luminosity, $\nu_B L_{\rm B}$ (ν_B is a central frequency of the B-band corresponding to 4400 Å). Parameters (a, b, c, d) are $(1.54, 0.24, 0.012, -0.0015)$ for hard X-ray, and $(0.80, -0.067, 0.017, -0.0023)$ for B-band. To obtain UV (1450 Å) luminosity, $L_{\rm UV}$, I use

$$M_{\rm UV} = M_B + 0.85, \tag{2.46}$$

where $M_{\rm UV}$ and M_B are $UV-$ and $B-$ band magnitudes, respectively. The B-band magnitude, M_B, is calculated with Eq. 2.45. The Eq. 2.46 is obtained by assuming the template SED presented in Kawaguchi et al. (2001). By using this template SED, I also obtain

$$L_{\rm UV} = 0.26 L_{\rm bol}. \tag{2.47}$$

I note that I do not consider the change of the radiation efficiency in the low-Eddington accreting regime (namely, $\dot{m} < 0.01\dot{m}_{\rm crit}$) since the bolometric correction for AGNs with

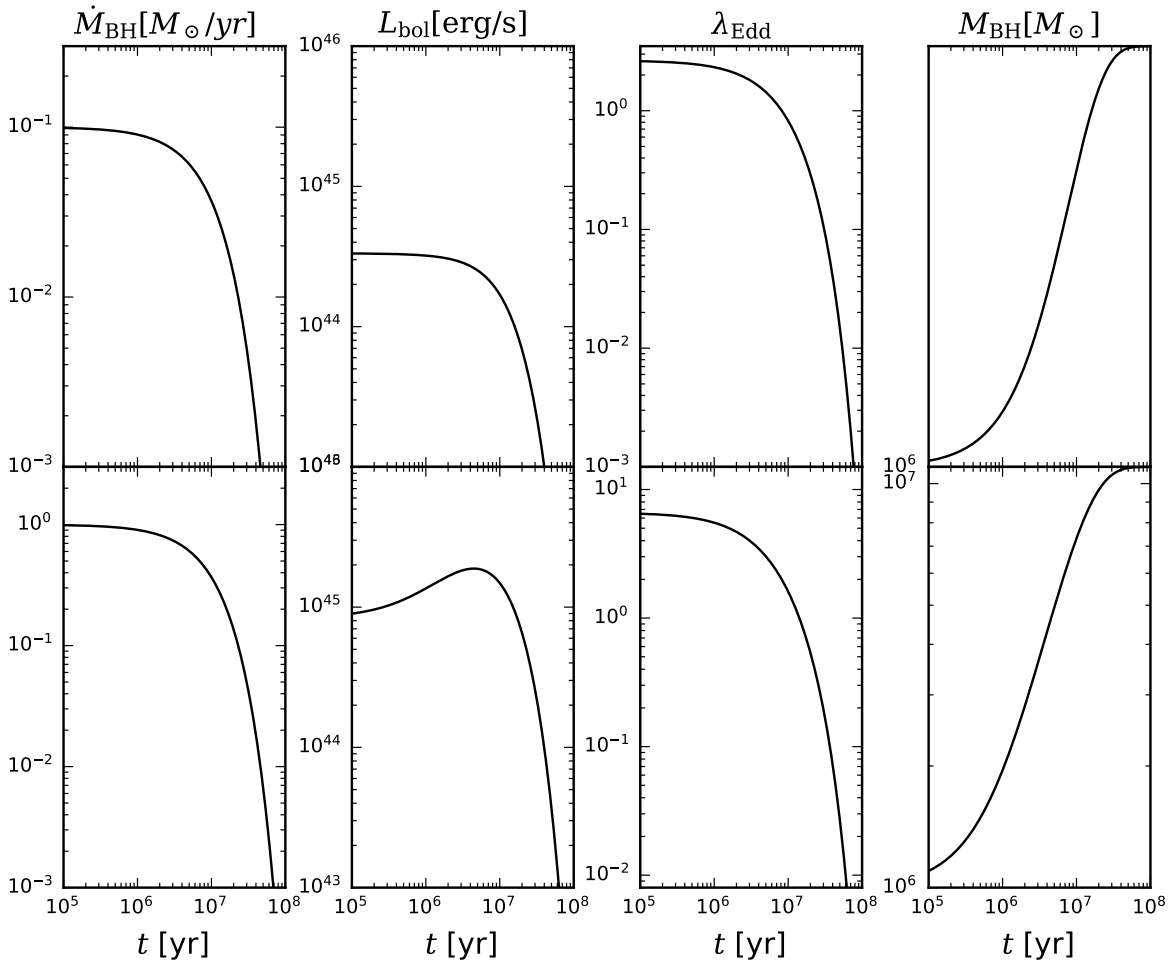

Figure 2.3: Examples of the growth history of model SMBHs with the initial SMBH mass of $10^6 M_\odot$. I assume $t_{\rm acc} = 10^7$ yr and $\Delta M_{\rm acc} = 10^6$ and $10^7 M_\odot$ in top and bottom panels, respectively. In this figure, I show the evolution of $\dot{M}_{\rm BH}, L_{\rm bol}, \lambda_{\rm Edd}$, and $M_{\rm BH}$ from left to right panels.

$\dot{m} < 0.01\dot{m}_{\rm crit}$ is unclear. The bolometric correction obtained by Marconi et al. (2004) consider the dependency on the bolometric luminosity. It would actually depend not only on the bolometric luminosity but also on the Eddington ratio (e.g. Lusso et al. 2012). It means that although the radiation efficiency should decrease in the low-Eddington accreting regime, the bolometric correction should become smaller (i.e. the fraction of X-ray radiation becomes larger). This effect is not considered in, e.g. Fanidakis et al. (2012). They introduce the change of the radiative efficiency without considering the shift of the bolometric correction. In this thesis, I do not introduce the change of the radiative efficiency to keep the consistency and to diminish the degree of freedom of the model.

2.6.4 "Radio mode" AGN feedback

I introduce the so-called radio-mode AGN feedback process to prevent gas in massive haloes from cooling and forming stars. Following Bower et al. (2006), gas cooling in a halo is quenched when the following two conditions are satisfied:

$$t_{\rm dyn}(r_{\rm cool}) < \alpha_{\rm cool} t_{\rm cool}, \tag{2.48}$$

and

$$\epsilon_{\rm SMBH} L_{\rm Edd} > L_{\rm cool}, \tag{2.49}$$

where $L_{\rm cool}$ is the cooling luminosity of the gas, $t_{\rm dyn}$ is the dynamical time of the halo, $\alpha_{\rm cool}$ and $\epsilon_{\rm SMBH}$ are free parameters which are determined to reproduce the bright-end of the LFs of galaxies at $z \sim 0$. I set $(\alpha_{\rm cool}, \epsilon_{\rm SMBH}) = (1.14, 2.19 \times 10^{-3})$.

2.7 Comparisons with Observations

We have the information of metal enrichment histories caused by star formation, and now we estimate luminosities of galaxies in some bands and the effect of dust attenuation using a spectral energy distribution (SED) model of galaxies (Bruzual & Charlot 2003).

To estimate the extinction of the starlight from galaxies, we assume that (1) the dust-to-cold gas ratio is proportional to the metallicity of the cold gas, (2) dust optical depth is proportional to the dust column density. The dust optical depth $\tau_{\rm dust}$ is then calculated as follows:

$$\tau_{\rm dust} = \tau_0 \left(\frac{M_{\rm cold}}{M_\odot}\right) \left(\frac{Z_{\rm cold}}{Z_\odot}\right) \left(\frac{r_d}{\rm kpc}\right)^{-2}, \tag{2.50}$$

where r_d is the effective radius of the galaxy disc and τ_0 is a kind of free parameter which should be chosen to fit the local observations (such as galaxy LFs). The extinction curve we adopt is that in Calzetti et al. (2000), and dust distribution is assumed to be the slab dust model (Disney et al. 1989).

The cold gas exhausted by starbursts immediately turns into stars and hot gas. It means that there is no cold gas, thus no dust in bulge immediately after the starburst. If a galactic disc is completely disrupted by violent merger events, then the optical depth becomes zero and the colour of galaxy will be too bluer than observational results. To avoid this problem, we treat the starburst timescale is not zero only when we calculate the luminosity of galaxies. We assign the starting time of the merger randomly in the current time step, and consider that the starburst timescale is one dynamical time of the bulge, r_b/V_b. We then calculate the

amount of remaining dust and gas components at the end of the time step. I use the slab model for dust geometry both in the normal star formation and the starburst phases. Dust optical depth is calculated by Eq. 2.50, where the r_d is replaced r_b.

We classify the galaxies into three types by the bulge-to-total luminosity ratio in B-band. In our model we use the criteria of Simien & de Vaucouleurs (1986); galaxies with $B/T > 0.6$, $0.4 < B/T \leq 0.6$, and $B/T \leq 0.4$ are classified as elliptical, lenticular, and spiral galaxies, respectively.

2.7.1 "Observable fraction" of AGNs

To compare the calculated AGN LFs with observed UV AGN LFs, I need to define "observable fraction" in UV-band, $f_{obs,UV}$, because we can only obtain the intrinsic luminosity of AGNs from our model. Since AGN obscuration and absorption processes are very complicated, I derive an empirical formula by the following procedures. Recent work (e.g. Aird et al. 2015; Ueda et al. 2014) has estimated the hydrogen column density distribution around AGNs by a compilation of available samples obtained by *Swift*/BAT, MAXI, *ASCA*, *XMM-Newton*, *Chandra* and *ROSAT*. Therefore, one can estimate the "intrinsic" luminosity in hard X-ray of observed AGNs by utilizing the hydrogen column density distribution. I thus use the observed hard X-ray LFs (Aird et al. 2015; Table 9) to obtain the "observable fraction". The procedures are as follows.

First, I convert hard X-ray luminosities to UV luminosities with Eqs 2.45 and 2.46 and I obtain "intrinsic" UV LFs. Second, I assume the shape of the observable fraction as

$$f_{obs,UV} = A(z) \left(\frac{L_{\rm bol}}{10^{46} {\rm erg/s}} \right)^{\beta(z)}. \tag{2.51}$$

I assume that A and β are a function of redshift, $A(z) = A_0\,(1+z)^{A_1}$ and $\beta(z) = \beta_0\,(1+z)^{\beta_1}$, considering that the dust-to-gas ratio evolves with redshift. The value of β_0 should be positive, considering the luminosity dependence of AGN obscuration (e.g. Lawrence 1991). Third, I fit parameters, A_0, A_1, β_0, and β_1 by a Markov Chain Monte Carlo (MCMC) method to fit observed UV LFs (see the caption of Fig. 4.7). After 10^5 iterations of the MCMC fitting, I obtain the best fit values $(A_0,\ A_1,\ \beta_0,\ \beta_1) = (0.16,\ -0.05,\ 0.07,\ 0.00)$ with which the observable fraction does not exceed 1.

Ricci et al. (2017a) suggest that observed UV LFs of AGNs are well explained by their hard X-ray LFs, whose hydrogen column densities are less than $10^{21-22}{\rm cm}^{-2}$. Since the modelling of the gas distribution surrounding an SMBH is difficult for SA models, I estimate the observable fraction by an empirical formulation.

Hopkins et al. (2007) propose an alternative formula for the "observable fraction". Here I show the difference of the derivation. Hopkins et al. (2007) derives an observable fraction as follows. They obtain intrinsic bolometric correction which is a similar shape to that of Marconi et al. (2004). By employing the observed hydrogen column density distribution (Ueda et al. 2003), they calculate the photoelectric absorption in $X-$ ray. For optical and mid-IR bands, they adopt a canonical gas-to-dust ratio and SMC-like dust attenuation curve (Pei 1992) to obtain the probability of observing AGNs in optical/mid-IR bands. By the bolometric correction and the correction of the photoelectric absorption and the dust attenuation, they obtain intrinsic bolometric AGN LFs. Using this bolometric AGN LF, they estimate the probability of observing AGNs with an intrinsic luminosity of hard-/soft- X-ray and optical

B-band. They fit the probability by the same function as Eq. 2.51, where $A(z) = f_{46}$ and $\beta(z) = \beta$. In there estimates, (f_{46}, β) is $(1.243, 0.066)$ in hard $X-$ ray (2-10 keV), $(0.260, 0.082)$ in $B-$ band (4400 Å).

The method for the estimation of the observable fraction in this thesis is slightly different from that of Hopkins et al. (2007). I convert hard X-ray (2-10 keV) LFs obtained from Aird et al. (2015) to UV (1450Å) LFs by using a bolometric correction (Marconi et al. 2004) and $M_{UV} = M_B + 0.85$ (Kawaguchi et al. 2001). The LFs obtained from these processes are regarded as the intrinsic UV LFs since hard X-ray (2-10 keV) LFs of Aird et al. (2015) are absorption-corrected. By comparing these intrinsic UV LFs with LFs obtained from observations, I obtain the parameters of observable fractions as $(A_0,\ A_1,\ \beta_0,\ \beta_1) = (0.16,\ 0.07,\ -0.05,\ 0.00)$ (Eq. 2.51).

To show the differences of observable fractions obtained by Hopkins et al. (2007) and by our new method, I present Fig. 2.4. The grey dotted line indicates intrinsic UV LFs and blue dashed and black solid lines show LFs considering observable fraction obtained from Hopkins et al. (2007) and this thesis, respectively. I assume that the observable fraction obtained by Hopkins et al. (2007) is the same in B and UV bands. I find that in such a simple assumption, the observable fraction obtained in this thesis is roughly consistent with those obtained by Hopkins et al. (2007), although they have a small (~ 20 %, at most) difference.

I note that UV LFs with observable fractions obtained from both Hopkins et al. (2007) and our calculation are inconsistent with observations at $z > 5.0$ since the fitting function of hard $X-$ ray LFs obtained from Aird et al. (2015) can explain the observational results only at $z < 5.0$. I also note that the scatter of the conversion from the hard X-ray to UV luminosity are not considered for deriving the observable fraction. Akiyama et al. (2018) suggest that this scatter has significant effect on the shape of the LFs (see Fig. 21 in Akiyama et al. (2018)).

2.8 Results for Galaxy Evolution Obtained with the Updated Model

I show the parameter fitting results and resulting properties of galaxies. The main results of this thesis on the statistical properties of SMBHs and AGNs appear in Sec 4.3.

2.8.1 New MCMC fitting results

First, I run the MCMC fitting with the ν^2GC -SS simulation to tune parameters. For the model calibration, I use observed $K-$ and $r-$ band LFs at $z \sim 0$ obtained from the Galaxy and Mass Assembly (GAMA) survey, $\mathrm{H_I}$ mass function (MF) at $z \sim 0$ extracted from the data of the Arecibo Legacy Fast ALFA (ALFALFA) survey, $M_{\rm BH} - M_{\rm bulge}$ relation at $z \sim 0$ (Eq. 11 Kormendy & Ho 2013), scaling relations of galactic discs and bulges at $z \sim 0$ (Courteau et al. 2007; Forbes et al. 2008; respectively) cosmic SFR density obtained from observations (UV- and IR-bands, and radio 1.4 GHz), $K-$ band LFs at $z = 1, 2, 3$ obtained with the UKIDSS Deep Survey (Cirasuolo et al. 2010), and AGN hard $X-$ray LFs at $z = 0.4, 1, 2$ (Ueda et al. 2014).

I summarised the fiducial values of our free parameters and related equations in Table 2.2. I run the calculation with 50000 realisations, excluding the initial 10000 steps of the "burn-in"

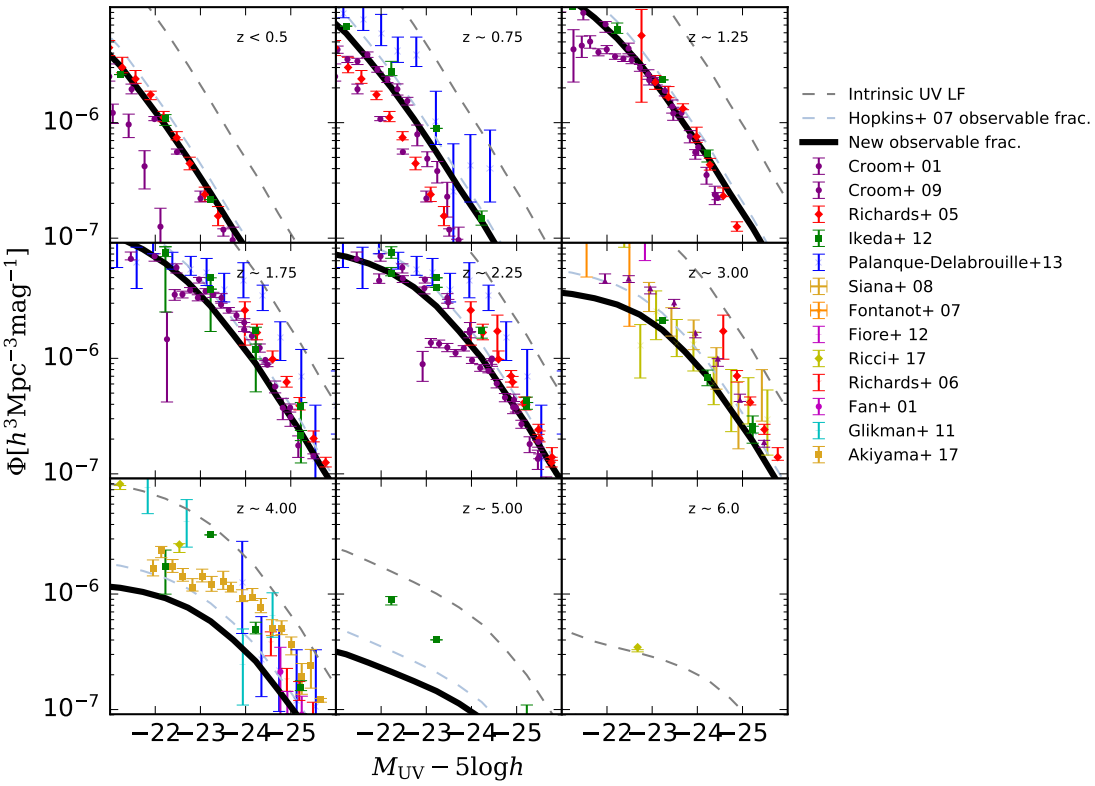

Figure 2.4: AGN LFs in UV- band(1450 Å) in $0.0 < z < 6.5$. Grey dashed line is the intrinsic UV LFs. Blue dashed and black solid lines are UV LFs considering observable fractions obtained from Hopkins et al. (2007) and this thesis, respectively. Observational results are obtained from Croom et al. (2001), Croom et al. (2009), Fan et al. (2001), Richards et al. (2005), Richards et al. (2006), Fontanot et al. (2007), Siana et al. (2008), Glikman et al. (2011),Fiore et al. (2012), Ikeda et al. (2012), Palanque-Delabrouille et al. (2013), Ricci et al. (2017a), and Akiyama et al. (2018).

phase (for more details, see Sec. 3.2 in Makiya et al. 2016). The reduced χ^2 decreases at 3.4 % of the initial value after the first 10000 iterations, and at 1.5 % after 20000 iterations. After 20000 iterations, χ^2 becomes a little larger (2.2 %/2.3 % of the initial value after 40000/50000 iterations). The dispersion of values of MCMC-fitted parameters after 50000 iterations is 1.69 / 1.29 times larger than that after 20000 / 40000 iterations. The averaged values of parameters, on the other hand, seems to be converged. The change of the averaged values of parameters is 4.7 % from 20000 to 50000 iterations and 1.4 % from 400000 to 50000 iterations. The increase of the iterations would thus cause the increase of the dispersion values.

I have checked the correlations between values of two different parameters by using the Pearson's r (Table 2.3). The correlation is weak for most combinations of two parameters although some ($\alpha_{\rm star}$ – $V_{\rm star}$, $\kappa_{\rm diss}$ – $\epsilon_{\rm SMBH}$, $M_{\rm h0}$ – $\alpha_{\rm bulge}$, $M_{\rm h0}$ – $t_{\rm loss,0}$, $\alpha_{\rm bulge}$–$t_{\rm loss,0}$, and $\gamma_{\rm gas}$ – $\gamma_{\rm BH}$) have strong correlations, $|r| \gtrsim 0.8$.

The MCMC fitting has two crucial problems. First, since the ν^2GC -SS simulation has only $70^3 h^{-3}{\rm Mpc}^3$, I cannot fit the bright end slope of AGN LFs. The larger box simulations are not realistic considering the computational cost. Second, I have to fit parameter values so that all observational results are equally well reproduced. In other words, I cannot prioritise observational properties to fit although some observational properties such as the size of galaxies depend on the performed methods to obtain, i.e. including larger uncertainties than other properties (e.g. luminosity). We, therefore, use the ν^2GC -SS simulation and refit some ill-fitted parameters by hand so that they are in 1σ in the MCMC-fitted values. The parameters which are refitted by hand are shown in Table 2.2. I cannot determine the values of $f_{\rm mrg}$, $\epsilon_{\rm DI,crit}$, $f_{\rm BH}$, $\gamma_{\rm gas}$, and $\gamma_{\rm BH}$ because of the degeneracy and the small box size.

Galaxies:

parameter	related equation	value range	MCMC best	MCMC dispersion	adopted value
$\alpha_{\rm star}$	Eq. 2.8	[-3.0,0.0]	-2.14	0.10	-2.14
$V_{\rm star}$ [km/s]	Eq. 2.8	[100.0,400.0]	211.30	14.37	197.00
$\epsilon_{\rm star}$	Eq. 2.8	[0.05,0.50]	0.48	0.02	0.46
$V_{\rm hot}$ [km/s]	Eq. 2.10	[50.0,400.0]	121.64	2.74	121.64
$\alpha_{\rm hot}$	Eq. 2.10	[0.0,4.0]	3.92	0.07	3.92
$\alpha_{\rm return}$	Sec. 2.3				0.00
$f_{\rm mrg}$	Sec. 2.4.1	[0.8,1.0]	0.98	0.01	0.81
$f_{\rm major}$	Sec. 2.4.1	[0.3,1.0]	0.89	0.08	0.89
$\kappa_{\rm diss}$	Eq. 2.36	[1.0,3.0]	2.70	0.20	2.75
$M_{\rm h0}[10^{14}M_\odot]$	Eq. 2.32	[0.1,10.0]	2.10	1.43	1.00
$\alpha_{\rm h}$	Eq. 2.32	[0.5,2.0]	1.82	0.13	1.82
$\epsilon_{\rm DI,crit}$	Eq. 2.22	[0.7,1.1]	1.05	0.01	0.75
$f_{\rm bar}$	Sec. 2.4.2	[1e-3,1.0]	0.63	0.10	0.63
$\tau_{\rm V0}$	Sec. 2.7				2.5×10^{-9}

SMBHs and AGNs:

$\alpha_{\rm cool}$	Eq.2.48	[0.8,1.2]	1.14	0.04	1.14
$\log(\epsilon_{\rm SMBH})$	Eq.2.49	[-3.0,0.0]	-2.66	0.53	-2.66
$f_{\rm BH}$	Eq.2.12	[1e-3,8e-2]	0.06	0.01	0.02
$M_{\rm seed}[M_\odot]$	Sec.2.6.1				10^3
$\alpha_{\rm bulge}$	Eq.4.2	[0.1,1.2]	0.77	0.24	0.58
$\tau_{\rm loss,0}$ [Gyr]	Eq.4.3	[0.1,5.0]	1.56	0.71	1.00
$\gamma_{\rm gas}$	Eq.4.3	[-5.0,0.0]	-3.28	0.41	-4.0
$\gamma_{\rm BH}$	Eq.4.3	[0.0,5.0]	4.40	0.42	3.5
$\dot{m}_{\rm crit}$	Eq.2.43				10.0

Table 2.2: Summary of free parameters in the fiducial model. Almost all parameters are fitted with the MCMC method (iteration = 50000). I show the (1) parameter name, (2) related equation or section, (3-5) parameter range, best fit value, and dispersion (if MCMC fitted parameter), and (6) adopted value.

	$\gamma_{\rm BH}$	$\gamma_{\rm gas}$	$\alpha_{\rm bulge}$	$\tau_{\rm loss,0}$	$f_{\rm BH}$	$f_{\rm bar}$	$\epsilon_{\rm DI,crit}$	$\log(\epsilon_{\rm SMBH})$	$\alpha_{\rm cool}$	$\alpha_{\rm h}$	$M_{\rm h0}$	$\kappa_{\rm diss}$	$f_{\rm major}$	$f_{\rm mrg}$	$\alpha_{\rm return}$	$\alpha_{\rm hot}$	$V_{\rm hot}$	$\epsilon_{\rm star}$	$V_{\rm star}$
$\alpha_{\rm star}$	-0.25	0.19	0.39	0.34	0.08	-0.16	0.06	0.31	-0.30	0.19	-0.34	-0.08	0.21	0.48	-0.17	0.05	-0.30	0.05	0.80
$V_{\rm star}$	-0.27	0.23	0.54	0.42	0.20	-0.13	-0.25	0.39	-0.37	0.12	-0.46	-0.21	0.28	0.51	-0.12	0.20	-0.02	0.44	
$\epsilon_{\rm star}$	-0.02	0.10	0.31	0.27	0.38	-0.22	-0.09	0.16	-0.18	0.11	-0.32	-0.20	0.26	0.17	0.13	0.20	-0.05		
$V_{\rm hot}$	0.22	-0.25	-0.20	-0.29	-0.36	0.33	-0.74	-0.21	0.16	-0.47	0.23	0.12	-0.35	-0.08	0.08	-0.62			
$\alpha_{\rm hot}$	-0.24	0.25	0.38	0.36	0.48	-0.31	0.29	0.26	-0.24	0.39	-0.33	-0.24	0.42	0.15	-0.07				
$\alpha_{\rm return}$	-0.06	0.07	-0.17	-0.26	-0.25	0.07	-0.09	-0.03	0.39	-0.03	0.35	0.14	-0.45	-0.19					
$f_{\rm mrg}$	0.23	-0.24	0.27	0.22	0.18	-0.29	-0.12	0.04	-0.29	-0.11	-0.38	0.08	0.24						
$f_{\rm major}$	-0.38	0.41	0.62	0.69	0.75	-0.47	0.18	0.23	-0.33	0.57	-0.71	-0.20							
$\kappa_{\rm diss}$	0.52	-0.59	-0.70	-0.71	-0.52	-0.28	-0.24	-0.80	0.69	-0.36	0.49								
$M_{\rm h0}$	0.29	-0.36	-0.82	-0.89	-0.79	0.16	-0.17	-0.45	0.73	-0.42									
$\alpha_{\rm h}$	-0.57	0.61	0.54	0.59	0.64	-0.50	0.34	0.46	-0.32										
$\alpha_{\rm cool}$	0.13	-0.19	-0.74	-0.70	-0.67	0.02	-0.19	-0.60											
$\log(\epsilon_{\rm SMBH})$	-0.61	0.67	0.72	0.68	0.42	0.10	0.23												
$\epsilon_{\rm DI,crit}$	-0.18	0.21	0.12	0.26	0.27	0.07													
$f_{\rm bar}$	-0.02	0.02	-0.14	-0.11	-0.36														
$f_{\rm BH}$	-0.26	0.38	0.74	0.79															
$\alpha_{\rm bulge}$	-0.59	0.66	0.91																
$\tau_{\rm loss,0}$	-0.57	0.61																	
$\gamma_{\rm gas}$	-0.94																		

Table 2.3: List of the Pearson's r.

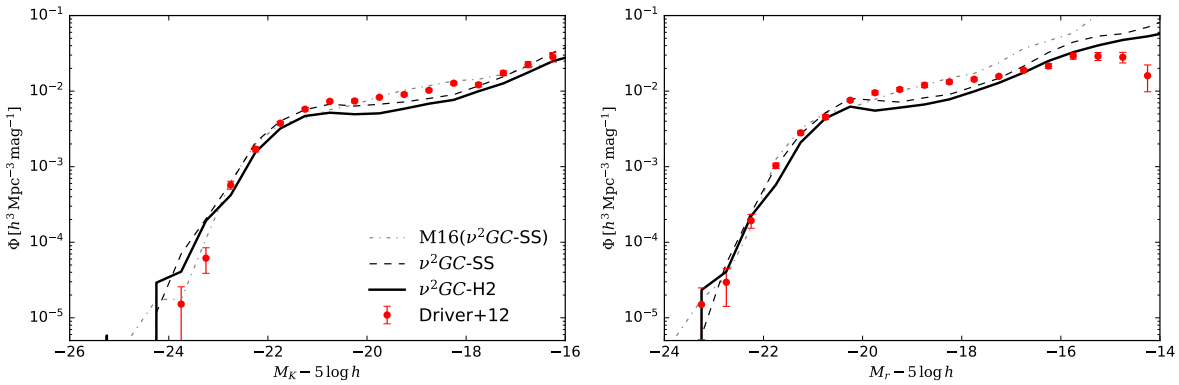

Figure 2.5: $K-$ and $r-$ band LFs of galaxies. Black dashed and solid lines show the results by the fiducial model with ν^2GC -SS and ν^2GC -H2 simulations, respectively. I show the result of M16 as grey dot-dashed lines. Red filled circles with error bars are observational estimates by the GAMA survey (Driver et al. 2012).

2.8.2 Properties of galaxies at $z \sim 0$

Fig. 2.5 shows the K- and r- band LFs at $z \sim 0$. The results of the fiducial model with the ν^2GC -SS and -H2 simulations shown to test the resolution effect. I overplot the results obtained by M16 in grey dash-doted lines. Red points with errorbars are the observational estimates by the GAMA survey (Driver et al. 2012). Fig. 2.6 shows the H$_\mathrm{I}$ MF at $z \sim 0$. I assume the relation between the cold gas mass and the atomic hydrogen gas mass, M_HI, as $M_\mathrm{HI} = 0.54 M_\mathrm{cold}$, which is the same relation used in M16.

The bright-end slopes of the LFs and the massive-end slope of the H$_\mathrm{I}$ MF are sensitive to the values of α_cool and ϵ_SMBH, which are both related to the radio-mode AGN feedback. The faint-end slopes are determined by the energy of the SN feedback determined by α_hot and V_hot. The low mass end slope of the H_I MF is also sensitive to the values of α_star and V_star, which determine the gas consumption timescale by star formation. Although the model explains the wide range of the observed LFs and H$_\mathrm{I}$ MF at $z \sim 0$, the number of galaxies with smaller H$_\mathrm{I}$ gas mass ($M_\mathrm{HI} < 10^8 M_\odot$) is under-predicted, which is the same trend as M16 and other SA models (e.g. Gonzalez-Perez et al. 2014; Lagos et al. 2014; Lacey et al. 2016). This is partly due to the insufficient resolution of the employed $N-$ body simulation. As shown in Fig. 2.6, the result with the ν^2GC -H2 simulation ($\sim 4^3$ times higher mass resolution than the ν^2GC -SS simulation) explains the H$_\mathrm{I}$ MF better than that with the ν^2GC -SS simulation and the result is nearly consistent with the recent observational estimates (Jones et al. 2018; green triangles) The modelling of the SFR might be important since the low mass end slope is sensitive to α_star and V_star. The modelling of the gas stripping and cooling of satellite galaxies should also be important. However, I do not use sub-halo merger trees in this work, and do not consider gas cooling for satellite galaxies. Since such less massive galaxies do not have an impact on the main results of this thesis, I leave this issue for future work.

I compare the predicted effective radius and rotation velocity of spiral galaxies at $z \sim 0$ with observations. I employ the ν^2GC -SS ν^2GC -H2 simulations to obtain the result. I use the data obtained from Courteau et al. (2007) who estimated the disc scale lengths from

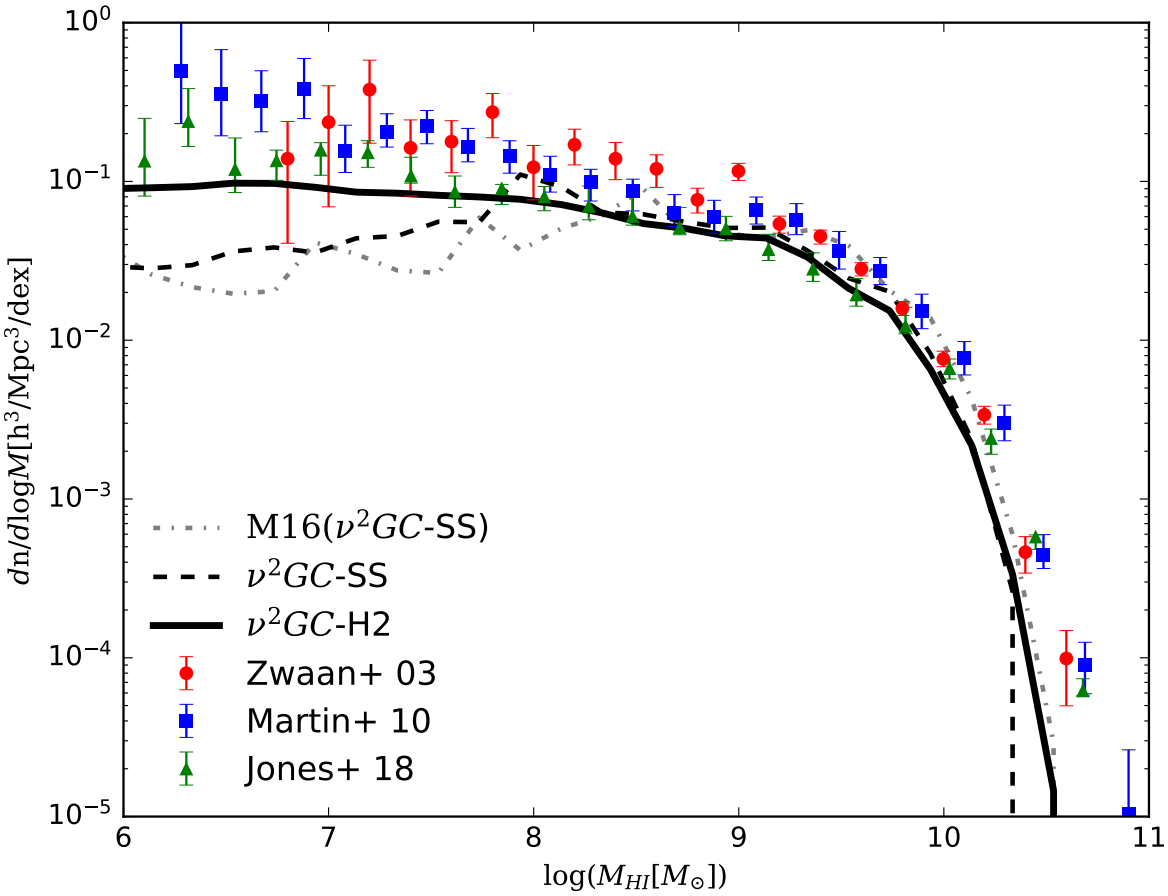

Figure 2.6: H_I MF at $z \sim 0$. Black dashed and solid lines show the results obtained from the fiducial model with ν^2GC -SS and ν^2GC -H2 simulations, respectively. I show the result of M16 as grey dot-dashed lines. Red filled circles, blue filled squares, and green filled triangles with error bars are observational data obtained from the HIPASS (Zwaan et al. 2003) and ALFALFA surveys (Martin et al. 2010 and Jones et al. 2018), respectively.

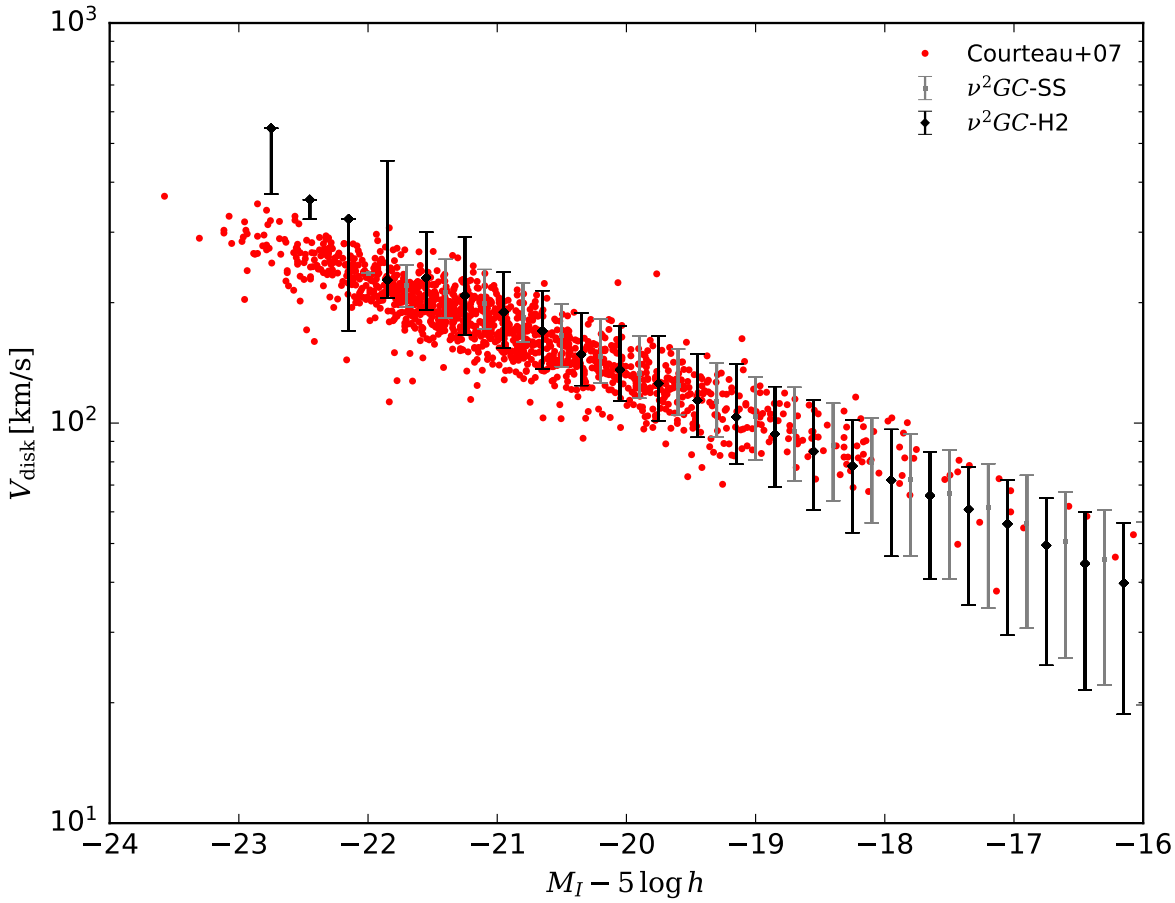

Figure 2.7: Rotation velocities of spiral galaxies as a function of $I-$ band magnitude. (Tully-Fisher relation). The black line shows the median value obtained by the model and the error bars show the 10th and 90th percentiles from the ν^2GC -SS ν^2GC -H2 simulations. Red points show the observational data obtained from Courteau et al. (2007).

$I-$ band image and the disc rotation velocities from H_α or $\rm H_I$ line width. Figs. 2.7 and 2.8 are the scaling relations between the rotation velocity and the $I-$ band magnitude (the so-called Tully-Fisher relation; Tully & Fisher 1977) and the effective radius and the $I-$ band magnitude, respectively. The data obtained from Courteau et al. (2007) are presented as red points. The results of their model are shown as black lines with error bars which are the 10th to 90th percentiles. The model results are consistent with the observational results and the effect of the mass resolution of the simulations is negligible.

Next, I compare the predicted effective radius and velocity dispersion of elliptical and S0 galaxies at $z \sim 0$ with observations since these values are used for calculating the dynamical time of bulges. Here I also employ the ν^2GC -SS and ν^2GC -H2 simulations, although the effect of the mass resolution of the simulations is negligible. I use the data obtained from Forbes et al. (2008) who calculate the half-light radii are from 2MASS $K-$band 20th isophotal by using an empirical relation based on Sérsic light profiles (Forbes et al. 2008). Figs. 2.9 and 2.10

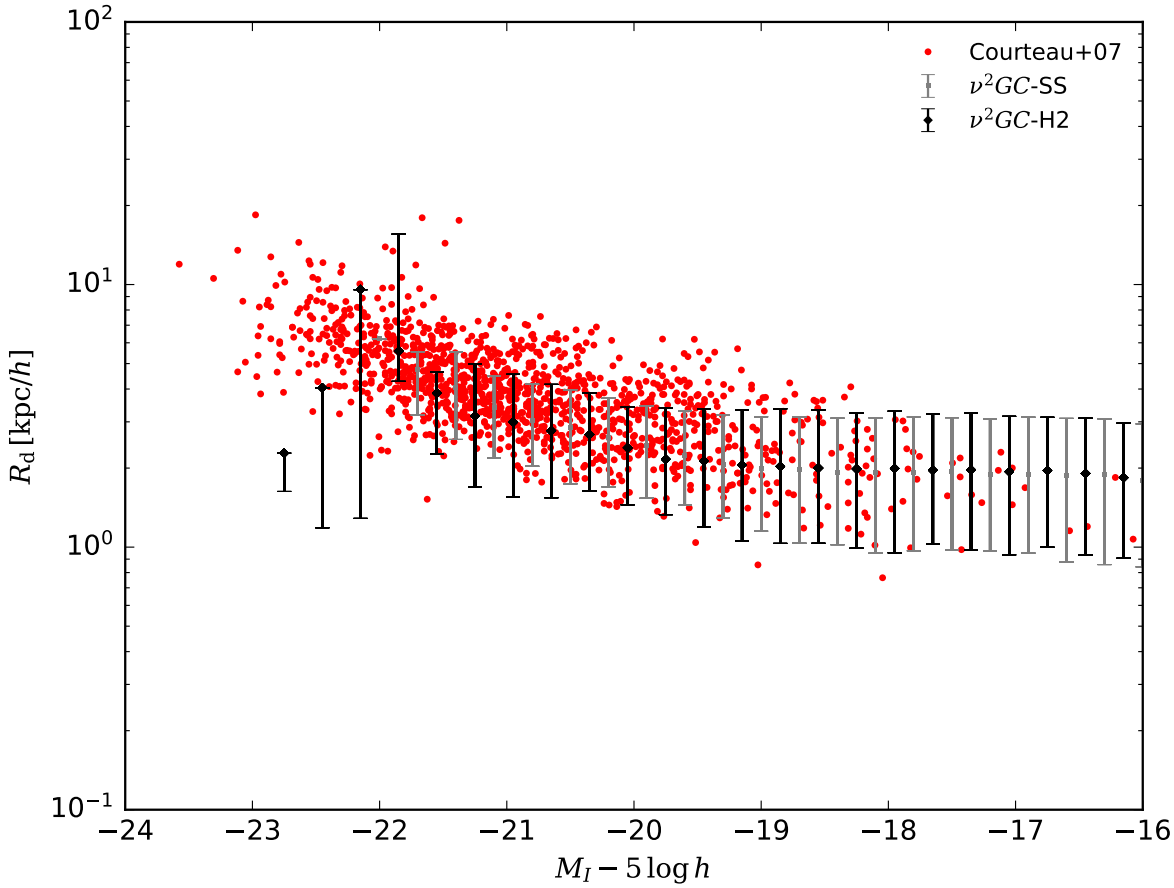

Figure 2.8: Effective radius of spiral galaxies as a function of $I-$ band magnitude. The black line shows the median value obtained by the model and the error bars show the 10th and 90th percentiles. I employ the ν^2GC -SS ν^2GC -H2 simulations. Red points show the observational data obtained from Courteau et al. (2007). I convert the scale length obtained by Courteau et al. (2007) to the effective radius with $R_{\rm d} = 1.68 r_{\rm ds}$.

are the scaling relations between the bulge velocity dispersion and the K-band magnitude (the so-called Faber-Jackson relation; Faber & Jackson 1976) and the effective radius and the $K-$band magnitude, respectively. The data obtained from Forbes et al. (2008) are shown in red points. The results of the fiducial model with ν^2GC -SS/-H2 are described as grey squares/black diamonds with error bars indicating 10th and 90th percentiles. For comparison, I overplot the model results with $M_{\rm DM,1}=0$ as grey diamonds with error bars. I find that the effective radius of bulges with $M_K - 5\log h < -23$ becomes smaller when I set $M_{\rm DM,1}=0$. The results obtained from the fiducial model have some discrepancies with the observational results, especially for the velocity dispersion while the bulge MF at $z\sim 0$ is consistent with observed bulge MF obtained from Moffett et al. (2016), and Thanjavur et al. (2016), as shown in Fig. 2.11.

The velocity dispersion obtained from the fiducial model becomes smaller with massive galaxies than those obtained from observations. There might be two possible reason for the inconsistency. First, due to the underestimate of gas mass especially in the small galaxies. I find that the model overproduces gas-poor galaxies, whose r-band magnitude are less than ~ -18.5. The dissipation process plays important roles for calculation of the velocity dispersion (Sec. 2.4). Since the dissipated energy becomes larger with mergers of more gas-rich galaxies, underestimation of the cold gas mass would cause the underestimation of the velocity dispersion. Another possibility to reproduce Faber-Jackson relation might be related with the estimation of the gravitational potential of galactic discs. Galaxies which experience bulge growths should contain a galactic disc. The potential energy of the remained disc is estimated assuming that the rotation velocity of the disc remain unchanged (Eq. 2.33). When the discs have a shallower potential, the bulge should display a larger velocity dispersion.

To check these two effects, I test arbitrary models with the gas fraction $f_{\rm gas,test}$ of the galaxy and that with 0.3 times smaller $E_{0,\rm disc}$ value. The new gas fraction, $f_{\rm gas,test}$ is described as:

$$f_{\rm gas,test} = f_{\rm gas} \times \left(\frac{M_{1d}}{10^{11} M_\odot} \right)^{-0.2}, \tag{2.52}$$

where $f_{\rm gas}$ and $M_{\rm 1d}$ are the same definition in Sec. 2.4.1 and 2.4. As an example, I consider a galaxy with $M_K - 5\log h \sim -20$. The re-estimated gas fraction, $f_{\rm gas,test}$ is $\sim$ 1.3 times larger than the fiducial value. I use $f_{\rm gas,test}$ instead of $f_{\rm gas}$ in Eq. 2.37, and re-estimate velocity dispersion. Fig. 2.12 shows Faber-Jackson relation obtained from these simple tests. The model result is roughly consistent with observational one. I conclude that the discrepancy of bulge velocity dispersion with observational estimates would become smaller when I can reproduce observed colour-magnitude relation and HI MF of less massive galaxies.

2.8.3 Galaxy evolution

I firstly show the cosmic SFR density as a function of redshift in Fig. 2.13. The black solid line is the model result obtained with the ν^2GC -SS simulation and points are the results obtained from observations in IR-bands (Pascale et al. 2009; Rodighiero et al. 2010), radio 1.4 GHz (Karim et al. 2011), UV-bands (Cucciati et al. 2012; Bouwens et al. 2014; Ouchi et al. 2004), and a compilation of various observations (Hopkins 2004; and therein). I find that the cosmic SFR density obtained by the fiducial model is consistent with the data over wide redshift range.

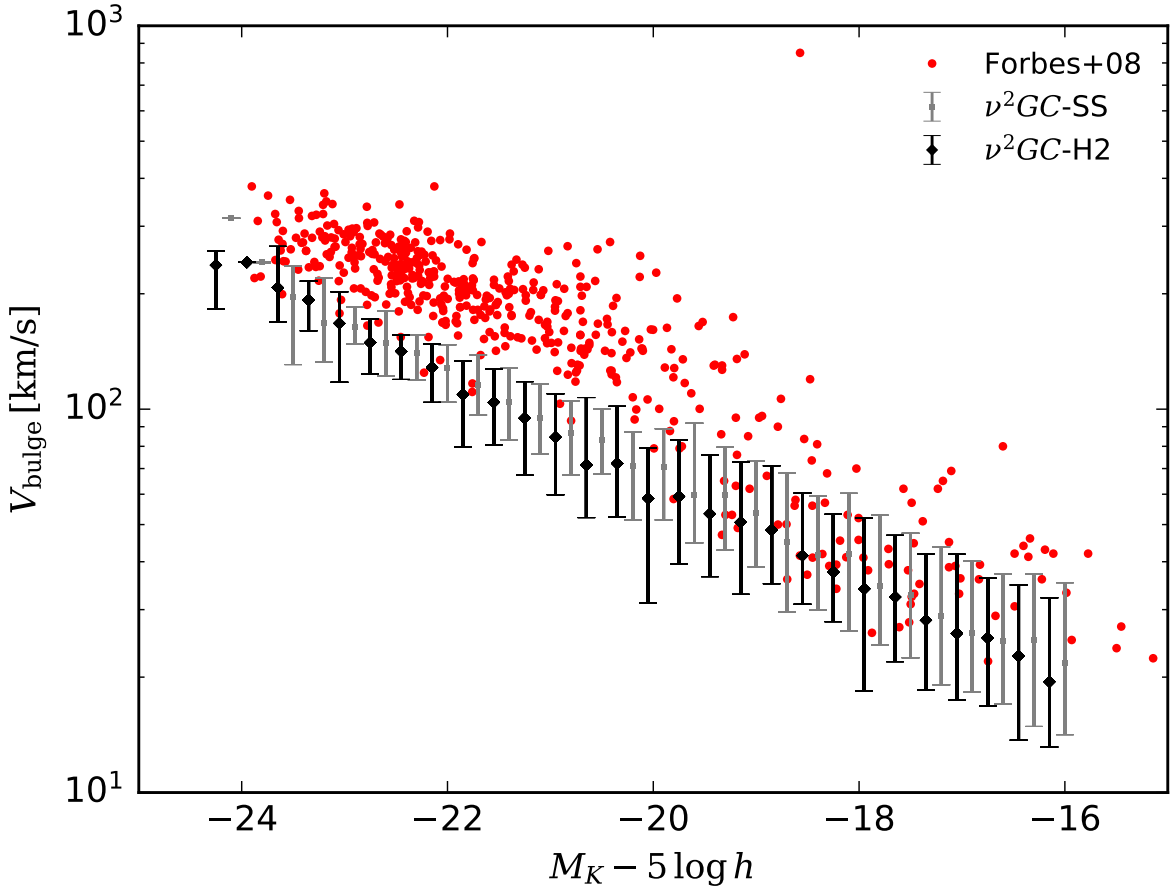

Figure 2.9: Velocity dispersions of elliptical and S0 galaxies as a function of $K-$ band magnitude (Faber-Jackson relation). The black line shows the median value obtained by the model and the error bars show the 10th and 90th percentiles from the ν^2GC -SS and ν^2GC -H2 simulations. Red points show the observational data obtained from Forbes et al. (2008).

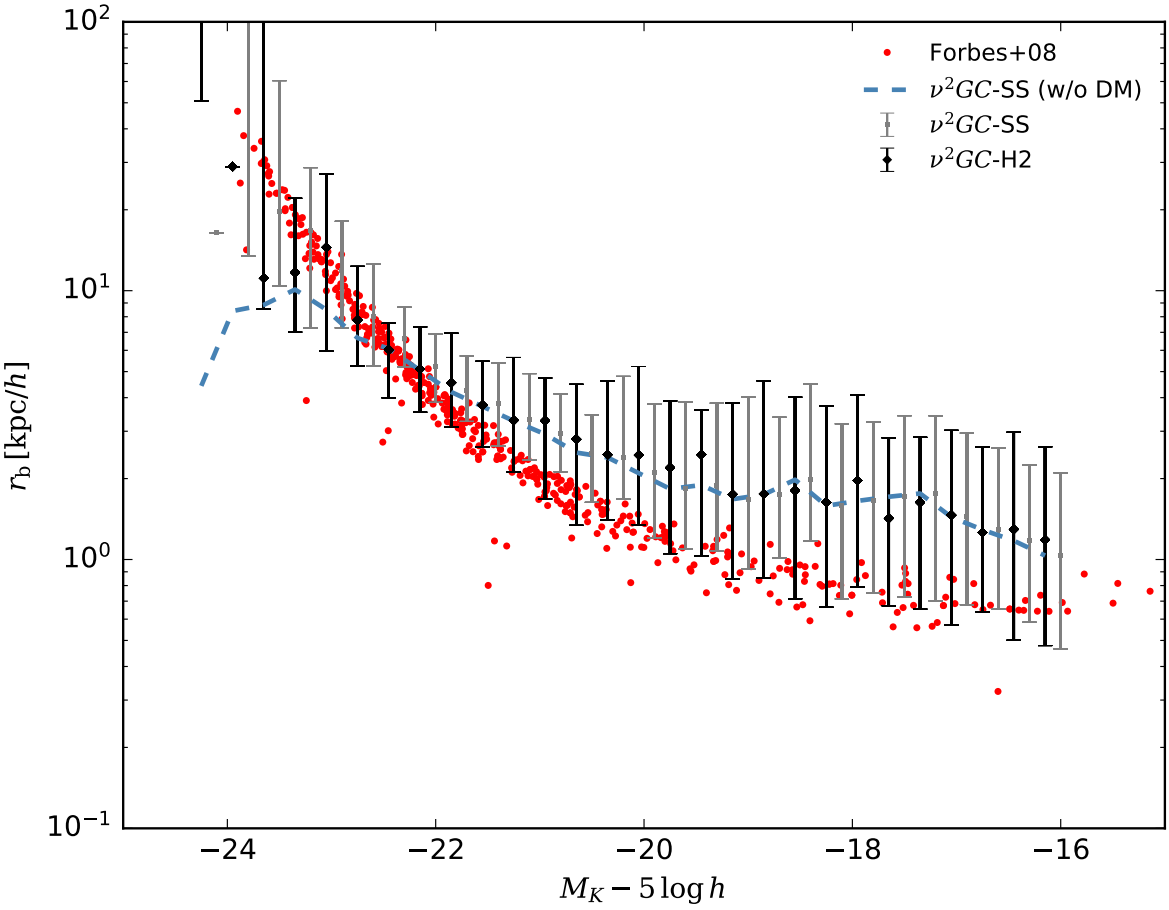

Figure 2.10: Effective radius of elliptical and S0 galaxies as a function of $K-$ band magnitude. The black line shows the median value obtained by the model and the error bars show the 10th and 90th percentiles. The grey line with errorbars shows the median value obtained by the model considering $M_{\rm DM,1} = 0$ from the ν^2GC -SS and ν^2GC -H2 simulations. Red points show the observational data obtained from Forbes et al. (2008).

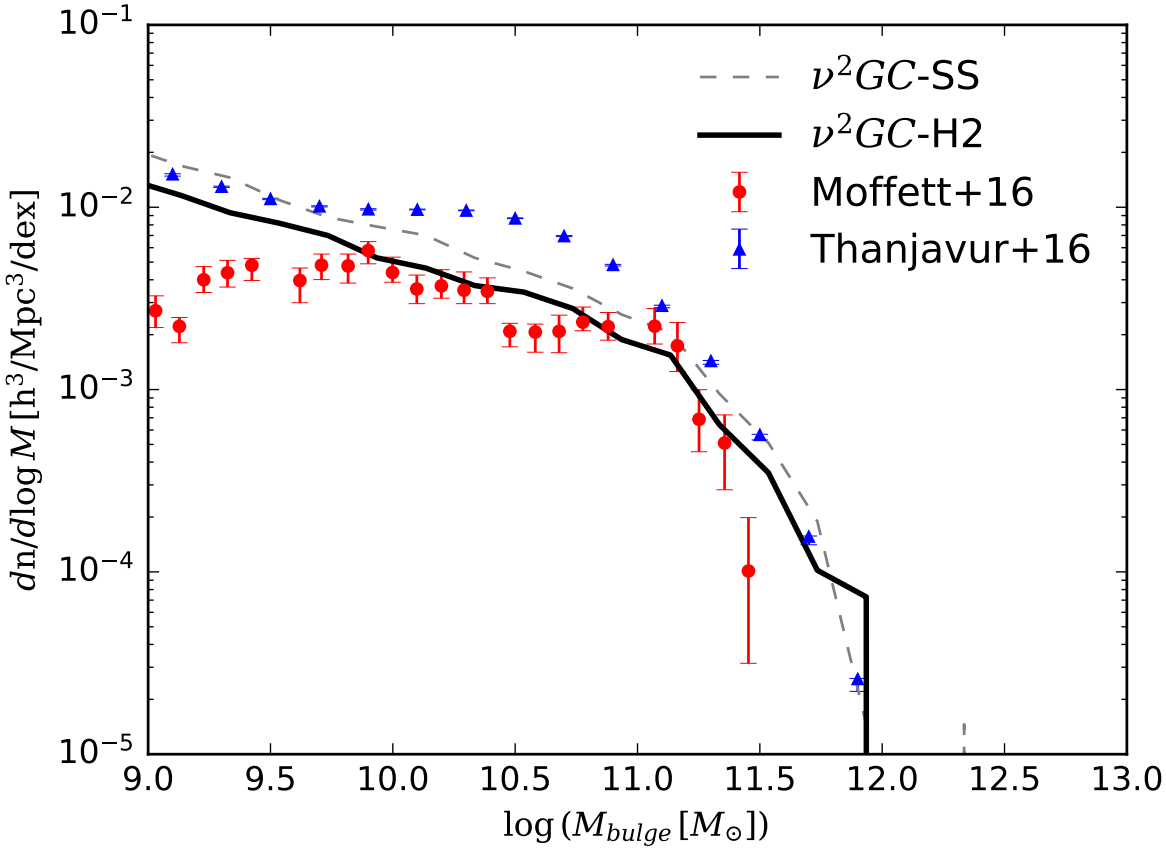

Figure 2.11: Bulge MF at $z \sim 0$ obtained with ν^2GC -SS and -H2 simulations. The black solid line denotes the result obtained from the model. Red filled circles and blue filled triangles present observed MFs obtained from Moffett et al. (2016) and Thanjavur et al. (2016), respectively.

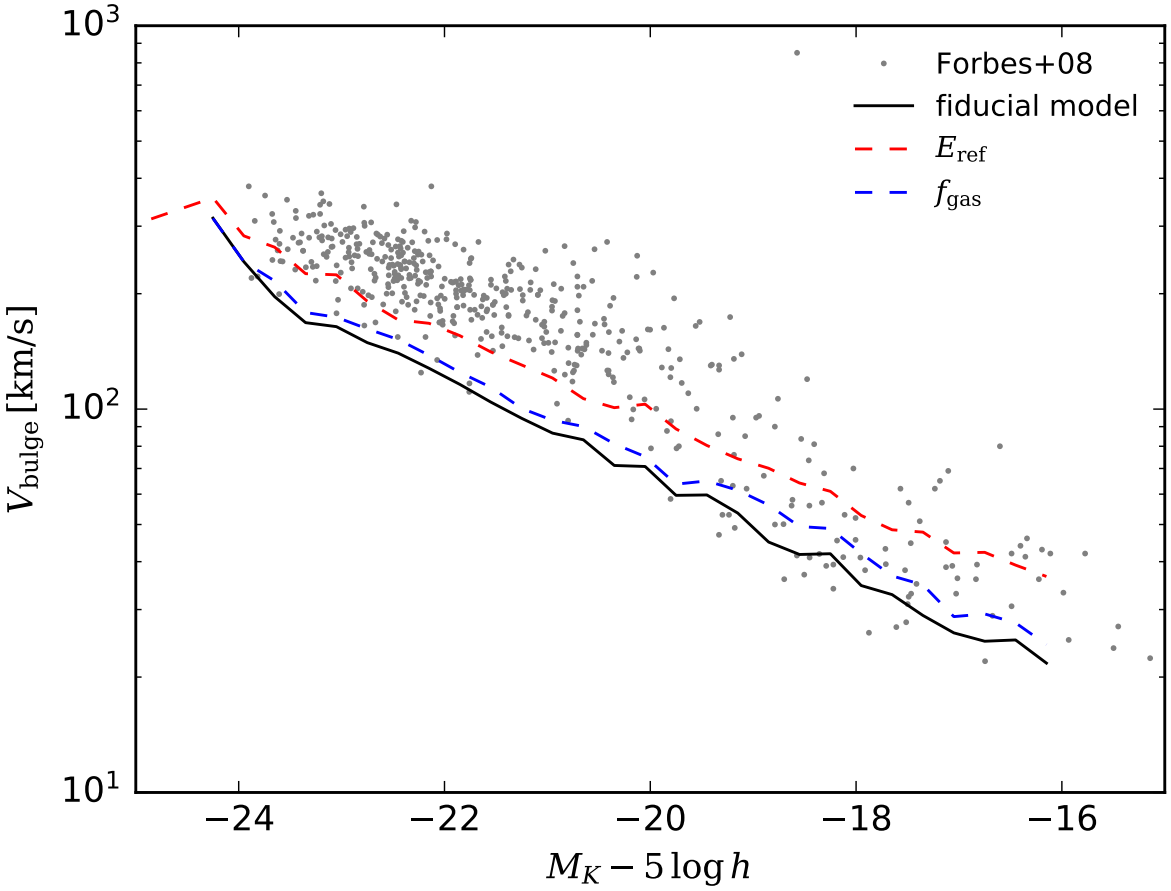

Figure 2.12: Velocity dispersions of elliptical and S0 galaxies as a function of $K-$ band magnitude (Faber-Jackson relation). The black solid, red dashed, and blue dashed lines show the median value obtained by the fiducial model (ν^2GC -SS), that by the artificially fixed gas fraction (Eq. 2.52), and that by the artificially fixed energy which remains in the galactic disc, respectively. Grey points show the observational data obtained from Forbes et al. (2008).

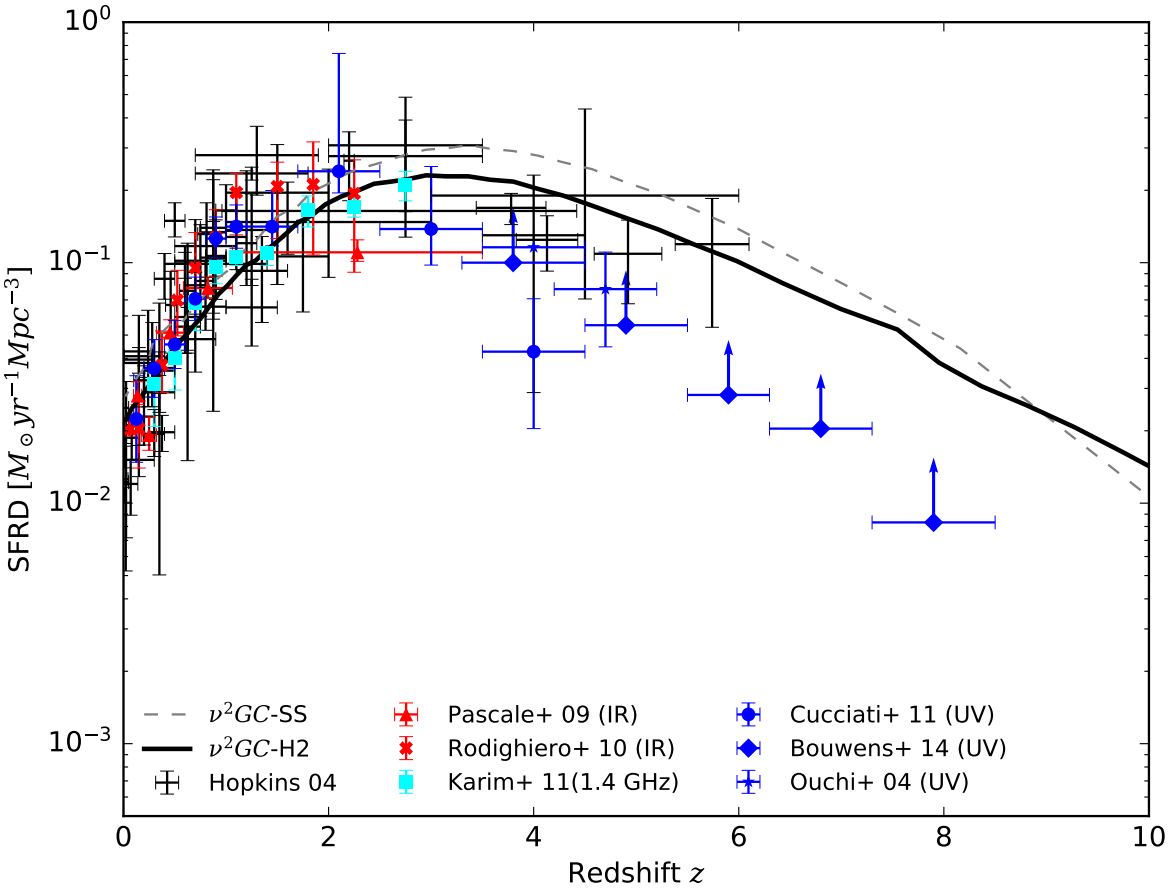

Figure 2.13: Cosmic SFR density as a function of redshift. The black solid line is the model results obtained with the ν^2GC-SS and ν^2GC-H2 simulations. Red filled triangles and stars and cyan filled squares are obtained from dust continuum emission (Pascale et al. 2009; Rodighiero et al. 2010; Karim et al. 2011; respectively). Blue filled circles, filled diamonds, and stars are from UV continuum emission (Cucciati et al. 2012; Bouwens et al. 2014; Ouchi et al. 2004; respectively). Black crosses are obtained from Hopkins (2004), which is a compilation of various other observational results.

Next, I present the evolution of $K-$ and $B-$ band LFs and stellar MFs of galaxies obtained by the fiducial model with the ν^2GC -M and -H2 simulations to show the result of bright and rare populations of galaxies. The LFs and MFs presented here are volume-weighted. The details of the calculation of LFs and MFs from the simulation are described in Appendix A.1.

Fig. 2.14 shows the model $K-$ band LFs (black solid lines) compared with observational results (Bell et al. 2003; Huang et al. 2003; Pozzetti et al. 2003; Drory et al. 2003; Caputi et al. 2006; Saracco et al. 2006; Devereux et al. 2009; Cirasuolo et al. 2010; Driver et al. 2012). Model LFs reproduce observational results well for $z < 3.5$ including faint-end slopes. The model of M16 also explains observed $K-$ band LFs for $z < 2.0$ well (Fig. 21 of M16), although it over estimates number density of less luminous galaxies ($M_K > -22$).

Fig. 2.15 compares the model $B-$ band LFs (black lines) with observational results (Norberg et al. 2002; Gabasch et al. 2004; Ilbert et al. 2005; Giallongo et al. 2005; Jones et al. 2006). The dust-attenuated model LFs are shown by the solid lines (for dust correction, see Sec. 2.7) and LFs without dust attenuation are shown by the dashed lines. I note that the data obtained from Norberg et al. (2002) and Jones et al. (2006) at $z < 0.25$ are not dust attenuation-corrected. Therefore, their results allow a fair comparison with the LF of the dust-attenuated model. The dust attenuation-corrected model LFs at $z > 0.8$ seem to be inconsistent with observational estimates. The observational data of Giallongo et al. (2005) are dust attenuation-corrected by assuming SMC and Calzetti extinction curves. Considering the correction for the dust attenuation, the model reproduces observed B-band LFs at $z < 3.5$ reasonably well. The data of Ilbert et al. (2005) and Gabasch et al. (2004) are not dust attenuation corrected. Since the bright-end of LFs of Giallongo et al. (2005), Ilbert et al. (2005), and Gabasch et al. (2004) are similar and the dust attenuation in B-band should have less impact than those suggested from the fiducial model, I conclude that some modifications of the dust attenuation are needed.

Fig. 2.16 shows the stellar MFs from $z \sim 0$ to $z \sim 4.5$. I adopt Chabrier IMF (Chabrier 2003) as described in Sec. 2.3. I compare our results (black lines) with observational estimates by Li & White (2009), Baldry et al. (2012), Santini et al. (2012), Muzzin et al. (2013), Moustakas et al. (2013), and Tomczak et al. (2014), who employ either a Chabrier IMF (Chabrier 2003) or Kroupa IMF (Kroupa 2001). [6] While the model can reproduce the massive end of the stellar MFs at $z < 3.5$, I find that the model underestimates the number of massive galaxies at $z > 3.5$ (bottom right panel). This similar feature is seen in other SA models (e.g. Hirschmann et al. 2012; Lacey et al. 2016). The derivation of stellar masses from observations is commonly performed by the broad-band SED fitting with galaxy templates assuming a single dust attenuation law. Alternatively, Mitchell et al. (2013) suggest that the discrepancy between SA models and observations in the stellar MFs at high redshifts stems from the uncertainties in the dust attenuation curve. For less massive galaxies, I also find that I overproduce their number density at $0.4 < z < 2.5$, which is the similar trend to other SA models (e.g. Weinmann et al. 2012). Some previous studies with SA models investigate this problem. Henriques et al. (2013) show that the ejected gas should be reincorporated into the system on a timescale which depends on the halo mass; the smaller halo should have the larger timescale, and the gas returns to the system more slowly. The importance of the timescale to reproduce SMFs are also proposed by White et al. (2015). They also suggest the

[6] Since the stellar mass difference between Chabrier and Kroupa IMF is only $\sim$ 0.04 dex (Muzzin et al. 2013), I assume a negligible difference in our results.

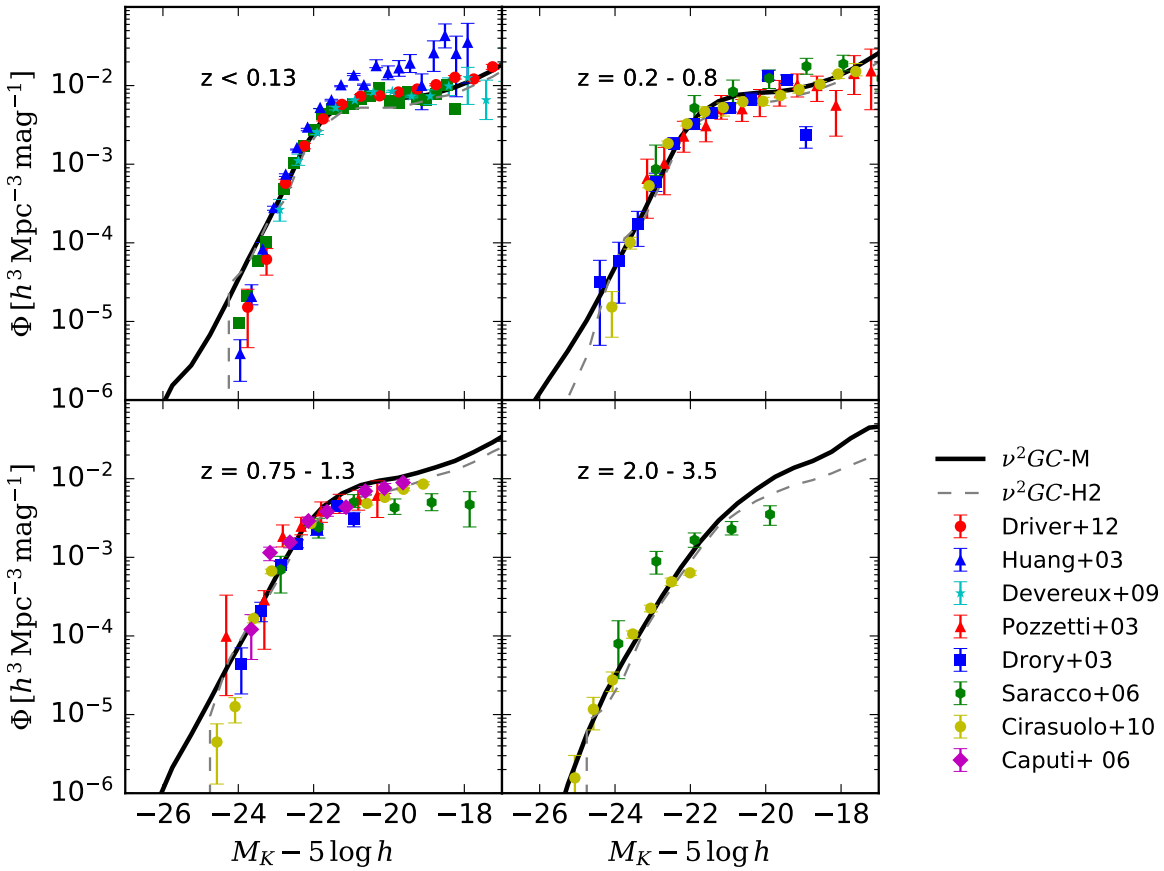

Figure 2.14: $K-$ band LFs of galaxies at $z < 0.13$, $z = 0.2 - 0.8$, $z = 0.75 - 1.3$, and $z = 2.0 - 3.5$. The model LFs (volume-weighted) by the ν^2GC -M simulation appear as black solid lines. Observational estimates are taken from Bell et al. (2003), Huang et al. (2003), Pozzetti et al. (2003), Drory et al. (2003), Caputi et al. (2006), Saracco et al. (2006), Devereux et al. (2009), Cirasuolo et al. (2010), and Driver et al. (2012).

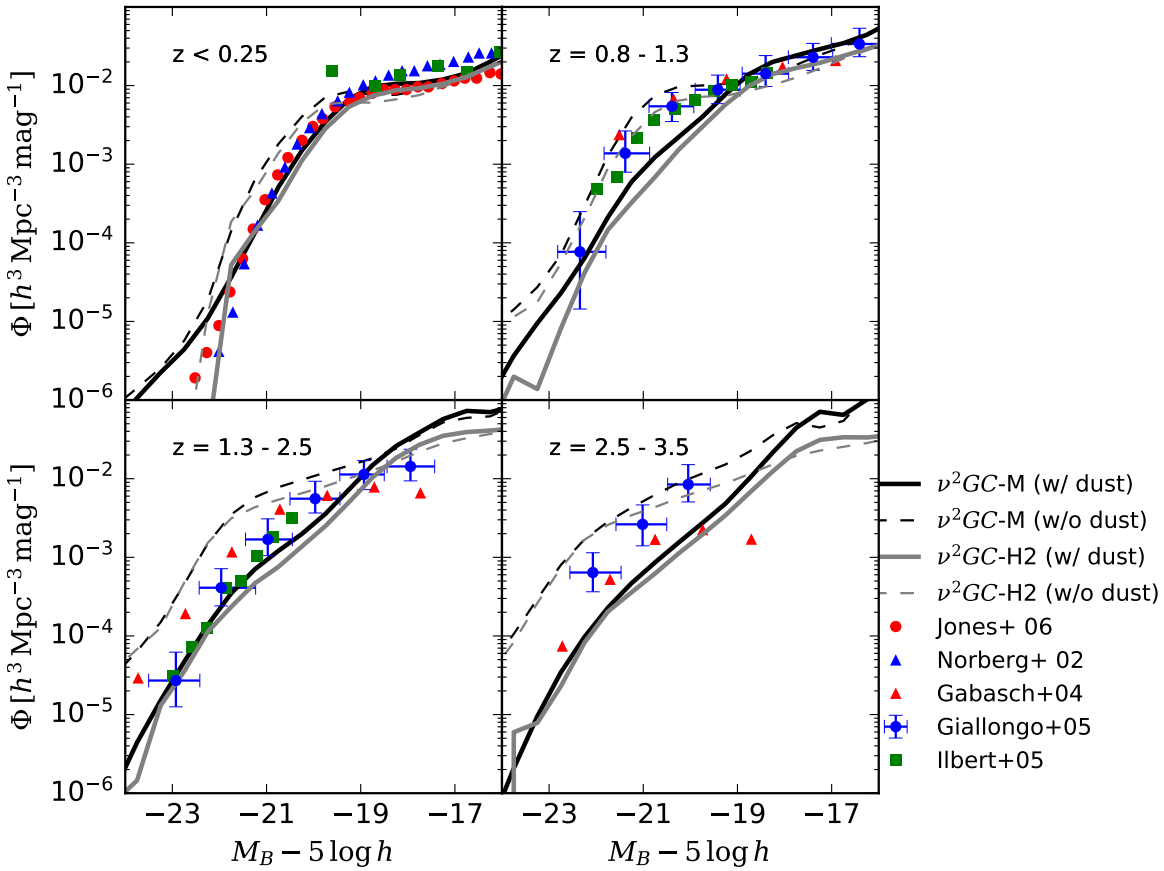

Figure 2.15: $B-$ band LFs of galaxies at $z < 0.25$, $z = 0.8 - 1.3$, $z = 1.3 - 2.5$, and $2.5 - 3.5$. The model LFs (volume-weighted) obtained with the ν^2GC -M and -H2 simulations appear in black solid and grey dashed lines (with dust attenuation) and black dashed lines (without dust attenuation). Observational results are obtained from Norberg et al. (2002); Gabasch et al. (2004); Ilbert et al. (2005); Giallongo et al. (2005); Jones et al. (2006).

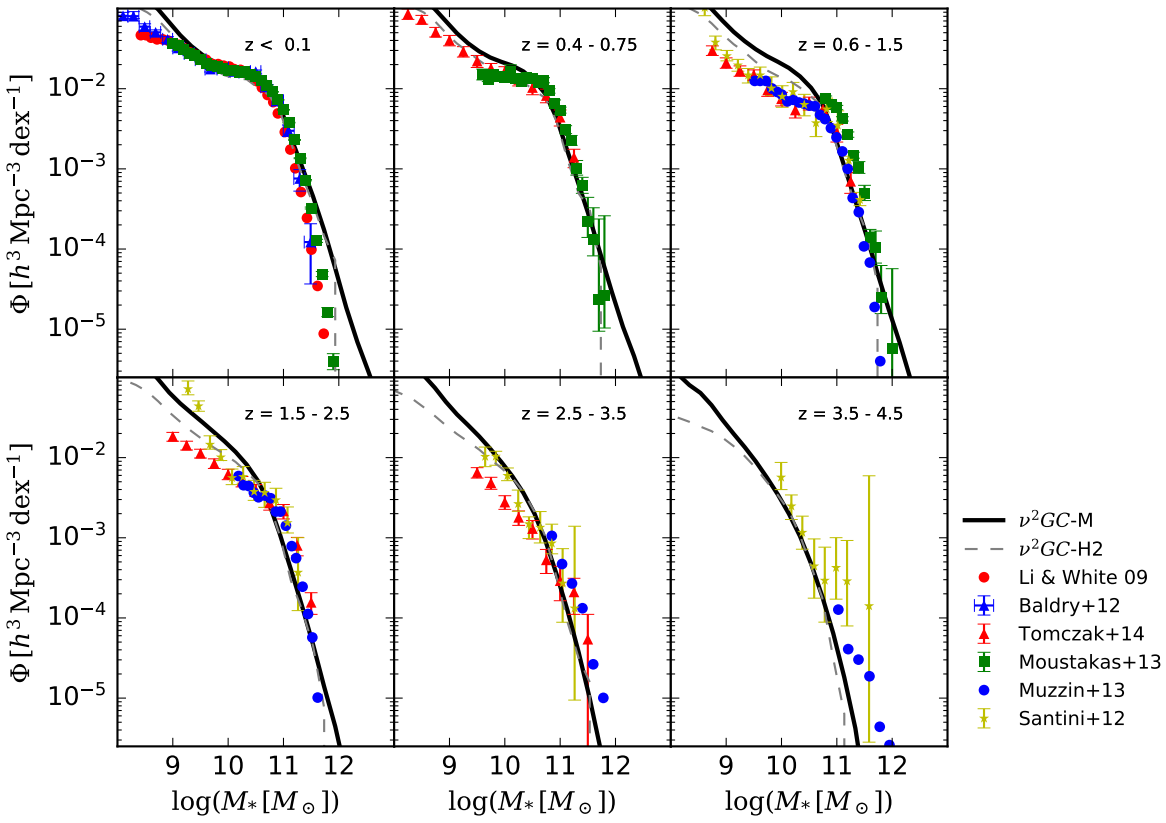

Figure 2.16: Stellar MFs at $z < 0.1$, $z = 0.4 - 0.75$, $z = 0.6 - 1.5$, $z = 1.5 - 2.5$, $z = 2.5 - 3.5$, and $z = 3.5 - 4.5$. The model MFs (volume-weighted) obtained with the ν^2GC -M and -H2 simulations are shown in black solid and grey dashed lines. Observational results are obtained from Li & White (2009), Baldry et al. (2012), Santini et al. (2012), Muzzin et al. (2013), Moustakas et al. (2013), Tomczak et al. (2014).

mass-loading factor which strongly depends on the redshift also plays a role in reproducing SMFs. White et al. (2015) imply a detailed comparison with observations are required to differentiate these two effects. Hirschmann et al. (2016) consider the decrease of the gas infall rate by "pre-heating" and find that their model can reproduce not only the low mass end of SMFs but also the metal enrichment of galaxies. I need to consider such effects in the ν^2GC , which I leave it for future studies to decrease of the degree of freedom. As White et al. (2015) suggest, the values of parameters which are required for reproducing SMFs strongly depends on the treatment of the reservoir of reheated and/or ejected gas in each SA models. The value of these parameters, therefore, have almost no constraints now.

For checking the mass resolution effect, I overplot the results with the ν^2GC -H2 simulation as grey dashed lines in Figs. 2.14 to 2.16, although the ν^2GC -H2 simulation has 8^3 times smaller box size than the ν^2GC -M simulation. I find the effect of the resolution is negligible.

I also present the relation between total stellar mass and SFR at $z < 6.0$ obtained from the fiducial model with the ν^2GC -M simulation and compare it with that obtained from

observations (Elbaz et al. 2007; Daddi et al. 2007; Salmon et al. 2015) in Fig. 2.17. I select all galaxies (central + satellite) without any luminosity or surface density limitations. The result is shown as the orange density map. In addition, blue points with errorbars show the relation for luminous galaxies with $M_{FUV} < -19.0$ (where M_{FUV} is the magnitude of the GALEX FUV band) obtained by the fiducial model, which are consistent with that of Salmon et al. (2015) at $z > 4.0$. The galaxies obtained by the fiducial model have larger SFRs than those obtained by observations when I take the selection effect into account at $z > 4$. Since the M_*-SFR relation obtained by Salmon et al. (2015) with $\log(M_*/M_\odot) > 10.3$ has a large dispersion, the slope of the M_*-SFR relation would not be strictly constrained. I note that the number of luminous galaxies obtained by the fiducial model with the ν^2GC -M simulation is 135.1, 180.9, and 108.1 times larger than that of Salmon et al. (2015) at $z \sim 4, 5$, and 6, respectively. The galaxies with $\log(M_*/M_\odot) > 10.5$ and $M_{FUV} < -19.0$ at $z \sim 2$ have smaller SFR than those predicted by the observational fitting. This could be a result of the AGN feedback effect (see also Sec. 4.4). At $z \sim 2$, gas cooling of most of such massive galaxies are quenched by the AGN feedback. The cold gas mass, thus, becomes smaller, resulting in lower SFRs.

Izumi et al. (2018) compare this relation obtained from the fiducial model employing the ν^2GC -L simulation with the data of four observed AGN host galaxies at $z \sim 6$. These four AGNs, which are optically low-luminosity quasars ($M_{UV} < -25$), are originally detected with Subaru Hyper Sprime Cam (HSC) (Matsuoka et al. 2017) and are observed with Atacama Large Millimeter/Submillimeter Array (ALMA) to investigate their host galaxies' properties. They find that the sample galaxies are on or *below* the so-called "main sequence" at $z \sim 6$, which are very rare population in the fiducial model of ν^2GC . Luminous quasars ($M_{UV} < -25$) at $z \sim 6$, on the other hand, have host galaxies with higher SFR than the "main sequence". The fiducial model of ν^2GC can reproduce such a bursty population. As shown in Fig. 8 in Izumi et al. (2018) and Fig. 2.17, the distribution of the SFR seems to have several sub-sequences. These sub-sequences should be artificial which result from time and mass resolution of the simulations and/or the discrete treatment of the time evolution of the hot gas density profiles and cooled gas mass. As I show in Sec. 2.2, the radial profiles of hot gas haloes remain unchanged until the DM halo mass doubles. It means that no hot gas distributes in $r < r_{\rm cool}$ until the DM halo mass doubles. Since the minimum halo mass of ν^2GC -M and -SS simulations is $8.79 \times 10^9 M_\odot$, the radial profile of the hot gas halo of galaxies with $M_* < 10^9 M_\odot$ is not updated from the formation time. A part of such galaxies, therefore, would contain an unphysically smaller amount of the cold gas.

I present the local SMBH MF in Fig. 2.18 and the $M_{\rm BH}$ – $M_{\rm bulge}$ relation (including both AGNs and quiescent BHs) in Fig. 2.19. I show the results with the ν^2GC -SS and ν^2GC -H2 simulations in both figures for checking the effect of the mass resolution. The model SMBH MF at $z \sim 0$ are shown as the grey dashed and black solid lines in Fig. 2.18. The SMBH MF is roughly consistent with the observational estimate (Shankar et al. 2004) (grey shaded region). The $M_{\rm BH}$–$M_{\rm bulge}$ relation at $z \sim 0$ is consistent with observations at $M_{\rm BH} > 10^{9.5} M_\odot$ (Fig. 2.19) since I adjust the parameter, $f_{\rm BH}$, to reproduce this relation. We, however, find that the median value of the $M_{\rm BH}$ – $M_{\rm bulge}$ relation obtained by the fiducial model deviates from the observational estimates for $M_{\rm bulge} < 10^{9.5} M_\odot$. I do not use such low mass galaxies for the model calibration since the observed sample is too small. Most observational data for less massive galaxies with $M_{\rm bulge} < 10^{9.5} M_\odot$ are AGN data. It is unclear whether the quiescent BHs with $M_{\rm bulge} < 10^{9.5} M_\odot$ have the same relation as the AGNs. In addition, the

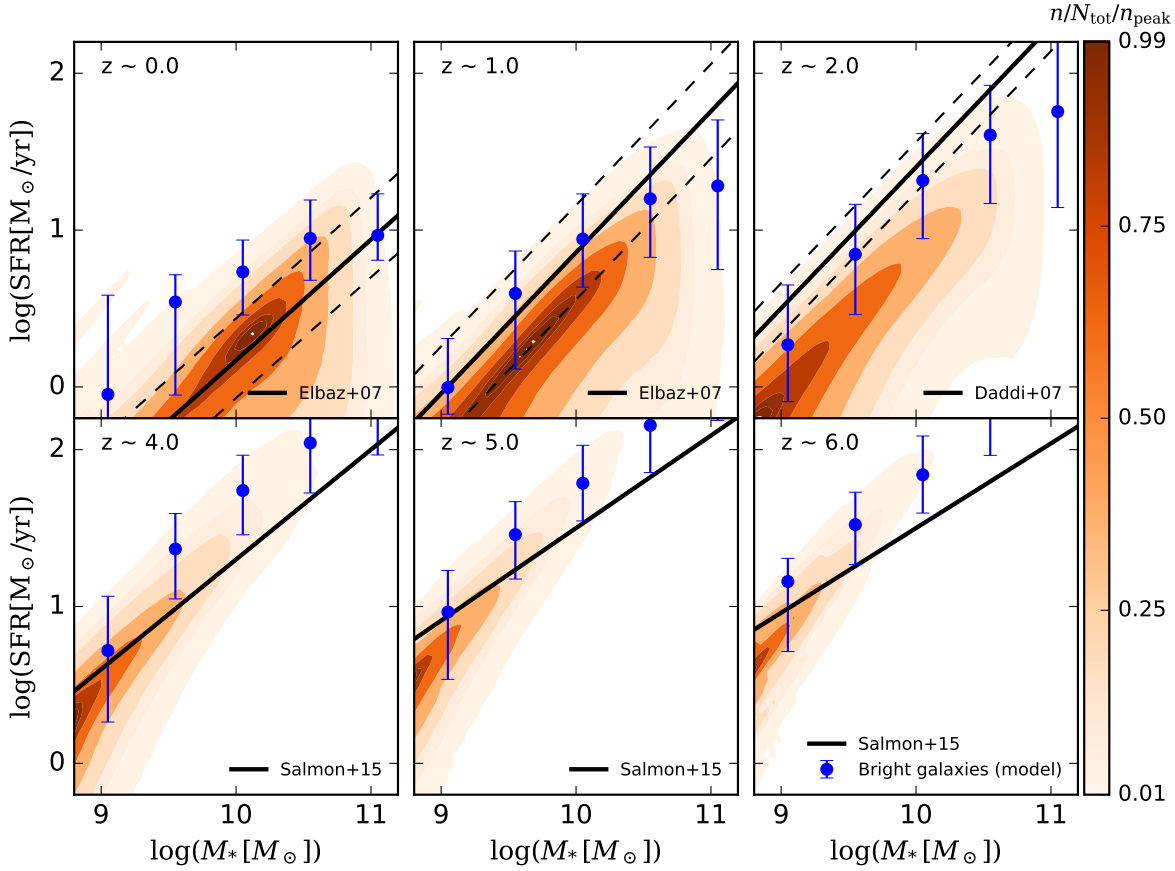

Figure 2.17: The relation between total stellar mass and SFR at $z < 6.0$. The model results (obtained with the ν^2GC -M simulation) including all galaxies and those including only luminous galaxies ($M_{FUV} < -19.0$) are shown by the orange colour map and the blue points with errorbars (10th and 90th percentiles), respectively. For comparison, I overplot the results obtained from observations at $z \sim 0$ and 1 (Elbaz et al. 2007), $z \sim 2$ (Daddi et al. 2007), and $z \sim 4, 5$, and 6 (Salmon et al. 2015).

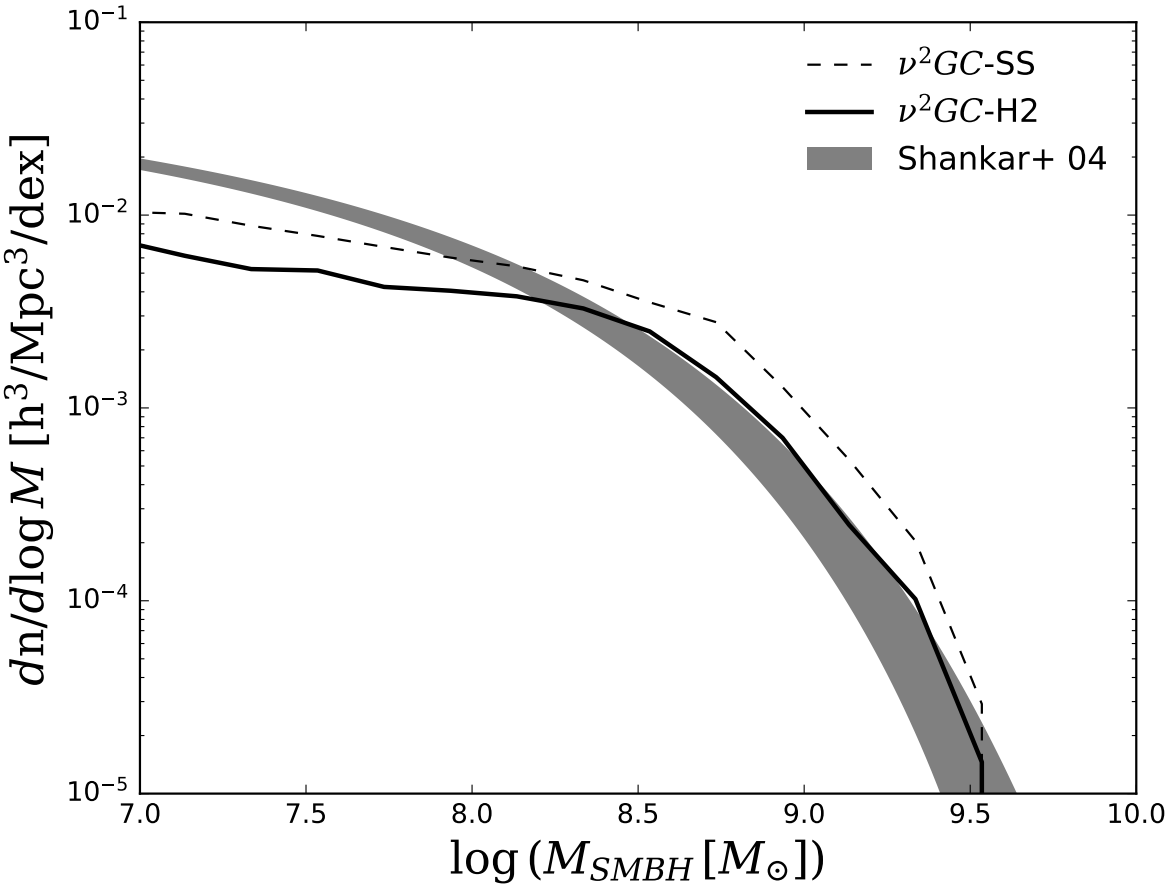

Figure 2.18: SMBH MF at $z \sim 0$. The model result obtained with the ν^2GC -SS and ν^2GC -H2 simulations appear in grey dashed and black solid lines with analytical fit to the observational data obtained from Shankar et al. (2004) in grey shaded region.

bulge mass of less massive galaxies is difficult to estimate by observations since the bulge is more rotational-support.

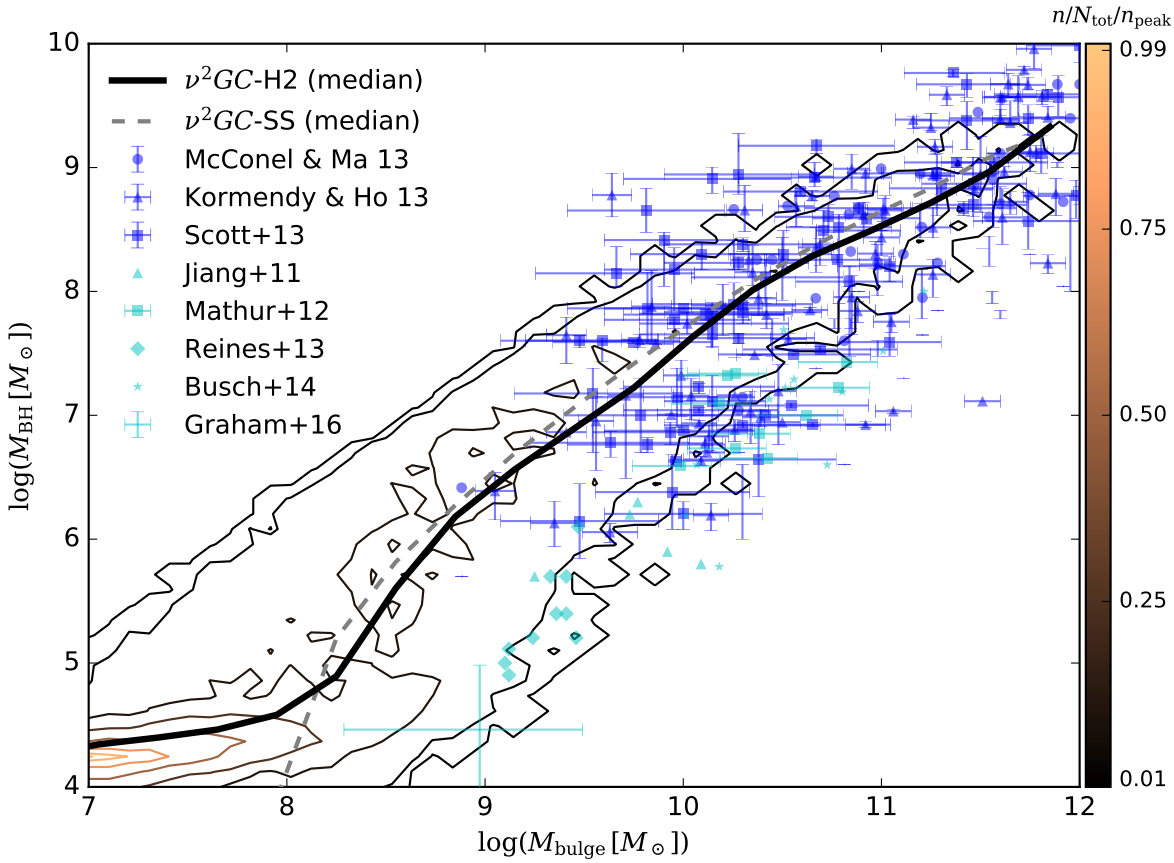

Figure 2.19: The relation between bulge mass and SMBH mass at $z \sim 0$. The colour contour and black solid line show the distribution and the median value of mock galaxies obtained from the fiducial model with the ν^2GC -H2 simulation, respectively. I overplot the result with the ν^2GC -SS simulation, for checking the effect of the mass resolution. Blue filled circles, triangles, and squares are observational results for quiescent BH systems (McConnell & Ma 2013; Kormendy & Ho 2013; Scott et al. 2013; respectively). Cyan filled triangles, squares, diamonds, stars, and pluses are observational results for AGNs Jiang et al. (2011), Mathur et al. (2012), Reines et al. (2013), Busch et al. (2014), and Graham et al. (2016), respectively.

Chapter 3

The effect of seed black hole mass on the $M_{\rm BH}$ – $M_{\rm bulge}$ relation

I explore the effect of varying the seed BH mass on the resulting BH mass – bulge mass relation at $z \sim 0$. When the mass of the seed is set at $10^5 M_\odot$, I find that the model results become inconsistent with recent observational results of the $M_{\rm BH}$ – $M_{\rm bulge}$ relation for dwarf galaxies. In particular, the model predicts that bulges with $\sim 10^9 M_\odot$ harbour larger BHs than observed. On the other hand, when I employ seed black holes with $10^3 M_\odot$, or randomly select their mass within a $10^{3-5} M_\odot$ range, the resulting relation is consistent with observation estimates, including the observed dispersion. I find that to obtain stronger constraints on the mass of seed BHs, observations of less massive bulges at $z \sim 0$ are a more powerful comparison than the relations at higher redshifts. In this chapter, I present the topical introduction in Sec. 3.1, the methods in Sec. 3.2, obtained results in 3.3. Finally, I discuss how to obtain the constraints on the seed BH mass more strictly and the validity of the model in Sec. 3.4.

3.1 Introduction

Observations have found luminous QSOs at $z > 6$, with the SMBH masses estimated at $\sim 10^9 M_\odot$ (Mortlock et al. 2011; Wu et al. 2015). Larger SMBH masses at higher redshifts require either (i) relatively heavier seed BHs with $\sim 10^5 M_\odot$ (e.g., Lodato & Natarajan 2006), or (ii) super-Eddington accretion for rapid growth of BHs (Rees 1992; Kawaguchi 2003). Both these mechanisms are potentially possible: (i) The massive seed BHs can be formed as the end products of gas collapse with virial temperatures $\geq 10^4$ K without molecular cooling (Begelman et al. 2006). (ii) Estimations of accretion rates and duration of the super-Eddington accreting AGNs, together with the observed trend of higher Eddington ratios at higher redshift (e.g., McLure & Dunlop 2004; Nobuta et al. 2012), indicate that BHs have grown via super-Eddington accretion in early Universe (Kawaguchi et al. 2004b). These two mechanisms have been actively discussed.

Because of the uncertainty of the BH formation mechanism and limited computational resources, most cosmological hydrodynamic simulations and SA models have treated the formation of BHs by putting a seed BH with a set mass at the centre of each galaxy. For example, in Barber et al. (2016), who use the EAGLE simulation, a seed BH of $10^5 h^{-1} M_\odot$ is placed by converting the bound gas particle with the highest density when a collapsed halo with

$\geq 10^{10}h^{-1}M_{\odot}$ contains no BHs. Okamoto et al. (2008a), on the other hand, employ a seed BH mass with $10^2 M_{\odot}$ and place the seed at the stellar density maxima when a virialised DM halo that consists of more than 1000 DM particles does not contain any BHs. Other cosmological simulations (e.g., Booth & Schaye 2009) assume that the seed BH mass is proportional to the gas mass in the host halo. SA models treat the birth of BHs in mainly two different ways. In the first, a central BH is born when a galaxy initially merges with other galaxies (e.g., Kauffmann & Haehnelt 2000; Enoki et al. 2003; Malbon et al. 2007; Lagos et al. 2009). In these models, the initial BH mass depends on the amount of the cold gas in the merging system. In the second method, a seed BH of a fixed mass is placed immediately after a galaxy forms: $10^2 M_{\odot}$ (Menci et al. 2003), $10^3 M_{\odot}$ (Fontanot et al. 2015), or $10^5 M_{\odot}$ (Makiya et al. 2016). For a deeper understanding of seed BHs from SA models, Pezzulli et al. (2016) and Valiante et al. (2016) focus on BH growth only in early Universe ($z \gtrsim 5$) and suggest that 100 $M_{\odot}$ seed BHs at $z \gtrsim 23$ accretes gas via major mergers at super-Eddington rates, forming $10^5 M_{\odot}$ BHs at $z \sim 17$. The mass of the seed BHs has previously been presumed to have only a small impact on the statistical properties of galaxies, AGNs and SMBHs, unless the mass accretion rate depends on black hole mass.

However, recent observations reach to galaxies with $M_{\rm BH} \lesssim 10^5 M_{\odot}$, which is comparable to the seed BH mass. (e.g., Graham 2012; Scott et al. 2013) have suggested that for $M_{\rm bulge} \lesssim 10^{10} M_{\odot}$, the $M_{\rm BH}$ – $M_{\rm bulge}$ relation becomes quadratic instead of the linear relation found for more massive bulges. It has also suggested that this quadratic relation continues down to $M_{\rm BH} \sim 10^5 M_{\odot}$. In this study, I focus on the possibility that the assumed seed BH mass distribution in theoretical models can affect the $M_{\rm BH}$ – $M_{\rm bulge}$ relation for $M_{\rm bulge} \lesssim 10^{10} M_{\odot}$.

3.2 Methods

In this study, I present results with $M_{\rm seed} = 10^3 M_{\odot}$ (hereafter 'light seed model') where $M_{\rm seed}$ is the seed BH mass, and $10^5 M_{\odot}$ ('massive seed model'). I also test the case in which $M_{\rm seed}$ takes uniformly random values in the logarithmic scale in the range of $3 \leq \log(M_{\rm seed}/M_{\odot}) \leq 5$ (hereafter 'random seed model').

As shown in Sec. 2.2, a galaxy is born when hot gas in the host halo cools efficiently. The hot gas cools by atomic cooling when the virial temperature, $T_{\rm vir}$, is larger than 10^4 K. I also consider the heating effect by the UV background. I employ fitting formulae of the characteristic halo mass, $M_c(z)$, obtained from Okamoto et al. (2008b), below which haloes become baryon deficient. I find that runs ν^2GC -SS and -L do not resolve haloes with $M_c(z)$ in any redshift, while the ν^2GC -H2 does resolve haloes with $M_c(z)$ at $z \lesssim 5$ and those with $T_{\rm vir} < 10^4$ K at $z \lesssim 3$. This difference, however, does not affect the main conclusion of this study as I will show later.

3.3 Results

In Fig. 3.1, I present the $M_{\rm BH} - M_{\rm bulge}$ relation at $z \sim 0$ predicted by the massive seed model (top panel) and light seed model (bottom panel). For the observational data with $M_{\rm BH} \lesssim 10^6 M_{\odot}$, I use the data obtained from Graham & Scott (2015) (hearafter GS15). This work re-estimated the bulge and BH masses obtained by previous work (Jiang et al. 2011; Mathur et al. 2012; Scott et al. 2013; Reines et al. 2013; Busch et al. 2014). I also plot LEDA

87300 whose BH mass is originally estimated by Baldassare et al. (2015) and re-evaluated by Graham et al. (2016). Almost all of the observational samples with $M_{\rm BH} \lesssim 10^6 M_\odot$ have active BHs. In our model, the $M_{\rm BH}$ – $M_{\rm bulge}$ relation does not change when I only plot AGNs.

Although all of our models reproduce the relation at $M_{\rm bulge} \gtrsim 10^{10} M_\odot$, the massive seed model is inconsistent with the recent observational estimates for dwarf galaxies with $M_{\rm bulge} \lesssim 10^{10} M_\odot$, in the sense that the predicted BH masses (shaded region) are larger than the observational estimates. I present the results by the N-body simulations with the same box size and different mass resolution (ν^2GC -SS and -H2) in all panels of Fig. 3.1. I find that the effect of the mass resolution of N-body simulations clearly appears with $M_{\rm bulge} \lesssim 10^9 M_\odot$. Nonetheless, the mass resolution does not affect our conclusion. Middle panel of Fig. 3.1 shows the result of the random seed model. I find that the random seed and light seed models reproduce the relation and its scatter well. These two successful models (light and random seed models) provide the same results in the range of $M_{\rm BH} \gtrsim 10^{5.5} M_\odot$ below which these models have significantly different slope of the relation. More observational data with $M_{\rm BH} \lesssim 10^{5.5} M_\odot$ are required for stronger constraints on the mass distribution of the seed BHs.

The sample of Jiang et al. (2011) seems to have the floor in the $M_{\rm BH}$ – $M_{\rm bulge}$ relation at $M_{\rm BH} \sim 10^{5-6} M_\odot$. Jiang et al. (2011) thus support the results obtained from the simulations of Volonteri & Natarajan (2009) with seed BHs of $10^5 M_\odot$. On the other hand, our model prefers the lower seed BH mass than $10^5 M_\odot$ to explain the $M_{\rm BH}$ – $M_{\rm bulge}$ relation obtained from Jiang et al. (2011).

The red dashed and dotted lines in Fig 3.1 depicts the scaling relations (Scott et al. 2013). [3] Our models exhibit the slightly lower $M_{\rm BH}$ – $M_{\rm bulge}$ relation than the scaling relation at $M_{\rm bulge} \gtrsim 10^{10} M_\odot$. In this region, $M_{\rm bulge}$ evaluated from observations is potentially biased in favor of larger stellar masses (e.g., Shankar et al. 2016).

Our models also exhibit the transition of the slope in the $M_{\rm BH}$ – $M_{\rm bulge}$ relations from quadratic to near-linear. I have confirmed that stellar feedback is responsible for the quadratic relation as suggested by Fontanot et al. (2015).

Next, I investigate the origin of the scatter of the $M_{\rm BH}$ – $M_{\rm bulge}$ relation. Fig. 3.2 indicates the distribution of the redshift at which galaxies newly form ($z_{\rm form}$). I predict that the scatter of the $M_{\rm BH}$ – $M_{\rm bulge}$ relation can be related to the difference of $z_{\rm form}$. Three solid lines indicate the relation with different ranges of $z_{\rm form}$: $z_{\rm form} < 4$, $4 \leq z_{\rm form} < 8$, and $8 \leq z_{\rm form}$. I find that more massive systems form at higher redshift. I also find that SMBHs become slightly massive with low $z_{\rm form}$ for a given $M_{\rm bulge}$ at $M_{\rm bulge} < 10^9 M_\odot$. This might be because large amount of gas gets accreted by the SMBHs immediately after $z_{\rm form}$. Galaxies which formed later are subject to gas-rich processes, such as major mergers or disc instabilities. On the other hand, galaxies hosting the same mass of the SMBHs with higher $z_{\rm form}$ have experienced more gas-poor processes of spheroid growth, such as dry mergers, than lower $z_{\rm form}$ counterparts since the time elapsed from their burth is longer; their bulges increase their masses without feeding central BHs.

Merrifield et al. (2000) suggest that $M_{\rm BH}/M_{\rm bulge}$ ratios are higher in galaxies with older stellar age, whose sample galaxies are $M_{\rm bulge} > 10^{10} M_\odot$. In my model, there are almost

[2] Originally obtained from Scott et al. (2013).

[3] Scott et al. (2013) classified galaxies by their bulge surface brightness profiles: core-Sérsic galaxies (bulge surface brightness profiles have a partially depleted core) and Sérsic galaxies (bulge surface brightness profiles are well-fitted by a single Sérsic model).

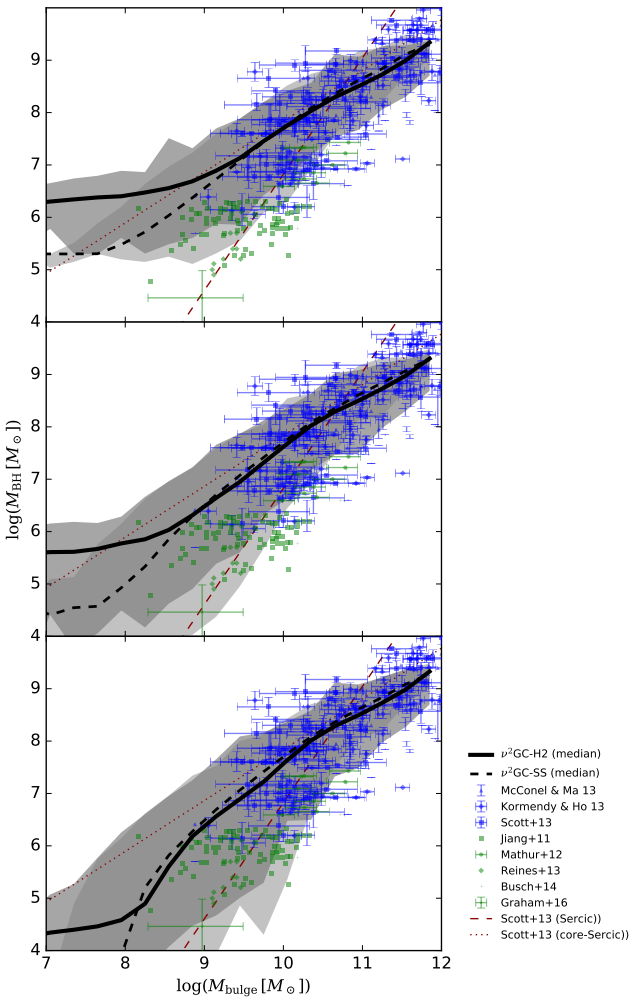

Figure 3.1: $M_{\rm BH}$ – $M_{\rm bulge}$ relations at $z \sim 0$ for different $M_{\rm seed}$; the massive (top), random (middle), and light (bottom) seed models. Black dashed and solid lines present the results of the ν^2GC -SS and -H2 simulations, respectively. Black lines track the median, and shaded regions indicate 0-100 percentile of the models. Blue filled symbols indicate observational results obtained from McConnell & Ma (2013), Kormendy & Ho (2013), and GS15[2](triangles, diamonds, and squares, respectively). Green symbols are AGN sample obtained from GS15,(see the text for more details). Green asterisks correspond LEDA 87300 (Graham et al. 2016; Baldassare et al. 2015). Red dot-dashed and dotted lines depict the scaling relations (Scott et al. 2013). Since the $M_{\rm BH}$ – $M_{\rm bulge}$ relation is sensitive to the mass of seed BHs, most seed BHs should not set to $10^5 M_\odot$ for reproducing the observed local relation.

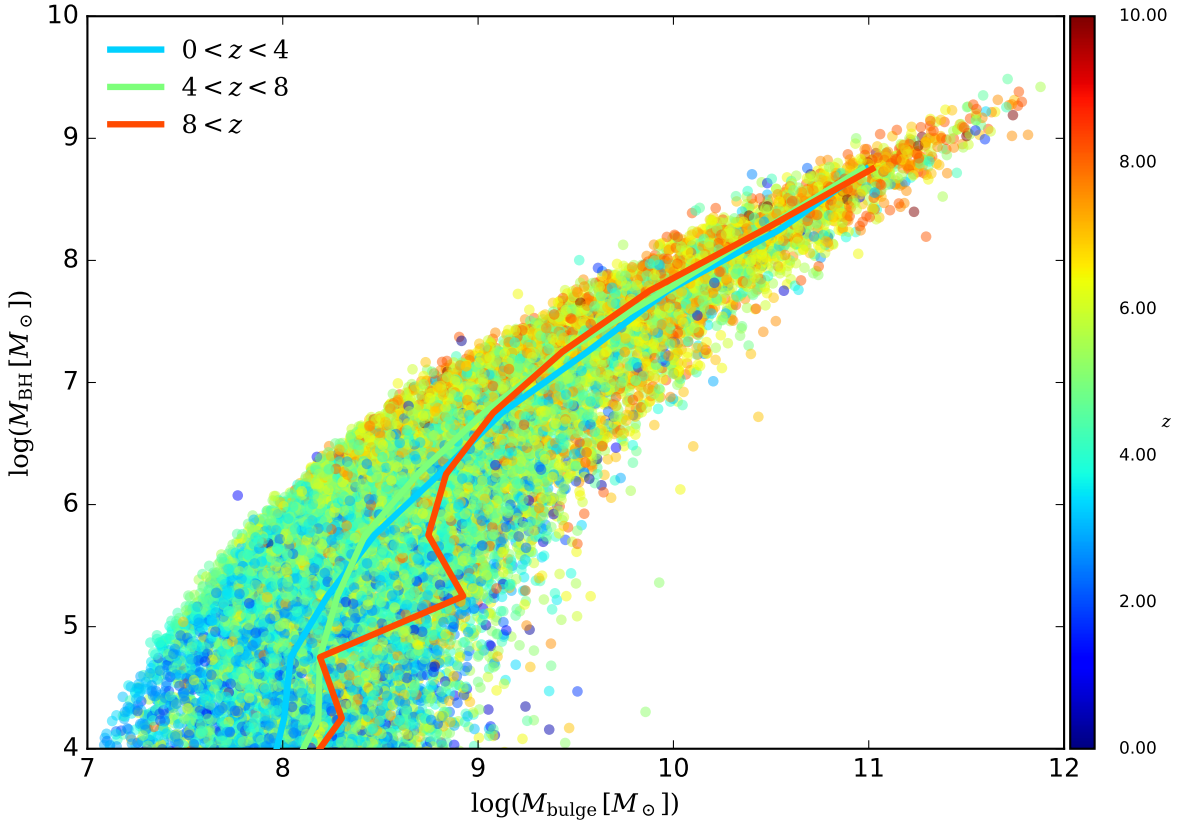

Figure 3.2: The $M_{\rm BH}$ – $M_{\rm bulge}$ relation at $z \sim 0$ with the ν^2GC -SS simulation and $M_{\rm seed} = 10^3 M_\odot$. The color indicates the redshift at which the host galaxies newly formed ($z_{\rm form}$). Solid lines shows the median value for different $z_{\rm form}$ ranges; $z_{\rm form} < 4$ (brue), $4 \leq z_{\rm form} < 8$ (green), and $8 \leq z_{\rm form}$ (red). For a given SMBH mass, bulges become more massive with higher $z_{\rm form}$.

no relation between $M_{\rm BH}/M_{\rm bulge}$ ratios and the $z_{\rm form}$, which is slightly inconsistent with Merrifield et al. (2000). However, we note that the observed stellar age of galaxies have large errors and degenerates the metallicity estimates.

3.4 Summary and Discussion

I have investigated how the mass of the seed BHs affects model predictions of the local $M_{\rm BH}$ – $M_{\rm bulge}$ relation by using ν^2GC . I find that seed BHs should not be dominated by those as massive as $10^5 M_\odot$ to reproduce the observed $M_{\rm BH}$ – $M_{\rm bulge}$ relation at $z \sim 0$ over a wide range of bulge masses down to $M_{\rm bulge} \lesssim 10^{10} M_\odot$. To obtain stronger constraints of the mass distribution for the seed BHs, observations of $M_{\rm BH} \lesssim 10^{5.5} M_\odot$ would be required.

The results in this study are consistent with cosmological hydrodynamic simulations performed by Anglés-Alcázar et al. (2015; 2017) which suggest that the $M_{\rm BH}$ – $M_{\rm bulge}$ relation converges independently of the seed BH mass at $M_{\rm bulge} \gtrsim 10^{10} M_\odot$ while at $M_{\rm bulge} \lesssim 10^{10} M_\odot$, seed BH mass becomes important in the scaling relation. Anglés-Alcázar et al. (2017) com-

pare BH mass – galaxy stellar mass relations at $z \sim 0$ with $10^4 h^{-1} M_\odot$ and $10^6 h^{-1} M_\odot$ seed BHs. They find that in the case with $10^6 h^{-1} M_\odot$ seed BHs, the relation has a floor which also appears in the $M_{\rm BH}$ – $M_{\rm bulge}$ relation in our massive seed model.

I explored whether the measurements of the $M_{\rm BH}$ – $M_{\rm bulge}$ relation at higher redshifts help to obtain further constraints on the mass of seed BHs. Fig. 3.3 depicts the ratio of the average BH masses in the light seed model ($\equiv \langle M_{\rm BH} \rangle_3$) and those in the massive seed model ($\equiv \langle M_{\rm BH} \rangle_5$), as a function of bulge masses obtained from the ν^2GC -H2 simulation. The difference in the seed mass clearly appears in galaxies with bulge mass below $3 \times 10^9 M_\odot$ at $z \sim 0, 1$ and 2. I find that the difference due to the seed mass becomes smaller at higher redshift for a given $M_{\rm bulge}$. Therefore observations of less massive bulges at $z \sim 0$ are more powerful than at higher redshifts for constraining the mass distribution of seed black holes. This conclusion might be against the expectation. Since the BHs at higher redshift have smaller time for their growth, one might think that the difference of the seed mass should remain for more massive galaxies. However, massive galaxies, which host massive BHs, grow by more gas-rich processes at higher redshift and the seed BH mass is negligibly smaller than the accreted gas mass. The difference of the seed mass, therefore, will be observable only for less massive galaxies as for galaxies at higher redshift.

Next I investigated SMBH MFs at $z \sim 6$ by using the ν^2GC -L simulation. Fig. 3.4 shows the results of the light and massive seed models (blue and red circles, respectively). The SMBH MF at $z \sim 6$ obtained from our model is nearly consistent with the estimation of Willott et al. (2010b) in the range of $M_{\rm BH} \gtrsim 10^7 M_\odot$. I find that an SMBH MF at $z \sim 6$ in the range of $M_{\rm BH} \gtrsim 10^{5.8} M_\odot$ does not depend on the mass of the seed BHs due to the large amount of cold gas that gets accreted by the BHs. This is true even when I employ the model without the disc instabilities, in which only mergers are the only trigger for a starburst and gas fueling to a BH.

Interestingly, the triggering mechanisms affect the shape of the SMBH MF. Without disc instabilities, the MF have a peaky shape. Therefore, to produce the broad distribution of SMBH mass at high redshift, the SMBH growth would be triggered by processes other than mergers of galaxies.

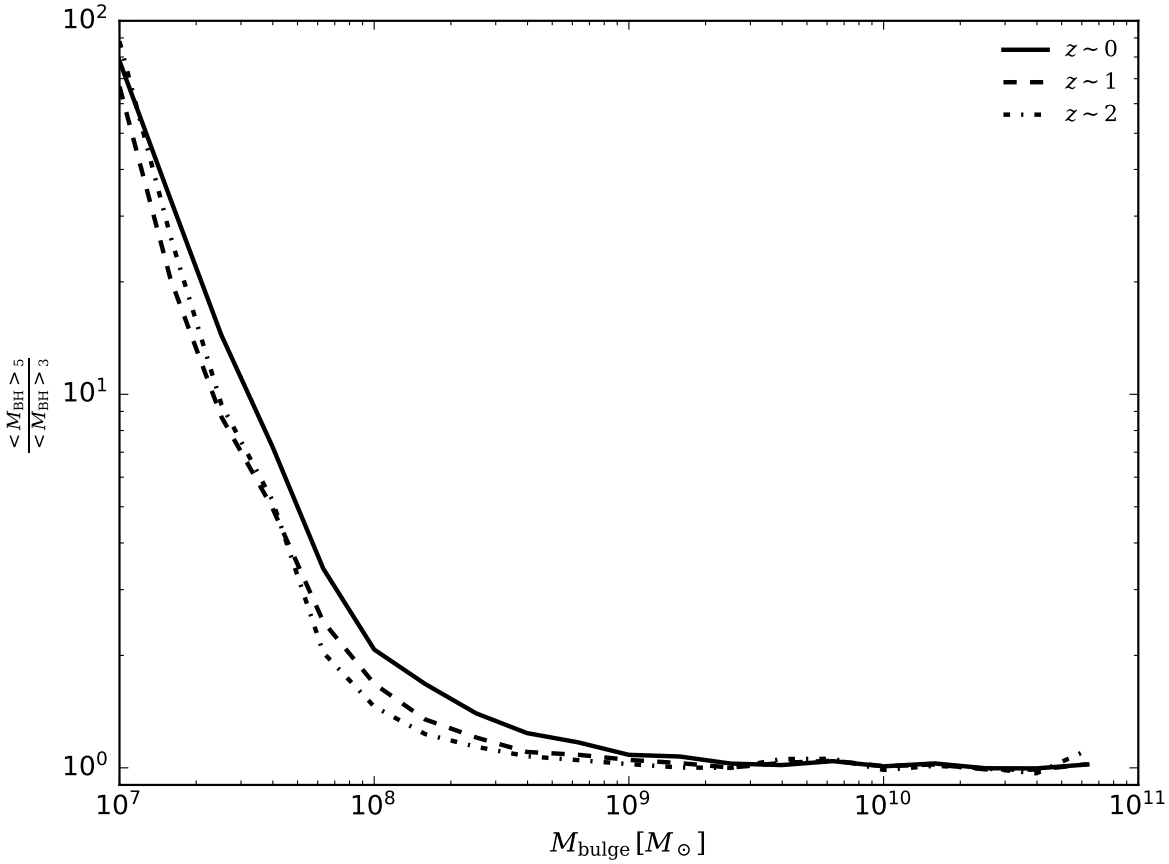

Figure 3.3: The difference of averaged SMBH mass due to the seed BH mass at $z \sim 2$ (dash-doted line), $z \sim 1$ (doted line), and $z \sim 0$ (solid line) as a function of their bulge stellar mass with the ν^2GC -SS simulation. The difference becomes smaller at higher redshift.

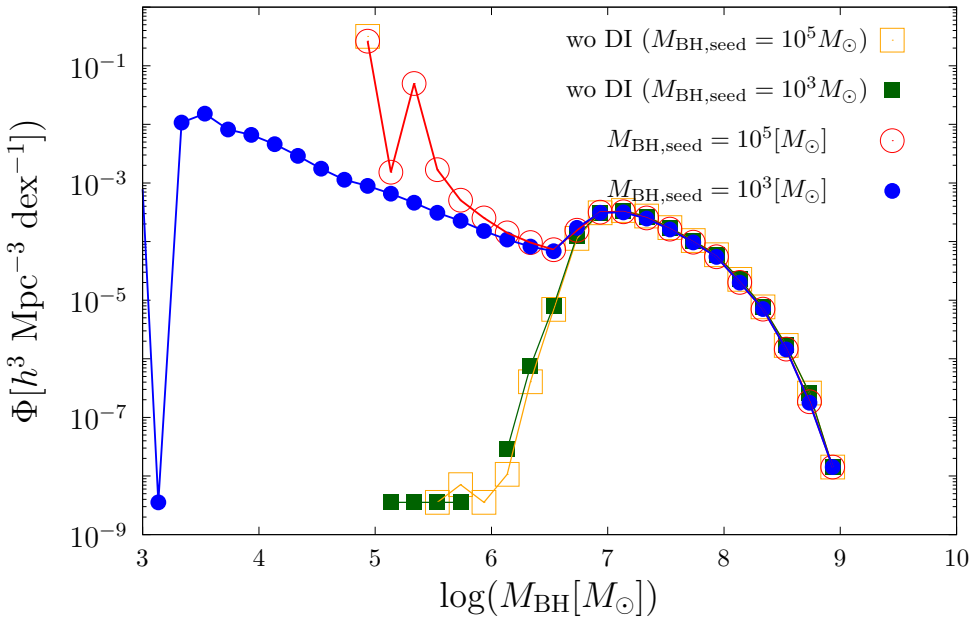

Figure 3.4: SMBH MF at $z \sim 6$ based on the largest cosmological N-body simulation (ν^2GC - L). Orange open and green filled squares with lines show the results of M16, red open and blue filled circles with lines show the results of light and massive seed models, respectively. Even at $z \sim 6$, SMBH MF does not depend on the mass of the seed BHs in the range of $M_{\rm BH} \gtrsim 10^{5.8} M_\odot$.

Chapter 4

The effect of the accretion timescale on AGN properties

I focus on the accretion timescale onto BHs. I find that the number density of AGNs at $z < 1.5$ and at hard X-ray luminosity $< 10^{44}$ erg/s is underestimated compared with recent observational estimates when I assume the exponentially decreasing accretion rate and the accretion timescale which is proportional to the dynamical time of the host halo or the bulge, as is often assumed in SA models. I show that to solve this discrepancy, the accretion timescale of such less luminous AGNs should be a function of the black hole mass and the accreted gas mass. This timescale can be obtained from a phenomenological modelling of the gas angular momentum loss in the circumnuclear torus and/or the accretion disc. Such model predicts a longer accretion timescale for less luminous AGNs at $z < 1.0$ than luminous QSOs whose accretion timescale would be 10^{7-8} yr. With this newly introduced accretion timescale, our model can explain the observed LFs of AGNs at $z < 6.0$. In this chapter, I present the topical introduction in Sec. 4.1, the methods in Sec. 4.2. Next, I present the obtained results in 3.3. Finally, I discuss how to discriminate the model effects in Sec. 4.4.

4.1 Introduction

Estimation of the accretion timescale is important as it reveals the co-evolution between SMBHs and their host galaxies. If all galaxies have undergone the AGN phase, the duration of the accretion phase should be short to explain the observed AGN LFs. In contrast, AGNs should be long-lived if a small fraction of galaxies have experienced this phase (e.g. Sołtan 1982).

There are some constraints on the accretion timescales obtained from previous studies (see Martini 2004; for more details). Yu & Tremaine (2002) estimate the timescale by comparing present-day mass density of BHs with the integrated accreted mass density in luminous AGN phases obtained from optical AGN LFs at various redshifts. They suggest that the average "AGN lifetime" is $3-13\times10^7$ years for $10^{8-9}M_\odot$ BHs if the radiation efficiency, η, is $0.1-0.3$. On the theoretical side, Kauffmann & Haehnelt (2000; hereafter KH00) estimate the AGN lifetime by using an SA model. They assume a constant radiation efficiency for AGNs, which are triggered only by major mergers of galaxies. They derive the average AGN lifetime to explain observed AGN LFs with $M_B \lesssim -23$ (where M_B is the $B-$ band absolute magnitude).

They suggest that the lifetime is $\sim 3 \times 10^7$ yr at $z = 0$ and that the timescale would scale with the dynamical time of the halo; $\propto (1+z)^{-1.5}$.

In these studies, the AGN lifetime is assumed to be the timescale within which SMBHs are observed as optical AGNs. This timescale is not necessarily equal to the accretion timescale onto SMBHs. Hopkins et al. (2005) estimate not the AGN lifetime but the "total" accretion timescale considering the obscured accretion phases by using hydrodynamic simulations. They suggest that the accretion onto an SMBH is not visible at first because gas and dust components are surrounding the nuclear region. After blowing out these components by AGN winds, AGNs can be observed as optical sources. The AGN lifetime is then ~ 20 Myr and the total accretion timescale is ~ 100 Myr for AGNs with $M_B < -22$.

There are still two uncertainties about the accretion timescale. One is the physical processes that govern the timescale. Several authors have proposed different mechanisms that determine the accretion timescale. KH00 suggest it is proportional to the dynamical time of the host halo. Norman & Scoville (1988) propose that the gas accretion continues during a starburst in its host galaxy, because they assume that the gas fueling to an SMBH is promoted by the mass loss from large star clusters. Granato et al. (2004) and Fontanot et al. (2006) assume the accretion rate to be determined by the viscosity of the accretion disc. The effect of these different assumptions on statistical properties of AGNs and SMBHs remains unclear.

It is also unclear whether the timescale of less luminous AGNs is the same order as that of luminous ones. Previous work has focused on the timescale of optical AGNs with $M_B < -22$ (hard X-ray (2-10 keV) luminosity, L_X, corresponds to $\sim 5 \times 10^{43}$ erg/s) whose SMBH mass is larger than $\sim 10^8 M_\odot$. Less luminous AGNs with $L_X \lesssim 10^{44}$ erg/s would have wide range of SMBH masses. The accretion timescale of such less luminous AGNs is not necessarily in the same order as luminous AGNs.

There is a well-known problem of SMBH growth scenario. Assuming that AGN activities are triggered only by mergers of galaxies and that the accretion timescale is $\sim 10^{7-8}$ yr, the number density of less luminous AGNs are underestimated in SA models. This implies that to explain the observed "anti-hierarchical trend" of SMBH growth, I need to consider other triggering mechanisms of SMBHs and/or to reconsider the accretion timescale. As an example, Hirschmann et al. (2012) assume that AGNs are triggered solely by galaxy mergers, and set the accretion timescale is proportional to the Salpeter timescale,

$$\frac{\eta \sigma_T c}{4\pi G m_p} \frac{L_{\rm Edd}}{L} \sim 4.5 \times 10^7 \left(\frac{\epsilon}{0.1}\right) \left(\frac{L_{\rm Edd}}{L}\right) \text{yr}, \tag{4.1}$$

for all AGNs, where $\eta = L/\dot{M}c^2$ is the radiation efficiency, and L is the bolometric luminosity of AGNs. Their model also underestimates the number density of less luminous AGNs at $z < 1.5$. They solve this problem by introducing a disc instability as a triggering mechanism of AGNs. Other SA models also try to reproduce AGN LFs by introducing additional triggering mechanisms of SMBH growth without reconsidering the accretion timescale.

4.2 Methods

4.2.1 Modellings of the accretion timescale

I test three types of the accretion timescale summarised in Table 4.1. The `KH00model`, $t_{\rm acc} = 3 \times 10^7 \ (1+z)^{-1.5}$ yr, means that the accretion timescale is proportional to the

Model Name	$t_{\rm acc}$	free parameters
`KH00model`	$3\times10^7(1+z)^{-1.5}$ yr	None
`Galmodel`	$\alpha_{\rm bulge}t_{\rm dyn,bulge}$	$\alpha_{\rm bulge}$
`GalADmodel`	$\alpha_{\rm bulge}t_{\rm dyn,bulge}+t_{\rm loss}$	$\alpha_{\rm bulge}, t_{\rm loss,0}, \gamma_{\rm BH}, \gamma_{\rm gas}$

Table 4.1: Summary of the accretion timescale model (Sec. 2.6.2).

dynamical time of the host halo (originally introduced by KH00).

Some SA models (e.g. Fanidakis et al. 2012; Pezzulli et al. 2017) instead use the `GalModel`, $t_{\rm acc} = \alpha_{\rm bulge}\, t_{\rm dyn,bulge}$ by assuming the accretion continues until the gas supply from the host galaxy continues. The accretion timescale is proportional to the dynamical time of the host bulge, $t_{\rm dyn,bulge} = r_{\rm b} \,/\, V_{\rm b}$ (where $r_{\rm b}$ and $V_{\rm b}$ are the size and 3D velocity dispersion of the bulge, respectively), and the coefficient, $\alpha_{\rm bulge}$, is a free parameter. I choose the value of $\alpha_{\rm bulge}$ so that the bright-end of the model AGN LFs are consistent with observed AGN LFs.

I newly introduce the `GalADmodel` in Chapter 4 considering that the accretion would continue when gas is left in the circumnuclear torus or the accretion disc even when there is no gas supply from the host galaxy. I assume that $t_{\rm acc}$ is the sum of the gas supply timescale from its host galaxy, which is assumed to relate with the dynamical time of the bulge, [1] and the timescale for the angular momentum loss of the accreted gas at $\lesssim 100$ pc, $t_{\rm loss}$:

$$t_{\rm acc} = \alpha_{\rm bulge}t_{\rm dyn,bulge} + t_{\rm loss}, \tag{4.2}$$

The second term of Eq. 4.2 includes the angular momentum loss timescale in a circumnuclear torus and/or in the accretion disc. I construct a simplified and phenomenological model for the angular momentum loss in the central region. The gas accretion should continue beyond the starburst phase of the host galaxies if the accreted gas requires a longer timescale to lose its angular momentum in the circumnuclear torus and the accretion disc . In this region, the gravitational potential is dominated by the SMBH. The timescale thus should depend on the mass of the SMBH. Considering a circumnuclear torus in which the mass accretion rate depends on the gravitational stability (e.g. Kawakatu & Wada 2008), the accretion timescale would become longer for the more massive SMBH. This timescale would also depend on the mass ratio between the accreted gas and the SMBH. When this ratio becomes higher, the self-gravity of the accreted gas works more effectively and thus the outer edge of the accretion disc becomes smaller. The dynamical timescale then becomes shorter. I hence describe $t_{\rm loss}$ as a function of $M_{\rm BH}$ and $\Delta M_{\rm acc}$:

$$t_{\rm loss} = \frac{t_{\rm loss,0}}{\rm Gyr}\left(\frac{M_{\rm BH}}{M_\odot}\right)^{\gamma_{\rm BH}}\left(\frac{\Delta M_{\rm acc}}{M_\odot}\right)^{\gamma_{\rm gas}}, \tag{4.3}$$

where $t_{\rm loss,0}$, $\gamma_{\rm BH}$, and $\gamma_{\rm gas}$ are free parameters which are tailored to match the observed AGN LFs from $z\sim0$ to 5. I set values of $t_{\rm loss,0}$, $\gamma_{\rm BH}$, and $\gamma_{\rm gas}$ to be 1 Gyr, 3.5, and -4.0, respectively. I show that $\gamma_{\rm BH}$ would be >0 and $\gamma_{\rm gas}$ would be $\lesssim 0$, considering the $\alpha-$viscosity in the accretion disc, and these signs would be the same by considering CNDs (Appendix 1.3.1).

[1] This also corresponds to the star formation timescale for a starburst (Nagashima et al. 2005).

When I use this model, I find that there are SMBHs whose accretion timescale exceeds the age of the Universe. In this case, I set $\dot{M}_{\rm BH} = 0$ implicitly assuming that accreted gas becomes gravitationally stable in a circumnuclear torus and/or a accretion disc, which cannot be accreted onto an SMBH. This treatment does not affect the shape of the AGN LFs since the accretion rates of such SMBHs are negligibly small.

There are some analytical estimates for the timescale of the angular momentum loss in a circumnuclear torus (e.g. Kawakatu & Umemura 2002; Kawakatu & Wada 2008), which have been employed by some SA models (e.g., Antonini et al. 2015; Bromley et al. 2004; Granato et al. 2004). I note that there are large uncertainties as to whether a circumnuclear torus with some common properties exists for all types of AGNs.

I show that the accretion timescale from the accretion disc to the SMBH has a negative (positive) dependency on the mass of the accreted gas (SMBH), following the viscous timescale in the accretion discs. I classify the accretion discs by their accretion rate following Kato et al. (2008). Then, I analytically calculate the radial velocity of the gas, $|v_{\rm r}|$, and the outer radius of the accretion disc which is determined as the boundary between self gravitating and non-self gravitating disc, $r_{\rm sg}$. The details appear in Kawaguchi et al. (2004a). Here I define the Schwarzschild radius, $r_{\rm Sch}$, as $2GM_{\rm BH}/c^2$, the distance from the BH normalised by $r_{\rm Sch}$, $\hat{r}$, the viscous parameter, α, and a non-dimensional variable, $f = 1 - \sqrt{3r_{\rm Sch}/r}$. The accretion rate is simply described as $\Delta M_{\rm acc}/t_{\rm vis}$ for this calculation, where $t_{\rm vis}$ is the viscous timescale determined as $t_{\rm vis} = r_{\rm sg}/|v_{\rm r}|$. The accretion rate normalised by the Eddington mass accretion rate, $\dot{m}$ (the Eddington mass accretion rate: $L_{\rm Edd}/c^2$), is employed. The disc is classified according to the dominant opacity and pressure sources as follows.

1. The outer region in which the main opacity source is (free-free) absorption and the gas is the dominant pressure source. Then
$$|v_{\rm r}| \propto \alpha^{4/5} M_{\rm BH}^{-1/5} \dot{m}^{3/10} \hat{r}^{-1/4} f^{-7/10}$$
and
$$r_{\rm sg}/r_{\rm Sch} \propto \alpha^{28/45} M_{\rm BH}^{-52/45} \dot{m}^{-22/45}.$$
I obtain $t_{\rm vis} \propto M_{\rm BH}^{15/2} \Delta M_{\rm acc}^{-41/4}$.

2. The middle region in which the main opacity source is electron scattering and the gas is the dominant pressure source. Then
$$|v_{\rm r}| \propto \alpha^{4/5} M_{\rm BH}^{-1/5} \dot{m}^{2/5} \hat{r}^{-2/5} f^{-3/5}$$
and
$$r_{\rm sg}/r_{\rm Sch} \propto \alpha^{14/27} M_{\rm BH}^{-26/27} \dot{m}^{-8/27}.$$
I obtain $t_{\rm vis} \propto M_{\rm BH}^{18/5} \Delta M_{\rm acc}^{-22/5}$.

3. The inner region in which the main opacity source is electron scattering and the radiation is the dominant pressure source. Then
$$|v_{\rm r}| \propto \alpha M_{\rm BH}^{0} \dot{m}^{2} \hat{r}^{-5/2} f^{1}$$
and
$$r_{\rm sg}/r_{\rm Sch} \propto \alpha^{2/9} M_{\rm BH}^{-2/9} \dot{m}^{4/9}.$$
I obtain $t_{\rm vis} \propto M_{\rm BH}^{6/5} \Delta M_{\rm acc}^{-4/5}$.

Considering these conditions, I conclude that the viscous timescale has a positive correlation to the BH mass and negative correlation to the accreted gas mass at all radii.

Next, I consider the Circumnuclear disc (CND). I consider the CND model of Kawakatu & Wada (2008), as an example, although the physical mechanisms of how the CND maintains its structure is still under discussion. In Kawakatu & Wada (2008), SNe occurred in the CND induces the tidal torque which enhances the gas accretion rate from the CND to the SMBH. When the CND becomes unstable considering from the Toomre criterion (Toomre 1964), then the star formation occurs and the accretion rate increases. Since the CND becomes stable for the massive SMBH, $\gamma_{\rm BH}$ should be positive. On the other hand, since the SFR becomes more significant for the more gas-rich galaxies, $\gamma_{\rm gas}$ should be negative. I cannot obtain constraints on the values of $\gamma_{\rm BH}$ and $\gamma_{\rm gas}$ since the model of CND is too complicated to construct a single phenomenological model of the accretion timescale (i.e. the outer radius of the CND depends on the SMBH mass, mass density of CND itself and their host galaxy; see Sec. 2.3 in Kawakatu & Wada 2008). With the simple assumptions (based on Kawakatu & Wada 2008), I estimate $\gamma_{\rm BH} \sim -0.5$ and $\gamma_{\rm gas} \sim 1.0$, assuming a constant star formation efficiency, constant surface densities of the host galaxy and CND, the outer radius of the CND which is proportional to $M_{\rm BH}^{0.5}$.

4.3 Results

I show the AGN properties obtained with ν^2GC . If nothing is stated, I employ the ν^2GC -M simulation. I do not consider an obscured phase (e.g. Hopkins et al. 2005), in which SMBHs do not appear as luminous AGNs at optical bands despite sufficiently large accretion rates onto SMBHs. To avoid this uncertainty, I compare the model results with observations by using AGN LFs in hard X-ray (2-10 keV) (see also Sec. 2.7.1).

4.3.1 The effect of the accretion timescale on AGN LFs

I present the luminosity of AGNs in the hard X-ray (2-10 keV) band because the effect of obscuration and absorption is small. I show how AGN LFs change when I use three different models of the accretion timescale in Fig. 4.1. Black lines show the model hard X-ray LFs with different accretion timescales. I also show the fitting function of the LFs from Aird et al. (2015) with grey dotted lines and observed data from Aird et al. (2015), Ueda et al. (2014), and La Franca et al. (2005). I have confirmed that the results have no statistical differences when I employ the high resolution N-body simulations.

Black dashed lines show the hard X-ray (2-10 keV) AGN LFs with the `KH00model`, which is the timescale proportional to the dynamical time of the host halo. The model is consistent with observational results at $\log(L_X/{\rm erg\ s^{-1}}) > 43.5$ within the dispersion of the observed data. We, however, find that the model underestimates the number density of AGNs at $z < 1.0$ with $\log(L_X/{\rm erg\ s^{-1}}) < 43.5$ (i.e., nuclei of Seyfert galaxies), whose UV (1450Å) magnitude, $M_{\rm UV}$, corresponds to ~ -20.6. Such less luminous AGNs are not considered in the estimation of the AGN lifetimes in KH00 and their lifetimes could significantly differ for luminous AGNs.

Black dot-dashed lines show hard X-ray AGN LFs by the model in which the `Galmodel`. This modelling is similar to previous SA models (e.g. Fanidakis et al. 2012; Shirakata et al. 2016; Pezzulli et al. 2017). The accretion timescale does not cause a big difference in the

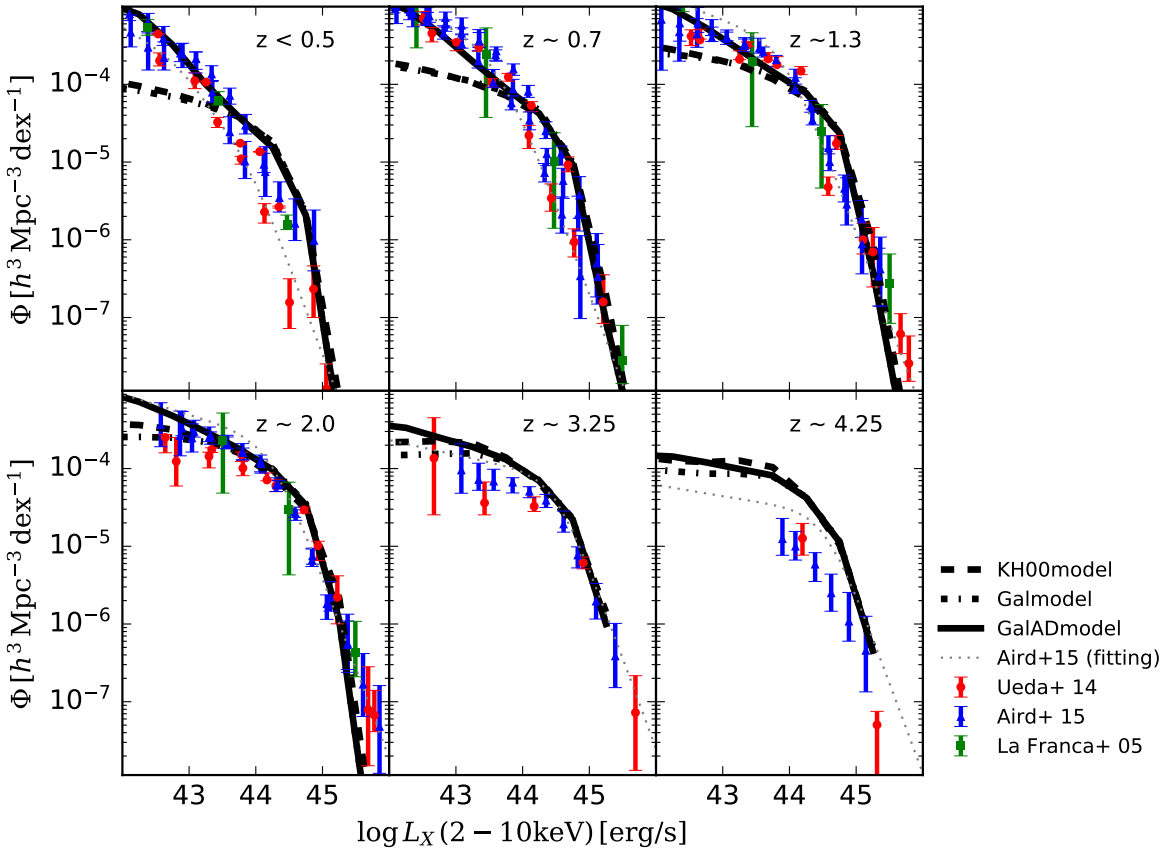

Figure 4.1: AGN LFs in hard $X-$ ray (2-10 keV) at $z < 0.5$, $z \sim 0.7$, $z \sim 1.3$, $z \sim 2.0$, $z \sim 3.25$, and $z \sim 4.25$. The model LFs are obtained with the ν^2GC -M simulation. Black dashed, dot-dashed, and solid lines are the model LFs with different models of accretion timescale; the `KH00model`, `Galmodel`, and `GalADmodel`, respectively. Observational results are obtained from Red circles, blue triangles, and green squares are the data taken from Ueda et al. (2014), Aird et al. (2015), and La Franca et al. (2005), respectively. Grey dotted lines show the fitting LFs of observed data (Aird et al. 2015).

faint-end slope of AGN LFs compared with that with the `KH00model`, since the `Galmodel` has the accretion timescale with the same order as the `KH00model` as shown later in Fig. 4.2.

Black solid lines show the hard X-ray AGN LFs with `GalADmodel`, implicitly considering the timescale of angular momentum loss in the circumnuclear torus and the accretion disc. The model enables us to reproduce not only bright-ends of the LFs but also the faint-ends, especially at $z < 1.5$. When this model of the accretion timescale is employed, a significant fraction of low-luminosity AGNs sustain their activity for a long time as I will show later. The model thus reproduces the both the bright and faint-ends of AGN LFs much better than the other models.

Next, Fig. 4.2 shows the redshift evolution of the accretion timescale of `KH00model` and `Galmodel`, and $t_{\rm loss}$. I select AGNs with $\log(L_X/{\rm erg\ s^{-1}}) > 41.0$. The red circles and blue squares with error bars show the median value of $\alpha_{\rm bulge}t_{\rm dyn,bulge}$ and $t_{\rm loss}$ with 25th and 75th percentiles. The redshift evolution of the dynamical time of the bulge (red circles) and the halo (black solid line) are similar although the difference becomes larger at higher redshift. This explains why the AGN LFs with the `KH00model` and `Galmodel` are similar. While $t_{\rm loss}$ distributes broadly, it is longer especially at lower redshift. This results in the increase of the number density of AGNs at $\log(L_X/{\rm erg\ s^{-1}}) < 43.5$ and $z < 1.5$. I also plot $t_{\rm loss}$ only for luminous AGNs with $\log(L_X/{\rm erg\ s^{-1}}) > 43.5$ as green triangles. The timescale is more than 1 order of magnitude shorter than that of AGNs with $\log(L_X/{\rm erg\ s^{-1}}) > 41.0$ at all redshifts.

The `GalADmodel` predicts the longer accretion timescales for the less luminous AGNs due to the effect of $t_{\rm loss}$ as shown in Fig. 4.3. This figure shows the relation between hard X-ray luminosity and timescales ($t_{\rm loss}$ and $\alpha_{\rm bulge}t_{\rm dyn,bulge}$) at $z \sim 0, 2$, and 4. I find that the timescale is almost constant ($\sim 2{\times}10^7$ yr) for AGNs with $\log(L_X/{\rm erg\ s^{-1}}) > 44.0$ (corresponds to $M_{UV} < -22.3$), which is consistent with the constraints obtained by previous studies (Yu & Tremaine 2002; Kauffmann & Haehnelt 2000; Hopkins et al. 2005). Less luminous AGNs, in contrast, have negative correlations between the timescale and L_X. I also find that the total accretion timescale becomes longer at lower redshift for all AGNs.

The results obtained with the `GalADmodel` naturally explains the evolution of the AGN number density, which is sometimes called "anti-hierarchical trend" of SMBH growth. Fig. 4.4 shows the number density of AGNs obtained with the `GalADmodel`, and those obtained from observations (Ueda et al. 2014; Aird et al. 2015). The reason why the model result shows mild anti-hierarchical trends would be partially because I consider the obscured fraction in hard X-ray (2-10 keV) is 0 at all redshift. To compare model results in more details, obscured fraction, which can be used in SA models has to be obtained.

4.3.2 The effect of the timescale on other properties of AGNs

To see dependencies of the accretion timescale on $M_{\rm BH}$ and $\Delta M_{\rm acc}$, I show the relation between AGN bolometric luminosity and BH mass, $M_{\rm BH}$ (top panels), and accreted gas mass onto an SMBH, $\Delta M_{\rm acc}$ (bottom panels) at $z \sim 0$, in Figs. 4.5 and 4.6. In Fig. 4.5, x-axes are the AGN bolometric luminosity at $t = t_{\rm start}$, $L_{\rm bol}(t_{\rm start})$, while these are AGN bolometric luminosity at the output time, $L_{\rm bol}(t_{\rm out})$, in Fig. 4.6. The left panels show the result with the `Galmodel` and the right panels show that obtained by the `GalADmodel`. I note that the model AGNs have a weak correlation between $M_{\rm BH}$ and $\Delta M_{\rm acc}$, of the form $M_{\rm BH} \propto \Delta M_{\rm acc}^{1.1}$, with a large dispersion. This positive correlation comes from the fact that the host galaxy of the heavier SMBH is more massive and has large amount of the cold gas.

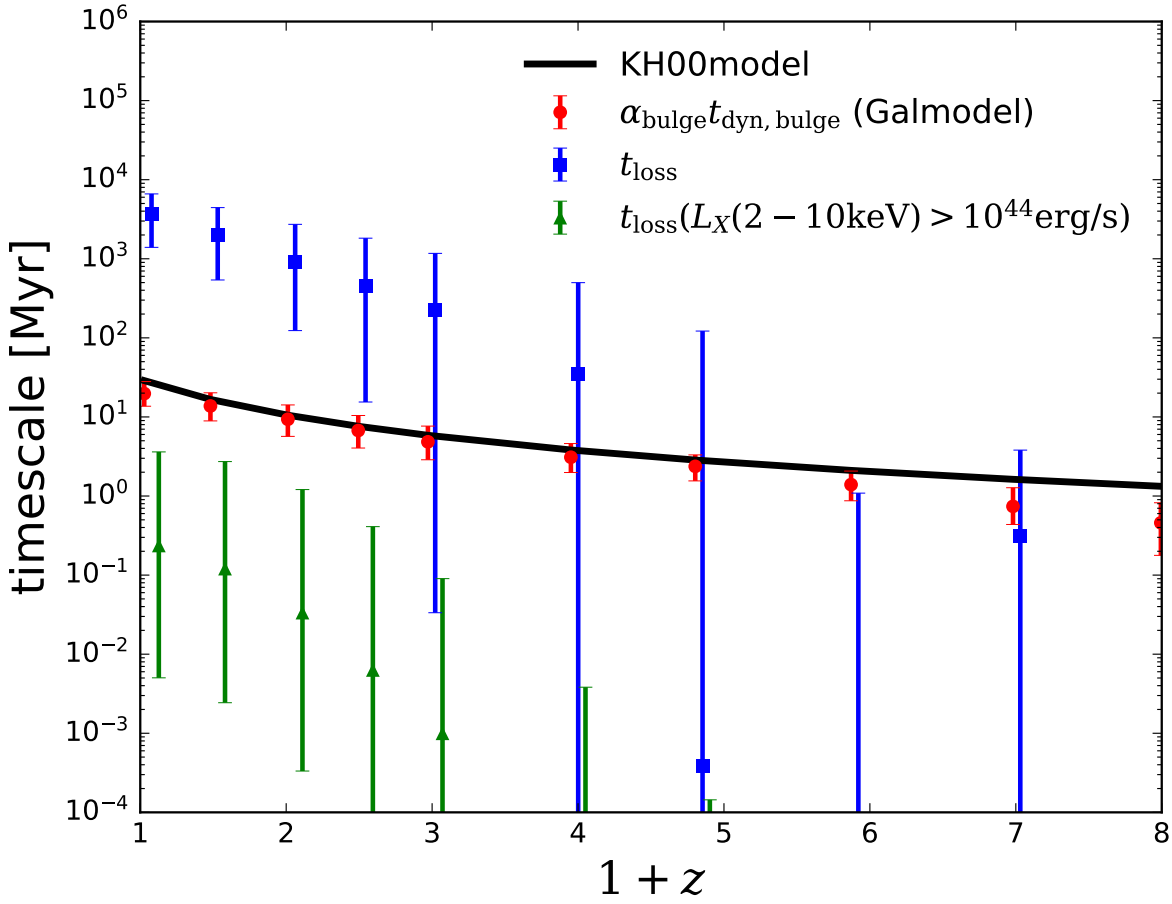

Figure 4.2: The redshift evolution of the accretion timescale with `KH00model`, `Galmodel`, and $t_{\rm loss}$. The black solid line shows the `KH00model`, which corresponds to the dynamical time of haloes. The red circles and blue squares with error bars show the median value of $t_{\rm dyn,bulge}$ and $t_{\rm loss}$ of AGNs with $\log(L_X/{\rm erg\ s^{-1}}) > 41.0$ obtained by the `GalADmodel`. The errorbars are 25th and 75th percentiles. I also show the value of $t_{\rm loss}$ of AGNs with $\log(L_X/{\rm erg\ s^{-1}}) > 44.0$ by green triangles.

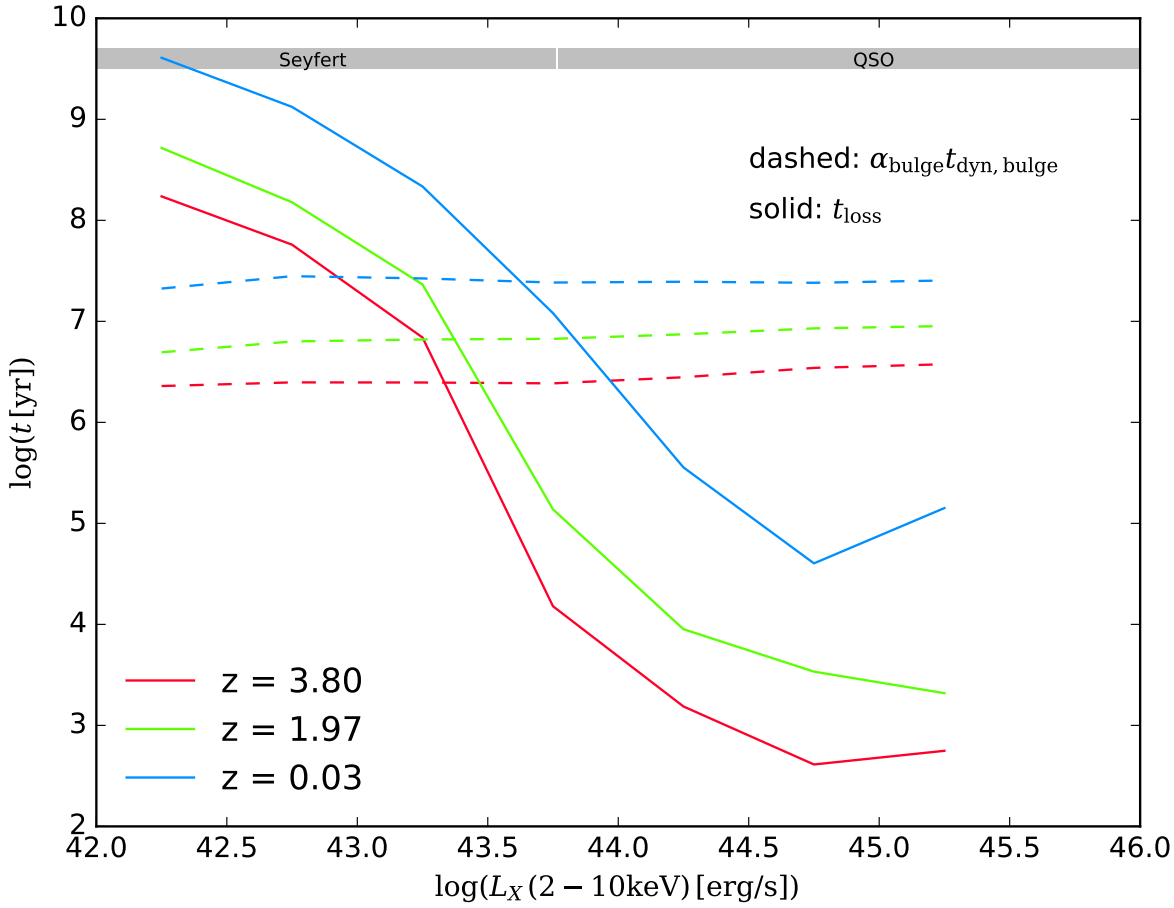

Figure 4.3: The relation between hard X-ray luminosity and two different timescales at $z \sim 0, 2$, and 4 (blue, green, and red lines, respectively) obtained with the `GalADmodel`. Solid and dashed lines describe $t_{\rm loss}$ and $\alpha_{\rm bulge} t_{\rm dyn,bulge}$, respectively.

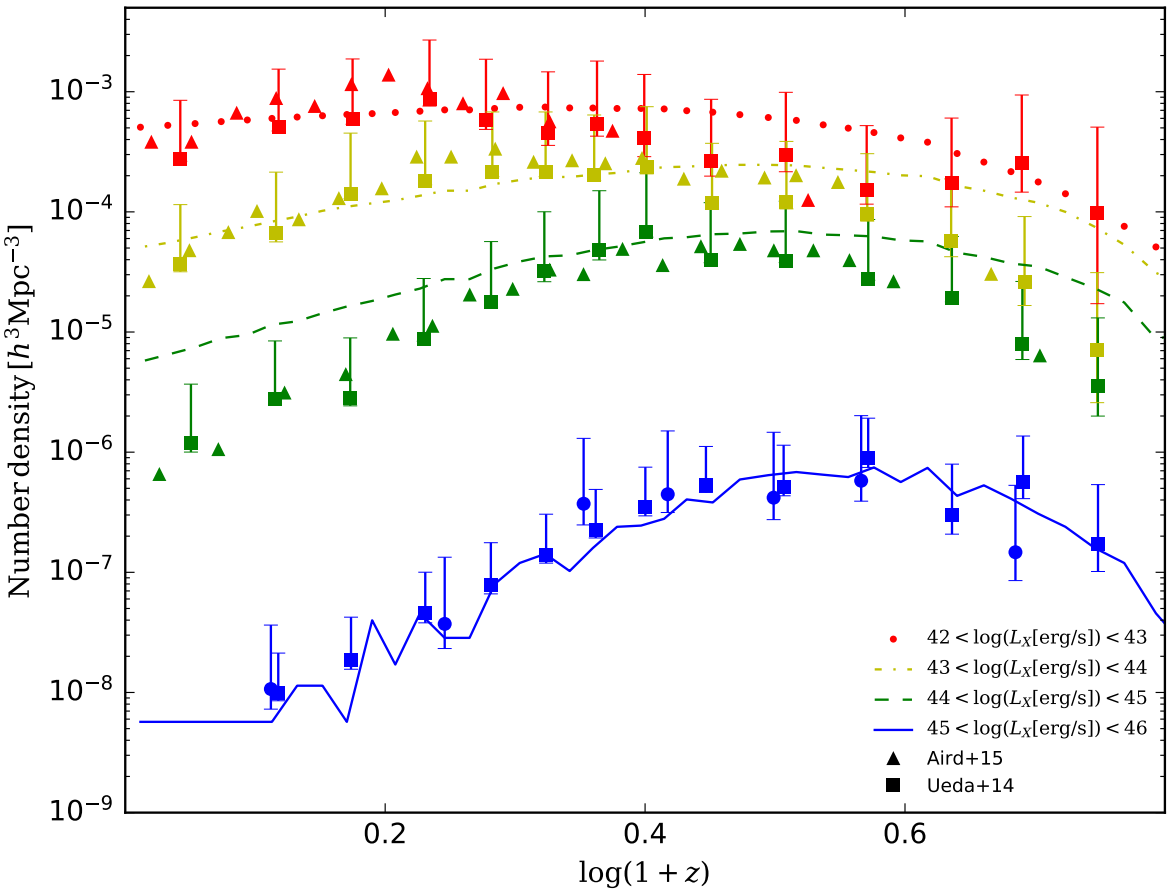

Figure 4.4: The redshift evolution of the AGN number density. Colour describes the luminosity bins ($\log(L_X/\mathrm{ergs}^{-1}) = [42, 43]$; red, $(\log(L_X/\mathrm{ergs}^{-1}) = [43, 44]$; yellow, $(\log(L_X/\mathrm{ergs}^{-1}) = [44, 45]$; green, and $(\log(L_X/\mathrm{ergs}^{-1}) = [45, 46]$; blue). The results obtained with `GalADmodel` are shown with lines. Filled squares with error bars and triangles are observational results (Ueda et al. 2014; Aird et al. 2015; respectively).

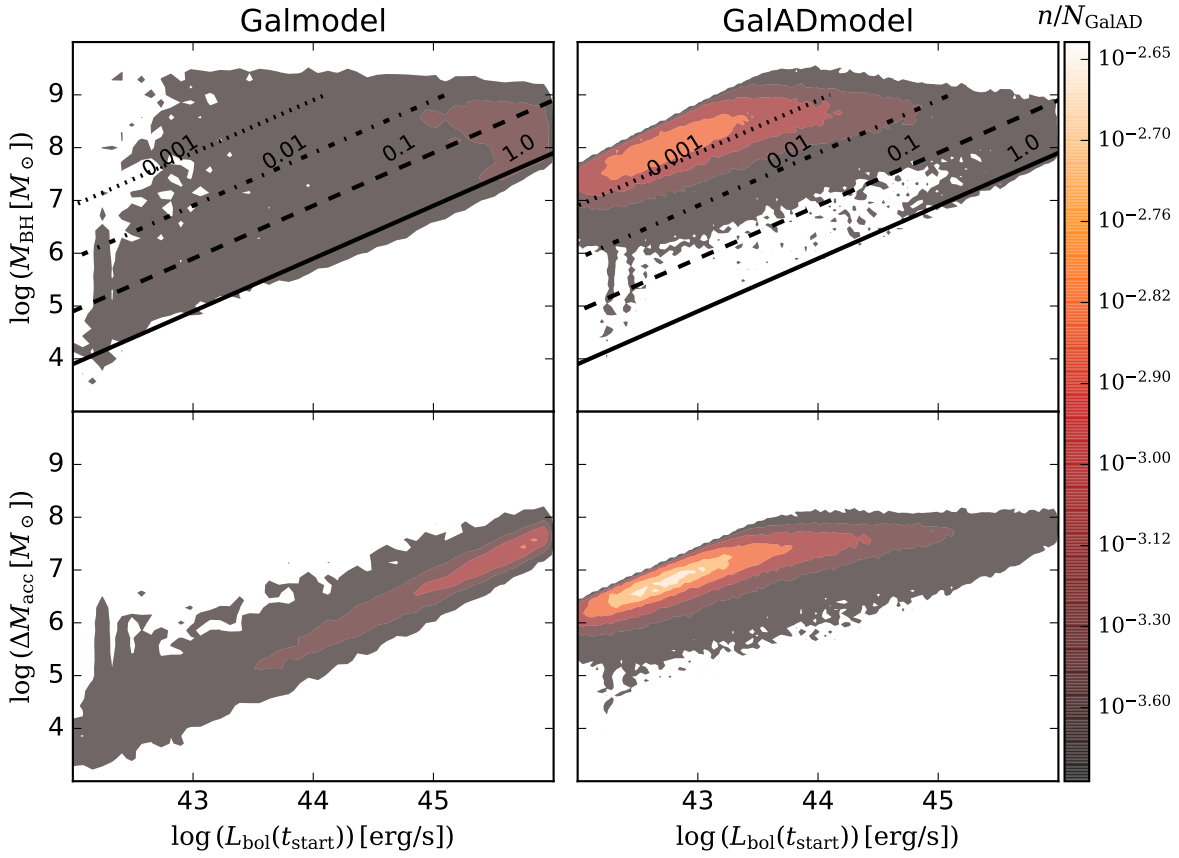

Figure 4.5: The relation between the AGN bolometric luminosity at $t = t_{\rm start}$, $L_{\rm bol}(t_{\rm start})$, and BH mass, $M_{\rm BH}$ (top) and accreted gas mass onto an SMBH, $\Delta M_{\rm acc}$ (bottom) at $z \sim 0$. The distributions are described as density contours, whose value is normalized by the number of total AGNs with `GalADmodel`. Left and right panels show the results obtained with the `Galmodel` and `GalADmodel`, respectively. Black solid, dashed, dot-dashed, and dashed lines show $\lambda_{\rm Edd} = 1, 0.1, 0.01$, and 0.001, respectively.

Fig. 4.5 shows the clear correlation between $L_{\rm bol}(t_{\rm start})$ and $\Delta M_{\rm acc}$ with the `Galmodel` (bottom left panel). Since $t_{\rm dyn,bulge}$ is similar for galaxies at the same redshift (see Fig. 4.2), the peak accretion rate, $\dot{M}_{\rm peak} \equiv \Delta M_{\rm acc}/t_{\rm acc}$, is mainly determined by $\Delta M_{\rm acc}$. The higher peak bolometric luminosity therefore implies a larger amount of the accreted gas. The relation between $L_{\rm bol}(t_{\rm start})$ and $M_{\rm BH}$ with the same model (top left panel) comes from the correlation, $M_{\rm BH} \propto \Delta M_{\rm acc}^{1.1}$.

The correlations obtained by the `GalADmodel` (right panels) show bimodal distributions, which are quite different from the model with the `Galmodel`. The peak accretion rate is proportional to $M_{\rm BH}^{-\gamma_{\rm BH}} \Delta M_{\rm acc}^{1-\gamma_{\rm gas}}$ if $\alpha_{\rm bulge} t_{\rm dyn,bulge}$ is smaller than $t_{\rm loss}$. Since $\gamma_{\rm BH} = 3.5$ and $\gamma_{\rm gas} = -4.0$, $\dot{M}_{\rm peak} \propto M_{\rm BH}^{-3.5} \Delta M_{\rm acc}^{5.0}$. The peak accretion rate, thus, can be written as $\dot{M}_{\rm peak} \propto \Delta M_{\rm acc}^{1.15}$ (or $\propto M_{\rm BH}^{1.05}$). These positive correlations appear as contour peaks at $\log(L_{\rm bol}(t_{\rm start})/{\rm erg\ s^{-1}}) < 44.0$.

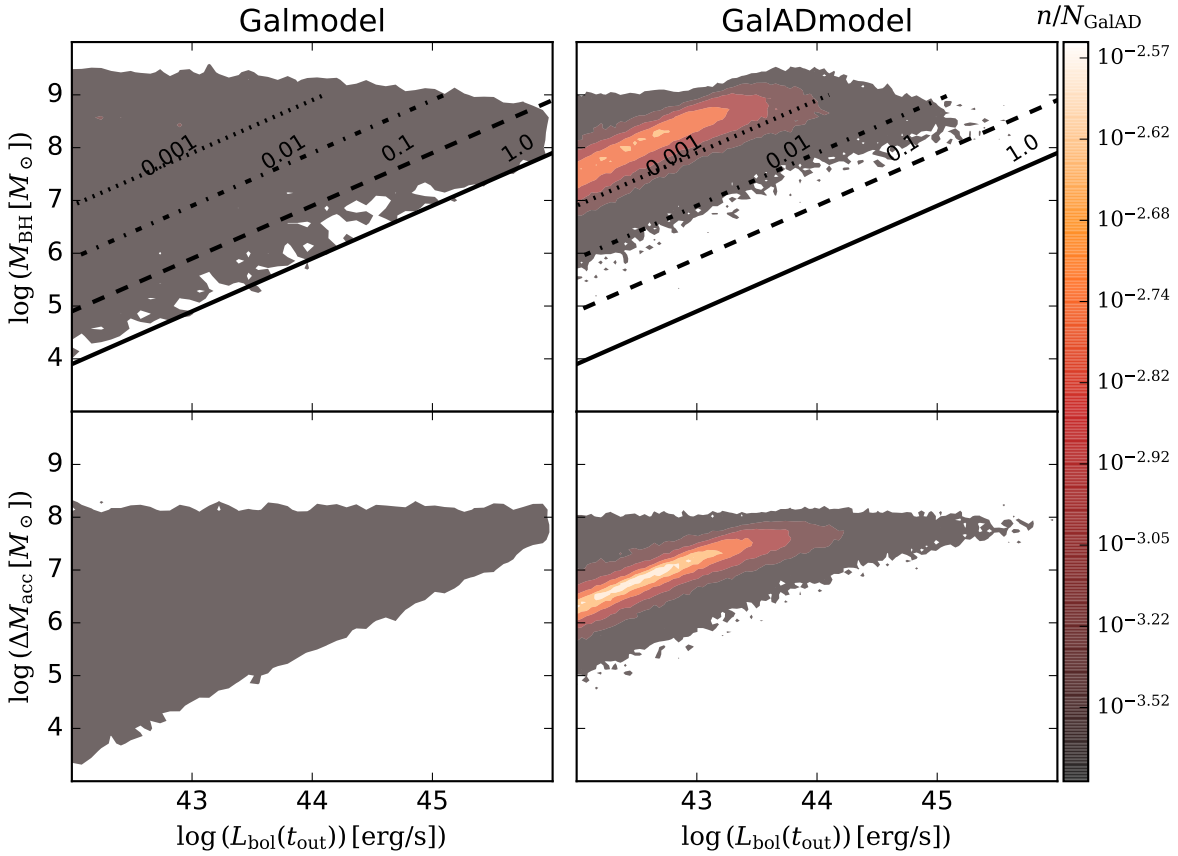

Figure 4.6: The same figure as 4.5 although the x-axis show the AGN bolometric luminosity at output time, $L_{\rm bol}$ instead of $L_{\rm bol,peak}$.

Fig 4.6 shows the same relations as shown in Fig. 4.5, but instead plotting bolometric luminosity estimated at an output time. Since $L_{\rm bol}(t_{\rm start})$ has positive correlations with $M_{\rm BH}$ and $\Delta M_{\rm acc}$ when the `Galmodel` is employed, the dispersions of the correlation between $L_{\rm bol}$ and $M_{\rm BH}$ and $\Delta M_{\rm acc}$ (left panels) reflect the elapsed time from their AGN activity.

The relation between AGN luminosity and SMBH mass allows us to compare theoretical models with observations and to potentially place a stronger constraint on the accretion timescale. There are numerous previous studies which present the relation between AGN luminosities and the SMBH mass at various redshifts (e.g., Schulze & Wisotzki 2010; Nobuta et al. 2012; Ikeda et al. 2017). Schulze & Wisotzki (2010) and Steinhardt & Elvis (2010) show the relation between the bolometric luminosity and the SMBH mass for broad line AGNs at $z < 0.3$ and $0.2 < z < 2.0$, respectively. Since their sample are limited at $\lambda_{\rm Edd} > 0.01$, I cannot distinguish the two models of the accretion timescale. If complete AGN sample with $\lambda_{\rm Edd} > 0.001$ are obtained, I could put a stronger constraint on the accretion timescale.

In Fig. 4.7, I present AGN LFs in $UV-$ band (1450 Å) from $z \sim 6.0$ to 0.0 obtained by the `GalADmodel`. The observable fraction is defined by Eq. 2.51. The results are roughly consistent with observed UV AGN LFs (Croom et al. 2001; 2009; Fan et al. 2001; Richards

et al. 2005; 2006; Fontanot et al. 2007; Siana et al. 2008; Glikman et al. 2011; Fiore et al. 2012; Ikeda et al. 2012; Palanque-Delabrouille et al. 2013; Ricci et al. 2017a; Akiyama et al. 2018), especially at $z > 1.5$. We, however, overproduce UV LFs at lower redshift. In such redshift range, I also overproduce hard X-ray LFs (see Fig. 4.1) compared with the fitting LFs of Aird et al. (2015) although the model LFs are consistent with observed data points within the range of a dispersion. I need to take the dispersion of observed hard X-ray LFs into account for estimating the observable fraction. The UV LFs do not place a strong constraint on the accretion timescale since the observed UV LFs are well determined only at $M_{\rm UV} < -20.8$ (corresponds to $\log(L_X/{\rm erg\ s^{-1}}) > 44.6$) because of the contamination of galaxies' emission (Parsa et al. 2016). The hard X-ray LFs obtained from models with the different assumption of the accretion timescale show little difference at $\log(L_X/{\rm erg\ s^{-1}}) > 44.6$.

I show Fig. 4.8 to show the effect of the timescale on the Eddington ratio distribution function (ERDF). The black solid and dashed lines are results obtained with `GalADmodel` and `Galmodel`, respectively. I select all AGNs with $M_{\rm BH} > 10^6 M_\odot$ and $L_{\rm bol} > 10^{43.5}$ erg/s at $z \sim 0$. The results at $\log(\lambda_{\rm Edd}) > -1.5$ are roughly consistent with that obtained by the observation (Schulze & Wisotzki 2010) at $z \sim 0.3$. We, however, note that it is difficult to compare model ERDFs with observations since (1) optical observational sample is limited in type-1 AGNs with well-estimated SMBH mass, (2) SMBH masses of X-ray AGNs are simply estimated from e.g., the BH mass – stellar mass relation, (3) observational sample seems to be incomplete for less massive SMBHs, and (4) the obscured fraction of AGNs would depend on both their luminosity and Eddington ratio (e.g. Oh et al. 2015; Khim & Yi 2017). Also, if there is an obscured growing phase before visible AGN phase suggested by, e.g. Hopkins et al. (2005), then the super-Eddington accreting phase should be preferentially missed.

Fig. 4.8 clearly show the difference caused by the implementation of the accretion timescale. The `GalADmodel` increases the number of AGNs with $\log(\lambda_{\rm Edd}) < -1.5$ and the difference between the two models becomes larger at smaller Eddington ratio. I find that the `GalADmodel` and `Galmodel` have no difference for active BHMF with AGNs $M_{\rm BH} > 10^6 M_\odot$, $L_{\rm bol} > 10^{43.5}$ erg/s, and $\lambda_{\rm Edd} > 0.03$ (roughly similar selection as that of Schulze & Wisotzki 2010). As I can expected from AGN LFs (Fig. 4.1), the ERDFs at $z > 1.0$ also have little difference between the `GalADmodel` and `Galmodel`. The evolution of the Eddington ratio appears in Sec 5

4.3.3 Triggers of the gas supply from host galaxies

Fig. 4.9 shows the fraction of AGN host galaxies at $0.0 < z < 7.0$ in each luminosity bin, divided by triggering situations. I classify the galaxies by the mass ratio of the merging galaxies; major (mass ratio $> 0.7 = f_{\rm major}$; blue dash dotted line), intermediate ($0.4 - 0.7$; green dotted line), and minor (¡ 0.4; red solid line). The grey dashed line shows the fraction of AGNs triggered only by a disc instability. For merger-driven AGN activities, the typical merging mass ratio becomes larger for more luminous AGNs. Interestingly, I find that the primary trigger of AGNs at $z < 4.0$ is mergers of galaxies, although, at higher redshift, disc instabilities become essential for less luminous AGNs. This result is inconsistent with Fanidakis et al. (2012) and Griffin, Lacey, Gonzalez-Perez, del P. Lagos, Baugh & Fanidakis (Griffin et al.), who suggest that disc instabilities and "hot halo mode accretion" are dominant triggering mechanisms of AGNs even at $z < 4.0$. As I described in Sec. 2.4.2, I employ the smaller $\epsilon_{\rm DI,crit}$ for reproducing the properties of star formation galaxies at $z > 4$. Also, I

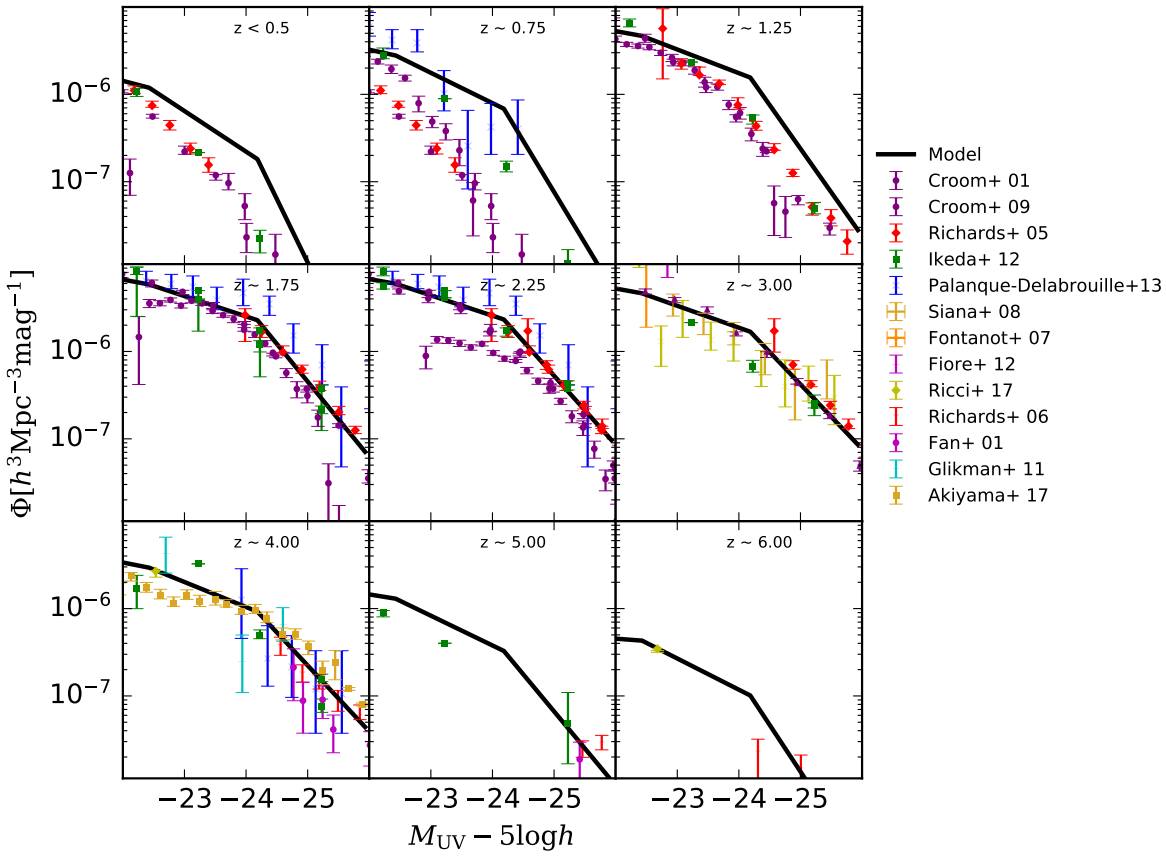

Figure 4.7: AGN LFs in UV- band(1450 Å) at $z < 0.5$, $z \sim 0.75$, $z \sim 1.25$, $z \sim 1.75$, $z \sim 2.25$, $z \sim 3.00$, $z \sim 4.00$, $z \sim 5.00$, and $z \sim 6.00$. The model LFs (volume-weighted) obtained with the ν^2GC -M simulation appear in black solid lines. Observational results are obtained from Croom et al. (2001), Croom et al. (2009), Fan et al. (2001), Richards et al. (2005), Richards et al. (2006), Fontanot et al. (2007), Siana et al. (2008), Glikman et al. (2011),Fiore et al. (2012), Ikeda et al. (2012), Palanque-Delabrouille et al. (2013), Ricci et al. (2017a), and Akiyama et al. (2018).

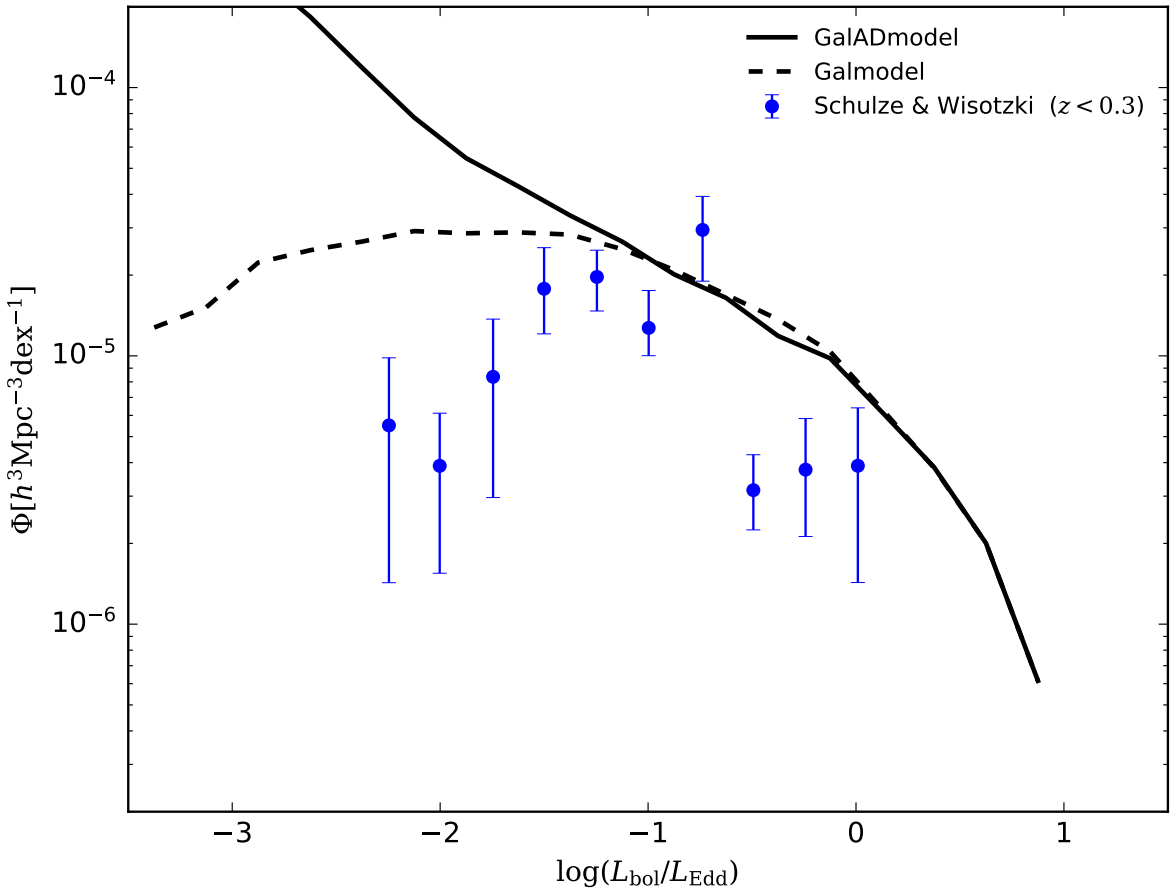

Figure 4.8: The ERDFs at $z \sim 0$ obtained with `GalADmodel` and `Galmodel` (black solid and dashed lines, respectively). In both models, AGNs with $M_{\mathrm{BH}} > 10^6 M_\odot$ and $L_X > 10^{43}$ erg/s are selected. Also, I compare the results with that obtained by Schulze & Wisotzki (2010) at $z \sim 0.3$ (blue filled circles with error bars).

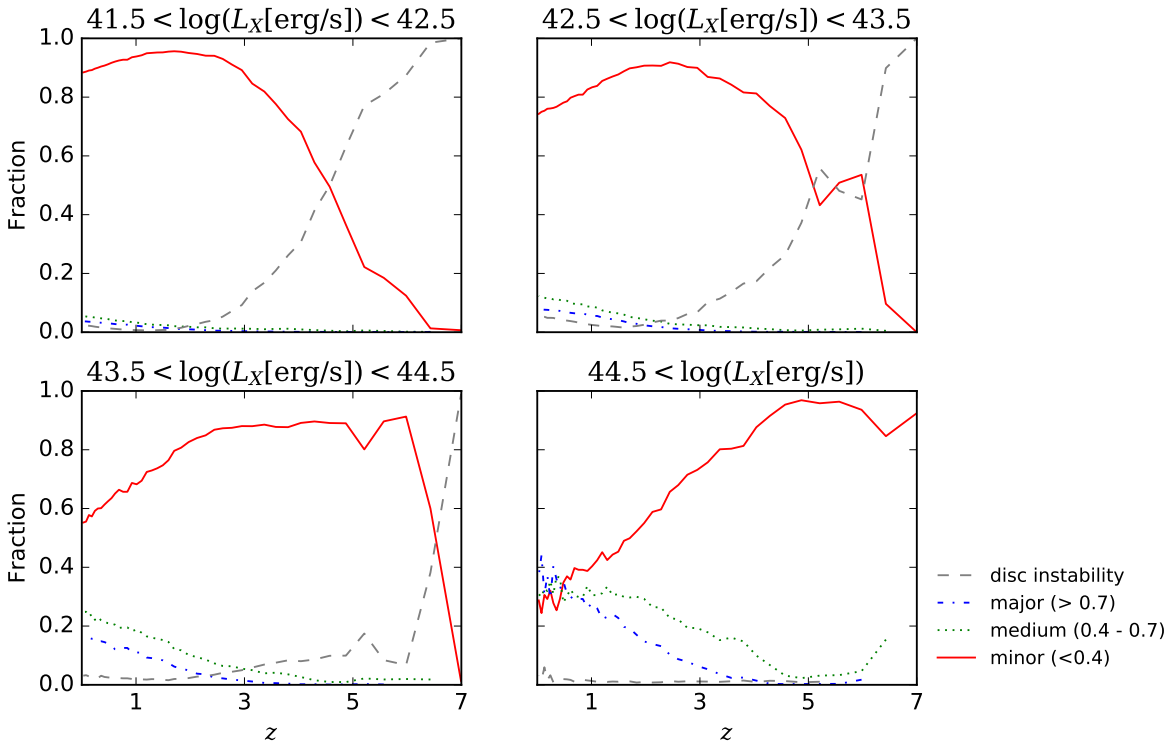

Figure 4.9: Fraction of the AGN host galaxies whose AGN activity is triggered by mergers of galaxies or disc instabilities. I pick out AGNs (in ν^2GC -M box) with $\log(L_X/\mathrm{ergs}^{-1}) = [41.5, 42.5]$, [42.5, 43.5], [43.5, 44.5], and > 44.5. Mergers are classified according to the mass ratio of merging galaxies: > 0.70 (major, blue dash dotted), between 0.4 and 0.7 (middle, grean dotted) and < 0.4 (minor,red solid). I also show the fraction of AGNs triggered only by the disc instability (grey dashed).

consider the effect of the bulge potential on the stability of galactic discs. With this effect, the number of disc-unstable galaxies becomes 60 % smaller at $z \sim 1$ with $\epsilon_{\mathrm{DI,crit}} = 0.75$. These are why our model suggests such low efficiency of disc instabilities as a triggering mechanism. The critical point is that *the observed number density of AGNs can be sufficiently reproduced at $z < 4$ only by mergers of galaxies, and the importance of disc instabilities and other processes should be investigated in more detail.* Our model predicts disc instabilities drive only less than 20% of AGNs at $z \sim 0$. I will come back this topic in Sec. 4.4.

4.4 Discussion

I have presented the latest results of an updated version of an SA model, ν^2GC. The most important changes are related to the bulge and SMBH growth model. I assume that the gas accretion onto the SMBH and the bulge growth are triggered by mergers of galaxies and disc instabilities. For bulge and SMBH growths by mergers of galaxies, I employ a phenomenological model proposed by Hopkins et al. (2009a), whose model is based on results

of hydrodynamic simulations. Along with this revision, I have also updated the way of calculating the velocity dispersion and size of bulges when bulges grow via minor mergers. For bulge and SMBH growths by disc instabilities, I employ a classical model originally proposed by Efstathiou et al. (1982). I consider the effect of the bulge potential on the gravitational stability of the disc.

I have investigated the effect of the accretion timescale on statistical properties of AGNs, such as their LFs. I stress that the impact of the accretion timescale especially for low luminosity ($L_X < 10^{44}$ erg/s) AGNs has been almost neglected in previous SA models. When I assume that the accretion timescale is proportional to the dynamical time of the host halo or the host bulge, as in the previous SA models, the number density of the low luminosity AGNs is one order of magnitude smaller than observational estimates. I have found that the number density of such less luminous AGNs becomes consistent with the observational data when I take a phenomenological and physically-motivated model for the timescale of the angular momentum loss in the circumnuclear torus and/or the accretion disc into account. The `GalADmodel` predicts that low luminosity AGNs at $z < 1.0$, such as local Seyfert-like AGNs, are mainly triggered by minor mergers. The contribution of disc instabilities is only less than 20 %.

Previous studies with SA models solve the inconsistent number density of less luminous AGNs by considering other AGN triggering mechanisms such as "efficient" disc instabilities (e.g. Hirschmann et al. 2012), fly-by interactions of galaxies (e.g. Menci et al. 2014), and the direct gas accretion from the hot halo (e.g. Fanidakis et al. 2012; "hot halo mode"). Hirschmann et al. (2012) suggest the importance of disc instabilities as a triggering mechanism of less luminous AGNs. We, however, have to note that the phenomenological modelling of disc instabilities in SA models would be too simple and is not supported by numerical simulations (see Athanassoula 2008). I have tried to make more physically reasonable modelling of disc instabilities in this thesis. For the first step, I include the stabilising effect by the bulge component and take smaller $\epsilon_{\rm DI}$ (Sec. 2.4.2). I then find that disc instabilities are not the main contributor to AGN triggering mechanisms. As another point, some SA models (e.g. Fanidakis et al. 2012; Griffin, Lacey, Gonzalez-Perez, del P. Lagos, Baugh & Fanidakis Griffin et al.) assume that a disc instability destroys a galactic disc entirely and all the gas is exhausted by a starburst forming a spheroidal galaxy just as major mergers. By these two effects (ignoring bulge potential and the complete destruction of a disc), some SA models are likely to overproduce the number density of AGNs induced by disc instabilities. Further updates are necessary to conclude that disc instabilities play a crucial role for the SMBH growth. Menci et al. (2014) suggest that fly-by interactions are important instead of disc instabilities. Although I do not introduce fly-by interactions, the random collision of galaxies may have similar effects. The "hot halo mode" (Fanidakis et al. 2012; Griffin, Lacey, Gonzalez-Perez, del P. Lagos, Baugh & Fanidakis Griffin et al.) is the same as our "radio mode" AGN feedback model, both of which are based on Bower et al. (2006). In our fiducial models, I do not calculate the AGN luminosity with this mode because the bolometric correction and the radiative efficiency are unclear. When I assume the same bolometric correction as that of QSOs, and the radiative efficiency is 0.1, the contribution of the radio mode AGN to the AGN LFs becomes the same order as that of AGNs induced by mergers of galaxies and disc instabilities at $L_X \sim 10^{41}$ erg/s at $z \sim 0$. The contribution becomes smaller at more luminous regime and at higher redshift. Our results based on the timescales show that observed AGN LFs can be reproduced without "radio mode" or "hot halo mode" accretions. Even without

the "radio mode" AGN feedback, `GalADmodel` produces a large number of AGNs with low Eddington ratios, which would be AGN jet and outflow sources. Considering the injected energy and momentum from the low Eddington ratio AGNs, they may have non-negligible impact on the star formation quenching of massive galaxies. I will examine which explanation is more plausible in a future study.

Marulli et al. (2008) suggest the importance of AGN light curve for determining the shape of AGN LFs. They assume three types of the Eddington ratio evolution models based on observations and hydrodynamical simulations. The faint end slope of AGN LFs at $z < 1.0$ are well fitted when they assume the constant Eddington ratio, namely, $= 0.3[(1+z)/4]^{1.4}$ at $z < 3$, and $= 1$ at $z > 3$. By using this Eddington ratio, the accretion timescale should be ~ 0.17 Gyr at $z \sim 0$, which is larger than the dynamical time of bulges (Fig. 4.2) and is qualitatively consistent with our suggestion. However, the model with this assumption of the constant Eddington ratio underestimates the number density of luminous AGNs at $z > 1$. They also introduce introduce AGN light curve with two stages; rapid, Eddington-limited growth phase, and longer quiescent phase with lower Eddington ratios. By using this light curve, the accretion timescale should be longer when the SMBH mass is smaller or the accreted gas mass is larger, which is the opposite to that suggested in the `GalADmodel`. The resulting faint end slope of AGN LFs at $z < 1$ is shallower than observations. They cannot explain the shape of the AGN LFs by changing just the Eddington ratio distribution. Finally they introduce SMBH mass dependency to the $f_{\rm BH}$ and successfully reproduce AGN LFs at $z < 5$.

Hydrodynamic simulations (e.g. Sijacki et al. 2015; Khandai et al. 2015; Hirschmann et al. 2014) do explain AGN LFs well, assuming Bondi-Hoyle-Littleton (BHL) accretion for all SMBH growths. Generally, hydrodynamic simulations assume that the "effective" accretion rate onto SMBHs is roughly 200 times larger than the BHL accretion rate, which is too small compared to that of observed AGNs (e.g. Ho 2009). The assumption of the accretion rate with ~ 200 times larger than the BHL accretion, independent of any properties of galaxies and SMBHs, might be a too simplified assumption. Besides, I must care about another uncertainty; different AGN feedback models are employed in different cosmological simulations, which reproduce AGN LFs at the same extent.

As I have shown, there are several prescriptions to explain the faint end slopes of AGNLFs at $z < 1$. For discriminating the models, comparisons of model results with observed properties of AGNs and their host galaxies are necessary. I have shown the relation between $M_{\rm BH}$ and L_X (Figs. 4.5 and 4.6,) the ERDF at $z \sim 0.3$ (Fig. 4.8), and the fraction of AGNs with different triggering mechanisms (Fig. 4.9). Since the difference between the `Galmodel` and `GalADmodel` is clear for low luminosity AGNs with the smaller SMBH masses, the comparisons with observations are challenging. The other possible way would be comparing the clustering properties with observations. Fanidakis et al. (2013) suggest that the host halo mass of luminous AGNs like QSOs and low luminosity ones is different. In their model, luminous AGNs are triggered by starbursts induced by mainly disc instabilities (and mergers of galaxies) and their typical host halo mass is $\sim 10^{12} M_\odot$. Low luminosity AGNs, on the other hand, are triggered mainly "hot halo mode" and their halo mass is larger than those of luminous AGNs, namely $\sim 10^{13} M_\odot$. The "hot halo mode" is efficient for cluster galaxies whose host halo is cooling inefficient. On the other hand, Oogi et al. (2016) suggest that when they assume AGNs are mainly triggered by mergers of galaxies, the host halo mass weakly depends on the AGN luminosities at $1 < z < 4$. The `GalADmodel` also shows the same trend as Oogi et al.

(2016) at $1 < z < 4$. We, thus, can discriminate effects of the accretion timescale and AGN triggering mechanisms by detailed comparisons with observational results. Also, statistical studies with archival data of observations might enable to estimate the fraction of AGNs triggered by minor mergers by using methods developed by Barrows et al. (2016). They use kinetic offsets between the stellar core and AGNs evaluated from emission lines such as Hβ. When the line emissions peak at different wavelength (i.e. have offset), this galaxy is classified as merging galaxy (examples are shown in Barrows et al. (2018)). In addition, the merging mass ratio of galaxies would be available from H-band images. By this analysis, we could detect galaxies in late-merger stages although only early stages (i.e. galaxy separation is large: more than 10 kpc) of "major" mergers can be detected with optical imaging observations.

One might think that the underproduction of less luminous AGNs results from the underestimation of the velocity dispersion of the bulge and/or the underestimation of the cold gas mass in galaxies. As shown in Fig. 2.9, the velocity dispersion of the bulge tends to be smaller than those obtained from observations, although the bulge size is broadly consistent with the observational data at $z \sim 0$ (Fig. 2.10). The dynamical time of the bulge evaluated in the fiducial model is statistically longer than the value estimated from the observed velocity dispersion and bulge size. I thus underestimate the gas accretion rate onto SMBHs since the peak accretion rate is proportional to $t^{-1}_{\rm dyn,bulge}$. In addition, low mass galaxies in the model seem to have smaller gas masses than observed galaxies (Fig. 2.6) due to the insufficient resolution, which could also cause the underestimation of the gas accretion rate. In Fig. 4.10, I check these effects and find that both are insufficient to compensate the underproduction of the less luminous AGNs. I compare hard X-ray LFs at $z \sim 0$ obtained by the following three models: (1) the `Galmodel` with the ν^2GC -SS simulation (black solid line), (2) the `Galmodel` with the ν^2GC -H2 simulation (black dotted line), and (3) the model with $t_{\rm acc} = 0.2 \times \alpha_{\rm bulge} t_{\rm dyn,bulge}$ (black dashed line). The number density of AGNs obtained by the model (3) becomes smaller than that obtained by the model (1) since $t_{\rm dyn,bulge}$ is set to be smaller, and the AGN activity shut off sooner. Also, I find no effect of the gas deficiency by comparing (1) and (2), while the number of galaxies with $M_{HI} < 10^8 M_\odot$ increases when I employ the ν^2GC -H2 simulation. The comparison (1) and (2), therefore, suggests the gas deficiency is not the cause of the underestimation of the abundance of the less luminous AGNs. Even at $z \sim 1$, the model (3) does not solve the inconsistency of the faint-end slope since the shorter accretion timescale causes the shallower slope. I have confirmed that the faint-end slope of the AGN LF at $z \sim 1$ also does not change with model (3). I conclude the underestimation of the gas mass of galaxies is not a primary cause of the underestimation of the number density of faint AGNs.

Another problem of the AGN LFs obtained with the ν^2GC is that there are no AGNs with $\log(L_X/{\rm erg\ s^{-1}}) > 45.3$ at $z > 2.6$. Such luminous AGNs do not appear even when I employ N-body simulations with larger volumes. The modelling of the radio-mode AGN feedback is likely to be responsible for this, which was originally proposed by Bower et al. (2006) and is similar to other SA models. Host halo masses of AGNs with $\log(L_X/{\rm erg\ s^{-1}}) \sim 45.0$ at $z \sim 4$ in the fiducial AGN model are $10^{12-13} M_\odot$. Such massive haloes could satisfy conditions of Eqs. 2.48 and 2.49 and the gas cooling is quenched even at high redshifts. This is shown in Fig. 4.11, which shows the fraction of galaxies whose gas cooling is quenched by the radio-mode AGN feedback. I find that about the half of galaxies are quenched when $M_{\rm halo} > 10^{12.5} M_\odot$ at $z \sim 4$.

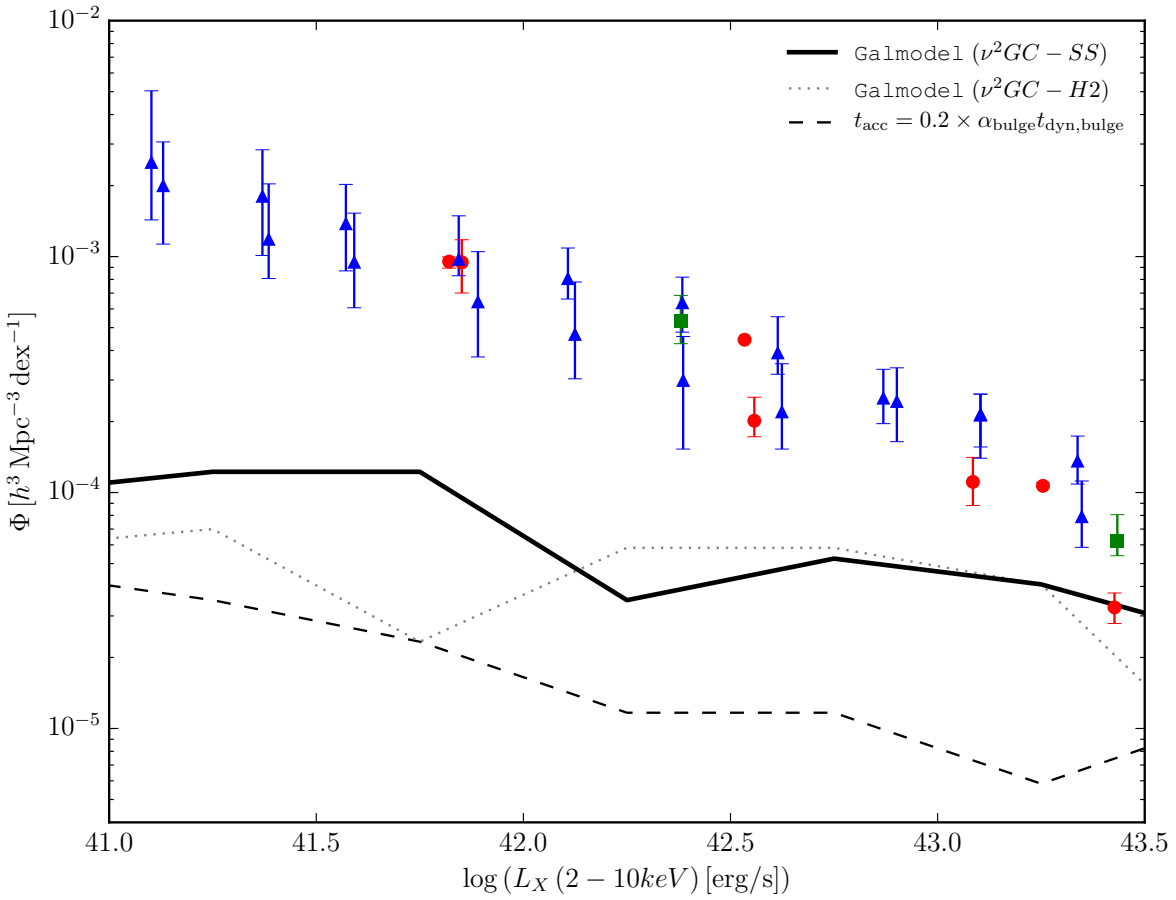

Figure 4.10: AGNLFs at $z \sim 0$. To check the effect of the determination of $t_{\rm dyn,bulge}$ and the accreted gas mass, I compare three models: (1) the `Galmodel` with the ν^2GC -SS simulation(black solid line), (2) the `Galmodel` with the ν^2GC -H2 simulation (black dotted line), and (3) the model in which $t_{\rm acc} = 0.2 \times \alpha_{\rm bulge} t_{\rm dyn,bulge}$ (black dashed line). Observational results is the same as the top left panel of Fig. 4.1.

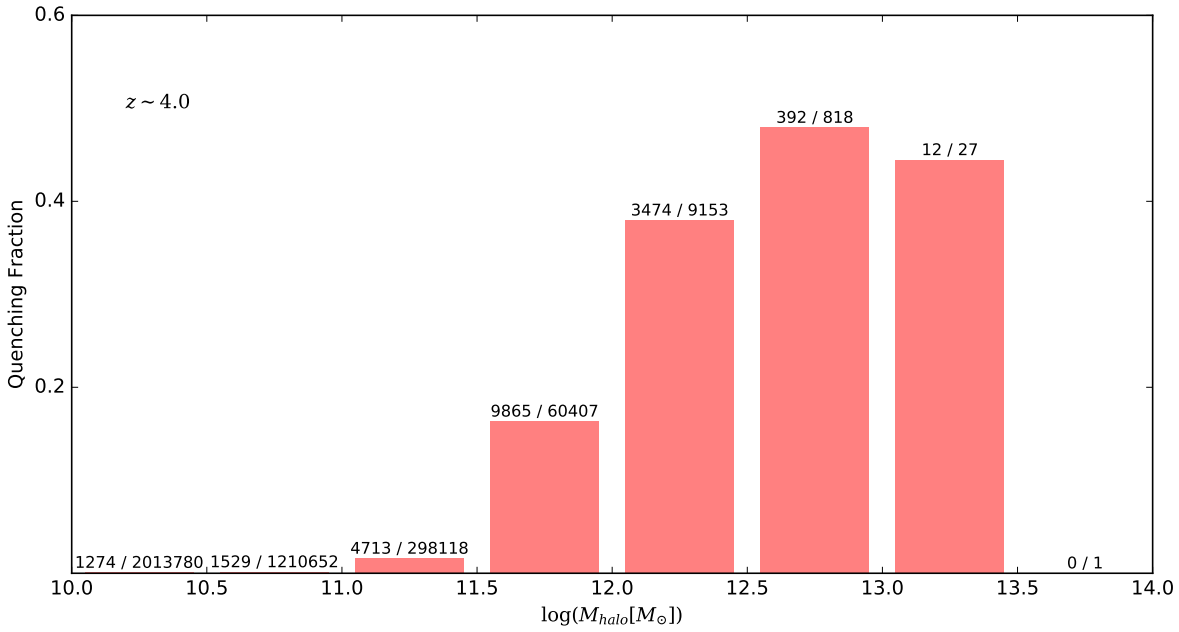

Figure 4.11: The fraction of central galaxies whose gas cooling is shut off the by radio-mode AGN feedback at $z \sim 4$. The x axis is the host halo mass of the galaxies. The number means $[Quenchedhalo]/[Totalhalo]$.

Chapter 5

Theoretical predictions of the ERDFs

I show the Eddington ratio distributions of SMBHs at a wide redshift range ($0 < z < 8$) obtained with the SA model. The distribution is broadly consistent with observational estimates at low redshift. I find that the growth rate of BHs at higher redshift is more likely to exceed the Eddington limit because the typical gas fraction of the host galaxies is higher at higher redshift. I also find that the super-Eddington growth is more common for less massive SMBHs, supporting an idea that SMBHs have grown via super-Eddington accretion. These results indicate the "slowing-down" of cosmic growth of SMBHs: the SMBH growth with a higher Eddington ratio peaks at higher redshift. I also show the effect of the sample selection on the shape of the ERDFs and find that shallower observations will miss AGNs with not only the smaller but also higher Eddington ratios. In this chapter, I present the topical introduction in Sec. 5.1, and the obtained results in 5.2. Finally, I show the additional predictions about the Eddington ratio in Sec. 5.3. The model and values of free parameters employed in this study are the same as those in 4.

5.1 Introduction

Sołtan (1982) find that the number density of local SMBHs is explained by integrating LFs of QSOs (i.e. the brightest class of AGNs) with the radiation efficiency, $\eta \equiv L_{\rm bol}/\dot{M}_{\rm BH}c^2 \sim 0.1$ ($L_{\rm bol}$ is the bolometric luminosity of AGNs). This argument also includes the important suggestion for the SMBH growth: the "super-Eddington growth" is not required. The accretion rate normalised by the Eddington accretion rate, $\dot{m}$, affects the properties of the accretion discs and determines the value of η because the structure and temperature distribution of the accretion discs depends on $\dot{m}$. The value of $\eta \sim 0.1$ is for the standard accretion disc (Shakura & Sunyaev 1973) with a sub-Eddington accretion, while a super-Eddington accretion ($\dot{m} \gg 10$) results in a much smaller η (Abramowicz et al. 1988). The Sołtan's argument and updated results later on (e.g. Yu & Tremaine 2002), thus, suggest that local SMBHs have grown mainly via sub-Eddington accretions.

However, based on observed accretion rates and inferred durations of super-Eddington AGNs together with the observed trend of higher Eddington ratios at higher redshift (McLure & Dunlop 2004), Kawaguchi et al. (2004b) argue that SMBHs have grown via super-Eddington

accretion in the early Universe. The number density of QSOs at the "knee" of the QSO LFs mostly governs the integrated energy density. The magnitude at the knee corresponds to about $10^{8-9} M_\odot$, assuming that all AGNs radiate at the Eddington luminosity. Therefore, the Sołtan's argument seems not to reject the super-Eddington growth of SMBHs with $M_{\rm BH} \lesssim 10^8 M_\odot$ and the contribution of the super-Eddington accretion for the cosmic growth of less massive SMBHs, which are the majority of SMBHs, is unclear.

Estimations of the ERDFs based on observational data suffer severely from a flux-limit, a matter of completeness, and a priori assumptions (e.g. log-normal distribution of ERDFs). For instance, ERDFs at $z = 2.15$ estimated by Kelly & Shen (2013; hereafter KS13) have a $\pm 1\sigma$ uncertainty in the number density for a given $L_{\rm bol}/L_{\rm Edd}$ of more than 2 dex. Despite the difficulties for obtaining the Eddington ratio, observations reveal the evolution of the ERDFs and relations between Eddington ratio and properties of the AGNs and their host galaxies. KS13 estimate the "growth timescale" defined as $t_s \ln(M_{\rm BH}/M_{\rm seed})/[10\eta E(L_{\rm bol}/L_{\rm Edd} \mid M_{\rm BH}, z)]$, where $t_s, M_{\rm seed}$, and $E(L/L_{\rm Edd} \mid M_{\rm BH}, z)$ are the Salpeter time, the seed BH mass and the mean value of $L_{\rm bol}/L_{\rm Edd}$ at a fixed $M_{\rm BH}$ and z, respectively, and $\eta = 0.1$ and $M_{\rm seed} = 10^6 M_\odot$. They find that the timescale for type-1 QSOs with $M_{\rm BH} > 5 \times 10^8 M_\odot$ at $z > 1.8$, is comparable to or longer than the age of the Universe, which suggests that such an SMBH population would have grown with the higher Eddington ratio at higher redshift. Indeed, recent observations find QSOs at $z > 6$ with $M_{\rm BH} > 10^8 M_\odot$ which are growing at $\lambda_{\rm Edd} \equiv L/L_{\rm Edd} \gtrsim 1$ (Mortlock et al. 2011; Wu et al. 2015; Bañados et al. 2018). Other observations (e.g. Nobuta et al. 2012; Shen & Kelly 2012; Lusso et al. 2012; Bongiorno et al. 2016; Aird et al. 2018) also show the Eddington ratio becomes higher at higher redshift.

Previous theoretical studies for the formation of galaxies and SMBHs (i.e. cosmological simulations and semi-analytic models of galaxy formation; hereafter SA models) also investigate the evolution of the ERDFs and find that super-Eddington growth is more common for SMBHs at higher redshift (e.g. Hirschmann et al. 2014; Sijacki et al. 2015). Furthermore, Menci et al. (2014) investigate how the ERDFs depend on the triggering mechanisms of AGN activities.

The contribution of the super-Eddington accretion to the cosmic growth of SMBHs is important to discuss the mass of seed BHs. Observations have found luminous quasars at $z > 6$, of which SMBH masses estimated as $> 10^9 M_\odot$ (e.g. Mortlock et al. 2011; Wu et al. 2015; Bañados et al. 2018). There are three possibilities for explaining the existence of such massive SMBHs in the early Universe: (1) their seed BH masses are large, namely, $> 10^5 M_\odot$, (2) their seed BHs are small ($10^{1-3} M_\odot$) and formed soon after the birth of the Universe, and then grow continuously with Eddington-limited accretion, and (3) their seed BHs are small ($10^{1-3} M_\odot$) and grow via super-Eddington accretion. However, "heavy seed BHs" should form only in special conditions (e.g. Omukai et al. 2008) and thus such "heavy seed BHs" should not be dominant (see also Shirakata et al. 2016). Although the formation time of the seed BH of SMBHs with $> 10^9 M_\odot$ at $z > 6$ is unclear, the super-Eddington growth might play a key role in the early growth of SMBHs since the typical Eddington ratio becomes higher at higher redshift (Wu et al. 2015).

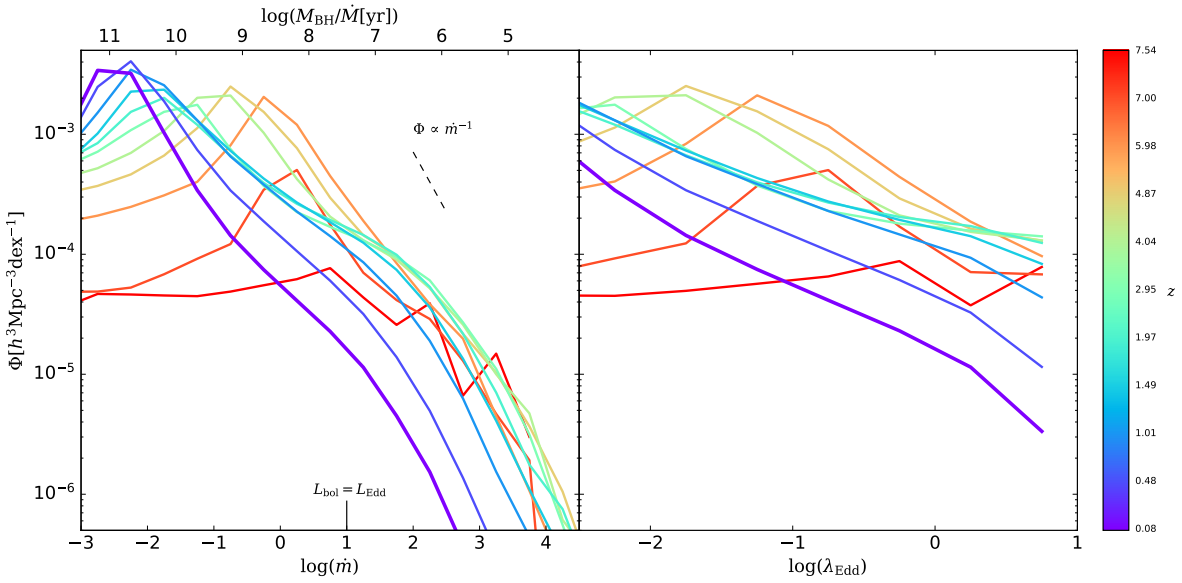

Figure 5.1: ERDFs of all AGNs obtained with the fiducial model. Left and right panels show the distribution of $\dot{m}$ and $\lambda_{\rm Edd}$, respectively. Colors describe redshifts ($0.0 < z < 8.0$). The black dashed line in the left panel shows the critical slope: $\Phi \propto \dot{m}^{-1}$. The thick solid lines describe the ERDF at $z \sim 0.08$. The growth timescale, $M_{\rm BH}/\dot{M}$, also appears in the left panel. The values of Φ monotonically increases from $z \sim 0.08$ to 5.98 with a similar shape and decreases at higher redshift with a flatter slope at $\log(\dot{m}) = 1$ and $\log(\lambda_{\rm Edd}) = 0$.

5.2 Results

5.2.1 Theoretical predictions

In Fig. 5.1, I show the ERDFs at $0.0 < z < 8.0$ with the fiducial model. The ERDF is defined as $\Phi = dn(z, \log \dot{m})/d\log(\dot{m})$, or $\Phi = dn(z, \log \lambda_{\rm Edd})/d\log(\lambda_{\rm Edd})$, which is the number density with a fixed $d\log(\dot{m})$ or $d\log(\lambda_{\rm Edd})$. The left and right panels show the distribution of $\dot{m}$ and $\lambda_{\rm Edd}$, respectively, for all AGNs (i.e. $M_{\rm BH} \geq M_{\rm seed}$ and $L_{\rm bol} > 0$). The bolometric luminosity corresponds to the Eddington luminosity when $\dot{m} = \dot{m}_{\rm crit}$. The dashed line in the left panel indicates a critical slope ($\Phi \propto \dot{m}^{-1}$) at which the gas accretion with different $\dot{m}$ contributes to SMBH growth equally (i.e. $\Phi\ \Delta\dot{m} = \Phi\ \dot{m}\ \Delta\log(\dot{m})$). The thick solid lines describe the ERDFs at $z \sim 0.08$. The values of Φ monotonically increases from $z \sim 0.08$ to 5.98 with a similar shape and decreases at higher redshift with a flatter slope at $\log(\dot{m}) = 1$ and $\log(\lambda_{\rm Edd}) = 0$. The slope of the ERDFs becomes shallower at higher redshift, meaning that the relative number of AGNs with higher Eddington ratio increases at higher redshift. Upper label in Fig. 5.1 shows SMBH growth timescale, $M_{\rm BH}/\dot{M}$. If the growth timescale is shorter than the age of the Universe at a given redshift, then the SMBH can acquire their mass by gas accretion until that redshift without requiring heavy (i.e. $\gtrsim 10^5 M_\odot$) seed BH. Thanks to the super-Eddington accretion, SMBHs can grow much faster than $M_{\rm BH}/(10\dot{M}_{\rm Edd}) \sim 30$ Myr (i.e. Salpeter timescale).

The reason why SMBH growths at higher redshift have higher Eddington ratio is shown

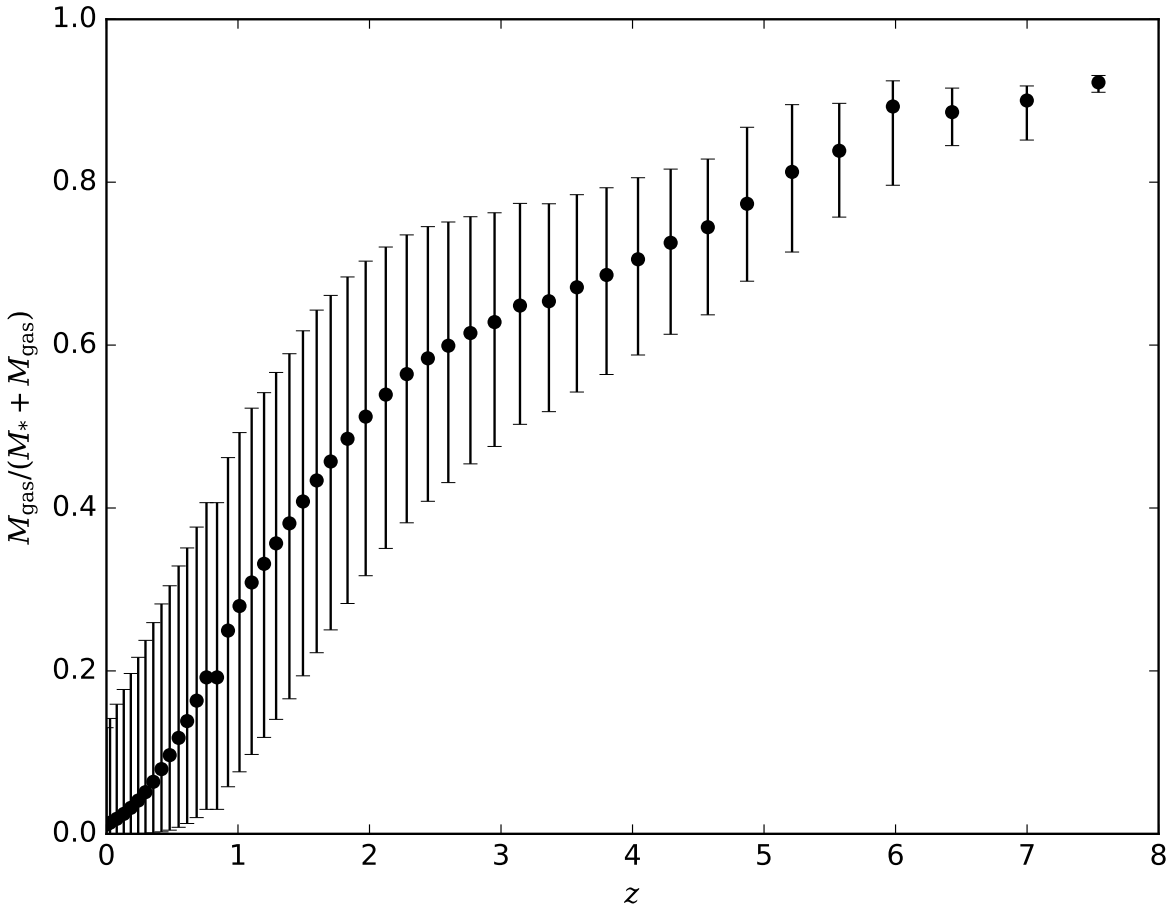

Figure 5.2: The redshift evolution of the gas fraction of AGN host galaxies obtained by the model. Black points show the median value at a redshift and error bars mean the 25 and 75 percentiles of the scatter.

in Fig. 5.2. The figure shows the evolution of the gas fraction of AGN host galaxies, defined as $M_{\rm gas}/(M_{\rm gas} + M_*)$, where $M_{\rm gas}$ and M_* are the cold gas and stellar masses of a galaxy (disc + bulge), respectively. The gas fraction is higher at higher redshift, e.g. 0.8 at $z \sim 5$. A higher gas fraction leads to a high $\dot{M}_{\rm BH}$, in general. Therefore, the Eddington ratio tends to be higher at higher redshift even if the SMBH mass is the same.

To present the mass dependence on the ERDFs, we show the ERDFs with different SMBH mass bins, $\log(M_{\rm BH}/M_\odot) = [6,7]$, $[7,8]$, $[8,9]$, and > 9, respectively, in Fig. 5.3. The colour of each line indicates the redshift, $0 < z < 8$, as shown in the colour bar. The thick solid lines describe the ERDFs at $z \sim 0.08$. The values of Φ for subsample with $\log(M_{\rm BH}) = [6,7], [7,8], [8,9]$, and > 9 monotonically increases with a similar shape from $z \sim 0.08$ to 2.95, 2.95, 1.97, and 1.49, respectively, and decreases at higher redshifts with a flatter slope at $\log(\dot{m}) = 1$ and $\log(\lambda_{\rm Edd}) = 0$. Our calculation shows that ERDFs, not only at higher redshift but also with less massive BHs tend to have flatter slopes, indicating that present day SMBHs are formed via super-Eddington accretion at higher redshifts.

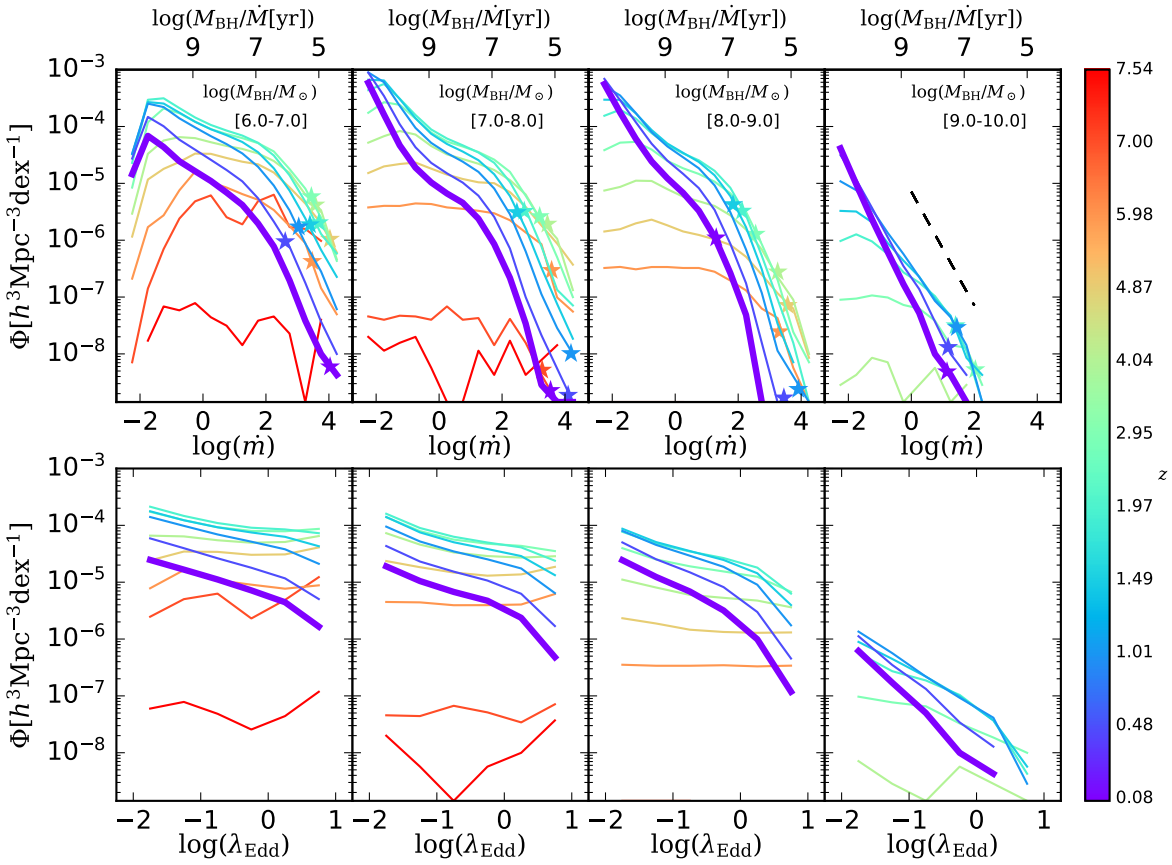

Figure 5.3: ERDFs of AGNs with $L_X > 10^{41}$ erg/s obtained with the fiducial model. Top and bottom panels show the distribution of $\dot{m}$ and $\lambda_{\rm Edd}$, respectively. Colors describe redshifts ($0.0 < z < 8.0$). I create four subsamples by $M_{\rm BH}$; $\log(M_{\rm BH}/M_\odot)$ is [6,7], [7,8], [8,9], and > 9, from left to right panels. The black dashed line in the right panel shows the slope $\Phi \propto (\dot{M}/\dot{M}_{\rm Edd})^{-1}$ and stars show the point at which the slope becomes -1. The growth timescale, $M_{\rm BH}/\dot{M}$, also appears in the top axis. The thick solid lines describe the ERDF at $z \sim 0.08$. The values of Φ for subsample with $\log(M_{\rm BH}) = [6-7], [7-8], [8.9]$, and > 9 monotonically increases from $z \sim 0.08$ to 2.95, 2.95, 1.97, and 1.49, respectively, and decreases at higher redshifts at $\log(\dot{m}) = 1$ and $\log(\lambda_{\rm Edd}) = 0$.

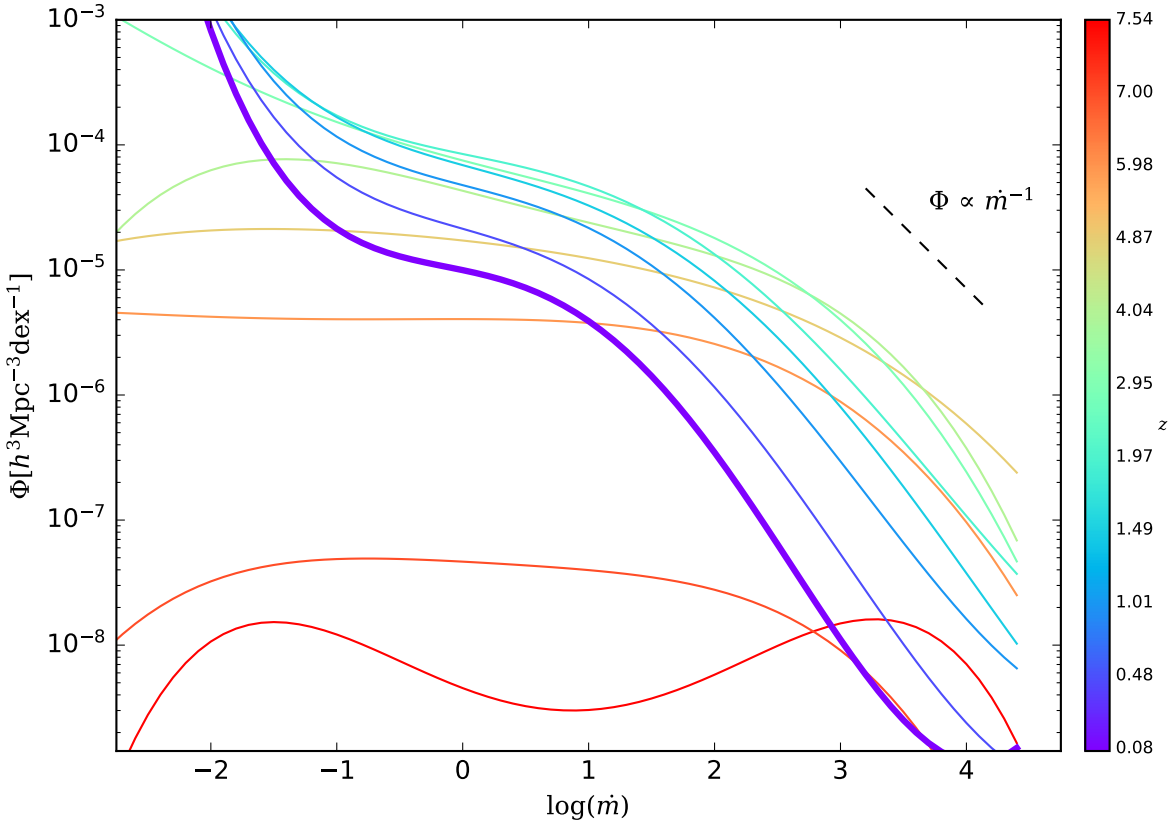

Figure 5.4: The ERDF fitting result in $\log(M_{\mathrm{BH}}[M_{\odot}]) = [7,8]$.

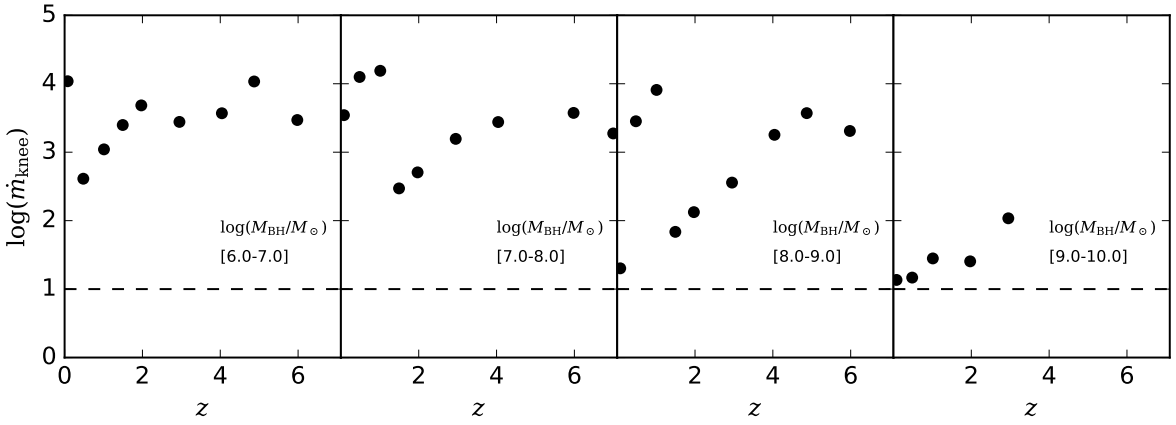

Figure 5.5: The evolution of the $\dot{m}$ at which the slope of ERDF becomes ~ -1 described as black circles and grey squares. Four panels show the results with the different $M_{\rm BH}$ bins. It is the same as stars in Fig. 5.3.

I then define $\dot{m}_{\rm knee}$ as $\dot{m}$ at which the ERDF has the critical slope (-1). Accretion with $\dot{m} = \dot{m}_{\rm knee}$ contributes to the SMBH growth most at that redshift and at that $M_{\rm BH}$ range. I obtain the points of contact by fitting ERDFs of $\dot{m}$ with fourth-order functions at $-2 < \log(\dot{m}) < 4$. An example of the fitting results is shown in Fig. 5.4 for $M_{\rm BH} = 10^{7-8} M_\odot$. Values of $\dot{m}_{\rm knee}$ have large uncertainties especially at higher redshift or with a higher SMBH mass, where obtaining smooth curves of the ERDF is difficult because of the low number density of AGNs. In these cases, an ERDF has several points of contact. I then define $\dot{m}_{\rm knee}$ as the most largest $\dot{m}$.

Fig. 5.5 shows the relation between $\dot{m}_{\rm knee}$ and redshift. I divide AGNs by the SMBH mass: $\log(M_{\rm BH}) = [6,7], [7,8], [8,9]$, and > 9. In all SMBH mass ranges, $\dot{m}_{\rm knee}$ increases towards higher redshift. Besides, $\dot{m}_{\rm knee}$ is larger for less massive SMBHs when I compare AGNs at a fixed redshift. These $\dot{m}_{\rm knee}$ evolutions in redshift and mass indicate that super-Eddington accretion is more common for less massive SMBHs and AGNs at higher redshift. This tendency is also suggested in Fig. 5.6, which shows the evolution of the mean slope of ERDFs in the range with $-3 \leq \log(\dot{m}) \leq 5$ from the fitting ERDFs. These results of the Eddington ratio evolution are consistent with another approach to constraining the SMBH growth by integrating the AGN LFs and the SMBH MFs (Sołtan 1982; Chokshi & Turner 1992), showing that the sub-Eddington accretion is responsible for SMBH growth at $M_{\rm BH} \gtrsim 10^9 M_\odot$ (e.g., Yu & Tremaine 2002; Fabian & Iwasawa 1999). For lower SMBH masses and higher redshifts, in contrast, our model shows that the super-Eddington accretion is the primary growth mode of SMBHs.

This dependence of ERDFs on the SMBH mass comes from the denominator of $\dot{m}$, i.e. $\dot{M}_{\rm Edd}$ itself, which is proportional to the SMBH mass. Fig. 5.7 shows the distribution of $\dot{M}_{\rm BH}$ with four SMBH mass bins at $z \sim 0, 1, 2$, and 4. As for the accretion rate, $\dot{M}_{\rm BH}$, which is not normalised by the Eddington accretion rate, the distribution has no clear trends with the SMBH mass. The distribution of $\dot{M}_{\rm BH}$ and $\dot{m}$ means that the accretion rate is not regulated by the SMBH mass nor the Eddington limit. I note that the accretion rate irrespective of the

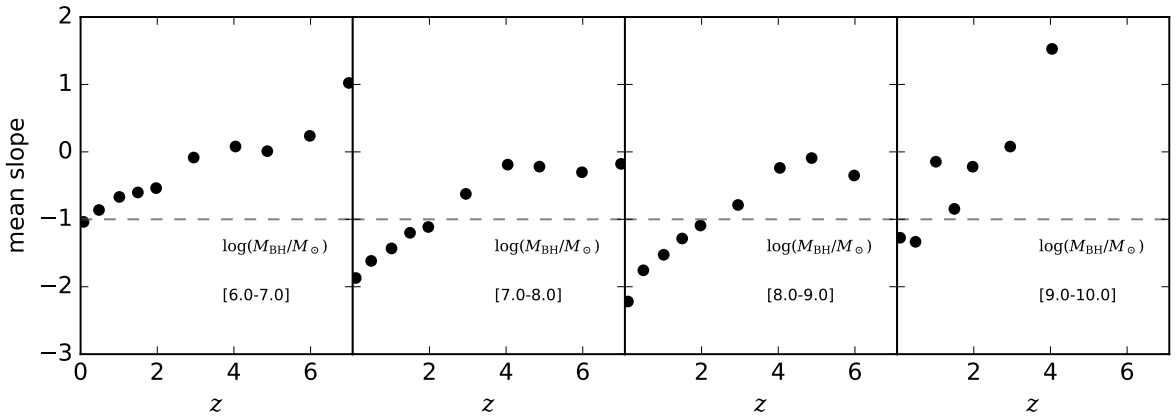

Figure 5.6: The evolution of the mean slope described as black circles. Four panels show the results with the different $M_{\rm BH}$ bins. The grey dashed line indicates the critical slope (-1).

SMBH mass nor the Eddington limit is also supported observationally (Collin & Kawaguchi 2004), where the maximum accretion rate of AGNs with different SMBH masses are the same at $z \sim 0$.

In this section, we have shown that the number fraction of AGNs with the super-Eddington growth is higher at higher redshift or for less massive SMBHs, as suggested from the slope of ERDFs. Here we focus on the SMBHs with $> 10^8 M\odot$ at $z \sim 0$ and investigate how dominant the super-Eddington growth is. As referred in Sec. 5.1, such SMBHs are considered to grow mainly with the sub-Eddington accretion rate. We derive the total number of QSOs (i.e. $L_X > 10^{44}$ erg/s) with $M_{\rm BH}(z = 0) > 10^8 M_\odot$, $n_{\rm tot}$. We also derive the number of QSOs with the same SMBH mass range, $n_{\rm se}$, whose acquired mass in the super-Eddington growth phase exceeds 50 % of the SMBH mass at the end of the AGN activity. The ratio between $n_{\rm se}$ and $n_{\rm tot}$ is ~ 0.5. The interpretetion of the result and explanation in the context of the Sołtan's argument is very complicated because of the uncertainties of the obscured fraction of AGNs, estimation of the SMBH MFs from observations, and so on. Therefore, now we are preparing another paper for this topic.

5.2.2 Comparisons with Observations

Here I compare my results with observations. I note that I do not assume the obscuration of AGNs for simplicity: I assume the obscured fraction is zero since it could depend on the bolometric luminosity and the Eddington ratio itself (e.g. Lusso et al. 2012) and the dependencies are unclear. The equivalent comparisons with observations cannot be made now.

Fig. 5.8 shows the comparison of the fiducial model with observations in the ERDF (Schulze & Wisotzki 2010; Nobuta et al. 2012). I select AGNs with a similar sample selection to each observational study (black lines). In this case, the model ERDF is roughly consistent with observations. Without the SMBH mass limit, however, the slope of the model ERDFs become flatter than observed since the accretion rate of less massive SMBHs in the model can easily reach and exceed the Eddington limit. The difference of the slope becomes larger

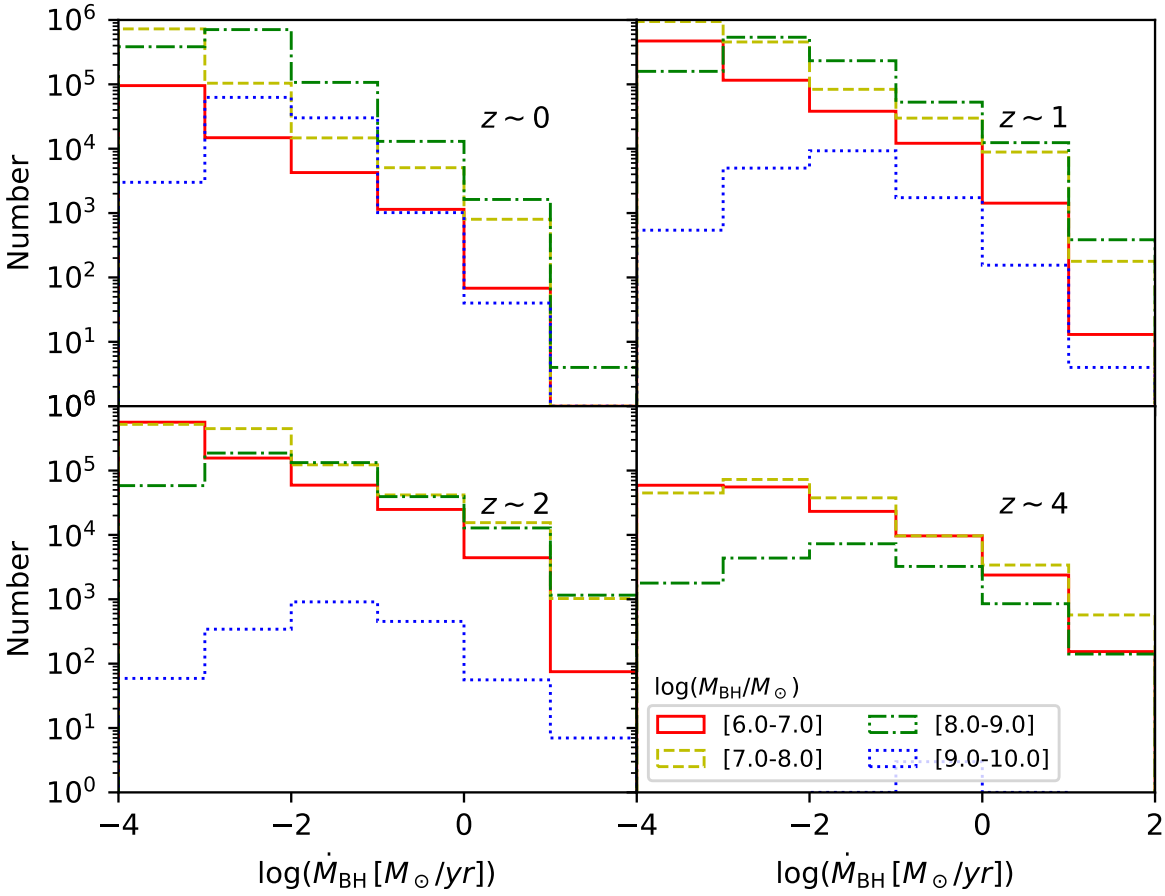

Figure 5.7: The number distributions of $\dot{M}_{\rm BH}$ with different SMBH mass ranges at $z = 0, 1, 2,$ and 4.

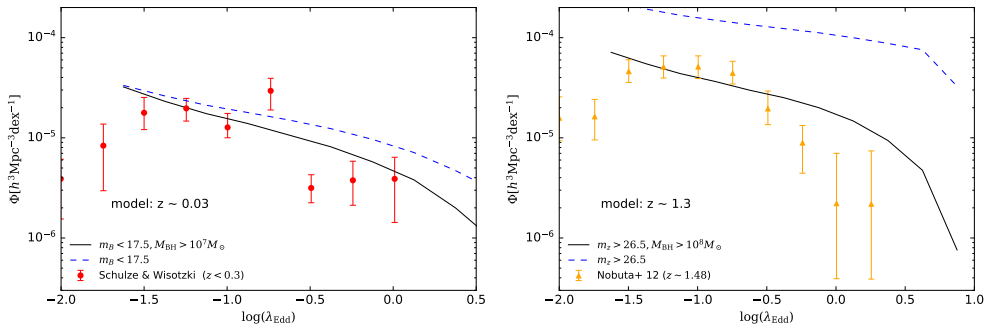

Figure 5.8: Comparisons of ERDFs with observations at $z < 0.3$ (Schulze & Wisotzki 2010; left panel, red circles) and at $z \sim 1.4$ (Nobuta et al. 2012; right panel, orange triangles). I select AGNs with the similar sample selection to each observation (black solid lines), where m_B and m_z are the apparent magnitude of B- and z- bands. I also show the results without imposing any limits for SMBH mass (blue dashed lines).

at higher redshift, which suggests the importance of deep observations (resulting in a weaker mass limit) to obtain ERDFs more accurately.

Fig. 5.9 shows the evolution of the number density of AGNs for different $\lambda_{\rm Edd}$ ranges. The model results for AGNs with $M_i < -22$ and those with $M_i < -22$ and $M_{\rm BH} > 10^{8.5} M_\odot$ are shown in the upper four panels, where M_i is the absolute magnitude in i-band. The latter selection is similar to that of KS13, based on SDSS data. Our results, especially with the latter sample selection, are consistent with the estimates of KS13. However, the results of KS13 have a discontinuous shape, which is likely to be originated by the difference of the emission lines used for the $M_{\rm BH}$ estimation. Since their typical equivalent-widths are different from line to line, the effective depth of spectroscopic surveys changes when one changes the emission line to use. In other words, observational determination of ERDFs at high redshift is very uncertain and is not yet ready for comparison with models. Deeper surveys such as those with Subaru Prime Focus Spectrograph are needed. I find that there is a trend that higher $\lambda_{\rm Edd}$ ranges present their peak number density at higher redshift, which is qualitatively consistent with KS13. Namely, the more rapid growth occurres at higher redshift, indicating the slowing-down, decelerating or slacking of cosmic SMBH growth. This trend can be seen in the bottom panels of Fig. 5.9, in which I present the redshift evolution of the number density of AGNs for each $\dot{m}$ and $\lambda_{\rm Edd}$ (left and right panels, respectively) indicated by the colour of lines. In these panels, I select all AGNs with $L_X > 10^{41}$ erg/s. While the number density of the higher Eddington ratio remains constant at $z \gtrsim 3$, that of the lower Eddington ratio gradually increases towards lower redshift, clearly indicating the slowing-down of cosmic SMBH growth.

As shown in Fig. 5.3, our model predicts that super-Eddington accretion becomes more important at higher redshift and for relatively lesser massive SMBHs. Observational determinations of ERDFs tend to underestimate the number density of super-Eddington accreting AGNs, whose optical flux is under the observational limit and/or whose SMBH mass has not been evaluated, and undervalue the importance of the super-Eddington growth (see also Fig. 5.8).

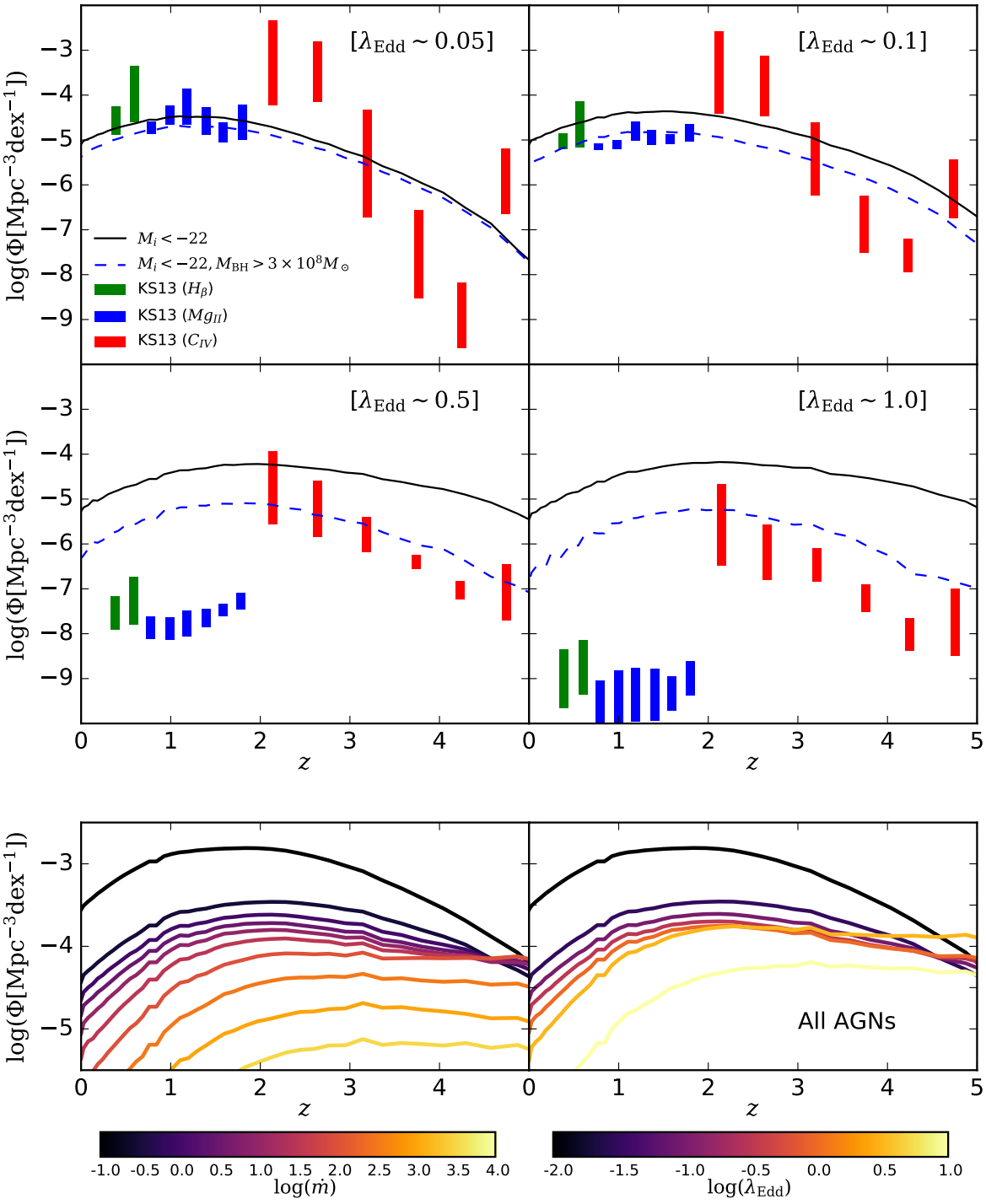

Figure 5.9: The redshift evolution of the number density of AGNs for different $\lambda_{\rm Edd}$ ranges at $0 < z < 5$. *Top four panels*: Comparisons with the model results with the observation (KS13). The black solid and blue dashed lines show the model results for AGNs with $M_i < -22$ and $M_i < -22$ and $M_{\rm BH} > 10^{8.5} M_\odot$, respectively. The latter ones are similar sample selection as KS13. Green, blue, and red bars indicate results with KS13, whose colour difference shows the results with different emission lines for estimating $M_{\rm BH}$ (H_β, Mg_{II}, and C_{IV}, respectively). *Bottom panels*: The redshift evolution of the number density with the fiducial model. I select all model AGNs with $L_X > 10^{41}$ erg/s. The colour indicates log($\dot{m}$) from -1 to 4 in the left panel and log($\lambda_{\rm Edd}$) from -2 to 1 in the right panel, as shown in colour bars.

Fig. 5.10 shows the ERDF at $0 < z < 6$ varying the sample selection. I show the results with different absolute luminosity cuts, $L_X > 10^{41}$, $> 10^{43}$, and $> 10^{44}$ erg/s, and flux cuts, $i < 18$ (SDSS-DR7 catalogue; Schneider et al. 2010), $g < 22$ (SDSS-DR10 catalogue; Pâris et al. 2017), and $i < 25.9$ (Subaru HSC-SSP wide layer; Aihara et al. 2017). I include all AGNs which satisfies the above cuts without considering the type-2 fraction or obscured fraction. I note that the model predicts the consistent ratio of local sub- and super-Eddington AGNs suggested by various low-z observation (Kawaguchi et al. 2004b). In Kawaguchi et al. (2004b), ranges for $\dot{m}$ are estimated from the disc model by Fig. 11 of Kawaguchi (2003), resulting in 80^{+10}_{-10} % objects in $\dot{m} = 3^{+7}_{-2.5}$, and 20^{+10}_{-10} % in $\dot{m} = 100^{+900}_{-90}$. When the shallower sample selections are applied, the number density of the AGNs with smaller Eddington ratios decreases. Also, the slope and the normalisation at a higher Eddington regime are affected by the sample selection since our model predicts that super-Eddington growth is more common for less massive SMBHs. The effect of the sample selection becomes more critical at higher redshift. The results imply that spectroscopic follow up observations and SMBH mass measurements including less luminous AGNs play a crucial role in obtaining nearly "complete" ERDFs and understanding the cosmic growth of SMBHs.

5.3 Discussion

I present a theoretical prediction for the ERDFs. The calculation is based on our SA model that has explained many observational properties of galaxies and AGNs, such as LFs, stellar MFs, $M_{\rm BH}$ – $M_{\rm bulge}$ relation, and scaling relations of local galaxies. I have found that SMBH growth via super-Eddington accretions become more significant at higher redshift. This tendency has been also suggested by previous observational studies (e.g. Nobuta et al. 2012) until $z \lesssim 1.4$, which I can broadly explain. Also, Wu et al. (2015) show that QSOs at $z > 6$ grow with $\lambda_{\rm Edd} \gtrsim 1$. Our model provides the detailed evolution of the Eddington ratio distribution beyond $z \sim 1.4$ and support the observed trend will continue from $z \sim 0$ to $z \sim 8$. Also, I have found that the SMBH growth with the higher Eddington ratio contributes to the SMBH growth of lesser massive SMBHs, indicating that SMBHs have grown via super-Eddington accretion. I have also found the slowing-down of the cosmic growth of SMBHs; a trend that higher $\lambda_{\rm Edd}$ ranges present their peak number density at higher redshift. To compare the model results with observations and to understand the SMBH growth, it is important to take into account the observed sample selection. Shallower observations tend to underestimate the number density of AGNs not only with lower but also higher Eddington ratios. The slope of ERDFs, therefore, is sensitive to the sample selection.

Previous studies with SA models have also presented the ERDFs. Fanidakis et al. (2012) give the evolution of ERDFs with $M_{\rm BH} > 10^6 M_\odot$. Their ERDFs show the almost no evolution of the slope for the high Eddington ratio, in contrast to this study. This is different from ERDFs obtained in this study. Hirschmann et al. (2012; 2014), on the other hand, predict flatter ERDF at higher redshift, which is broadly consistent with our result. In Hirschmann et al. (2012; 2014), they employ constant (= 0.01) Eddington ratio for AGNs triggered by disc instabilities and an Eddington ratio distribution for AGNs triggered by mergers obtained by merger simulations, which suggest that an AGN host galaxy with a higher cold gas fraction produce an AGN with a higher Eddington ratio. Both Fanidakis et al. (2012) and Hirschmann et al. (2014) show the bimodal distribution of ERDFs, which are caused by the different

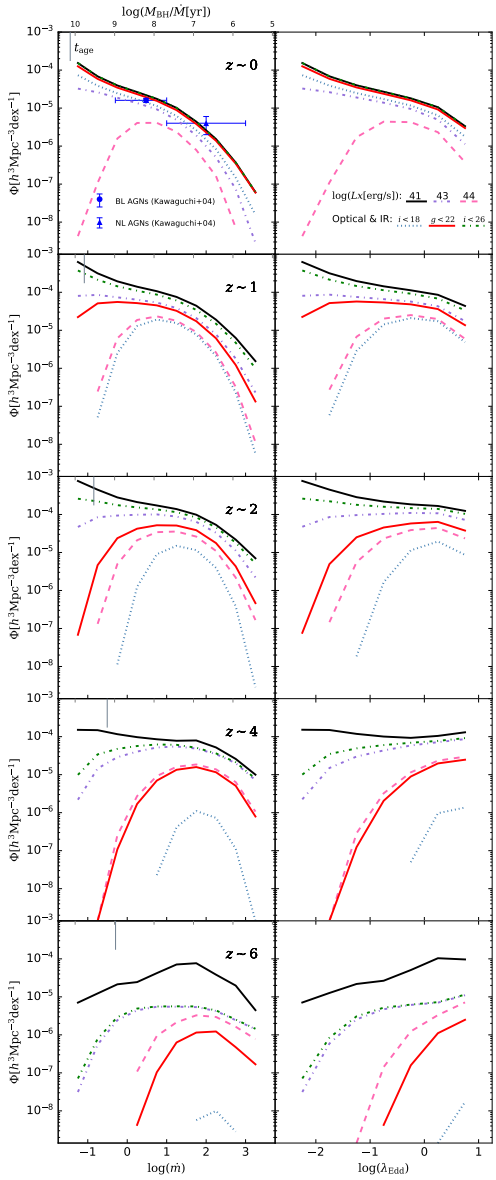

Figure 5.10: The ERDF with varying the sample selection at $0 < z < 6$. Left and right panels show the distribution functions of $\dot{m}$ and $\lambda_{\rm Edd}$, respectively. I employ different absolute luminosity cuts with X-ray, $L_X > 10^{41}$, $> 10^{43}$, and $> 10^{44}$ erg/s (black solid, purple dot-dashed, and pink dashed lines), and flux cuts with optical and infrared, $i < 18$, $g < 22$, and $i < 25.9$ (blue dotted, red solid, and green dot-dashed lines). The flux cuts in optical and infrared correspond to those of SDSS-DR7 (Schneider et al. 2010), SDSS-DR12 (Pâris et al. 2017), and forthcoming Subaru HSC-SSP survey catalogue with wide layers (Aihara et al. 2017). I overplot the result obtained by Kawaguchi et al. (2004b) for the relative fraction of broad and narrow line AGNs at $z < 0.5$. We also indicate the age of the Universe at each redshift, $t_{\rm age}$. SMBHs, whose growth timescale ($M_{\rm BH}/\dot{M}_{\rm BH}$) is shorter than $t_{\rm age}$, can acquire their mass by the current $\dot{M}_{\rm BH}$ and do not require heavy seed BHs such as $\gtrsim 10^5 M_\odot$.

accretion disc properties (i.e. advection-dominated accretion flow and standard disc) and/or different accretion mode (i.e. hot-halo mode and starburst/QSO mode). The evolution of the peak in the ERDF in the standard disc regime is broadly consistent with our results; the peak move to lower Eddington ratio at lower redshift. Since the advection-dominated accretion flow regime is out of the observable regime and the bolometric correction in this regime is unclear.

Observationally, there have been some studies about the relation between the Eddington ratio and properties of AGN host galaxies, [1] which are also essential for understanding the cosmic growth and coevolution of SMBHs and their host galaxies. Bongiorno et al. (2016) obtain L_X/M_* and its distribution instead of the Eddington ratio. They argue that the shape of the distribution is independent of the stellar mass although the normalisation is different. Jones et al. (2017) assume the local relationships between the SMBH mass and bulge mass (Häring & Rix 2004), and ERDFs with a Schechter function irrespective of SMBH mass. They show that under these assumptions, the mean halo occupation distribution of AGNs with $\lambda_{\rm Edd} > 0.01$ has a constant value in haloes with $10^{9.5-14} M_\odot$. Bernhard et al. (2018), on the other hand, suggest the suppression of AGNs with $\lambda_{\rm Edd} < 0.1$ in galaxies with $M_* < 10^{10-11} M_\odot$ to explain both observed AGN LFs and relationship between SFR and L_X.

In Sec. 5.2, I have shown that the shape of ERDFs depends on the redshift and mass of SMBHs. The mass dependence of the ERDFs is still unclear in observations. Although Bongiorno et al. (2016) find no dependence of ERDFs on the stellar mass, their results are obtained with the assumption of $M_{\rm BH} = 0.002 M_*$ at $z < 2.5$. This assumption is reasonable and can be compared with our model results for local bulge-dominated galaxies. However, since the host galaxies of AGNs have various morphologies (e.g. Bruce et al. 2015) and the fraction of disc-dominated galaxies becomes higher with less massive galaxies (e.g. Lang et al. 2014), the mass of SMBHs could be smaller than $0.002 M_*$ especially for less massive galaxies at higher redshift. Therefore, the assumption of the mass ratio between SMBHs and their host galaxies can affect the mass dependence on the ERDFs. I will obtain further constraints on the ERDFs at least $z \sim 0$ by obtaining the host halo and stellar mass of X-ray AGNs by observations, as suggested by Jones et al. (2017) in future studies.

Bernhard et al. (2018) estimate ERDFs separately for star-forming/quiescent host galaxies by requiring to explain observed AGN LFs in hard X-ray and stellar MFs. They use the same assumption of $M_{\rm BH} = 0.002 M_*$ as Bongiorno et al. (2016) for obtaining the Eddington ratio. They find that ERDFs of AGNs in star-forming galaxies at $0 < z < 2$ have peaky shape and the peak $\lambda_{\rm Edd}$ shifts toward higher value with redshift. In their estimate, the peak is at $\log(\lambda_{\rm Edd}) = -1.7$ at $z \sim 0.2$ and $\log(\lambda_{\rm Edd}) = -0.4$ at $z \sim 2.0$ when the mass-independent ERDFs are assumed. However, the Eddington ratio for star-forming host galaxies obtained by our fiducial model distributes broadly (in contrast to the suggestion by Bernhard et al. 2018) as shown in Fig. 5.11. I define star-forming galaxies by their specific star formation rate (sSFR) larger than $10^{-11} {\rm yr}^{-1}$ (Ilbert et al. 2013), which is the similar definition to Bernhard et al. (2018). The slope of ERDFs for star-forming host galaxies becomes shallower at higher redshift in agreement with Bernhard et al. (2018) in the sense that $\lambda_{\rm Edd}$ becomes larger at higher redshift on average. Similar to the whole sample (Figs. 5.1 and 5.3), the ERDFs of AGNs in star-forming galaxies show that larger $\lambda_{\rm Edd}$ is more common at higher redshift.

[1] Since the "true" Eddington ratio is difficult to estimate, we sometimes use the AGN luminosity (X-ray luminosity, especially) divided by the stellar mass of the host galaxy as a proxy for the Eddington ratio.

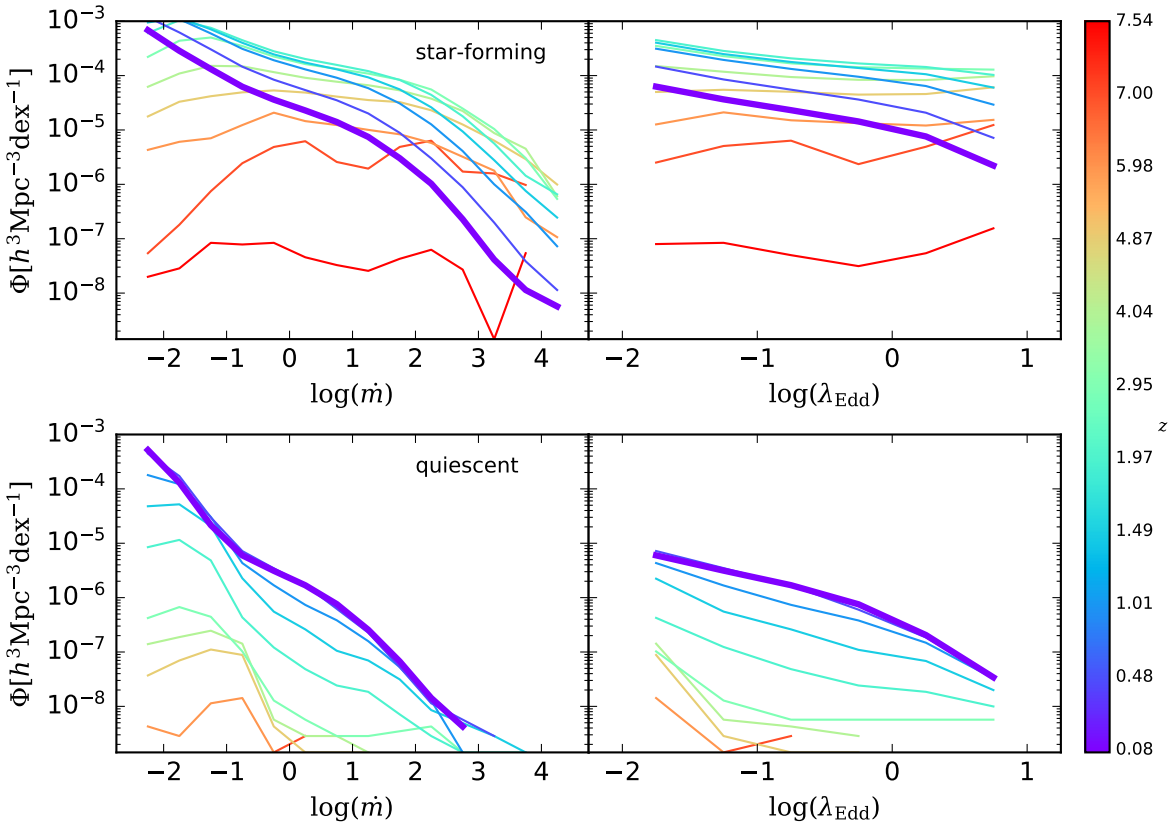

Figure 5.11: ERDFs at $0 < z < 8$ of star-forming (sSFR $> 10^{-11}\mathrm{yr}^{-1}$) and quiescent galaxies (top and bottom panels, respectively.)

ERDFs for quiescent galaxies, on the other hand, distributes in low Eddington ratio range. Also, quiescent galaxies at $z > 5$ do not host AGNs with $L_X > 10^{41}$ erg/s. Since the methods for obtaining ERDFs are different, the direct comparison with Bernhard et al. (2018) is still difficult although it is important for constraining the triggering mechanisms and the duty cycle of AGNs.

Finally, I focus on the difference of the ERDF caused by the different triggering mechanisms of AGNs. Although mergers of galaxies are important for triggering AGNs, an observational study shows that AGNs in merging galaxies do not have the higher Eddington ratio compared with those in galaxies without mergers (Weigel et al. 2018). I perform a Kolmogorov-Smirnov test to check the statistical difference of ERDFs by triggering mechanisms at $z < 4$ (since the sample size is small at larger redshift). I classify AGNs with $L_X > 10^{41}$ erg/s and $\log(\lambda_{\mathrm{Edd}}) > -2.5$ by their triggering mechanisms: (1) major mergers and minor mergers, and (2) mergers (major + minor) and disc instabilities. I find that in both cases, the p-value is less than 3 percent, which means that two distributions have different shape at all redshift bins. I show the ERDFs of AGNs with different triggering mechanisms at $z \sim 0.5$ in the top panel of Fig. 5.12. Dotted line shows AGNs triggered by disc instabilities and dashed and solid lines are AGNs triggered by minor and major mergers, and dot

dashed line describes the sum of dashed and solid lines (i.e. AGNs triggered by mergers), respectively. As for merger-driven AGNs, I find that the ERDF shape is similar independent of the merging mass ratio, although the p-value is small. On the other hand, AGNs triggered by disc instabilities tend to have a flatter distribution. To show these differences more clearly, I show the ratio of the normalised ERDFs in the bottom panel of Fig. 5.12. Since ERDFs of AGNs triggered by disc instabilities have a flatter shape, the difference becomes larger at larger $\lambda_{\rm Edd}$.

Our result shows that AGNs triggered by major mergers do not have higher $\lambda_{\rm Edd}$ than those triggered by other mechanisms, which is broadly consistent with Weigel et al. (2018). They suggest that major mergers of galaxies do not necessarily trigger AGNs with high Eddington ratios or rapid SMBH growths. The relation between the shape of the ERDFs and the triggering mechanisms of AGN activities will provide an important information for the cosmic growth of SMBHs and galaxies. If the major mergers tend to induce AGNs with higher Eddington ratio, it means that the SMBH growth via major mergers are more rapid and the SMBH growth rate will depend on the environment of its host galaxy.

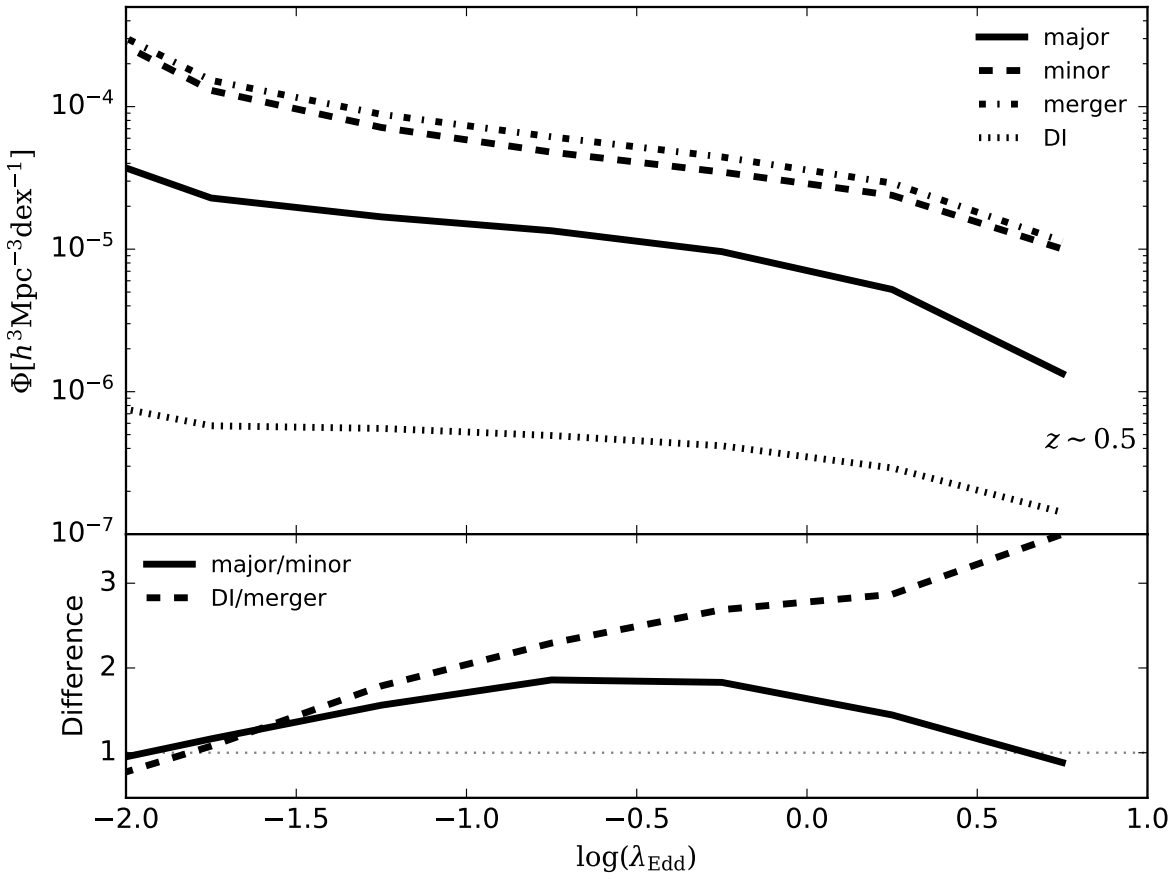

Figure 5.12: *Top:* ERDF of AGNs at $z \sim 0.5$, which are triggered by major mergers, minor mergers, mergers (major + minor), and disc instabilities (DI). These subsamples are described as solid, dashed, dot-dashed, and dotted lines, respectively. We define major mergers by the mass ratio of the merging galaxies (> 0.4). *Bottom:* The difference of the ERDF shape between (1) major and minor mergers (black solid line) and (2) mergers and disc instabilities (black dashed line). The y axis shows the ratio of the ERDFs normalised by the total number of AGNs which are triggered by each mechanism (i.e. major mergers, minor mergers, mergers, and disc instabilities). This panel shows, therefore, only the difference in the shape, not in the normalisation. The grey dotted line means no difference.

Chapter 6

Summary and Future Prospects

I have updated a semi-analytic model of galaxy formation, *"New Numerical Galaxy Catalogue"* (ν^2 GC). To understand the co-evolution between galaxies and SMBHs, I have investigated some effects related to the SMBH growth and have made theoretical predictions for the co-evolution by using ν^2GC . In this thesis, I have focused on the effect of the (1) the seed BH mass, and (2) the accretion timescale onto SMBHs. As for the seed BH mass, I have found that to explain the relation, the seed BH mass should be dominated by $10^3 M_\odot$, not by direct collapse BHs with $10^5 M_\odot$. For the accretion timescale, I have found that the timescale for the angular momentum loss in the central region, such as the accretion disc and circumnuclear disc plays an important role in less luminous ($L_X < 10^{44}$ erg/s) AGNs at low redshift. Finally, I have shown the theoretical prediction of the Eddington ratio distribution functions at $0 < z < 8$. The distribution is qualitatively consistent with observational estimates at low redshift. I have found that the growth rate of BHs at higher redshift exceeds the Eddington limit more easily because the typical gas fraction of the host galaxies is higher at higher redshift. Moreover, I also find that the super-Eddington growth is more common for less massive SMBHs, supporting an idea that SMBHs have grown via super-Eddington accretion. These results indicate the "slowing-down" of cosmic growth of SMBHs.

Theoretical predictions shown in this thesis could be validated by comparing (forthcoming) observational results and theoretical results obtained with other formulae. To get more stringent constraints on the seed BH mass distribution, observations of less massive galaxies at low redshift is more powerful than those of massive galaxies at high redshift because the difference resulting from the seed BH mass becomes difficult to detect. For the accretion timescale, hydrodynamic simulations for the central region of galaxies will provide information about the dynamics and structure. Also, recent ALMA observations have succeeded from observations of the circumnuclear disc in local Seyfert galaxies (e.g. Izumi et al. 2016). Further observations will also play a role in constraining the model predictions. As I mentioned in Sec. 4.4, if the model of the accretion timescale introduced in this thesis is assumed, then the AGN triggering mechanisms can be explained mergers of galaxies. Then, if the definite results, which support the importance of the triggering mechanisms other than galaxy mergers, are obtained, the model of accretion timescale can be rejected. For this indirect approach for constraining the accretion timescale, the AGN host halo mass and the Eddington ratio distribution are useful. AGN host halo mass has been investigated by using the data obtained by the HSC-SSP. The comparison with the HSC-SSP data is left for our future studies. To

reveal the cosmic growth of SMBHs and galaxies, the ERDF is important (see Chapter 5). I have shown the importance of the observational sample selection to obtain the ERDF by observations. When the date from deep surveys becomes available, we can compare the model prediction with observations and evaluate the model in more details.

I want to stress the importance of future observations of less luminous AGNs in the local Universe. Recent observations (e.g. SDSS York et al. 2000, CFHQs Willott et al. 2005, Pan-STARRS1 Bañados et al. 2014, and SHELLQS Matsuoka et al. 2016) have mainly focused on observations of AGNs (usually only QSOs) at higher redshift. As I have described, however, observations of less luminous AGns in the local Universe are crucial for obtaining more strong constraints on the seed BH mass, accretion timescale, and the distribution of the Eddington ratio, although such observations are not the main stream of current observational strategy. That is why the results of this thesis should impact on the future studies of the co-evolution between galaxies and SMBHs.

There are remaining questions about the co-evolution. First, the growth of SMBHs in the early Universe. Observations have found more than 100 SMBHs at $z \sim 6$ (e.g. Willott et al. 2010b; Matsuoka et al. 2016), and several SMBHs exceeds $z > 7$ (e.g. Bañados et al. 2018). If we believe the estimated SMBH and dynamical masses of such high-z QSOs and AGNs, the relation between the SMBH mass and dynamical mass of their host galaxies seems to have two sequences; for bright QSOs, their SMBHs are "over-massive" compared to the local relation, although less luminous ones seem to follow the local relation. Such a trend cannot be explained by any theoretical methods, both hydrodynamic simulations and SA models. Although we have to care about the error of the observational estimates and the sample size, the origin of this inconsistency will be investigated soon.

Second, AGN triggering mechanisms. The model of disc instabilities and "hot mode" accretion employed in SA models have to be made more physically plausible. Since SA models are one-zone calculations, they cannot treat perturbations induced by dynamical effects in details. The treatment of the disc instabilities, thus, is too simple (e.g. Athanassoula 2008). Also, the origin of the "hot mode" accretion is unclear. We need to understand "what is the hot mode accretion?" in the future.

Finally, the classification of AGNs and their spectra. According to the unified model, optical AGNs are classified with type 1 and 2 by the observing direction, which is related to the obscuring material. However, this classification does not correspond to the obscured and unobscured AGNs classified in X-ray bands. Also, there are AGNs which can be observed only in infrared bands, not in optical and X-ray bands. Such "obscured" AGNs are considered to be the preceding phase before the optically observable phase (e.g. Hopkins et al. 2005), although this suggestion has been evaluated only a few merging galaxies by hydrodynamic simulation. Radio properties of AGNs are also important. Radio-loud AGNs usually have jets, which affect the properties of the gas surrounding the nuclei. It is unclear what physical mechanisms or properties determines the radio properties of AGNs. In summary, to understand the growth history of AGNs and their connection to the galaxy evolution, we need the "unified model", including optical, X-ray, infrared, and radio properties of AGNs. However, the variation of the AGN spectra makes it difficult. The bolometric correction and the conversion from the accretion rate to the bolometric luminosity depends on the Eddington ratio. Also, the infrared spectra depend on the dust distribution surrounding nuclei. Problems are complicated and correlated with each other, which means that the problems cannot be solved with a single approach. Therefore, to understand the co-evolution of galaxies and SMBHs, collaborations

between theoretical studies and observations are essential. Such collaborations are what I have aimed at, and I will continue to search any fruitful collaborations.

Acknowledgements

In the first, I deeply appreciate comments from examiners, K. Sorai (chief), T. Kozasa, K. Kuramoto, and T. Okamoto, which drastically improve the quality of the thesis. I would like to thank E. J. Tasker and A. R. Pettitt for thorough English proofreading. I thank J. Aird to give the fitting function of hard X-ray LFs of AGNs. I appreciate the fruitful comments from the observational side by M. Akiyama, W. He, T. Izumi, T. Kawamuro, Y. Kimura, Y. Matsuoka, T. Nagao, M. Niida, K. Onishi, M. Onoue, A, Schulze, K. Terao, Y. Ueda, and T. Yamashita. I also thank N. Kawakatsu, M. Nomura, K. Omukai, K. Sugimura, M. Umemura, and K. Wada for theoretical comments.

The studies in this thesis could not be achieved without my colleagues. I thus thank M. Enoki, T. Ishiyama, M. A. R. Kobayashi, R. Makiya, M. Nagashima, K. Ogura, K. Okoshi, and T. Oogi for the collaborations. They always answer my questions about physics and the calculation methods of ν^2GC even when the questions were very tiny or basic ones. I deeply appreciate collaborations, fruitful comments, and guidance by T. Kawaguchi, who has always cared about me. I has felt him as my second supervisor.

I owe a lot to laboratory members. Especially, I feel so grateful for supporting my research and determining career paths given by A. Habe. He always cares about my poor environments and my research. Also, I would like to thank Y. Yamamoto and M. Tanaka for providing useful script files, roommates in the laboratory (H. Ichihashi, M. Tanaka, and Y. Yamamoto) for sharing research progress and relaxation time, which improves the quality of my research time. I also thank S. Ishiki, K. Shima, and Y. Fujimoto for giving me good advice, and all laboratory members for useful discussions.

Finally, I feel grateful for the supervision by T. Okamoto for six years. He always gives me fruitful advice and comments. Also, he never control my research and he allows me to choose my research following my own interests. I am happy to be one of his student.

I have been supported by the Sasakawa Scientific Research Grant from The Japan Science Society (29-214), a grant from the Hayakawa Satio Fund awarded by the Astronomical Society of Japan, and JSPS KAKENHI (18J12081).

Bibliography

Abdurro'uf Akiyama M., 2017, MNRAS, 469, 2806

Abramowicz M. A., Czerny B., Lasota J. P., Szuszkiewicz E., 1988, ApJ, 332, 646

Aihara H., et al., 2017, Publications of the Astronomical Society of Japan, 70

Aird J., Coil A. L., Georgakakis A., Nandra K., Barro G., Pérez-González P. G., 2015, MNRAS, 451, 1892

Aird J., Coil A. L., Georgakakis A., 2018, MNRAS, 474, 1225

Akiyama M., et al., 2018, PASJ, 70, S34

Anglés-Alcázar D., Özel F., Davé R., Katz N., Kollmeier J. A., Oppenheimer B. D., 2015, ApJ, 800, 127

Anglés-Alcázar D., Davé R., Faucher-Giguère C.-A., Özel F., Hopkins P. F., 2017, MNRAS, 464, 2840

Antonini F., Barausse E., Silk J., 2015, ApJ, 812, 72

Antonucci R. R. J., Miller J. S., 1985, ApJ, 297, 621

Assef R. J., et al., 2015, ApJ, 804, 27

Athanassoula E., 2008, MNRAS, 390, L69

Bañados E., et al., 2014, AJ, 148, 14

Bañados E., et al., 2018, Nature, 553, 473

Baldassare V. F., Reines A. E., Gallo E., Greene J. E., 2015, ApJ, 809, L14

Baldry I. K., et al., 2012, MNRAS, 421, 621

Barber C., Schaye J., Bower R. G., Crain R. A., Schaller M., Theuns T., 2016, MNRAS, 460, 1147

Barnes J. E., Hernquist L. E., 1991, ApJ, 370, L65

Barrows R. S., Comerford J. M., Greene J. E., Pooley D., 2016, ApJ, 829, 37

Barrows R. S., Comerford J. M., Greene J. E., 2018, ApJ, 869, 154

Baugh C. M., Cole S., Frenk C. S., 1996a, MNRAS, 282, L27

Baugh C. M., Cole S., Frenk C. S., 1996b, MNRAS, 283, 1361

Baugh C. M., Lacey C. G., Frenk C. S., Granato G. L., Silva L., Bressan A., Benson A. J., Cole S., 2005, MNRAS, 356, 1191

Begelman M. C., Volonteri M., Rees M. J., 2006, MNRAS, 370, 289

Bell E. F., McIntosh D. H., Katz N., Weinberg M. D., 2003, ApJS, 149, 289

Bennett C. L., et al., 2003, ApJS, 148, 1

Bennett C. L., et al., 2013, ApJS, 208, 20

Benson A. J., Cole S., Frenk C. S., Baugh C. M., Lacey C. G., 2000, MNRAS, 311, 793

Benson A. J., Bower R. G., Frenk C. S., Lacey C. G., Baugh C. M., Cole S., 2003, ApJ, 599, 38

Bentz M. C., Peterson B. M., Netzer H., Pogge R. W., Vestergaard M., 2009, ApJ, 697, 160

Bernhard E., Mullaney J. R., Aird J., Hickox R. C., Jones M. L., Stanley F., Grimmett L. P., Daddi E., 2018, MNRAS, 476, 436

Bett P., Eke V., Frenk C. S., Jenkins A., Helly J., Navarro J., 2007, MNRAS, 376, 215

Bigiel F., Leroy A., Walter F., Brinks E., de Blok W. J. G., Madore B., Thornley M. D., 2008, AJ, 136, 2846

Binney J., Tremaine S., 1987, Galactic dynamics,

Bongiorno A., et al., 2016, A&A, 588, A78

Booth C. M., Schaye J., 2009, MNRAS, 398, 53

Bouwens R. J., et al., 2014, ApJ, 793, 115

Bower R. G., Benson A. J., Malbon R., Helly J. C., Frenk C. S., Baugh C. M., Cole S., Lacey C. G., 2006, MNRAS, 370, 645

Bridle A. H., Hough D. H., Lonsdale C. J., Burns J. O., Laing R. A., 1994, AJ, 108, 766

Bromley J. M., Somerville R. S., Fabian A. C., 2004, MNRAS, 350, 456

Bruce V., Dunlop J., Mortlock A., Kocevski D., McGrath E., Rosario D., 2015

Bruzual G., Charlot S., 2003, MNRAS, 344, 1000

Bureau M., Freeman K. C., 1999, AJ, 118, 126

Burlon D., Ajello M., Greiner J., Comastri A., Merloni A., Gehrels N., 2011, ApJ, 728, 58

Burns J. O., Gregory S. A., Holman G. D., 1981, ApJ, 250, 450

Busch G., et al., 2014, A&A, 561, A140

Calzetti D., Armus L., Bohlin R. C., Kinney A. L., Koornneef J., Storchi-Bergmann T., 2000, ApJ, 533, 682

Cao X., 2009, MNRAS, 394, 207

Caputi K. I., McLure R. J., Dunlop J. S., Cirasuolo M., Schael A. M., 2006, MNRAS, 366, 609

Chabrier G., 2003, ApJ, 586, L133

Chandrasekhar S., 1943, ApJ, 97, 255

Chokshi A., Turner E. L., 1992, MNRAS, 259, 421

Christodoulou D. M., Shlosman I., Tohline J. E., 1995, ApJ, 443, 551

Cicone C., et al., 2015, A&A, 574, A14

Cirasuolo M., McLure R. J., Dunlop J. S., Almaini O., Foucaud S., Simpson C., 2010, MNRAS, 401, 1166

Cole S., Aragon-Salamanca A., Frenk C. S., Navarro J. F., Zepf S. E., 1994, MNRAS, 271, 781

Cole S., Lacey C. G., Baugh C. M., Frenk C. S., 2000, MNRAS, 319, 168

Collin S., Kawaguchi T., 2004, A&A, 426, 797

Courteau S., Dutton A. A., van den Bosch F. C., MacArthur L. A., Dekel A., McIntosh D. H., Dale D. A., 2007, ApJ, 671, 203

Covington M. D., Primack J. R., Porter L. A., Croton D. J., Somerville R. S., Dekel A., 2011, MNRAS, 415, 3135

Cowie L. L., Binney J., 1977, ApJ, 215, 723

Croom S. M., Smith R. J., Boyle B. J., Shanks T., Loaring N. S., Miller L., Lewis I. J., 2001, MNRAS, 322, L29

Croom S. M., et al., 2009, MNRAS, 399, 1755

Croton D. J., et al., 2006, MNRAS, 365, 11

Cucciati O., et al., 2012, A&A, 539, A31

Daddi E., et al., 2007, ApJ, 670, 156

Davis T. A., Bureau M., Cappellari M., Sarzi M., Blitz L., 2013, Nature, 494, 328

De Lucia G., Fontanot F., Hirschmann M., 2017, MNRAS, 466, L88

Dekel A., Silk J., 1986, ApJ, 303, 39

Devereux N., Hriljac P., Willner S. P., Ashby M. L. N., Willmer C. N. A., 2009, in Jogee S., Marinova I., Hao L., Blanc G. A., eds, Astronomical Society of the Pacific Conference Series Vol. 419, Galaxy Evolution: Emerging Insights and Future Challenges. p. 171 (arXiv:0902.0778)

Dey A., et al., 2008, ApJ, 677, 943

Diamond-Stanic A. M., Rieke G. H., 2012, ApJ, 746, 168

Disney M., Davies J., Phillipps S., 1989, MNRAS, 239, 939

Donley J. L., Rieke G. H., Alexander D. M., Egami E., Pérez-González P. G., 2010, ApJ, 719, 1393

Driver S. P., et al., 2012, MNRAS, 427, 3244

Drory N., Bender R., Feulner G., Hopp U., Maraston C., Snigula J., Hill G. J., 2003, ApJ, 595, 698

Efstathiou G., 2000, MNRAS, 317, 697

Efstathiou G., Jones B. J. T., 1979, MNRAS, 186, 133

Efstathiou G., Lake G., Negroponte J., 1982, MNRAS, 199, 1069

Eisenhardt P. R. M., et al., 2012, ApJ, 755, 173

Elbaz D., et al., 2007, A&A, 468, 33

Elitzur M., Ho L. C., 2009, ApJ, 701, L91

Elmegreen B. G., 2006, ApJ, 648, 572

Enoki M., Nagashima M., 2007, Progress of Theoretical Physics, 117, 241

Enoki M., Nagashima M., Gouda N., 2003, PASJ, 55, 133

Enoki M., Inoue K. T., Nagashima M., Sugiyama N., 2004, ApJ, 615, 19

Enoki M., Ishiyama T., Kobayashi M. A. R., Nagashima M., 2014, ApJ, 794, 69

Faber S. M., Jackson R. E., 1976, ApJ, 204, 668

Fabian A. C., Iwasawa K., 1999, MNRAS, 303, L34

Fabian A. C., Nulsen P. E. J., 1977, MNRAS, 180, 479

Fabian A. C., Sanders J. S., Allen S. W., Crawford C. S., Iwasawa K., Johnstone R. M., Schmidt R. W., Taylor G. B., 2003, MNRAS, 344, L43

Fan X., et al., 2001, AJ, 121, 54

Fan X., et al., 2003, AJ, 125, 1649

Fanidakis N., Baugh C. M., Benson A. J., Bower R. G., Cole S., Done C., Frenk C. S., 2011, MNRAS, 410, 53

Fanidakis N., et al., 2012, MNRAS, 419, 2797

Fanidakis N., et al., 2013, MNRAS, 435, 679

Fender R. P., Belloni T. M., Gallo E., 2004, MNRAS, 355, 1105

Ferrarese L., Merritt D., 2000, ApJ, 539, L9

Fiore F., et al., 2012, A&A, 537, A16

Floyd D. J. E., Kukula M. J., Dunlop J. S., McLure R. J., Miller L., Percival W. J., Baum S. A., O'Dea C. P., 2004, MNRAS, 355, 196

Fontanot F., Monaco P., Cristiani S., Tozzi P., 2006, MNRAS, 373, 1173

Fontanot F., Cristiani S., Monaco P., Nonino M., Vanzella E., Brandt W. N., Grazian A., Mao J., 2007, A&A, 461, 39

Fontanot F., Monaco P., Shankar F., 2015, MNRAS, 453, 4112

Fontanot F., De Lucia G., Hirschmann M., Bruzual G., Charlot S., Zibetti S., 2017, MNRAS, 464, 3812

Forbes D. A., Lasky P., Graham A. W., Spitler L., 2008, MNRAS, 389, 1924

Freiburghaus C., Rosswog S., Thielemann F.-K., 1999, ApJ, 525, L121

Gabasch A., et al., 2004, A&A, 421, 41

Gatti M., Shankar F., Bouillot V., Menci N., Lamastra A., Hirschmann M., Fiore F., 2016, MNRAS, 456, 1073

Giallongo E., Salimbeni S., Menci N., Zamorani G., Fontana A., Dickinson M., Cristiani S., Pozzetti L., 2005, ApJ, 622, 116

Glikman E., Djorgovski S. G., Stern D., Dey A., Jannuzi B. T., Lee K.-S., 2011, ApJ, 728, L26

Gnedin N. Y., 2000, ApJ, 542, 535

Gonzalez-Perez V., Lacey C. G., Baugh C. M., Lagos C. D. P., Helly J., Campbell D. J. R., Mitchell P. D., 2014, MNRAS, 439, 264

Graham A. W., 2012, ApJ, 746, 113

Graham A. W., Scott N., 2015, ApJ, 798, 54

Graham A. W., Ciambur B. C., Soria R., 2016, ApJ, 818, 172

Granato G. L., De Zotti G., Silva L., Bressan A., Danese L., 2004, ApJ, 600, 580

Griffin A. J., Lacey C. G., Gonzalez-Perez V., del P. Lagos C., Baugh C. M., Fanidakis N., , arXiv:1806.08370

Guo Q., et al., 2016, MNRAS, 461, 3457

Hamilton A. J. S., Kumar P., Lu E., Matthews A., 1991, ApJ, 374, L1

Häring N., Rix H.-W., 2004, ApJ, 604, L89

Hasinger G., Miyaji T., Schmidt M., 2005, A&A, 441, 417

Henriques B. M. B., White S. D. M., Thomas P. A., Angulo R. E., Guo Q., Lemson G., Springel V., 2013, Monthly Notices of the Royal Astronomical Society, 431, 3373

Heyl J. S., Cole S., Frenk C. S., Navarro J. F., 1995, MNRAS, 274, 755

Hickox R. C., Mullaney J. R., Alexander D. M., Chen C.-T. J., Civano F. M., Goulding A. D., Hainline K. N., 2014, ApJ, 782, 9

Hirschmann M., Somerville R. S., Naab T., Burkert A., 2012, MNRAS, 426, 237

Hirschmann M., Dolag K., Saro A., Bachmann L., Borgani S., Burkert A., 2014, MNRAS, 442, 2304

Hirschmann M., De Lucia G., Fontanot F., 2016, Monthly Notices of the Royal Astronomical Society, 461, 1760

Ho L. C., 2009, ApJ, 699, 626

Ho L. C., Sarzi M., Rix H.-W., Shields J. C., Rudnick G., Filippenko A. V., Barth A. J., 2002, PASP, 114, 137

Hopkins A. M., 2004, ApJ, 615, 209

Hopkins P. F., Hernquist L., Martini P., Cox T. J., Robertson B., Di Matteo T., Springel V., 2005, ApJ, 625, L71

Hopkins P. F., Hernquist L., Cox T. J., Di Matteo T., Robertson B., Springel V., 2006, The Astrophysical Journal Supplement Series, 163, 1

Hopkins P. F., Richards G. T., Hernquist L., 2007, ApJ, 654, 731

Hopkins P. F., Cox T. J., Younger J. D., Hernquist L., 2009a, ApJ, 691, 1168

Hopkins P. F., Hernquist L., Cox T. J., Keres D., Wuyts S., 2009b, ApJ, 691, 1424

Huang J.-S., Glazebrook K., Cowie L. L., Tinney C., 2003, ApJ, 584, 203

Ikeda H., et al., 2011, ApJ, 728, L25

Ikeda H., et al., 2012, ApJ, 756, 160

Ikeda H., Nagao T., Matsuoka K., Kawakatu N., Kajisawa M., Akiyama M., Miyaji T., Morokuma T., 2017, ApJ, 846, 57

Ilbert O., et al., 2005, A&A, 439, 863

Ilbert O., et al., 2013, A&A, 556, A55

Ishiyama T., Enoki M., Kobayashi M. A. R., Makiya R., Nagashima M., Oogi T., 2015, PASJ, 67, 61

Izumi T., Kawakatu N., Kohno K., 2016, ApJ, 827, 81

Izumi T., et al., 2018, Publications of the Astronomical Society of Japan, 70

Jahnke K., Macciò A. V., 2011, ApJ, 734, 92

Jiang C. Y., Jing Y. P., Faltenbacher A., Lin W. P., Li C., 2008, ApJ, 675, 1095

Jiang C. Y., Jing Y. P., Lin W. P., 2010, A&A, 510, A60

Jiang Y.-F., Greene J. E., Ho L. C., 2011, ApJ, 737, L45

Jones D. H., Peterson B. A., Colless M., Saunders W., 2006, MNRAS, 369, 25

Jones M. L., Hickox R. C., Mutch S. J., Croton D. J., Ptak A. F., DiPompeo M. A., 2017, ApJ, 843, 125

Jones M. G., Haynes M. P., Giovanelli R., Moorman C., 2018, Monthly Notices of the Royal Astronomical Society, 477, 2

Karim A., et al., 2011, ApJ, 730, 61

Kato S., Fukue J., Mineshige S., 2008, Black-Hole Accretion Disks — Towards a New Paradigm —. Kyoto Univ. Press

Kauffmann G., 1996, MNRAS, 281, 475

Kauffmann G., Haehnelt M., 2000, MNRAS, 311, 576

Kauffmann G., White S. D. M., Guiderdoni B., 1993, MNRAS, 264, 201

Kauffmann G., Guiderdoni B., White S. D. M., 1994, MNRAS, 267, 981

Kauffmann G., Colberg J. M., Diaferio A., White S. D. M., 1999, MNRAS, 303, 188

Kawaguchi T., 2003, ApJ, 593, 69

Kawaguchi T., Shimura T., Mineshige S., 2001, ApJ, 546, 966

Kawaguchi T., Pierens A., Huré J.-M., 2004a, A&A, 415, 47

Kawaguchi T., Aoki K., Ohta K., Collin S., 2004b, A&A, 420, L23

Kawakatu N., Umemura M., 2002, MNRAS, 329, 572

Kawakatu N., Wada K., 2008, ApJ, 681, 73

Kelly B. C., Shen Y., 2013, ApJ, 764, 45

Kennicutt Jr. R. C., 1998, ApJ, 498, 541

Khandai N., Di Matteo T., Croft R., Wilkins S., Feng Y., Tucker E., DeGraf C., Liu M.-S., 2015, MNRAS, 450, 1349

Khim H., Yi S. K., 2017, The Astrophysical Journal, 846, 155

Kobayashi C., Springel V., White S. D. M., 2007a, MNRAS, 376, 1465

Kobayashi M. A. R., Totani T., Nagashima M., 2007b, ApJ, 670, 919

Kormendy J., Barentine J. C., 2010, ApJ, 715, L176

Kormendy J., Ho L. C., 2013, ARA&A, 51, 511

Kormendy J., et al., 1996a, ApJ, 459, L57

Kormendy J., et al., 1996b, ApJ, 473, L91

Krolik J. H., Begelman M. C., 1988, ApJ, 329, 702

Kroupa P., 2001, MNRAS, 322, 231

Kroupa P., 2002, Science, 295, 82

Kuijken K., Merrifield M. R., 1995, ApJ, 443, L13

Kuo C. Y., et al., 2011, ApJ, 727, 20

La Franca F., et al., 2005, ApJ, 635, 864

Lacey C., Cole S., 1993, MNRAS, 262, 627

Lacey C., Silk J., 1991, ApJ, 381, 14

Lacey C. G., et al., 2016, MNRAS, 462, 3854

Lagos C. D. P., Cora S. A., Padilla N. D., 2008, MNRAS, 388, 587

Lagos C. D. P., Padilla N. D., Cora S. A., 2009, MNRAS, 395, 625

Lagos C. D. P., Lacey C. G., Baugh C. M., Bower R. G., Benson A. J., 2011, MNRAS, 416, 1566

Lagos C. d. P., Davis T. A., Lacey C. G., Zwaan M. A., Baugh C. M., Gonzalez-Perez V., Padilla N. D., 2014, MNRAS, 443, 1002

Lang P., et al., 2014, ApJ, 788, 11

Lawrence A., 1991, MNRAS, 252, 586

Li C., White S. D. M., 2009, MNRAS, 398, 2177

Lin C. C., Shu F. H., 1964, ApJ, 140, 646

Lin C. C., Shu F. H., 1966, Proceedings of the National Academy of Science, 55, 229

Liu H. T., Feng H. C., Bai J. M., 2017, MNRAS, 466, 3323

Lodato G., Natarajan P., 2006, MNRAS, 371, 1813

Lusso E., et al., 2012, MNRAS, 425, 623

Lynden-Bell D., 1967, MNRAS, 136, 101

Lynden-Bell D., 1969, Nature, 223, 690

Maeder A., 1992, A&A, 264, 105

Magorrian J., et al., 1998, AJ, 115, 2285

Mahadevan R., 1997, ApJ, 477, 585

Makino J., Hut P., 1997, ApJ, 481, 83

Makino N., Sasaki S., Suto Y., 1998, ApJ, 497, 555

Makiya R., Totani T., Kobayashi M. A. R., Nagashima M., Takeuchi T. T., 2014, MNRAS, 441, 63

Makiya R., et al., 2016, PASJ, 68, 25

Malbon R. K., Baugh C. M., Frenk C. S., Lacey C. G., 2007, MNRAS, 382, 1394

Marconi A., Risaliti G., Gilli R., Hunt L. K., Maiolino R., Salvati M., 2004, MNRAS, 351, 169

Martin A. M., Papastergis E., Giovanelli R., Haynes M. P., Springob C. M., Stierwalt S., 2010, ApJ, 723, 1359

Martini P., 2004, Coevolution of Black Holes and Galaxies, p. 169

Marulli F., Bonoli S., Branchini E., Moscardini L., Springel V., 2008, MNRAS, 385, 1846

Mathur S., Fields D., Peterson B. M., Grupe D., 2012, ApJ, 754, 146

Matsuoka Y., et al., 2016, ApJ, 828, 26

Matsuoka Y., et al., 2017, Publications of the Astronomical Society of Japan, 70

McConnell N. J., Ma C.-P., 2013, ApJ, 764, 184

McLure R. J., Dunlop J. S., 2004, MNRAS, 352, 1390

McNamara B. R., et al., 2000, ApJ, 534, L135

Melbourne J., et al., 2012, AJ, 143, 125

Menci N., Cavaliere A., Fontana A., Giallongo E., Poli F., 2002, ApJ, 575, 18

Menci N., Cavaliere A., Fontana A., Giallongo E., Poli F., Vittorini V., 2003, ApJ, 587, L63

Menci N., Gatti M., Fiore F., Lamastra A., 2014, A&A, 569, A37

Merrifield M. R., Forbes D. A., Terlevich A. I., 2000, MNRAS, 313, L29

Mihos J. C., Hernquist L., 1994, ApJ, 431, L9

Mineshige S., Kawaguchi T., Takeuchi M., Hayashida K., 2000, PASJ, 52, 499

Mitchell P. D., Lacey C. G., Baugh C. M., Cole S., 2013, MNRAS, 435, 87

Mitchell P. D., et al., 2018, MNRAS, 474, 492

Mo H. J., Mao S., White S. D. M., 1998, MNRAS, 295, 319

Mo H., van den Bosch F. C., White S., 2010, Galaxy Formation and Evolution

Moffett A. J., et al., 2016, MNRAS, 457, 1308

Monaco P., Benson A. J., De Lucia G., Fontanot F., Borgani S., Boylan-Kolchin M., 2014, MNRAS, 441, 2058

Mortlock D. J., et al., 2011, Nature, 474, 616

Moustakas J., et al., 2013, ApJ, 767, 50

Muzzin A., et al., 2013, ApJ, 777, 18

Nagashima M., Yoshii Y., 2004, ApJ, 610, 23

Nagashima M., Yahagi H., Enoki M., Yoshii Y., Gouda N., 2005, ApJ, 634, 26

Navarro J. F., Frenk C. S., White S. D. M., 1997, ApJ, 490, 493

Negroponte J., White S. D. M., 1983, MNRAS, 205, 1009

Nobuta K., et al., 2012, ApJ, 761, 143

Norberg P., et al., 2002, MNRAS, 336, 907

Norman C., Scoville N., 1988, ApJ, 332, 124

Oh K., Yi S. K., Schawinski K., Koss M., Trakhtenbrot B., Soto K., 2015, ApJS, 219, 1

Okamoto T., Nemmen R. S., Bower R. G., 2008a, MNRAS, 385, 161

Okamoto T., Gao L., Theuns T., 2008b, MNRAS, 390, 920

Omukai K., Schneider R., Haiman Z., 2008, ApJ, 686, 801

Onishi K., Iguchi S., Davis T. A., Bureau M., Cappellari M., Sarzi M., Blitz L., 2017, Monthly Notices of the Royal Astronomical Society, 468, 4663

Oogi T., Habe A., Ishiyama T., 2015

Oogi T., Enoki M., Ishiyama T., Kobayashi M. A. R., Makiya R., Nagashima M., 2016, MNRAS, 456, L30

Oogi T., Enoki M., Ishiyama T., Kobayashi M. A. R., Makiya R., Nagashima M., Okamoto T., Shirakata H., 2017, MNRAS, 471, L21

Osterbrock D. E., 1978, Proceedings of the National Academy of Science, 75, 540

Ouchi M., et al., 2004, ApJ, 611, 685

Palanque-Delabrouille N., et al., 2013, A&A, 551, A29

Pâris I., et al., 2017, Astronomy & Astrophysics, 597, A79

Parsa S., Dunlop J. S., McLure R. J., Mortlock A., 2016, MNRAS, 456, 3194

Pascale E., et al., 2009, ApJ, 707, 1740

Pei Y. C., 1992, ApJ, 395, 130

Peterson B. M., 1993, PASP, 105, 247

Peterson B. M., Wandel A., 1999, ApJ, 521, L95

Pezzulli E., Valiante R., Schneider R., 2016, MNRAS, 458, 3047

Pezzulli E., Volonteri M., Schneider R., Valiante R., 2017, MNRAS, 471, 589

Planck Collaboration et al., 2014, A&A, 571, A1

Planck Collaboration et al., 2016, A&A, 594, A13

Pozzetti L., et al., 2003, A&A, 402, 837

Prada F., Klypin A. A., Cuesta A. J., Betancort-Rijo J. E., Primack J., 2012, MNRAS, 423, 3018

Rees M. J., 1992, in Duschl W. J., Wagner S. J., eds, Physics of Active Galactic Nuclei. Berlin, Springer-Verlag, p. 662

Reines A. E., Greene J. E., Geha M., 2013, ApJ, 775, 116

Ricci F., Marchesi S., Shankar F., La Franca F., Civano F., 2017a, MNRAS, 465, 1915

Ricci C., et al., 2017b, Nature, 549, 488

Richards G. T., et al., 2005, MNRAS, 360, 839

Richards G. T., et al., 2006, AJ, 131, 2766

Richstone D., Bower G., Dressler A., 1990, ApJ, 353, 118

Rodighiero G., et al., 2010, A&A, 515, A8

Rosario D. J., et al., 2012, A&A, 545, A45

Roukema B. F., Quinn P. J., Peterson B. A., Rocca-Volmerange B., 1997, MNRAS, 292, 835

Roychowdhury S., Huang M.-L., Kauffmann G., Wang J., Chengalur J. N., 2015, MNRAS, 449, 3700

Salmon B., et al., 2015, ApJ, 799, 183

Salpeter E. E., 1955, ApJ, 121, 161

Salpeter E. E., 1964, ApJ, 140, 796

Sanders D. B., Mirabel I. F., 1996, ARA&A, 34, 749

Santini P., et al., 2012, A&A, 538, A33

Saracco P., et al., 2006, MNRAS, 367, 349

Sarzi M., Rix H.-W., Shields J. C., Rudnick G., Ho L. C., McIntosh D. H., Filippenko A. V., Sargent W. L. W., 2001, ApJ, 550, 65

Schmidt M., 1959, ApJ, 129, 243

Schneider D. P., et al., 2010, AJ, 139, 2360

Schulze A., Wisotzki L., 2010, A&A, 516, A87

Scott N., Graham A. W., Schombert J., 2013, ApJ, 768, 76

Shakura N. I., Sunyaev R. A., 1973, A&A, 24, 337

Shankar F., Salucci P., Granato G. L., De Zotti G., Danese L., 2004, MNRAS, 354, 1020

Shankar F., Marulli F., Bernardi M., Mei S., Meert A., Vikram V., 2013, MNRAS, 428, 109

Shankar F., et al., 2016, MNRAS, arXiv:1603.01276

Shen Y., Kelly B. C., 2012, ApJ, 746, 169

Shirakata H., Okamoto T., Enoki M., Nagashima M., Kobayashi M. A. R., Ishiyama T., Makiya R., 2015, MNRAS, 450, L6

Shirakata H., et al., 2016, MNRAS, 461, 4389

Shirakata H., et al., 2019, MNRAS, 482, 4846

Shlosman I., 2006, The Obscuring Tori of AGN: Merging Disk Wind With Radiative Transfer, HST Proposal

Siana B., et al., 2008, ApJ, 675, 49

Sijacki D., Springel V., Di Matteo T., Hernquist L., 2007, MNRAS, 380, 877

Sijacki D., Vogelsberger M., Genel S., Springel V., Torrey P., Snyder G. F., Nelson D., Hernquist L., 2015, Monthly Notices of the Royal Astronomical Society, 452, 575

Simien F., de Vaucouleurs G., 1986, ApJ, 302, 564

Smoot G. F., et al., 1992, ApJ, 396, L1

Sołtan A., 1982, MNRAS, 200, 115

Somerville R. S., Primack J. R., 1999, MNRAS, 310, 1087

Somerville R. S., Popping G., Trager S. C., 2015, MNRAS, 453, 4337

Springel V., et al., 2005, Nature, 435, 629

Steinhardt C. L., Elvis M., 2010, MNRAS, 402, 2637

Sutherland R. S., Dopita M. A., 1993, ApJS, 88, 253

Telfer R. C., Zheng W., Kriss G. A., Davidsen A. F., 2002, ApJ, 565, 773

Thanjavur K., Simard L., Bluck A. F. L., Mendel T., 2016, MNRAS, 459, 44

Thompson T. A., Quataert E., Murray N., 2005, ApJ, 630, 167

Toba Y., et al., 2015, PASJ, 67, 86

Tomczak A. R., et al., 2014, ApJ, 783, 85

Toomre A., 1964, ApJ, 139, 1217

Toomre A., 1977, in Tinsley B. M., Larson D. Campbell R. B. G., eds, Evolution of Galaxies and Stellar Populations. p. 401

Treister E., Schawinski K., Urry C. M., Simmons B. D., 2012, ApJ, 758, L39

Tully R. B., Fisher J. R., 1977, A&A, 54, 661

Ueda Y., Akiyama M., Ohta K., Miyaji T., 2003, ApJ, 598, 886

Ueda Y., Akiyama M., Hasinger G., Miyaji T., Watson M. G., 2014, ApJ, 786, 104

Urrutia T., Lacy M., Becker R. H., 2008, ApJ, 674, 80

Urry C. M., Padovani P., 1995, PASP, 107, 803

Valiante R., Schneider R., Volonteri M., Omukai K., 2016, MNRAS, 457, 3356

Vanden Berk D. E., et al., 2001, AJ, 122, 549

Vignali C., Brandt W. N., Schneider D. P., 2003, AJ, 125, 433

Volonteri M., Natarajan P., 2009, MNRAS, 400, 1911

Wada K., Habe A., 1995, MNRAS, 277, 433

Wagner A. Y., Bicknell G. V., Umemura M., Sutherland R. S., Silk J., 2016, Astronomische Nachrichten, 337, 167

Wang L., Xu D., Gao L., Guo Q., Qu Y., Pan J., 2018

Watarai K.-y., Fukue J., Takeuchi M., Mineshige S., 2000, PASJ, 52, 133

Weigel A. K., Schawinski K., Treister E., Trakhtenbrot B., Sanders D. B., 2018, MNRAS, 476, 2308

Weinmann S. M., Pasquali A., Oppenheimer B. D., Finlator K., Mendel J. T., Crain R. A., Macciò A. V., 2012, MNRAS, 426, 2797

Wetzel A. R., 2011, MNRAS, 412, 49

White S. D. M., Frenk C. S., 1991, ApJ, 379, 52

White S. D. M., Rees M. J., 1978, MNRAS, 183, 341

White C. E., Somerville R. S., Ferguson H. C., 2015, The Astrophysical Journal, 799, 201

Whittle M., 1992, ApJS, 79, 49

Willott C. J., Delfosse X., Forveille T., Delorme P., Gwyn S. D. J., 2005, ApJ, 633, 630

Willott C. J., et al., 2010a, AJ, 139, 906

Willott C. J., et al., 2010b, AJ, 140, 546

Wu K. K. S., Fabian A. C., Nulsen P. E. J., 1998, MNRAS, 301, L20

Wu X.-B., et al., 2015, Nature, 518, 512

York D. G., et al., 2000, AJ, 120, 1579

Yoshii Y., Arimoto N., 1987, A&A, 188, 13

Yu Q., Tremaine S., 2002, MNRAS, 335, 965

Zamorani G., et al., 1981, ApJ, 245, 357

Zwaan M. A., et al., 2003, AJ, 125, 2842

van den Bosch F. C., Jaffe W., van der Marel R. P., 1998, MNRAS, 293, 343

van der Marel R. P., 1994, MNRAS, 270, 271

Appendix A

Appendix

A.1 The Calculation of Luminosity and Mass Functions

I describe the calculation of the volume-weighted LFs and MFs from the model output. I obtain LFs and MFs from the model at discrete output redshifts. On the other hand, LFs and MFs are estimated from observations in continuous redshift ranges. I thus should estimate model LFs and MFs in the same redshift ranges as observations by averaging model LFs and MFs. I will now describe the derivation of the model LFs. The calculation of MFs is the same as that of LFs, with the magnitude replaced by the logarithmic stellar mass.

The average model LFs have the constant co-moving volume (dV), while the solid angle ($d\Omega$) is constant for observations. The luminosity function, $\phi(z, M)$, in which z and M are the redshift and magnitude, respectively, is described as follows:

$$\phi(z, M) = \frac{dN(z, M)}{dV}, \tag{A.1}$$

where $N(z, M)$ is the number density of objects over the whole sky at z with a magnitude, M. The differential volume (co-moving), dV, is written with the differential solid angle, $d\Omega$, as

$$dV = \frac{cr^2(z)}{H(z)} dz d\Omega. \tag{A.2}$$

I calculate the model LF at a magnitude (M) which is averaged in a redshift range ($z_0 < z < z_n$), $\bar{\phi}(M)$, as follows:

$$\bar{\phi}(M) = \frac{\sum_{i=0}^{n} W_i \phi_i(z_i)}{\sum_{i=0}^{n} W_i}, \tag{A.3}$$

$$W_i = \frac{r^2(z_i) dz_i}{H(z_i)}, \tag{A.4}$$

$$dz_i = (z_{i+1} - z_{i-1})/2, \tag{A.5}$$

where i means the corresponding output number, $r(z)$ and $H(z)$ are the line-of-sight distance and Hubble parameter, respectively. At the larger redshift, the weight becomes larger. Then I can obtain averaged LFs/MFs at a constant solid angle.